Searches for leptophilic dark matter with astrophysical experiments

Von der Fakultät für Mathematik, Informatik und Naturwissenschaften der RWTH Aachen University zur Erlangung des akademischen Grades einer Doktorin der Naturwissenschaften genehmigte Dissertation

vorgelegt von

M. Sc. Leila Ali Cavasonza
aus Finale Ligure, Savona, Italien

Berichter:	Universitätsprofessor Dr. rer. nat. Michael Krämer
	Universitätsprofessor Dr. rer. nat. Stefan Schael

Tag der mündlichen Prüfung: 13.05.16

Diese Dissertation ist auf den Internetseiten der Universitätsbibliothek online verfügbar

RWTH Aachen University

Leila Ali Cavasonza

Institut für Theoretische Teilchenphysik und Kosmologie

Searches for leptophilic dark matter with astrophysical experiments

PhD Thesis

February 2016

Supervisors:

Prof. Dr. Michael Krämer
Prof. Dr. Stefan Schael

Zusammenfassung

Suche nach leptophilischer dunkler Materie mit astrophysikalischen Experimenten

Die Natur der dunklen Materie (DM) zu verstehen ist eines der wichtigsten Ziele der Teilchen- und Astroteilchenphysik. Große experimentelle Anstrengungen werden unternommen, um die dunkle Materie nachzuweisen, in der Annahme, dass sie neben der Gravitationswechselwirkung eine weitere Wechselwirkung mit gewöhnlicher Materie hat. Die dunkle Materie in unserer Galaxie könnte gewöhnliche Teilchen durch Annihilationsprozesse erzeugen und der kosmischen Strahlung einen zusätzlichen Beitrag hinzufügen. Deswegen sind präzise Messungen der Flüsse kosmischer Strahlung äußerst wichtig. Das AMS-02 Experiment misst die Flüsse geladener Teilchen mit zuvor unerreichter Genauigkeit. Vielversprechende DM Kandidaten ergeben sich sowohl im Kontext vollständiger Erweiterungen des Standardmodelles der Teilchenphysik, als auch aus sogenannten minimalen Modellen. Diese Modelle können durch präzise Messungen kosmischer Strahlung getestet werden. Für einen aussagekräftigen Vergleich mit diesen Messungen müssen zwei Voraussetzungen erfüllt sein. Erstens braucht man vollständige Vorhersagen für die durch DM Annihilationsprozesse erzeugten Teilchenflüsse. Zweitens ist eine zuverlässige Beschreibung der astrophysikalischen Flüsse nötig, um das Signal dunkler Materie vom Hintergrund astrophysikalischer Quellen unterscheiden zu können. In dieser Arbeit wird eine spezifische Klasse von Modellen betrachtet, in denen die dunkle Materie in niedrigster Ordnung nur in ein Paar aus einem Elektron und einem Positron annihiliert. Zuerst wird der Einfluss elektroschwacher Korrekturen auf die Vorhersage für die dunkle Materie Signale besprochen. In diesem Zusammenhang wird der Anwendungsbereich eines modellunabhängigen Formalismus für die Beschreibung elektroschwacher Strahlung eingegrenzt. Elektroschwache Strahlung ist besonders wichtig im Kontext dieser leptophilen Modelle, weil sie Hadronen, Neutrinos und Photonen erzeugt, die sonst vernachlässigt würden. Danach wird ein phänomenologisches Modell betrachtet, das die Flüsse von Elektronen und Positronen beschreibt, unter der Annahme, dass astrophysikalische Quellen glatte Flüsse ohne lokale Strukturen erzeugen. Das Modell beinhaltet zwölf Parameter, die durch eine Anpassung an die von AMS-02 gemessenen Flüsse von Elektronen und Positronen bestimmt werden. Die Annihilation von dunkler Materie würde zusätzliche charakteristische Strukturen im Spektrum dieser Flüsse erzeugen. Da keine entsprechenden Strukturen in den von AMS gemessenen Spektren gefunden werden, werden neue Obergrenzen auf den Annihilationswirkungsquerschnitt für leptophile Modelle bestimmt. Unter der Annahme, dass der Annihilationswirkungsquerschnitt an dieser Obergrenze liegt, werden Vorhersagen für den Antiprotonenfluss aus Zerfällen elektroschwacher Eichbosonen berechnet. Diese Flüsse können mit verfügbaren Messungen verglichen werden. Abschließend wird die Produktion leptophiler dunkler Materie am Large Hadron Collider untersucht. Für ein minimales Modell wird der Produktionswirkungsquerschnitt für dunkle Materie berechnet, der in leptophilen Szenarien schleifeninduziert ist.

Abstract

Searches for leptophilic dark matter with astrophysical experiments

One of the most exciting goals of particle and astroparticle physics is the understanding of the nature of dark matter (DM). A huge experimental effort is made to detect DM, under the assumption that some interaction with Standard Model particles exists, besides gravitation. In particular, DM in our Galaxy might annihilate into standard model particles and provide an additional contribution to cosmic ray fluxes. Precise measurements of the cosmic rays fluxes are therefore crucial. The AMS-02 experiment measures the fluxes of charged cosmic rays with unprecedented precision. From the theory side, viable dark matter candidates are provided both as byproducts of well motivated extensions of the standard model and by minimal models. Cosmic rays measurements can be used to probe these DM models. For this, two ingredients are necessary. First, appropriate predictions for the fluxes due to dark matter annihilation in the Galaxy are needed. Second, to be able to detect this exotic cosmic rays contributions, a reliable description of the fluxes of astrophysical origin is required. In this work, we focus on a specific class of DM models, the so-called leptophilic models, where DM annihilates at tree-level only into electron-positron pairs. We first discuss the importance of the inclusion of electroweak (EW) radiation for the theoretical predictions for the DM-induced cosmic ray fluxes. In particular, we study the range of applicability and limitations of a model-independent formalism to include the emission of EW gauge bosons. The inclusion of EW radiation is particularly relevant for leptophilic models, as it induces fluxes of hadrons, neutrinos and photons, that would otherwise be neglected. We then introduce a phenomenological model for the electron and positron fluxes of astrophysical origin. Under the assumption that the energy spectra of astrophysical fluxes are smooth, this model describes them with twelve parameters. We determine these parameters by fitting the model to the AMS-02 measurements of electron and positron fluxes. Dark matter annihilation in the Galaxy would induce additional spectral features on top of the smooth background. Given the absence of statistically significant spectral features in the AMS-02 measurements, we derive new upper limits on the DM annihilation cross section for leptophilic models in general. Assuming that the DM annihilation cross section is close to this upper limit, we obtain predictions for the expected antiproton flux due to the decay of EW gauge bosons. These fluxes can be compared to available measurements. Finally, we briefly study leptophilic DM at the Large Hadron Collider. We consider a specific model and compute the DM production cross section, that is loop-induced in the scenario under study.

Contents

1 Introduction **3**

I Basics **7**

2 General facts about Dark Matter **8**
2.1 Evidence for the existence of Dark Matter 8
2.2 Dark Matter candidates 11
2.2.1 WIMP dark matter 12
2.3 Dark Matter distribution 19
2.4 Dark Matter detection 20
2.4.1 LHC searches 21
2.4.2 Direct detection 22
2.4.3 Indirect detection 23

3 General facts about cosmic rays **28**
3.1 Cosmic rays propagation 30
3.1.1 Positrons and electrons 31
3.1.2 Antiprotons 33
3.2 Solar modulation 33

II Theoretical prediction for dark matter indirect detection **35**

4 Predictions for dark matter indirect detection **36**
4.1 Primary flux from dark matter annihilation in the Galaxy 37
4.1.1 Universal extra dimension model 38
4.1.2 Supersymmetric model 38
4.2 Inclusion of electroweak radiation 40
4.3 Fluxes at Earth 41

5 Fragmentation functions approximation **43**
5.1 The formalism 43
5.1.1 Generalised splitting functions 45
5.2 Comparison to full calculation 46
5.2.1 UED model - vector dark matter 47
5.2.2 SUSY model - Majorana dark matter 50
5.3 Summary 51

III Dark Matter searches with AMS-02 data **59**

6 Modelling of the background **60**
6.1 Background modelling 61
6.2 Fit to electron and positron fluxes 63
6.3 Overall energy uncertainty 64
6.4 Fit to positron fraction and total lepton flux 68

7 Constraining the DM annihilation cross section **69**
7.1 Limits setting 70
7.2 Results for the upper limits on the $2 \to 2$ annihilation cross section and discussion 71
7.3 Inclusion of EW radiation: predictions for antiproton fluxes 73
7.4 Results for the antiproton predictions and discussion 73
7.5 Summary 74

IV Dark Matter searches at the LHC **86**

8 Leptophilic dark matter at the LHC **87**
8.1 The model 87
8.2 Computation of the partonic cross section 88
8.2.1 The amplitudes 88
8.2.2 The loop integrals 91
8.2.3 The cross section 91
8.3 Computation of the hadronic cross section 92

9 Conclusions **96**

V Appendix **100**

A Computation of generalised splitting functions **101**
A.1 More on the Sudakov parametrisation 101
A.2 Explicit calculations 103

B Coefficients A, B and C for generic mediator mass **112**

C Fit to positron fraction and total lepton flux: results. **113**

D Upper limits - uncertainties **116**

E Upper limits from other channels **119**

F Antiproton signals from DM annihilation **121**

G Passarino Veltman reduction **123**

Chapter 1

Introduction

The Standard Model of particle physics (SM) [1–8] provides an extraordinarily precise description of the electroweak and of the strong interactions in terms of a renormalisable quantum field theory. The SM has been tested over more than forty years and its predictions match the experimental measurements with remarkably high precision. The recent discovery of the Higgs boson at the Large Hadron Collider (LHC) [9, 10], predicted by the SM electroweak symmetry breaking mechanism, was one of its most prominent successes. However, it is clear that the SM cannot be the ultimate theory describing elementary particles and their interactions at the fundamental level. Evidence for physics beyond the Standard Model (BSM) comes both from observations and from theoretical arguments. First of all, the SM cannot embed general relativity to provide a quantum description of gravity (*e.g.* [11]). In addition, the observation of neutrino oscillations is in conflict with the SM, where neutrinos are exactly massless. Already this fact shows that an extension of the SM is necessary, in order to provide a mechanism generating the neutrino masses. Overwhelming evidence for BSM physics is provided also by cosmology. One of the most striking examples is the presence of non-luminous matter that accounts for 80% of the total amount of matter in the Universe, whose nature remains unexplained within the SM. This is the main subject of this thesis. Moreover, also the accelerating expansion of the Universe, as well as the matter-antimatter asymmetry and the observed isotropy and homogeneity of the Universe up to very large scales do not find a particle-physics explanation within the SM.

From a theoretical perspective, it is desirable to achieve a description of the gauge couplings of $U(1)$, $SU(2)_L$ and $SU(3)_c$ of the SM in terms of only one gauge group, to obtain a unified description of the electromagnetic, weak and strong interactions. The running of the gauge couplings is governed by the renormalisation group equations and it is known that the SM couplings do not meet at some common scale, while this can be achieved in many so-called grand unified theories. Providing a satisfactory explanation for the smallness of the mass of the Higgs boson in comparison to the Planck scale, the so-called hierarchy problem, also requires extensions of the SM in most scenarios. These models often naturally accommodate other unrelated issues, for instance providing DM candidates.

The main goal of fundamental particle physics nowadays is providing a framework to consistently include and explain all these phenomena.

From the theory side, many attempts have been made to provide viable extensions of the SM, in agreement with observations. A common feature of these BSM theories

is the presence of new particles and interactions. According to many BSM models, like Supersymmetry, new physics phenomena should manifest themselves at the electroweak (EW) scale. A huge effort is ongoing in the experimental community to discover directly or indirectly these hypothetical new states.

A particularly exciting challenge is the investigation of the nature of dark matter, namely the non luminous sort of matter which makes up 80% of the total amount of matter in the Universe. This non luminous matter interacts gravitationally with the ordinary matter. This is essentially the only certain fact about dark matter. There is overwhelming evidence for the existence of dark matter but its nature is still unknown. Dark matter is a particularly attractive subject, as it lies at the interface of particle and astroparticle physics, astrophysics and cosmology. In fact, dark matter was first discovered through astronomical measurements and further confirmed by cosmological observations. The most appealing scenario is that dark matter is made of one or more new particles and many well motivated extensions of the SM provide viable dark matter candidates. Experimental searches in general assume that dark matter interacts not only gravitationally but also via other interactions with SM particles. The second most common assumption is that the mass of the dark matter particle is at the EW scale. This assumption could be regarded as a mere theoretical prejudice, but provides very appealing and interesting scenarios, that can be experimentally tested, as we discuss later on. Under these assumptions, dark matter could be produced at the LHC. A second possibility is to detect dark matter via its interactions with ordinary matter in highly sophisticated detectors on Earth. Finally, dark matter in our Galaxy might annihilate into SM particles and provide an additional contribution to cosmic ray fluxes. All these different searches are very challenging. For instance, the interaction rate of dark matter with ordinary matter is expected to be extremely low, requiring detectors with very low backgrounds. In astrophysical experiments, the astrophysical component in cosmic ray fluxes is often subject to very large uncertainties. The study of these (and many more) issues has provided inspiration for new ideas and directions both on the theoretical and on the experimental side.
Currently, none of the dark matter searches has claimed a discovery[1]. Indirect searches have found some intriguing anomalies with respect to the expectation from standard astrophysics. The discovery of a line at 3.5 keV by X-rays satellites [14, 15], the measurement of an excess in the positron fraction by the PAMELA and AMS-02 experiments [16–18] and, more recently, the discovery of an excess in gamma rays at the Galactic Centre [19–21] are not consistent with the expectations. All or some of these phenomena could originate from known, but not entirely understood, or unknown astrophysical phenomena. On the other hand, an explanation in terms of dark matter annihilation in the Galaxy is also viable making these anomalies particularly interesting.

In general the absence of clear experimental signals allows to constrain or exclude dark matter models. This is the context of the work presented in this thesis. For the main part of this thesis, we restrict ourselves to the study of the constraints that can be deduced from the measurements performed by the AMS-02 experiment [22], a spaceborne experiment that measures fluxes of charged cosmic rays with very high accuracy. We first discuss the importance of including the emission of EW gauge bosons when obtaining theoretical predictions for the dark matter fluxes at Earth. More specifically, we

[1]The DAMA Collaboration [12, 13] has claimed the discovery of a signal, that cannot be explained by standard sources. However, this discovery is still very debated.

study the applicability of a model-independent approximation to include EW emission, involving generalised splitting functions [23] by comparing the results of the approximation to the exact calculations in two specific models. We consider leptophilic dark matter i.e. scenarios where dark matter annihilates at leading order only into electron-positron pairs. One of the main reasons for this choice is that the rôle of EW radiation is particularly relevant for these models. We compute constraints on the dark matter annihilation cross section using the AMS-02 electron and positron flux measurements. Note that these limits apply to leptophilic dark matter models in general, not only to the specific models we use for our studies. To obtain reliable and robust constraints an appropriate description of the astrophysical background is required. We address this issue by introducing a phenomenological model to describe the electron and positron fluxes of astrophysical origin, under the simple assumption that these fluxes are smooth. A contribution due to dark matter annihilation in the Galaxy would provide additional features on top of this smooth background. Given the absence of relevant features in the AMS measurements, we place upper limits on the dark matter annihilation cross section. Including also the effects of EW radiation, we consistently obtain predictions for antiproton fluxes even within purely leptophilic models. We show how these contributions can allow to further constrain this class of models, by comparing to antiproton and antiproton-to-proton ratio measurements.

Finally, we investigate the possibility of studying leptophilic dark matter models at the LHC, where the production of this kind of dark matter is loop-induced. For this study, we compute the cross section for leptophilic dark matter production at the LHC for a specific leptophilic dark matter model.
This thesis is organized as follows:

- In Chapter 2 a brief review of the main observational evidences for dark matter is given. It is not possible to discuss or review all extensions of the SM providing viable dark matter candidates. We only recall how these models can be classified and discuss the so-called WIMP paradigm. We present two specific dark matter candidates relevant to our discussion, namely the Supersymmetric neutralino and the first Kaluza-Klein excitation of the photon in the context of theories with Universal Extra Dimension. Finally, we outline the main features of the possible experimental detection methods. The discussion of collider searches and direct detection experiments is concise. On the contrary, special attention is devoted to the indirect detection methods.

- In Chapter 3 basic facts and issues about cosmic rays are summarised. Special attention is given to the propagation of cosmic rays in the Galaxy. In particular, the relevant models and their uncertainties are discussed. Finally, the semi-analytical approach used for the propagation of the stable Standard Model particles produced via dark matter annihilation is illustrated.

- In Chapter 4 we describe how theoretical predictions for indirect detection experiments are obtained. First, we consider the dark matter annihilation process in the halo, producing the primary flux. With particular emphasis, we discuss on the inclusion of electroweak radiation. More specifically, we show why electroweak corrections play a crucial role in obtaining consistent theoretical predictions for dark matter indirect detection. We then discuss the computation of the secondary flux, produced by the evolution of the final states of the primary process.

- In Chapter 5 we illustrate a model independent method to include the emission of EW gauge bosons using improved fragmentation functions, in analogy to the QCD and QED cases. We study the range of applicability and assess the quality of this method comparing to the exact calculation in two specific cases.

- In Chapter 6 we obtain a reliable phenomenological description of the astrophysical background and discuss the related issues. Special attention is devoted to the discussion of the fits of the phenomenological model to the AMS-02 data.

- In Chapter 7 model independent constraints on the dark matter annihilation cross section are presented. We describe our analysis to obtain upper limits on dark matter annihilation cross sections in a model unspecific manner. We emphasise the importance of the inclusion of low energy effects, like solar modulation, in our analysis. In addition, we discuss the uncertainties coming from astrophysical parameters that enter the propagation method or the choice of the dark matter scenario. We then investigate the impact of electroweak emission in the annihilation process. Strictly speaking, the limits we obtain are no longer model-independent, as we have to consider a specific model to include the electroweak corrections. Finally, we discuss our results and the open issues.

- In Chapter 8 we investigate the possibility of distinguishing leptophilic models from more general models at the LHC within a very simple model. The main part of this chapter is devoted to the calculation of the cross section for dark matter production.

- In Chapter 9 we summarise our results and conclude.

Part I

Basics

Chapter 2

General facts about Dark Matter

Observations at very different scales consistently point towards the existence of an unknown, non-luminous matter component in the Universe, that we can detect through its gravitational effects. The evidence for the existence of the so-called *dark matter* is overwhelming. More than eight decades have passed from the first suggestion that some sort of non-luminous matter must exist, according to astronomical observations [24]. However, the nature of dark matter still remains unexplained and constitutes one of the most relevant and exciting questions of our time. A huge effort is being performed both on the experimental and on the theoretical side to answer this question. The most appealing scenario consists in assuming that the dark matter is made of one or more new particles, that have until now eluded all detection attempts.

In Section 2.1, a brief overview of the evidence for the existence of dark matter is given. After that, possible models providing dark matter candidates are discussed in Sec. 2.2. For a comprehensive review see for instance [25–27]. In Section 2.4, dark matter detection methods are shortly illustrated. The discussion of collider and direct searches is brief, while we focus on indirect detection techniques. In fact, the aim of this work is to discuss issues specific to theoretical prediction for dark matter indirect detection experiments and the constraints on a specific class of models that can be obtained from the measurements performed by the AMS-02 collaboration.

2.1 Evidence for the existence of Dark Matter

In this section, some of the most relevant experimental evidences for the existence of dark matter are discussed. Until now, dark matter has been observed only through its gravitational effects at different scales, ranging from astronomic observations in our Galaxy up to cosmological scales. This wide range of observation not only confirmed the existence of a large amount of non-luminous matter in the Universe, but also allowed to deduce some of its properties.

From a historical point of view, the first hints for non-luminous matter in the Universe came from the studies of the Coma Galaxy Cluster published by F. Zwicky in 1933 [24]. Measuring the velocity of the galaxies in the cluster and applying the virial theorem, he was able to deduce the gravitational potential and from it the total mass of the cluster. Comparing this result against the mass deduced from the luminous matter in the Coma Cluster, he discovered large discrepancies between the two values. In other words, the visible matter could not account for the observed velocity of the galaxies in the cluster.

Even though Zwicky's calculation are now known to be inaccurate, the conclusions were correct.

At the end of the 1970s, the measurements of the velocity of stars in galaxies performed by V. Rubin [28] further supported the idea that a sizeable amount of non-luminous matter exists. More specifically, for a star outside the mass bulk of the galaxy, the velocity is expected to decrease with $v \sim \frac{1}{\sqrt{r}}$, according to Newton's gravitation laws[1]. The measurements revealed strong discrepancies with respect to the expected behaviour. In fact, the velocity is more or less constant with the distance from the galactic centre. This result suggested the existence of a big halo of dark matter distributed around the galaxies, whose mass is of the order of 10-1000 times the luminous mass, depending on the system under study. This scenario could also consistently explain the high velocity of galaxies in the Coma Cluster measured by Zwicky.

On larger scales, gravitational lensing measurements [29] further support the dark matter scenario. A gravitational lens is a massive object (for instance a cluster of galaxies or a black hole) located between an observer and a distant source. The light travelling from the source to the observer is bent because of the presence of the lens, as first predicted by Einstein [30]. The phenomena due to gravitational lensing can be classified in three categories. First, strong lensing induces multiple images of the distant source or the so-called Einstein ring. Second, weak lensing produces distortions of the image of the source. Third, microlensing is the phenomenon where no distortion can be seen, but the amount of light due to the presence of a lens varies with time and this variation can be measured. Of these, the weak lensing phenomena are relevant to dark matter studies. In fact, the magnitude of the deformation induced by the lens is proportional to its mass. Hence, measuring the distortion, the mass of the lens can be obtained. Also with this method very large mass-to-light ratios are obtained. In addition, this technique can be used to reconstruct the mass distribution in galaxy cluster collisions. These studies have shown that the gravitational centre does not correspond to the ordinary matter's centre(*e.g* [31, 32]). Namely, the dark matter halos do not take part in the collision and continue their motions unperturbed. These measurements allow to place limits on the dark matter self interaction cross section .

Finally, from the measurements of the temperature anisotropies of the Cosmic Microwave Background (CMB) performed by WMAP [33] and Planck [34–36] the abundances of baryonic and non-baryonic matter can be precisely deduced. The temperature fluctuations power spectrum is perfectly fitted by the ΛCDM cosmological model (the so-called standard model of cosmology). Two of the main ingredients of this model are a dark matter component and the presence of dark energy, to account for the accelerated expansion of the Universe. The CMB power spectrum (Fig. 2.1) is characterised by the presence of acoustic peaks, due to the oscillation of the baryon-photon plasma in the early universe. From the relative size of the acoustic peaks, the baryonic matter density can be deduced and, from this, the dark matter density can be inferred. From the most recent Planck results [36] the following values for the baryonic matter, dark matter, and

[1]With a more refined argument one obtains ($r > R$)

$$v(r) \propto \left(\frac{r}{2R}\right)^2 \left[I_0\left(\frac{r}{2R}\right) K_0\left(\frac{r}{2R}\right) - I_1\left(\frac{r}{2R}\right) K_1\left(\frac{r}{2R}\right)\right] \overset{r\to\infty}{\to} \frac{1}{\sqrt{r}},$$

where I_0, I_1, K_0, K_1 are the modified Bessel functions of the first and second type.

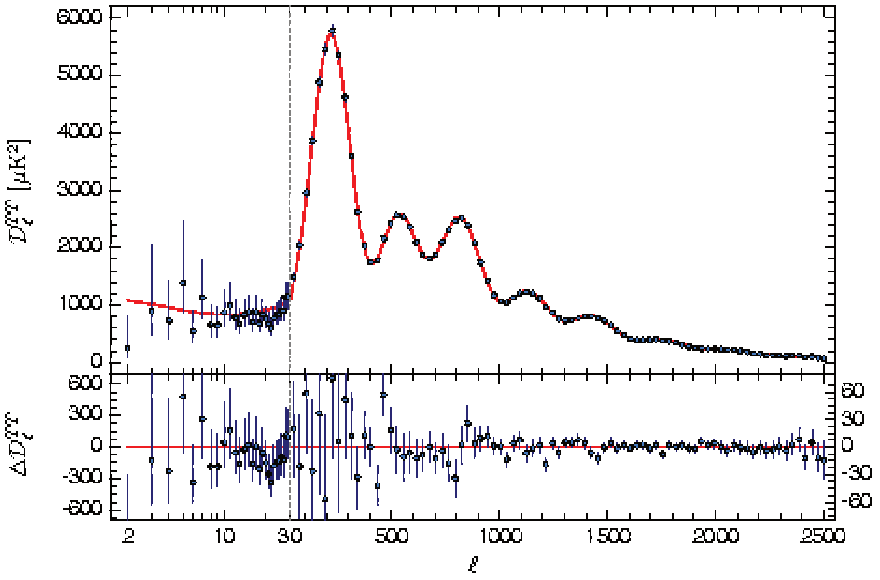

Figure 2.1: The multipole expansion of the temperature power spectrum measured by Planck [36]. The red line shows the best-fit curve obtained by fitting the ΛCDM *cosmological model to the data. The lower panel shows the residuals. (Figure taken from Ref. [36])*

dark energy densities are

$$\Omega_b = 0.049, \qquad \Omega_{\mathrm{DM}} = 0.265 \qquad \text{and} \qquad \Omega_\Lambda = 0.686, \tag{2.1}$$

respectively, where Ω is the ratio of the density with respect to the critical density:

$$\begin{aligned} \Omega_i &= \frac{\rho_i}{\rho_c}, \quad i = \{b, DM, \Lambda\} \\ \rho_c &= \frac{8\pi G}{3H_0^2}, \end{aligned} \tag{2.2}$$

where G and H_0 are the gravitation constant and the Hubble parameter, respectively.

To summarise, from the large collection of observations and under the assumption that the dark matter consists of one or more new particles, the following properties of dark matter can be deduced:

- massive, to account for the observed gravitational effects;
- neutral or with very small charge;
- mostly non-baryonic, to be consistent with the Plank measurements, according to which baryons constitute 1/6 of the total matter in the Universe only. A small component of baryonic dark matter is in principle allowed.
- small interaction (if any) with the Standard Model sector, otherwise it would have already been observed;

- small self-interaction cross section , to be consistent with the observation of collisions of galaxy clusters.

In the next section, we discuss a selection of possible dark matter candidates consistent with these properties.

2.2 Dark Matter candidates

In the last decades, a plethora of extensions of the Standard Model has been proposed, to provide viable non-baryonic dark matter candidates, namely dark matter scenarios consistent with the available observations.

Although the particle-explanation of the dark matter puzzle is usually considered as the most appealing scenario, other attempts were made to explain the observed discrepancies at astronomical scales by introducing modifications of the gravitation laws. These are the so-called Modified Newtonian Dynamic theories (MOND) [37]. However, it has been shown that predictions according to MOND scenarios disagree with large scale structure formation and fail in describing a stable universe [38]. Moreover, even if modified gravitation theories can to some extent account for the observed rotation curve of stars, they fail in explaining contemporaneously *e.g.* the observed lensing phenomena and rotation curves [39].

Therefore, in the following we always assume that the dark matter puzzle has a particle-physics explanation[2]. Before examining exotic candidates, note that it is not excluded that a small fraction of baryonic dark matter exists. Possible candidates would be the so-called massive astrophysical compact halo objects (MACHOs) [41, 42], like brown dwarfs ore black holes or neutron stars. Searches for MACHOs have set an upper limit on the viable total amount of baryonic dark matter [43]. However, Big-Bang nucleosynthesis and CMB studies strongly further restrict the possible baryonic dark matter amount [44].

Turning to non-baryonic dark matter, the only viable candidate within the Standard Model would be the neutrino. However, neutrinos are relativistic particles and they would be hot dark matter particles, namely particles that were relativistic at the time of decoupling. Such a scenario, where all the dark matter in the Universe is hot, is in conflict with large scale structure formation simulations, as shown in Ref. [45].

Therefore, dark matter is assumed to be completely or mostly constituted of particles that were non-relativistic at the time of decoupling, and goes under the name of *cold dark matter*[3] [49].

A huge number of possible extensions of the Standard Model provide possible cold dark matter candidates. There are several ways to classify these models. On a very general basis, they can be distinguished between model motivated by other theoretical reasons than the dark matter puzzle and so-called ad hoc/minimal constructions. Examples of candidates with robust theoretical motivation are for instance sterile neutrinos, the supersymmetric neutralino, and the axion. An other possibility is to classify dark matter models according to the properties of the dark matter candidates. For instance,

[2]Note that other viable "non-particle" explanations for dark matter exist, like primordial black hole, *e.g.* [40]. However, we do not explore these scenarios in this thesis.

[3]There is also the possibility of having warm dark matter [46, 47] or that dark matter is a mixture of relativistic and non-relativistic particles [48]. These options are not discussed here.

according to the possible mass range, or the production mechanism (*e.g.* thermal freeze out, non-thermal, misalignment), or the mediation scheme to the SM (*e.g.* weak scale mediator, Higgs portal, etc.).

One of the best motivated dark matter candidates is the axion or, more generally, axion-like particles (ALP) [50, 51]. The axion is the would-be Goldstone boson of the spontaneously broken Peccei-Quinn symmetry, introduced to solve the strong CP problem [52–54]. Although the standard Peccei-Quinn axion has already been ruled out by experiments, generalisations of the Peccei-Quinn model [55–58] still solve the strong CP problem and provide viable dark matter candidates. The mass of the ALP is in general very small and it can range from 10^{-6} eV up to some eV. Both cosmological and astrophysical observations provide constraints on possible ALP scenarios [59–61] and experimental axion searches are a very active field, *e.g.* [62, 63].

Another well motivated dark matter candidate are sterile neutrinos [64–66]. These can be added to the Standard Model as right-handed partners of the neutrinos in order to provide neutrinos a mass, via the seesaw mechanism. Sterile neutrinos are in general singlets under the Standard Model gauge symmetry group and the allowed mass range is very wide (from few eV up to the GUT scale, 10^{15} GeV).

Many other dark matter candidates have been proposed in the Literature, like super heavy dark matter or WIMPzillas [67–70], non-topological solitons [71, 72], SIMPs (Strongly Interacting Massive Particles) [73], FIMPs (Feebly Interacting Massive Particles) [74] etc. A complete review of all possible dark matter candidates is well beyond the scope of this thesis. Therefore, we close this section discussing in some detail the most popular dark matter candidate in the Literature, the Weakly Interacting Massive Particle (WIMP) and two of its manifestations: the supersymmetric neutralino and the first Kaluza-Klein (KK) excitation of the hypercharge boson. These are the models used later for our phenomenological study. In the very simple set-up we choose, this models provide leptophilic dark matter candidates, namely the dark matter couples only to electrons and positrons at tree-level. However, we do not choose the neutralino and the KK hypercharge boson because we believe them to be the most promising WIMP dark matter candidates, but rather as proxies for Majorana dark matter and vector dark matter, respectively. Furthermore, we consider leptophilic models as the role of electroweak corrections in dark matter indirect detection predictions is particularly prominent, as we discuss in Chapter 4, and because one has the highest sensitivity when comparing against AMS-02 lepton flux measurements, as we argue in Chapter 7.

2.2.1 WIMP dark matter

WIMPs are widely considered to be one of the most appealing and best motivated dark matter candidates. In general, they are stable neutral particles with masses ranging from few GeV up to few TeV. The interactions with Standard Model particles have the typical strength of the weak interactions. In other words, the annihilation cross section into Standard Model particles is of the order of the picobarn. In the standard paradigm, WIMPs were in thermal equilibrium in the early universe when the temperature was larger than the mass of the dark matter particle ($T \gg M_{\rm DM}$) and both the annihilation with its antiparticle into Standard Model particles DM $\overline{\rm DM} \to f\bar{f}$ and the inverse process $f\bar{f} \to$ DM $\overline{\rm DM}$ could take place. Here f is the generic Standard Model species with $m_f < M_{\rm DM}$ so that the reaction is kinematically allowed. The following discussion holds

both in case the dark matter particle and its antiparticle coincide (*i.e.* for Majorana particles) and in case they are distinguishable particles. In this regime of thermal and chemical equilibrium, the WIMPs number density[4] is given by

$$n_{\rm DM} = g_{\rm DM}\frac{3}{4}\frac{\zeta(3)}{\pi^2}T^3 \qquad \text{with} \qquad T \gg M_{\rm DM}, \tag{2.3}$$

where $g_{\rm DM}$ is the number of possible spin states and ζ is the Riemann zeta-function ($\zeta(3) \simeq 1.20$). Because of the expansion of the Universe, at some point the temperature becomes smaller than the dark matter mass and the number density at equilibrium drops exponentially:

$$n_{\rm DM} \simeq \frac{g_{\rm DM}}{(2\pi)^{3/2}}(M_{\rm DM}T)^{3/2}e^{-M_{\rm DM}/T} \qquad \text{with} \qquad T < M_{\rm DM}. \tag{2.4}$$

When the annihilation rate Γ becomes smaller than the expansion rate H, $\Gamma \lesssim H$, the annihilation DM $\overline{\rm DM} \to f\bar{f}$ cannot take place any longer and the number of dark matter particles remains constant as first noticed in Refs. [75, 76] and constitutes the *relic cosmological abundance*. This mechanism is known as *freeze-out* mechanism, see Fig. 2.2. The annihilation rate depends on the dark matter annihilation cross section , $\Gamma = \langle\sigma v\rangle\, n_{\rm DM}$. The time evolution of the dark matter number density is governed by the Boltzmann equation, that in this specific case reads

$$\frac{dn_{\rm DM}}{dt} + 3\frac{\dot{a}}{a}n_{\rm DM} = \langle\sigma v\rangle\left((n^{(0)}_{\rm DM})^2 - n^2_{\rm DM}\right), \tag{2.5}$$

where a is the scale factor of the Universe, $H = \dot{a}/a$ is the Hubble expansion rate. On the l.h.s. the second term takes into account the expansion of the Universe. On the r.h.s. the first term accounts for the creation of WIMPs from the inverse reaction $f\bar{f} \to$ DM $\overline{\rm DM}$, while the second term accounts for the depletion of WIMPs because of the annihilation process DM $\overline{\rm DM} \to f\bar{f}$. At equilibrium the two contributions are equal. The dark matter number density at equilibrium $n^{(0)}_{\rm DM}$ reads

$$n_{\rm DM} = \int \frac{d^3k}{(2\pi)^3} f_{\rm DM}(\vec{k}), \tag{2.6}$$

or, for the generic species i

$$n_i = \int \frac{d^3k}{(2\pi)^3} f_i(\vec{k}), \tag{2.7}$$

where the distribution function is given by

$$f_i(\vec{k}) = \frac{g_i}{(2\pi)^3\hbar^3}\frac{1}{e^{[(E_i-\mu_i)/k_BT]}+\alpha} \simeq e^{\mu_i/k_BT}e^{-E_i/k_BT} \quad \text{if } T < E_i - \mu_i, \tag{2.8}$$

with $\alpha = +1$ for the Fermi-Dirac distribution, $\alpha = -1$ for the Bose-Einstein distribution and $\alpha = 0$ for the Boltzmann distribution. The chemical potential μ_i is conserved at equilibrium. The thermal averaged cross section $\langle\sigma v\rangle$ that appears in the r.h.s of the Boltzmann equation can be in general computed as

$$\begin{aligned}\langle\sigma v\rangle = \frac{1}{n^2_{\rm DM}}\int &\frac{d^3Q_1}{(2\pi)^3 2Q_1^0}\frac{d^3Q_2}{(2\pi)^3 2Q_2^0}\frac{d^3p_1}{(2\pi)^3 2p_1^0}\frac{d^3p_2}{(2\pi)^3 2p_2^0}e^{-(Q_1^0+Q_2^0)/k_BT} \\ &(2\pi)^4\delta^{(3)}(Q_1+Q_2-p_1-p_2)|M|^2,\end{aligned} \tag{2.9}$$

[4] In this context, number density means number of particles per comoving volume.

where $|M|^2$ is the squared matrix element for the process $\mathrm{DM}(\mathrm{Q}_1)\ \overline{\mathrm{DM}}(\mathrm{Q}_2) \to f(p_1)\bar{f}(p_2)$. An exact fully analytic solution of the Boltzmann equation is not known. We provide here an approximate solution obtained assuming that the thermal averaged annihilation cross section is energy independent following Ref. [25]. For a more accurate treatment we refer the interested Reader to [77, 78].
In a radiation dominated early Universe, the Hubble parameter has the following dependence on the temperature:

$$H(T) = \left(\frac{4\pi^3 G}{45(\hbar c)^3}\right)^{1/2} g_*^{1/2}(k_B T)^2 \simeq 1.66 g_*^{1/2}\frac{T^2}{M_{\rm Pl}}, \tag{2.10}$$

where G is the gravitation constant, $\hbar$ the reduced Planck constant, c the speed of light, $g_*^{1/2}$ the effective number of relativistic degrees of freedom[5], k_B the Boltzmann constant, and $M_{\rm Pl}$ the Planck mass.
At high temperatures the Hubble parameter scales as $H \sim T^2$, while the number density scales as $n_{\rm DM} \sim T^3$. Hence, we can neglect the expansion term in the l.h.s. of Eq. (2.5). On the contrary, at low temperature the variations in the number density due to dark matter annihilation into Standard Model particles and viceversa become negligible when compared to expansion term $3Hn_{\rm DM}$. To determine the freeze-out temperature T_f, one has to solve $\Gamma(T_f) = H(T_f)$. For weakly interacting particles, the freeze-out temperature is approximately $T_f \sim M_{\rm DM}/20$ [77]. For $T < T_f$ the dark matter number density remains constant. Since also the entropy density $s \simeq 0.4 g_* T^3$ is conserved, the quantity $n_{\rm DM}/s$ is also constant and, in particular, it has the same value at freeze-out and today. This allows us to compute the relic abundance today. In fact, at freeze-out we can write $n_{\rm DM}/s$ as

$$\begin{aligned}
\left(\frac{n_{\rm DM}}{s}\right)(T_f) &= \frac{H}{\langle\sigma v\rangle s}, \qquad \text{as } \Gamma(T_f) = H(T_f) \\
\left(\frac{n_{\rm DM}}{s}\right)(T_f) &= \frac{1.66 g_*^{1/2} T_f^2}{M_{\rm Pl}\langle\sigma v\rangle 0.4 g_* T_f^3} = \frac{100}{M_{\rm DM} M_{\rm Pl}\, g_*^{1/2}\langle\sigma v\rangle}
\end{aligned} \tag{2.11}$$

and this equals the value today, $\left(\frac{n_{\rm DM}}{s}\right)_{\rm today}$. The dark matter density can be expressed in terms of the critical density $\rho_c = 3H^2/8\pi G$:

$$\Omega_{\rm DM} h^2 = \frac{M_{\rm DM} n_{\rm DM}}{\rho_c}. \tag{2.12}$$

Knowing the value of the entropy density today, $s \simeq 4000\mathrm{cm}^{-2}$, from Eq. (2.11) we obtain the number density today. Moreover, the value of the critical density today is $\rho_c \simeq 10^{-5} h^2$ GeV cm^{-3}, with $h = H/(100\mathrm{km\,s^{-1}Mpc^{-1}})$. The dark matter relic abundance becomes

$$\Omega_{\rm DM} h^2 = \frac{3 \times 10^{-27}\mathrm{cm^3 s^{-1}}}{\langle\sigma v\rangle}. \tag{2.13}$$

From the measurements one has $\Omega_{\rm DM} h^2 \simeq 0.11$. From Eq. (2.13) it is clear that for cross sections of the order of weak interaction cross sections the dark matter relic abundance

[5] At a given temperature T the effective number of degrees of freedom is [77] $g_* = \sum_B g_{i_B}\left(\frac{T_{i_B}}{T}\right)^4 + \frac{7}{8}\sum_F g_{i_F}\left(\frac{T_{i_F}}{T}\right)^4$, where the sums run over all bosonic (B) and fermionic (F) species that are relativistic at that given temperature and T_{i_B} and T_{i_F} are the decoupling temperatures of the particles of kind i.

matches the measured values. This remarkable coincidence is probably the strongest motivation for *weakly* interacting massive particles.

Supersymmetry and UED are two frameworks that can provide a neutral stable massive particle with the correct annihilation cross section to account for the observed dark matter abundance. We briefly summarise the motivations and main features of these two classes of models and the dark matter candidates they provide.

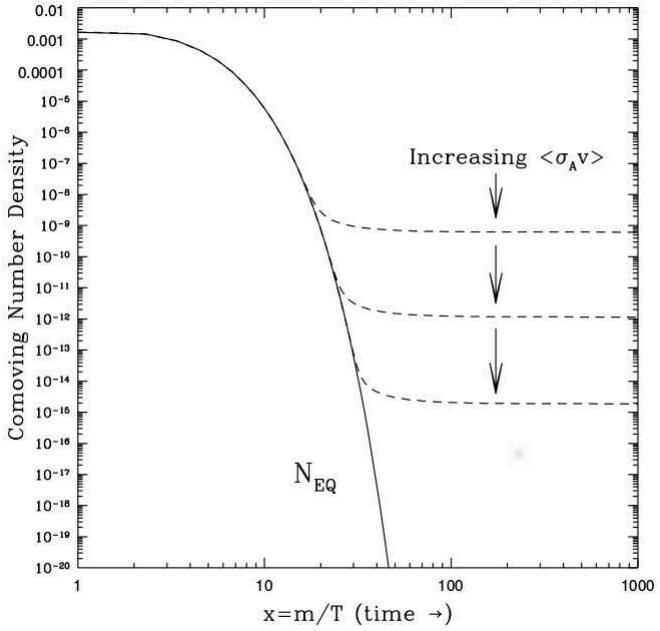

Figure 2.2: Evolution of the dark matter number density with time. The impact of the value of the thermal averaged annihilation cross section on the freeze-out mechanism is shown. Picture from Ref. [77].

Supersymmetry

Supersymmetric models are extensions of the Standard Model, where an additional symmetry connecting fermionic and bosonic degrees of freedom is added to the Standard Model symmetries. More specifically, according to the Coleman-Mandula theorem [79] and under very general assumptions, the most general Lie algebra of symmetry operators commuting with the S-matrix is the one of the generators of the Poincare group and internal symmetries generators. However, it is yet possible to enlarge the Lie algebra of operators commuting with the S-matrix if also spinorial operators are taken into account besides the usual bosonic operators, as stated by the Haag-Lopusanski-Sohnius theorem [80]. In other words, if also anticommutation relations between generators of the symmetry group are allowed (in addition to the usual commutation relation of the generators of the Poincare group), it is possible to build a new extended Lie algebra whose generators still commutes with the S-matrix and that encompasses the Poincare group. In summary, supersymmetry (SUSY) is the most general symmetry group whose generators commute with the S-matrix. This theoretical argument would be already enough to make supersymmetry worth to be studied.

Nevertheless, supersymmetry has several other features that make it attractive as beyond-the-Standard Model theory. First, Supersymmetry provides naturally a solution to the so-called "weak-instability problem" or "hierarchy problem", namely the fact that the mass of the Higgs boson receives at one-loop contributions in principle of the order of the Planck mass and that some remarkable cancellation has to take place in order to get to the measured value $m_H \simeq 125\,\text{GeV}$. These large contributions to the self-energy of the Higgs come for instance from the massive fermion loops, like the top-quark loop. Supersymmetry predicts the existence of a scalar partner of the top-quark, whose contribution to the self-energy of the Higgs boson would be exactly the same but of opposite sign, cancelling the so-called quadratic divergencies. Second, gauged supersymmetry (also called supergravity) provides a natural connection with gravity [81, 82]. Third, already in minimal realisations of supersymmetry, gauge coupling unification is achieved at one-loop level, contrarily to the Standard Model.

As already mentioned, in supersymmetric models each Standard Model degree of freedom is associated to a so-called superpartner, namely new fermionic degrees of freedom are introduced for each Standard Model bosonic degree of freedom and viceversa. More specifically, the superpartners of matter fields (sleptons and squarks) are spin-0 scalars and the superpartners of the gauge fields (gauginos) are spin-$\frac{1}{2}$ fermions. In addition, a second Higgs doublet is required for technical reasons (see for instance Refs. [83–85]), that implies the presence of four new Higgs bosons in addition to the "Standard Model Higgs". If supersymmetry were unbroken, the Standard Model particle and its superpartner would have exactly the same mass. However, no such particles has ever been observed. Therefore supersymmetry must be a spontaneously broken symmetry. The SUSY breaking mechanism is unknown, so all possible renormalisable terms consistent with the symmetry group of the theory must be included in the Lagrangian. Thus, a large number of parameters is necessary to describe supersymmetry [86]. The

Matter fields & partners	spin-0	spin-1/2	$SU(3)_c, SU(2)_L, U(1)_Y$
squarks & quarks (3 families)	$(\tilde{u}_L, \tilde{d}_L)$ $\tilde{\bar{u}}_L \sim (\tilde{u}_R)$ $\tilde{\bar{d}}_L \sim (\tilde{d}_R)$	(u_L, d_L) $\bar{u}_L \sim (u_R)^c$ $\bar{d}_L \sim (d_R)^c$	3 , 2, 1/3 $\bar{3}$, 1, −4/3 $\bar{3}$, 1, 2/3
sleptons & leptons (3 families)	$(\tilde{\nu}_{eL}, \tilde{e}_L)$ $\tilde{\bar{e}}_L \sim (\tilde{e}_R)$	(ν_{eL}, e_L) $\bar{e}_L \sim (e_R)^c$	1 , 2, −1 1 , 1, 2
higgs & higgsinos	(H_u^+, H_u^0) (H_d^0, H_d^-)	$(\tilde{H}_u^+, \tilde{H}_u^0)$ $(\tilde{H}_d^0, \tilde{H}_d^-)$	1 , 2, 1 1 , 2, −1
Gauge fields & partners	spin-1/2	spin-1	$SU(3)_c, SU(2)_L, U(1)_Y$
gluinos & gluons	$\tilde{g}$	g	8, 1, 0
winos & Ws	$\tilde{W}^{\pm}$, $\tilde{W}^0$	$W^{\pm}$, W^0	1, 3, 0
binos & B	$\tilde{B}$	B	1, 1, 0

Table 2.1: Supersymmetric particles and their quantum numbers in the MSSM.

Minimal Supersymmetric Standard Model (MSSM hereafter) [84] contains all Standard Model particles and superpartners and two Higgs doublets (see Tab. 2.1). The charged higgsinos and the charged gauginos (superpartners of the charged Higgs bosons and of the W) can mix after electroweak (EW) symmetry breaking as they carry the same quantum numbers. The mass eigenstates are called charginos. Similarly, the mixing

of the superpartners of the photon, of the Z boson and of the neutral Higgs bosons induces four neutral particles, the neutralinos. To define the MSSM, an additional discrete symmetry is introduced, the R-parity, with $R = (-1)^{3(B-L)+2S}$, where B, L, S are the baryon number, the lepton number and the spin operators, respectively. R-parity forbids lepton-violating and baryon-violating operators that are strongly constrained by observations. Moreover, it prevents fast proton decay. The inclusion of R-parity has another consequence relevant for our discussion. From its definition, one sees that Standard Model particles have $R = +1$, while the superpartners have $R = -1$. This implies that supersymmetric particles are always pair-produced at colliders and that the lightest supersymmetric particle (LSP) is stable[6]. The LSP is in many scenarios the lightest of the four neutralinos. Being neutral, it represents a natural dark matter candidate. The neutralino is not the only possible dark matter candidate within SUSY models. Also the gravitino and the sneutrinos represent viable dark matter candidates in some scenarios. However, the neutralino remains the by far most studied supersymmetric dark matter candidate.

Because of the unknown nature of the SUSY breaking mechanism, the MSSM is described by about 120 parameters, including the masses of the new particles, the vacuum expectation values (vevs) of the two Higgs doublets, mixing angles and couplings[7]. This large number of parameters makes the phenomenology of the MSSM (and of more general scenarios we do not mention here) very challenging. In order to have more predictive models, additional assumptions are usually added. This can be done for example selecting a specific SUSY breaking mechanism or assuming some specific relation among the parameters at high scale, *e.g.* the Planck scale. One of the simplest scenarios that can be achieved is the *constrained Minimal Supersymmetric Standard Model* (cMSSM). Under very strong simplifying assumptions, the model is described by only 5 parameters. In particular, one assumes that at the Planck scale all the gaugino masses and Higgs' masses have the same value m_0, and the same for all sfermion masses, $m_{1/2}$. Moreover, all trilinear scalar coupling are assumed to have the same strength, A_0. In addition to these parameters, $\tan\beta$ represents the ratio of the vevs of the two Higgs doublets and the parameter μ, that is the strength of the bilinear coupling of the two different Higgs doublets.

In Chapters 4 and 5 we will consider a simple SUSY scenario, with the neutralino as LSP.

Universal Extra Dimensions

Several extra dimensional scenarios have been proposed in the Literature as extensions of the Standard Model, for instance in [90–94]. The idea was first introduced by Kaluza [95], in order to extend general relativity to more than 4 dimensions. Few years later, Klein [96] introduced the idea that the additional dimension could be compactified and microscopic.

Extra dimensional theories have solid theoretical motivation and in some cases pro-

[6] R-parity violating supersymmetric models have been proposed and studied in the Literature [87, 88]. However, in general they do not naturally provide viable dark matter candidates. Therefore, we do not consider them here.

[7] For a complete discussion of SUSY particle spectra and parameters, as well as more formal aspects we refer to Refs. [83–85, 89]

vide viable dark matter scenarios[8]. They can be sorted in two classes. In ADD [90, 91] or Randall-Sundrum models [93, 94], the extra-dimension(s) is large compared to the Planck scale. These models are further distinguished in models where only gravity can propagate in the bulk, while Standard Model fields are confined in the usual 3 spatial dimension or other models, where gauge bosons and the Higgs boson propagate in the bulk, while fermion do not [99, 100]. In the second class of models, the extra dimensions are small compared to the Planck scale. This is the case in Universal Extra Dimension models (UED). Here all particles can propagate in the additional dimensions, that are compactified. In the following we focus only on the latter class of models.

One of the strongest motivations for UED in contrast to other scenarios is that rapid proton decay is strongly suppressed [101, 98] and, therefore, the predicted rate agrees with the experimental bounds. In addition, gauge anomalies cancel in UED models with three generations of fermions, as shown in [102]. Finally, and most important for our discussion, UED models provide viable candidates for non-baryonic dark matter.

Extending the Standard Model to $4 + d$ dimensions and allowing all particles to propagate in the additional dimensions (compactified, with R being the compactification radius), all $4 + d$ dimensional fields can be written in terms of a decomposition in so-called KK modes. For instance, for one extra dimension, $d = 1$, gauge boson fields can be decomposed as:

$$\begin{aligned} A_\mu(x^\mu, y) &= \frac{1}{\sqrt{\pi R}} \left(A_{\mu,0}(x^\mu) + \sqrt{2} \sum_{n=1}^{\infty} A_{\mu,n}(x^\mu) \cos\left(\frac{ny}{R}\right) \right) \\ A_5(x^\mu, y) &= \sqrt{\frac{2}{\pi R}} \sum_{n=1}^{\infty} A_{5,n}(x^\mu) \sin\left(\frac{ny}{R}\right), \end{aligned} \tag{2.14}$$

where x^μ are the usual space-time coordinates and y is the coordinate along the fifth dimension. The same decomposition holds for Higgs boson fields. To have fermionic fields in 5D it is necessary to introduce two fermionic 5D fields for each Dirac field of the Standard Model. This is due to the impossibility of constructing a 5D analogous of the γ_5 matrix [98]. This technical issue can be circumvented and also fermionic fields admit a decomposition in terms of KK modes. The $n = 0$ of the KK tower corresponds to the Standard Model fields, while we call the higher modes *KK excitation* of a given Standard Model particle.

The mode-number n is related to the momentum along the extra dimension(s). As momentum is a conserved quantity, the KK-number should be a conserved quantity. However, the compactification procedure[9] breaks the translation invariance along the compactified dimension(s) and, therefore, the mode number conservation is broken to the so-called KK-parity conservation. KK-parity is analogous to R-parity in supersymmetry. Its action on the states is $P = (-1)^n$. Standard Model particles are clearly KK-even, while the first KK modes are KK-odd. Similarly to SUSY, KK-parity implies that KK-odd particles are pair produced at colliders and that the lightest KK-odd particle (LKP) is stable. If the LKP is neutral, it can serve as dark matter candidate.

[8] For a complete discussion of extra dimensional models, plese refer to Refs. [97, 98] and references therein.

[9] In UED the extra dimensions are orbifolded [97, 98]. This means that the compactification is not on the circle, but rather the circle is mapped onto a line with two fixed points.

At tree-level the masses of the KK-modes are given by [98, 103]

$$M^2 = M_{(0)}^2 + \frac{n^2}{R^2}, \tag{2.15}$$

where M denotes the mass of a generic Standard Model species. Given that $1/R \sim 1$ TeV, then $1/R \gg M$, namely the spectrum at tree-level is rather compressed. However, loop corrections break this degeneracy of the masses of the tower of KK-modes and, in general, the masses of the $n > 0$ modes turn out to be significantly larger than the masses of the Standard Model particles. In many UED scenario, the LKP are either the first excitation of the neutral gauge bosons $(B^{(1)}, W_3^{(1)})$ or the first excitation of the neutrino $(\nu^{(1)})$, namely non-baryonic neutral particles, and they both provide viable dark matter candidates. We focus on the neutral gauge boson partners, as these will be relevant later on. After EW symmetry breaking, mixing between the $B^{(n)}$ and $W_3^{(n)}$ fields is induced at all levels. At $n = 0$ the mixing is the standard Standard Model mixing in the EW sector parametrised by the Weinberg angle. For a generic value of n, the mass matrix is given by [103]

$$\begin{pmatrix} \frac{1}{4}g_1^2v^2 + \frac{n^2}{R^2} + \delta M_1^2 & \frac{1}{4}g_1g_2v^2 \\ \frac{1}{4}g_1g_2v^2 & \frac{1}{4}g_2^2v^2 + \frac{n^2}{R^2} + \delta M_2^2 \end{pmatrix}, \tag{2.16}$$

where g_1 and g_2 are the $U(1)_Y$ and $SU(2)_L$ couplings, v is the vev of the Higgs field and R the compactification radius. Because of the radiative corrections δM_1^2 and δM_2^2, the mixing is different for each value of n, namely the mixing is parametrised at each level by a different Weinberg angle. However, with reasonable assumption on δM_1^2 and δM_2^2[10] the mixing angle for $n = 1$ is essentially zero and therefore the lightest mass eigenstate is essentially $B^{(1)}$. Moreover, as EW symmetry breaking effects introduce corrections of order $v^2R^2 \ll 1$, one can neglect these effects in first approximation. This amounts to treating the hypercharge boson effectively as the photon, but neglecting the couplings to gauge bosons [11].

In the simple UED model we consider in Chapters 4 and 5, we take the $B^{(1)}$ to be the LKP and we neglect EW symmetry breaking effects.

2.3 Dark Matter distribution

The modelling of the dark matter distribution in galaxies and in particular, in the Milky Way, is crucial for dark matter direct and indirect detection experiments, as well as the value of its local density and the velocity distribution.

Studies of the distribution of dark matter are performed via N-body simulations, that suggest that the dark matter profile is the same for all masses([26] and refs. therein). However, there is no common agreement on the dark matter distribution profile. The most used dark matter profiles in the Literature are the Navarro, Frenk and White (NFW) profile [104, 105] and the Einasto profile [106, 104]. There is at the moment no agreement on the shape of the dark matter profile in the Milky Way and in galaxies, in general. We give here the explicit form of the most studied dark matter profiles in the

[10] More specifically, $\delta M_2^2 - \delta M_1^2 \gg g_1g_2v^2$ as argued in Ref. [97].

[11] This generates sometimes some confusion in the Literature, as the word "KK-photon" is used to denote both the $B^{(1)}$ and the $\gamma^{(1)}$.

Literature, as these are relevant when computing predictions for dark matter detection experiments. The dark matter distribution in galaxies is usually assumed to have a spherical symmetry and the dependence on the distance from the centre of the galaxy r is parametrised in the following ways:

$$\rho(r) = \begin{cases} \rho_s \frac{r}{r_s}\left(1+\frac{r}{r_s}\right)^2 & \text{NFW;} \\ \rho_s \exp\left(-\frac{2}{\alpha}\left(\left(\frac{r}{r_s}\right)^\alpha - 1\right)\right) & \text{Einasto;} \\ \frac{\rho_s}{1+\left(\frac{r}{r_s}\right)^2} & \text{Isothermal;} \\ \frac{\rho_s}{\left(1+\frac{r}{r_s}\right)\left(1+\left(\frac{r}{r_s}\right)^2\right)} & \text{Burkert;} \\ \rho_s \left(\frac{r}{r_s}\right)^a \left(1+\frac{r}{r_s}\right)^b & \text{Moore;} \end{cases} \tag{2.17}$$

where the value of α for the Einasto profile is different in different simulations, with central value $\alpha = 0.17$, while for the Moore profile $a = 1.16$ and $b = -1.84$ [107]. The constant r_s and ρ_s are related to the virial mass of the Galaxy. Typical values are $r_s = 28.44$ kpc, $\rho_s = 0.033$ GeV/cm^3 [107–109].

Both the local density and the velocity distribution of the dark matter particles can be determined from measurements of the rotations curves of the Milky Way. The allowed range for the local density is $\rho_\odot = 0.2-0.8$ GeV/cm^3, but the typical value considered in the Literature is $\rho_\odot = 0.3$ GeV/cm^3 [26, 107]. The central value for the average velocity is $\bar{v} = \langle v^2 \rangle^{1/2} \simeq 270$ km/s. These parameters are subject to large uncertainties, due to the difficulty in measuring precisely the rotation curve of our own Galaxy.

These uncertainties have a relevant impact in the interpretation of experimental results, as we will discuss later on.

2.4 Dark Matter detection

A huge experimental effort is devoted to the investigation of the nature of Dark Matter. To this aim, a plethora of experiments all over the world is running, exploiting very different techniques, with special focus on the detection of WIMPs. If dark matter was produced and in thermal equilibrium in the early universe, it is reasonable to assume that some kind of interaction with the standard sector exists. Under this assumption, there are three possible ways to search for dark matter, apart from observing its gravitational effects. First, it could be produced at colliders like the LHC via Standard Model particles annihilation. Second, one could measure the recoil energy due to the scattering of dark matter particles of the halo against nuclei. These are the so-called direct detection experiments. Third, assuming that dark matter in the galactic halo can annihilate or decay in Standard Model particles, additional contributions to the cosmic rays fluxes are expected besides those of astrophysical origin. Indirect detection experiments aim at the detection of these exotic components in cosmic ray fluxes.

These three approaches are complementary. For example, the discovery of a new neutral massive particle at the LHC would not be sufficient to claim the discovery of dark matter. Consistent signatures have to be confirmed by direct and/or indirect detection experiments.

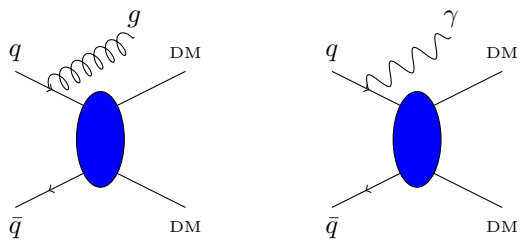

Figure 2.3: Examples of diagrams relevant to mono-jet and mono-photon searches at the LHC. The blue bubble schematically represents the unknown interaction responsible for dark matter production at the LHC.

In this section, the main features of collider searches and direct detection experiments are summarised[12]. A more complete discussion of dark matter searches at the LHC and direct searches can be found *e.g.* in [110] and [111]. More attention is devoted to indirect detection experiments, like the AMS-02 experiment, as our focus are theoretical predictions for this class of experiments and the possible constraints that one can deduce from the AMS-02 measurements.

2.4.1 LHC searches

If dark matter is somehow coupled to the Standard Model , dark matter could be produced at the Large Hadron Collider. Dark matter searches performed by the CMS and ATLAS collaborations [112, 113] are a subset of the searches for physics beyond the Standard Model. As already mentioned, if the LHC would discover a new massive neutral particle, only a consistent observation for instance by astrophysical experiments would confirm it being dark matter.

If dark matter particles were produced at the LHC, they would escape the detectors, like neutrinos. Therefore one searches for missing transverse momentum (or missing transverse energy MET) and at least one more object in the calorimeter or in the muon system to trigger on. According to their final states, the searches are called mono-jet, mono-photon, mono-Z/W or mono-H searches, see Fig. 2.3. Other searches assume that heavier coloured new particles can be produced, that subsequently decay into WIMPs and Standard Model particles. Finally, searches for invisible Higgs decays can also probe WIMPs production at colliders.

In single-bin counting experiments, one compares the measured number of events in the region of interest (after appropriate cuts to maximise the signal-to-background ratio) with the predictions according to the Standard Model, that constitutes the background for all searches for new particles. If no significant deviations from the expected background are observed, one can place upper limits (UL) on the maximum number of dark matter signal events $N_{\rm UL}$ consistent with the measurements, and this limit can be converted into an upper limit on the cross section , $\sigma_{\rm UL}$:

$$\sigma_{\rm UL} = \frac{N_{\rm UL}}{\mathcal{L} \times A_{\rm th} \times \epsilon}, \tag{2.18}$$

[12]We do not aim at a complete review of all experimental techniques and experiments trying to detect dark matter. This would be far beyond the scope of this thesis.

where $\mathcal{L}$ is the integrated luminosity of the analysed dataset, $A_{\rm th}$ is the acceptance and ϵ the efficiency. This limit on the cross section can be interpreted in terms of specific dark matter models to constrain the parameters space. Strictly speaking, the computation of the $\sigma_{\rm UL}$ in Eq. 2.18 is model dependent, as the acceptance has to be computed via MonteCarlo simulation to know what fraction of events is left after applying for instance p_T cuts and for this a specific models has to be chosen. Also the interpretation of the bounds in terms of specific dark matter scenario is model dependent.

A huge number of searches are performed by the ATLAS and CMS collaborations at the LHC in order to explore as many scenarios as possible. Recent summaries of the results and future plans can be found for instance in [110, 114, 115] and in [110, 116, 117] for ATLAS and CMS, respectively.

2.4.2 Direct detection

Direct detection experiments aim at measuring the interaction rate of dark matter particles with Standard Model particles. In other words, the dark matter particles that constitute the dark matter halo around our Galaxy may interact with ordinary particles, for instance via elastic or inelastic scattering on nuclei or elastic scattering on electrons [13]. Elastic scattering on nuclei is considered the most promising option and many experiments are build to measure the recoil energy of nuclei due to elastic scattering with dark matter particles.

The signal rate for a WIMP dark matter particle is given by [118]

$$R \simeq \frac{\rho_{\rm DM}}{M_{\rm DM}} \frac{\langle v_{\rm DM} \rangle \sigma}{A}, \tag{2.19}$$

where $\rho_{\rm DM}$, $M_{\rm DM}$ and $v_{\rm DM}$ are the local dark matter density, the mass of the WIMP and its velocity relative to the target, respectively. We denote the interaction cross section of a dark matter particle by σ and the nucleus mass number with A. With standard values for the parameters[14] one obtains for the rate ~ 0.01 events/kg $\cdot$ day corresponding to $\sim 10^{-7}$ Bq/kg. This is an extremely low rate if compared, for instance, to the air we breath, that has an activity of about 10 Bq/kg. This already shows one of the main challenges of direct detection experiments, namely the reduction of the background, that is in general several orders of magnitude larger than the signal one tries to detect.

Moreover, although the recoil energy is completely fixed by kinematics, the full recoil spectrum (Eq. (2.20) [118]) depends on poorly known quantities, like the nuclear form factors $F(E)$ for the nuclear species under study.

$$\frac{dR}{dE} \simeq \frac{dR}{dE}\Big|_0 F^2(E) \exp(-\frac{E}{E_c}), \tag{2.20}$$

where $\frac{dR}{dE}\Big|_0$ is the rate at zero momentum transfer and E_c depends on the dark matter mass and the nuclear species constituting the target. There are many ongoing studies trying to obtain more accurate predictions for the nuclear form factors. However, these still constitute a large source of uncertainty.

[13] There are other possibilities. For instance, conversion of particles to photon, as axions would do, but we do not consider such scenarios here.

[14] For instance $\rho_{\rm DM} = 0.3$ GeV/cm^3, $M_{\rm DM} = 10$ GeV, $\langle v_{\rm DM} \rangle = 230$ km/s, $\sigma = 10^{-38}$ cm^2, $A = 40$.

There are two possible ways to search for dark matter with direct detection experiments, both being exploited in running experiments. The first one consists in making a specific assumption for the nature of the dark matter particle, build a detector minimising the relevant backgrounds and try to detect the interactions that are expected according to the model (or class of models) chosen. For this approach, an accurate knowledge of the backgrounds and extremely pure materials to build the detectors are needed. This approach is clearly strongly dependent on the dark matter assumptions made. A second possibility is based on the fact that annual modulations are expected in the signal rate. This is due to the fact that the Solar System, and hence the Earth, moves in the Galaxy with a typical velocity of ~ 230 km/s. Moreover, the Earth revolves around the Sun with a velocity of about ~ 30 km/s. Thus, in each energy bin, the measured rate is expected to exhibit an annual modulation. With this approach, a specific assumption on the nature of the dark matter particle is not necessary. However, the amplitude of the modulation strongly depends on the assumption made for the dark matter velocity distribution and on the dependence of the interaction cross section on the velocity. Therefore, also this approach is model dependent. On the other hand, a precise knowledge of the background is less important, as one searches for the modulation.

Several techniques are being exploited in order to detect the interactions of dark matter with nuclei in a detector. The first technique consists in looking for *scintillation light* in solid scintillators (crystals) or liquid scintillators (noble gas/liquid). Atoms in the target are excited because of scattering with dark matter particles and emit scintillation light. This is the technique exploited by the DAMA Collaboration [12, 119, 120], with NaI crystals, and by the XMASS experiment [121, 122], with liquid Xenon. A second technique consists in measuring the signal due to *ionization* of atoms, again both in crystals and in noble liquids or gas. This technique is for instance applied by CoGeNT [123], with germanium crystals. The third technique consists in measuring the deposited energy in the target, using *cryostatic bolometers*. In this case the energy is transferred to the lattice and the vibrations can be measured. This technique was used by the CRESST [124, 125] experiment. Many of the experiments running at the moment exploit combinations of two of these techniques, as this allows for a more efficient background reduction. For instance, the liquid Xenon detectors of the Xenon10, Xenon100 and (planned) Xenon1T [126–130], and Lux [131–133] experiments and the liquid Argon detector of the DarkSide experiment [134, 135] search both for scintillation and ionisation light. Experiments like ROSEBUD [136, 137] and CRESST-II [138, 139] combine bolometric techniques with scintillation light measurements. Finally, the SuperCDMS [140, 141] and Edelweiss [142, 143] experiments combine bolometric techniques with the measurement of ionisation light.

Up to now, only the DAMA-Libra collaboration has claimed the detection of a dark matter signal [12, 13]. However, this result is still controversial. The status of direct detection experiments is summarised in Fig. 2.4.

2.4.3 Indirect detection

In many well motivated dark matter scenarios, dark matter was in thermal equilibrium with Standard Model particles in the early universe. It is reasonable to assume that the same annihilation processes DM $\overline{\text{DM}} \to$ SM SM can still take place. A measurable flux of particles originating from dark matter annihilation in our Galaxy is expected

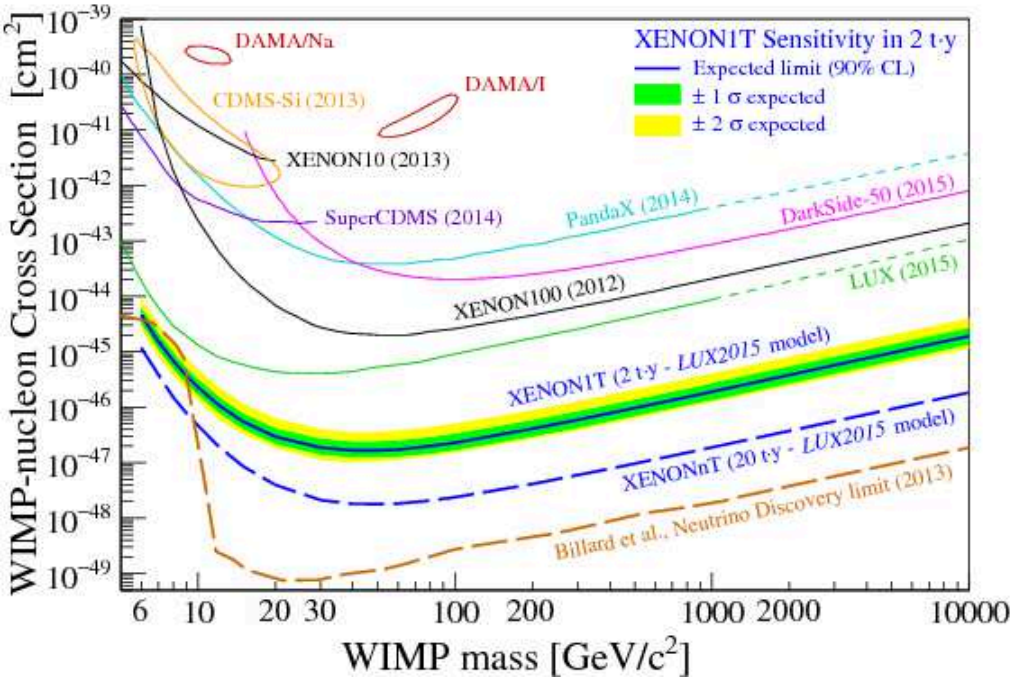

Figure 2.4: Status of dark matter direct detection experiments, from [130]. The plot shows the observed and projected upper bound on the WIMP-nucleon cross section as a function of the WIMP mass obtained by several experiments.

from those regions, where the dark matter density is supposed to be particularly high, like the centre of the Milky Way, the galactic halo or dwarf spheroidal galaxies. Dwarf galaxies are small galaxies, where a particularly high mass-to-light ratio is measured and they are therefore expected to be dark matter dominated.

Dark matter indirect detection experiments aim at measuring the exotic contribution in cosmic ray fluxes due to dark matter annihilation (or decay, in some scenarios) in the Galaxy. As the nature of dark matter is unknown, all possible final states have to be taken into account. Dark matter could in principle annihilate into quarks or charge leptons, gauge bosons, Higgs bosons or neutrinos. No direct coupling to photons is allowed as dark matter is neutral[15]. However, photons may be produced via loop-induced annihilation processes. Some of these primary annihilation products decay, hadronise, emit QED or QCD radiation and in general all stable Standard Model particles, $e^+, e^-, p, \bar{p}, \nu, \gamma$, are produced[16].

Both ground-based and space-borne experiments are currently measuring cosmic rays, neutrinos and gamma ray fluxes with very high precision and spanning a very large energy range, to be sensitive to this exotic contribution. The indirect dark matter searches can be sorted in two categories. First, specific searches are designed to investigate particular signatures expected from dark matter annihilation according to a given prediction. For instance, line searches in the gamma-ray spectrum belong to this

[15]In some models, milli-charged dark matter can feature a small tree-level coupling to photons, for example in [144]. We don not consider this possibility here.

[16]In principle, also deuteron and antideuteron are produced. However, we do not discuss these searches here.

first class. Indeed, the motivation for these searches is that no astrophysical source or process would produce such a feature in the spectrum. The observation of such a signal would in priciple represent a smoking-gun for dark matter annihilation in the Galaxy. The second strategy consists in searching for features in the data that are not accounted for by conventional astrophysical models and that could be due to the presence of dark matter in the galactic halo, without basing the search on some specific model or expected feature.

Unfortunately, in both cases, the backgrounds or foregrounds relevant to the searches are very often not completely understood. For instance, analysing X-rays satellites measurements, a line at 3.5 keV has been found. Even though a dark matter interpretation of this feature is possible, an explanation in terms of poorly known atomic lines is also viable [14, 15, 145]. Similarly, the intriguing rise in the positron fraction measured for instance by PAMELA and confirmed by the AMS-02 experiment [16–18] allows for explanations in terms of astrophysical sources as well as more exotic scenarios like dark matter annihilation in the Galaxy. The modelling of the astrophysical backgrounds is a very active field of work, given its crucial rôle in the interpretation of dark matter indirect experiments' measurements.

We now briefly discuss a selection of ongoing neutrino, gamma-rays and charged antimatter searches.

Neutrinos may be produced directly by processes like DM $\overline{\text{DM}} \to \nu\nu$ or come from the particle-physics evolution of other final states, for instance the decay of electroweak gauge bosons.

Since neutrinos travel unaffected through the Galaxy, they point directly at the production point. Neutrino searches are in general very challenging, given their tiny interaction rates. Very large neutrino telescopes like IceCUBE [146, 147] at Antarctica or Super-Kamiokande [148, 149] in Japan measure for dark matter searches the neutrino flux coming from the Sun, that could include a component due to the annihilation of dark matter particles captured inside the Sun.

In particular, the IceCUBE experiments uses photomultipliers distributed in about 1 km^3 of ice to detect Cherenkov light emitted by charged particles travelling in the ice. In fact, via neutrino interactions with nucleons in the ice, charged leptons are produced, in particular muon, that can by detected measuring the Cherenkov emission.

Using the IceCUBE measurements, upper limits on the direct annihilation cross section of dark matter into neutrinos can be placed in the cross section /dark matter mass parameter space over a very large range of masses, from 20 GeV up to 10 TeV.

Gamma rays from dark matter annihilation mostly come from the production and decay of pions. As already mentioned, loop-induced annihilation into photons is possible, but in general suppressed. In addition, if dark matter annihilates into charged fermions and/or gauge bosons, the decay and evolution of these particles would generate photons. For models where dark matter annihilates into electron-positron pairs, photons can be produced through inverse Compton scattering on the CMB or on galactic starlight, through e^+, e^- pair annihilation, bremsstrahlung or synchrotron radiation in the galactic magnetic field.

Photons as neutrinos point to the production point. Differently from neutrinos, they interact with the interstellar medium and can be absorbed. The flux of photons expected

at Earth coming from a given direction can be expressed as [107, 150]

$$\frac{d\Phi_\gamma}{d\Omega dE} = \frac{1}{2}\frac{r_\odot}{4\pi}\left(\frac{\rho_\odot}{M_{\rm DM}}\right)^2 \int_{l.o.s}\frac{ds}{r_\odot}\left(\frac{\rho(r(s,\theta))}{\rho_\odot}\right)^2 \sum_f \langle\sigma v\rangle_f \frac{dN_\gamma^f}{dE}, \tag{2.21}$$

with $r_\odot$ and $\rho_\odot$ are the location of the Earth and the local dark matter density, respectively. The factor

$$J = \int_{l.o.s}\frac{ds}{r_\odot}\left(\frac{\rho(r(s,\theta))}{\rho_\odot}\right)^2, \tag{2.22}$$

is usually called the "J-factor" and accounts for the amount of dark matter along the line of sight connecting the Earth (where the experiments are performed) and the observed location. The variable r is centred on the Galactic Centre and is defined as $r(s,\theta) = \sqrt{s^2 + r_\odot^2 - 2r_\odot s\cos\theta}$. The sum runs over all possible final states f in which the dark matter can annihilate, with cross section $\langle\sigma v\rangle_f$ and dN_γ^f/dE is the flux of photons obtained from the evolution of the final state f.

Both atmospheric Cherenkov telescopes, like HESS [151–153], VERITAS [154–156] and MAGIC [157, 158], and satellite-borne telescopes, like Fermi-LAT [159–164] measure fluxes of γ-rays from the galactic centre, dwarf spheroidals and the halo. Atmospheric Cherenkov telescopes measure the particle shower induced by the interaction of high energetic γ-rays with the atmosphere. The HESS collaboration was able to set upper limits on the dark matter annihilation cross section in the very high mass range (300 GeV − 10 TeV) observing the Milky Way centre. The future Cherenkov Telescope Array CTA [165, 166] will have an improved flux sensitivity with respect to HESS, VERITAS and MAGIC. The Large Area Telescope on the Fermi Gamma Ray Satellite can measure γ-rays in the range from 20 MeV up to 300 GeV. Gamma rays are converted into electron-positron pairs in the detector, that leave a visible track in a silicon tracker. After, they reach a solid scintillator calorimeter, where the energy of the particles is measured. Even though some intriguing excess at the galactic centre has been found in the Fermi-LAT data, the origin of this signal is very debated [19–21].

Charged particles are primary dark matter annihilation products in many dark matter models, for example, via the processes DM $\overline{\rm DM} \to l^+l^-/q\bar{q}$. Since antimatter in the Galaxy is very rare, experiments aim at measuring antimatter fluxes, like positron or antiproton, as these channels are more sensitive to an exotic component.

Differently from neutrinos and photons, charged particles are deflected by the galactic magnetic fields during propagation from the production point to the Earth. Therefore, information about the production point is lost and all points in the halo contribute to the flux measured at a given location. The fluxes at Earth, namely the fluxes after propagation, are governed by a diffusion-loss equation, both in the case of positrons and antiprotons [107, 167]. We postpone the discussion of the propagation of charged cosmic rays to the next Chapter, where we also discuss approximate solutions specific for dark matter induced fluxes, as proposed in [107].

The positron and the antiproton fluxes are considered golden channels to probe dark matter annihilation in the Galaxy studying charged particles. Several experiments have measured the positron fraction (the ratio of the positron flux over the total positron and electron flux) and/or the separate lepton fluxes, *e.g.* CAPRICE [168], HEAT [169], AMS-01 [170], PAMELA [171], Fermi-LAT [172] and AMS-02 [17, 18]. In particular,

the positron fraction has attracted a lot of attention in the last few years. A rise in the positron fraction was reported by AMS-01, CAPRICE and HEAT and subsequently confirmed both by the PAMELA and the AMS-02 experiment (simply AMS from now on), that measured the positron fraction up to 100 GeV and 500 GeV, respectively. They observed a rise in the positron fraction that disagrees with the expectation according to conventional models, where positron are mostly secondary particles and the flux is supposed to decrease above about ~ 10 GeV.

The AMS-02 experiment is a space-borne magnetic spectrometer and has been operating on the International Space Station since early 2011. It measures the fluxes and the composition of charged cosmic rays (electron/positrons, antiprotons/protons and nuclei up to iron) with very high precision and over a wide energy range. Its two most prominent scientific goals are the study of antimatter in the Universe and the search for signals due to dark matter annihilation. In addition, precise measurements of secondary to primary cosmic rays components, like the boron-to-carbon ration (B/C) will improve the understanding and modelling of the propagation of charged particles in the Galaxy. This represents a crucial issue for dark matter searches using astrophysical measurements. In fact, the large uncertainties due to the modelling of the propagation of cosmic rays strongly affect theoretical predictions for fluxes originating from dark matter annihilation in the halo and prevent from drawing solid conclusions when comparing the expectations according to a given model to the measured fluxes. The AMS detector consists in several sub-detectors and this redundancy allows for higher accuracy in the determination of the energy, velocity and charge of the particles passing through the detector.

The very precise measurement of the positron flux [173] over the range $0.5 - 500$ GeV has shown significant deviations from the expected behaviour. In fact, positrons are assumed to be mostly secondary particles, while the hardening of the flux of positrons for $E \gtrsim 10$ GeV suggests the existence of a primary source of positrons. The determination of the nature of this source of primary positrons is of major importance, as it could be due (completely or partially) to exotic sources of positrons, like dark matter annihilating in the galaxy, or to some misinterpreted or unknown astrophysical phenomena.
Also the measurement of the antiproton flux or antiproton-to-proton ratio play a very important role in dark matter searches with astrophysical experiment, as large amounts of antiprotons are usually expected if dark matter annihilates into quarks. The available measurement performed by PAMELA [174] in the range from 60 MeV to 180 GeV does not feature a large excess as the positron fraction, allowing for placing limits on the annihilation cross section of dark matter into quarks in some dark matter scenarios. The preliminary antiproton-to-proton ratio measurements of AMS [175] extend over a wider range of energies (up to about 350 GeV). According to these latest results, it is not possible to completely exclude the presence of a small signal of exotic origin, but it is definitely to early to draw any robust conclusion.

The interpretation of the AMS measurements in terms of dark matter annihilation in the Milky Way is extensively discussed in Chapters 6 and 7.

Chapter 3

General facts about cosmic rays

Cosmic rays (CR) were discovered in 1912 by Victor Hess [176–178] measuring the ionisation of the air with a balloon experiment. The ionisation at high altitude was larger than the ionisation on the surface of the Earth, consistently with a cosmic origin of this new sort of radiation. Because of their high penetrating power, they were at the beginning believed to be gamma rays and therefore were dubbed "cosmic rays" by Robert Millikan. In the 30s it was proven that the CR are charged particles, studying the dependence of the flux on the latitude[1].

The discovery of the cosmic radiation was certainly one of the most relevant discovery of the last century both for astrophysics and particle physics. Studying CR new particles were discovered, like the e^+, the $\mu^\pm$ and the $K-$mesons. Before the accelerators era, CR were used as source of energetic particles. Even nowadays, the most energetic particles found in CR are by far more energetic than any particle accelerated at the LHC [2].
In this chapter, we briefly revise the main features of the CR. In particular, we focus on their propagation, as this constitutes one of the main ingredients of our later discussion.

Cosmic rays are often distinguished into "primary" and "secondary" components, where primary CR are those directly produced by the astrophysical sources, while secondaries are produced through the interaction of the primaries with the interstellar medium. Electron, protons, helium, carbon and all nuclei produced in stars constitute the primary CR. On the other hand, positrons, antiprotons, lithium, beryllium and boron are mostly secondaries. Measuring a primary component of positrons or antiprotons is of great interest as it may hint at exotic sources like dark matter annihilation of the galaxies or be due to unknown or poorly modelled astrophysical sources. In the latter case, these astrophysical sources would represent an additional background for dark matter searches and would have to be correctly accounted for. Moreover, precise measurements of secondary light nuclei are relevant in order to better constrain parameters describing the cosmic ray propagation through the Galaxy. This issue is crucial for dark matter indirect searches and the precise determination of these fluxes is one of the goals of the AMS experiment.

CR are mostly made of atomic nuclei. More specifically, at low energies about 2%

[1] In the Literature, "cosmic rays" can refer both to charged particles only (electron, positrons, protons, nuclei, etc) and more generally to all sort of particles impinging on the Earth, hence also neutrinos and photons. In the following we refer only to charged particles.

[2] Protons with 10^{20} eV energy have been observed in CR. To obtain such energies with the LHC, it should be as long as the orbit of Mercury!

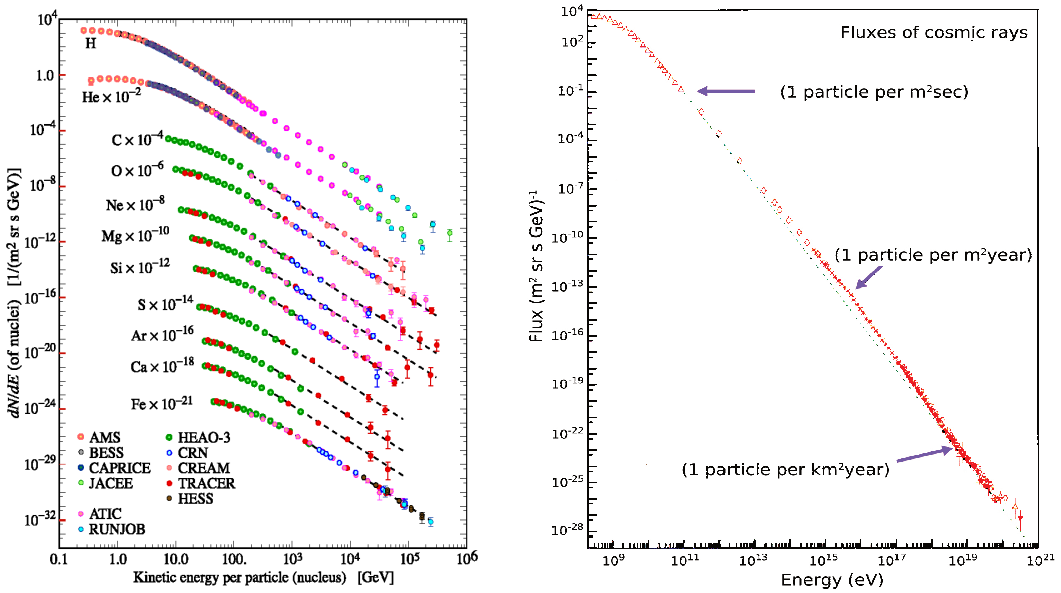

Figure 3.1: Left: different components of CR. The fluxes are shown as a function of the kinetic energy per nucleus. Figure from Ref. [179].
Right: cosmic rays energy spectrum as function of energy. Image credit: Simon Swordy.

of CR are electrons and positrons, about 80% of the nuclei are protons, 14% is helium ($Z = 2$) and the remaining is an admixture of heavier species, as shown in Fig. 3.1. On the other hand, the exact CR composition at high energies is still unknown. Comparing the elements abundance in CRs and in the Solar System it was found that protons and helium are slightly less abundant than in the Solar System, while elements like lithium, beryllium, boron (Z=3-5) and scandium, titanium, vanadium, chromium, manganese ($Z = 21 - 25$) are more abundant. These elements are in fact secondaries and are produced via spallation of carbon (Z = 6), oxygen (Z=8), and iron (Z = 26)([180] and Refs. therein). The typical path length for CR can be estimated from the measurements of the abundances to be about 50 $\mathrm{kg\,m^{-2}}$. On the other hand, the density of the interstellar medium in the disk is estimated to be 10^6 $\mathrm{kg\,m^{-2}}$, therefore CR are mostly confined in the Galaxy. However, a fraction of CR is believed to have extragalactic origin[3]. Studying the CR energy spectrum, one finds that the energy of CR varies over an enormous range from few MeV up to above 10^{20} eV and the differential flux varies over about 30 orders of magnitudes, as shown in Fig. 3.1. The CR flux does not show special spectral features up to about 10^{15} eV, then a steepening of the slope ("knee") is observed for energy in the range $10^{15} - 10^{18.5}$ eV and after the spectrum flattens again ("ankle")[4]. The flux is well approximated by a simple power law, suggesting that CR

[3]There is also a small fraction of CR that originates from solar flairs, namely in the Solar System.
[4]Note that the very precise measurements of the proton flux by AMS [181] reveal a more complex behaviour than the simple "knee-ankle" paradigm we discuss here.

are produced in non-thermal processes

$$\frac{dN}{dEd\Omega dAdt} \simeq E^{-\gamma}, \quad \text{with} \quad \gamma \sim \begin{cases} 2.7 & 10^{11}\text{ eV} < \text{E} < 10^{15}\text{ eV} \\ 3.1 & 10^{15}\text{ eV} < \text{E} < 10^{18.5}\text{ eV} \\ 2.0 & E > 10^{18.5}\text{ eV}. \end{cases} \tag{3.1}$$

It is believed that the particles with highest energies $E \gtrsim 10^{15}$ eV are of extragalactic origin. The nature of the CR sources is still very debated. In the usual paradigm CR are accelerated by supernovae shock waves in the Galaxy, but also active galactic nuclei and gamma rays bursts have been suggested as possible extra-galactic CR sources, as well as exotic sources like dark matter annihilation or decay in the Galaxy.

Particular relevant for dark matter searches is the modelling of the propagation of CR through the Galaxy. Indeed, the uncertainties on the propagation models strongly affect the predictions for the expected fluxes of charged CR, measured for example by PAMELA or AMS. In the next section, we revise the main phenomena affecting CR during propagation and the so-called Green function formalism, that provides approximated solutions, that we will use later on for our phenomenological studies.

3.1 Cosmic rays propagation

Charge particles interact with the interstellar medium and the galactic magnetic field during propagation through the Galaxy. Therefore, the resulting flux at the detection point is significantly different from the flux at the production point.
In general, the equation that governs the number density per unit of energy of a given species $\psi = dN/dE$ reads [167][5]

$$\frac{d\psi}{dt} + \frac{\partial(V_C\psi)}{\partial z} - \mathcal{K}(E)\triangle\psi + \frac{\partial}{\partial E}\left(b(\vec{x},E)\psi - \mathcal{K}_{EE}(E)\frac{\partial\psi}{\partial E}\right) = Q(\vec{x},E), \tag{3.2}$$

and applies in the region where CR diffuse. This region is usually modelled as a thick disk, that has in the middle the galactic disk formed by stars and dust where the acceleration of primary CR occurs. The central disk has a radius of about 20 kpc from the centre of the Galaxy and a half thickness of about 100 pc. The intergalactic medium is assumed to be in a volume surrounding the central disk, so starting at $r = 20$ kpc and with a half-thickness $z = \pm L$. The value of L is affected by large uncertainties and lies in the range $L \sim 1 - 15$ kpc. The term $Q(\vec{x},E)$ on the r.h.s. represents the source term. The convective velocity $V_C = V_C\hat{z}$ is only vertical and represents the convective motion away from the disk. Typical values are $V_C \sim 5 - 15$ km/s. The space diffusion coefficient $\mathcal{K}(E)$ is in general parametrised as

$$\mathcal{K}(E) = K_0\beta\left(\frac{R}{1GV}\right)^{\delta}, \tag{3.3}$$

where R is the rigidity of the particle, β the velocity, and δ and K_0 have to be determined using CR measurements. Note that the diffusion coefficient is usually taken to be the same everywhere. The term $b(\vec{x},E)$ accounts for the energy losses, that are induced

[5] We mostly follow the discussion in [167] throughout this section.

by different phenomena, depending on the CR species. The reacceleration coefficient $\mathcal{K}_{EE}(E)$ can be written as

$$\mathcal{K}_{EE}(E) = \frac{2}{9}\frac{E^2\beta^2}{\mathcal{K}(E)}V_a^2, \tag{3.4}$$

where V_a is called the Alfven velocity and is the velocity in the Galaxy of the scattering centres with whom CR interact. This results into diffusion in momentum space.

The general solution for the flux at location of the Earth $\vec{x}_s$ can be written in terms of Green functions [167]:

$$\psi(\vec{x}_\odot, E) = \int dE_s d\vec{x}_s \mathcal{G}(\vec{x}_\odot, E, E_s) Q(\vec{x}_s, E_s), \tag{3.5}$$

where E_s and $\vec{x}_s$ are the energy and the location of the source, respectively. The boundaries of the integral over E_s depend on the type of source and on the type of particle. The integral over $\vec{x}_s$ extends over the whole diffusive zone. The Green function represents the probability that a particle produced at the source with energy E_s reaches the Earth with energy E.

We now write the diffusion-loss equation in the particular cases of positrons/electrons and antiprotons/protons propagation through the Galaxy and present the approximate solutions for the special case where dark matter annihilation in the Galaxy plays the rôle of the source term. Numerical codes like GALPROP [182] numerically solve the equation-loss equation for all CR species and provide more accurate results. The drawback is that keeping track of the approximations and assumptions behind the calculations becomes complicated. In the next sections, we follow the discussion presented in [107].

3.1.1 Positrons and electrons

The diffusion-loss equation for positrons and electrons reduces to

$$-\mathcal{K}(E)\triangle\psi + \frac{\partial(b(\vec{x}, E)\psi)}{\partial E} = Q(\vec{x}, E) \tag{3.6}$$

since reacceleration effects and galactic convection are negligible in comparison to spatial diffusion and energy losses. The most relevant processes that induce energy losses are the emission of synchrotron radiation and the inverse Compton scattering on the CMB and on starlight. The factor b can be approximately written as

$$b(E) = -\frac{E^2}{E_0\tau_\odot} \tag{3.7}$$

where $E_0 = 1$ GeV and $\tau_\odot \simeq 6\cdot 10^{15}$ s [107, 167]. Note that we are neglecting the dependence of b on the location, while this factor is in principle position dependent. In fact, the magnitude of the Galactic magnetic field is not constant and also the composition of the starlight depends on the position. However, this dependence on the location is very difficult to include in the simple semi-analytical treatment we are discussing.

We now specialise to the case where the source consists in dark matter annihilation in the Galaxy. In this case, the r.h.s. of the diffusion-loss equation reads

$$Q(\vec{x}, E) = \eta\left(\frac{\rho(\vec{x})}{M_{\rm DM}}\right)^2 \sum_f \langle\sigma v\rangle_f \frac{dN_{e^\pm}^f}{dE}, \tag{3.8}$$

where $\eta = 1/2$ for Majorana fermion dark matter and $\eta = 1/4$ for distinguishable particles. The source term depends on the distribution of the dark matter in the Galaxy and on the specific model under study. The sum over f represents a sum over all channels with a non-zero branching ratio into electrons and positrons. Note that it is customary to assume a steady state in the diffusion region and the diffusion-loss equation in Eq. (3.2) becomes

$$\frac{\partial(V_C\psi)}{dz} - \mathcal{K}(E)\triangle\psi + \frac{\partial}{\partial E}\left(b(\vec{x},E)\psi - \mathcal{K}_{EE}(E)\frac{\partial\psi}{\partial E}\right) = Q(\vec{x},E), \tag{3.9}$$

At the end, the quantity we are interested in is the differential flux $d\Phi/dE(t,\vec{x},E)$ ($\mathrm{m^{-2}s^{-1}sr^{-1}GeV^{-1}}$), that is related to ψ simply by

$$\frac{d\Phi}{dE}(t,\vec{x},E) = \frac{\beta}{4\pi}\psi. \tag{3.10}$$

and the solution for the differential positron/electron flux is given by

$$\frac{d\Phi_{e\pm}}{dE}(\vec{x},E) = \frac{\beta}{4\pi b(\vec{x},E)}\eta\left(\frac{\rho(\vec{x})}{M_{\mathrm{DM}}}\right)^2\sum_f\langle\sigma v\rangle_f\int_E^{M_{\mathrm{DM}}}dE_s\frac{dN^f_{e\pm}}{dE}I(\vec{x},E,E_s), \tag{3.11}$$

where the function I contains all information about the dark matter halo model and the propagation parameters and is related to the Green functions in Eq. (3.5):

$$I(\vec{x},E_s,E) = \int d\vec{x}_s\mathcal{G}(\vec{x},E,E_s)\left(\frac{\rho(\vec{x}_s)}{\rho(\vec{x})}\right)^2. \tag{3.12}$$

In case $\vec{x} = \vec{x}_\odot$, Eq. (3.11) can be written as

$$\frac{d\Phi_{e\pm}}{dE}(\vec{x},\epsilon) = \frac{\beta}{4\pi b(E)}\eta\left(\frac{\rho_\odot}{M_{\mathrm{DM}}}\right)^2\sum_f\langle\sigma v\rangle_f\int_E^{M_{\mathrm{DM}}}d\epsilon_s\frac{dN^f_{e\pm}}{dE}(\epsilon_s)\mathcal{I}(\vec{x},\lambda(\epsilon,\epsilon_s)), \tag{3.13}$$

where $\epsilon = E/1\,\mathrm{GeV}$ and the normalisation of the flux is given by $b_T(\epsilon) = \epsilon^2/\tau_\odot$. The functions λ_D and $\mathcal{I}$ are defined by

$$\lambda_D = \lambda_D(\epsilon,\epsilon_s) = \sqrt{4\mathcal{K}_0\tau_\odot(\epsilon^{\delta-1} - \epsilon_s^{\delta-1})/(1-\delta)} \tag{3.14}$$

and

$$\mathcal{I}(\lambda_D) = a_0 + a_1\tanh\left(\frac{b_1-\ell}{c_1}\right)\left[a_2\exp\left(-\frac{(\ell-b_2)^2}{c_2}\right) + a_3\right], \tag{3.15}$$

with $\ell = \log_{10}(\lambda_D/\mathrm{kpc})$.
The values of the parameters describing $\mathcal{I}(\lambda_D)$ as well as possible choice of δ and K_0 for viable propagation models are listed in [107]. We will use this approximate treatment to propagate fluxes of particles produced via dark matter annihilation for our phenomenological studies.

3.1.2 Antiprotons

In the case of antiprotons, the general equation Eq. (3.9) in the stationary case reduces to

$$\frac{\partial(V_C\psi)}{dz} - \mathcal{K}(K)\triangle\psi = Q(\vec{x}, E), \tag{3.16}$$

where energy losses are neglected as the effects are much smaller than spacial diffusion and convection. Note that it is convenient to write the equation for $\psi = dN/dK$, where $K = E - m_p$ is the kinetic energy of the antiprotons. In this case, the spatial diffusion term can be written as

$$\mathcal{K}(K) = K_0\beta\left(\frac{p}{\mathrm{GeV}}\right)^{\delta}, \qquad p = \sqrt{K^2 + 2m_pK}. \tag{3.17}$$

The source is again dark matter annihilation in the galactic halo. However, for antiprotons two more effects have to be taken into account. In fact, antiprotons interact with hydrogen and helium in the interstellar medium. If they elastically collide, the antiprotons loose a significant fraction of their energy and are usually called tertiary antiprotons. In this approximated formalism they are neglected [107]. If the antiprotons annihilate with hydrogen or helium in the interstellar medium, a "negative source" term has to be included, in order to take into account this depletion effect. The source term reads

$$Q = Q_{\mathrm{DM}} - 2h\delta(z)\Gamma_{\mathrm{ann}}\psi, \tag{3.18}$$

where the prefactor of $\Gamma_{\mathrm{ann}}\psi$ is to account for the fact that annihilation mostly take place on the galactic disk and Q_{DM} is again given by Eq. (3.8). The flux at the location of the Earth $\vec{x}_\odot$ is given by

$$\frac{d\Phi_{\bar{p}}}{dK}(\epsilon, r_\odot) = \eta\frac{\beta}{4\pi}\left(\frac{\rho_\odot}{M_{DM}}\right)^2 R(K)\sum_f \langle\sigma v\rangle_f \frac{dN_{\bar{p}}^f}{dK}, \tag{3.19}$$

where the function R is defined as

$$\log_{10}\left[R(K)/\mathrm{Myr}\right] = a_0 + a_1\kappa + a_2\kappa^2 + a_3\kappa^3 + a_4\kappa^4 + a_5\kappa^5, \tag{3.20}$$

$\kappa = \log_{10}(K/\,\mathrm{GeV})$ and the parameters describing the R functions for the different dark matter halo models and propagation parameters are listed in Ref. [107].

This approximated semi-analytical method gives rather accurate results, especially if the goal is to estimate the uncertainties associated with the choice of different dark matter profiles and/or propagation models. In Chapter 4 and 7, we use the approximated solution Eqs. (3.13) and (3.19) to compute the fluxes at Earth.

3.2 Solar modulation

After propagation through the Galaxy, CR particles enter the Solar System and interact with the solar wind, produced in corona of the Sun. The charged particles are deflected by the solar wind and the less energetic particles do not reach the Earth and are therefore "invisible" for us. This suppression of the flux due to the solar wind goes under the name of *solar modulation* and is particularly relevant for low energy particles ($E \lesssim 10$ GeV). The intensity of the CR fluxes anti-correlates with the solar activity, that has a 11-years

periodicity. In fact, when the solar activity is more intense, the effects of the solar wind are more relevant and the fluxes of charged particles are more suppressed. On the other hand, when the activity is lower more particles can reach the Earth. An example of the effects of solar modulation on carbon flux is shown in Fig. 3.2.

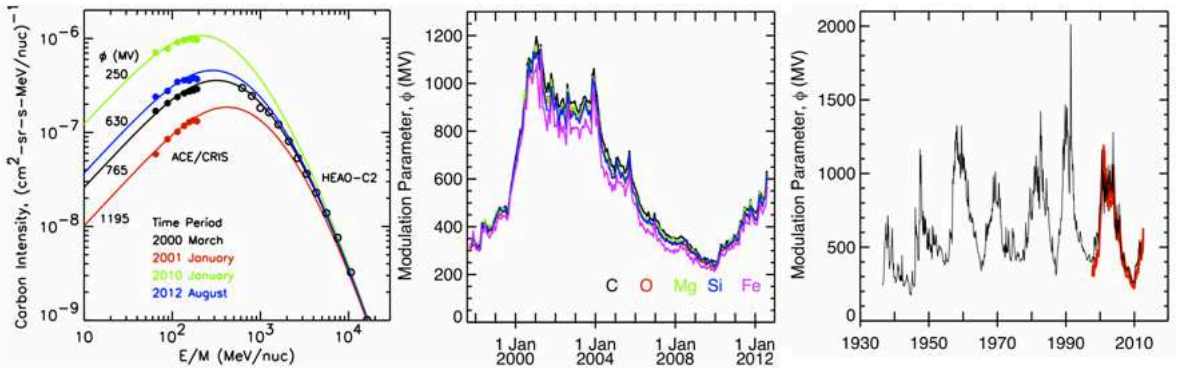

Figure 3.2: Effects of solar modulation on the carbon flux (left panel). Intensity of the solar modulation parameters for different nuclear species (central panel). Evolution of the solar modulation parameter over several solar cycles (right panel). The region in red is the one considered in the left and central panels. Credit: ACE collaboration, `http://www.srl.caltech.edu/ACE/`.

Charged CR fluxes can be corrected to take into account solar modulation using the force-field approximation [183]. The fluxes of a given species f at Earth $\Phi^f_\odot(E)$ are obtained from the fluxes at the outskirts of the Solar System $\Phi^f(E)$ as

$$\frac{d\Phi^f_\odot(E,t)}{dE} = \frac{E^2}{E^2+\Psi^2(t)} \frac{d\Phi^f(E+\Psi(t),t)}{dE} \tag{3.21}$$

where $\Psi(t)$ is the effective potential.
In Chapter 7 we use this approximation to account for solar modulation when computing the fluxes at Earth that we compare to the electron and positron fluxes measured by AMS.

Part II

Theoretical prediction for dark matter indirect detection

Chapter 4

Predictions for dark matter indirect detection

In this Chapter, we describe how theoretical prediction for dark matter indirect detection experiments are obtained, with particular focus on the importance of the emission of electroweak gauge bosons. In general, if dark matter exists as thermal relic, then the same annihilation reaction $\chi\overset{(-)}{\chi} \to f\bar{f}$ that were taking place in the Early Universe can still take place, at a rate parametrised by the thermally averaged annihilation cross section $\langle\sigma v\rangle$ today. The computation of the thermally averaged cross section is then the first ingredient needed to obtain the *primary flux*, namely the flux of Standard Model particles directly produced via dark matter annihilation in the Galaxy. The nature of these primary Standard Model particles depends on the dark matter model under study (leptons, quarks, gauge bosons, Higgs bosons). These particles can in general decay, fragment, hadronise or emit radiation and the particles produced through these processes (*e.g.* electron, positrons, photons or antiprotons) constitute the *primary flux of stable Standard Model particles*. Particularly relevant is the inclusion of electroweak emission, as extensively discussed in Sec. 4.2. We generally call *evolution of the final state* all the phenomena after which only stable particles are left at the production point. This stable particles then propagate through the Galaxy and we refer to the flux at detection point as to *secondary flux*. Neutrinos and photons travel a straight line and carry important information about the location of the annihilation. As discussed in Sec. 3.1 charged particles on the other hand are deflected by the galactic magnetic field, interact with the interstellar medium and reach the Solar System with complicated trajectories. All information on the production point is lost and therefore the whole galactic halo contributes to the fluxes of these particles. Eventually, other phenomena take place as the particles arrive close to the heliosphere. For instance solar modulation plays an important role, as discussed in Chapter 7.

In this Chapter we discuss all the steps necessary to obtain predictions for fluxes originating from dark matter annihilation. These will be eventually compared to the AMS measurements of fluxes of charged cosmic rays (electrons and positrons and, in the future, antiprotons).

In Sections 4.1.1 and 4.1.2 we present the two specific dark matter candidates we consider throughout the discussion, namely the first Kaluza-Klein excitation of the photon in Universal Extra Dimensions [97, 184] and a pure bino neutralino in a very simple

version of the MSSM [25, 185]. Note that we choose these candidates as they provide good proxies for Majorana dark matter and vector dark matter, respectively. Moreover, they come as byproduct of complete theories, meaning that it is possible to perform calculations in a well defined framework. As already stated, we did not choose these theories, because we believe them to provide the most appealing dark matter models available.

In Section 4.2, we focus on the importance of the inclusion of electroweak radiation, when computing the yield of primary particles, produced through dark matter annihilation. This constitutes the main part of the discussion about theoretical predictions for dark matter indirect detection experiments. In Chapter 5 we discuss a model independent formalism to include the dominant contributions due to electroweak gauge bosons emissions.

In Section 4.3 we describe how the evolution of the final state and the propagation through the Galaxy are computed.

4.1 Primary flux from dark matter annihilation in the Galaxy

The flux of the primary annihilation products is related to the thermally averaged cross section $\langle \sigma v_{cm} \rangle$, which multiplied by the number density of dark matter particles gives the frequency of dark matter annihilations in the Galaxy. As we assume that the dark matter is a non-relativistic particle, the thermally averaged cross section can be expressed as a power expansion in the velocity of the dark matter [e.g. 25]:

$$\langle \sigma v_{cm} \rangle = a + b v_{cm}^2 + \mathcal{O}(v^4), \tag{4.1}$$

where a corresponds to s-wave annihilation ($L = 0$), while b contains contributions coming both from the s-wave and p-wave annihilation. Note that the p-wave annihilation is velocity suppressed, see *e.g.* Ref. [186]. As for dark matter annihilating in the halo $v_{\rm cm} \sim 10^{-3}$, we retain only the first term of the expansion a[1].

The leading order cross section for dark matter annihilation in the specific cases we consider are known and can be found in the Literature [97, 184, 187, 188]. We have checked these results against our analytical calculations, `MadGraph 5` [189, 190] and `CalcHEP` [191] results. To perform these checks (and for later use) we needed to obtain the cross section times velocity in the low velocity limit with `MadGraph 5`. Under the assumption that only the a term of Eq. (4.1) contributes, the cross section times velocity is a constant in the $v_{\rm cm} \to 0$ limit. We therefore performed several runs for $v_{\rm cm} \in [0.1, 0.0001]$ and identified the values of the velocity where the $\langle \sigma v_{cm} \rangle$ becomes constant. We find that for $v_{\rm cm} \sim 10^{-2}$ we correctly reproduce the expected behaviour and we use this value as reference value for the calculations with `MadGraph 5`.

For the generation of the hard process, we use a in-house Montecarlo events generator. Again, we check that the events are generate correctly against MadGraph 5.

[1] Note that what we (improperly) call $v_{\rm cm}$ actually is $\beta = v_{\rm cm}/c$.
This approximation would not be appropriate when computing the relic dark matter density since the cross sections in general exhibit a relevant velocity dependence at the freeze-out epoch.

4.1.1 Universal extra dimension model

We first consider a simple model with universal extra dimensions, where the dark matter candidate is the first Kaluza-Klein (KK) mode of the photon ($B^{(1)}$), namely a vector boson. The annihilation $B^{(1)}B^{(1)} \to e^+e^-$ proceeds via the exchange of Kaluza-Klein electrons, as shown in Fig. 4.1.

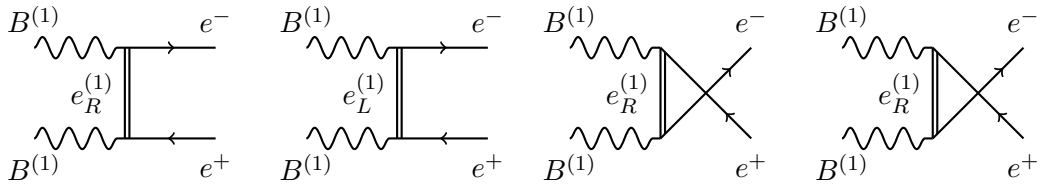

Figure 4.1: Leading order contributions to the KK photon annihilation into electron/positron pairs, $B^{(1)}B^{(1)} \to e^+e^-$.

The leading order annihilation cross section is given by [97, 184, 187]

$$\langle \sigma v \rangle = \frac{\alpha_{\rm EM}^2 \pi^2}{\cos^4 \theta_w} \frac{Y_L^4 + Y_R^4}{72\pi s^2 v} (10(2M_{\rm DM}^2 + s)\text{arctanh(v)} - 7\text{sv}), \tag{4.2}$$

where v is given by

$$v = \sqrt{1 - \frac{4M_{\rm DM}^2}{s}} \tag{4.3}$$

and $\alpha_{\rm EM}$ is the QED coupling constant, θ_w the weak angle, $\sqrt{s}$ is the centre of mass energy and the hypercharges $Y_L = -1$ and $Y_R = -2$ for the electron.

Retaining only the first term of the small velocity expansion we obtain

$$\langle \sigma v \rangle|_{v \to 0} = \frac{20M_{\rm DM}^2 + 3s}{72\pi s^2}. \tag{4.4}$$

For the sake of simplicity we neglect effects due to electroweak symmetry breaking and assume that the mediator and dark matter candidate are mass degenerate.

4.1.2 Supersymmetric model

We consider now a supersymmetric MSSM scenario, where the dark matter candidate is a pure bino neutralino ($\tilde{\chi}_0$), namely a Majorana fermion. The annihilation $\tilde{\chi}_0\tilde{\chi}_0 \to e^+e^-$ proceeds via t- and u-channel exchange of left and right sleptons (Fig. 4.2). For simplicity,

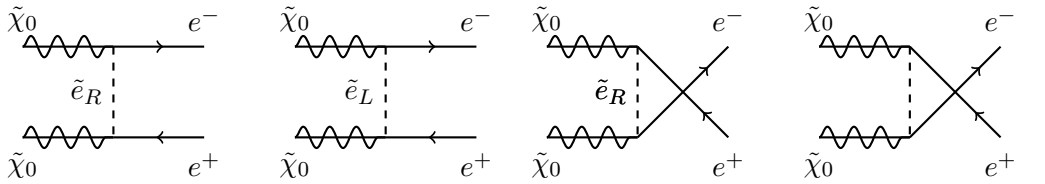

Figure 4.2: Leading order contributions to the bino neutralino annihilation into electron-positron pairs, $\tilde{\chi}_0\tilde{\chi}_0 \to e^+e^-$.

we neglect neutralinos and sleptons mixing, therefore the intermediate particles are only

left and right selectrons.
The thermally averaged annihilation cross section retaining only the first term in the $v \to 0$ expansion is given by [188]

$$\langle \sigma v \rangle = \frac{\alpha_{\rm EM}^2 25\pi m_e^2 \sqrt{M_{\rm DM}^2 - m_e^2}}{16 M_{\rm DM} \cos^4\theta_w (M_{\rm DM}^2 + m_{\tilde{e}} - m_e^2)^2}, \tag{4.5}$$

where $M_{\rm DM}$, $m_{\tilde{e}}$ and m_e are the masses of the dark matter candidate, of the selectron and of the electron, respectively. As in the previous UED case, the dark matter candidate and the intermediate particles are degenerate in mass.

The leading order cross section of this process is helicity suppressed, as first noticed in [192, 193] and vanishes for vanishing electron mass. A complete and clear explanation of the helicity suppression can be found in [186] and in the next paragraph we briefly illustrate the main points of the discussion in [186].

Helicity suppression of the leading order cross section

The process we are studying has two Majorana fermions as initial state, namely two identical fermions, and two Dirac fermions in the final state, namely two distinguishable particles. The annihilation cross section can be written in a partial waves expansion as $\sigma v = \sum_L a_L v^{2L}$, where L is the total orbital angular momentum of the pair of initial state fermions. The relative velocity of the dark matter particles in our Galaxy is $v \sim 10^{-3}$, therefore the contribution for $L \geq 1$ are strongly suppressed. Only the contribution for $L = 0$ does not suffer of a significant velocity suppression. The total spin of the initial state can be $S = 0$ in the antisymmetric configuration or $S = 1$ in the symmetric configuration. Since a pair of Majorana fermions is even under charge-conjugation, namely $C = (-1)^{L+S} = +1$, we deduce that $S = 0$ if $L = 0$. The parity of the pair is defined as $P = (-1)^{L+1}$. Then we have $CP = (-1)^{S+1}$, with $S = 0$, namely the unsuppressed state is CP-odd. Because of CP invariance, also the final state must be in the $S = 0$ configuration. More specifically, in the limit where the mass of the final state fermions is zero (our case of interest), momentum eigenstates are also helicity h eigenstates. We set $h = +1$ for a particle moving along the positive z direction, namely we identify the positive helicity direction with the direction $\vec{p}_z$. For an antiparticle moving along the positive z direction, the momentum is therefore in direction $-\vec{p}_z$. The two-particle final state can be decomposed as customary into a singlet

$$|l = 0, m = 0\rangle = \frac{1}{\sqrt{2}} \left(|\vec{p}_z, -\vec{p}_z\rangle - |-\vec{p}_z, +\vec{p}_z\rangle \right) \tag{4.6}$$

and a triplet

$$\begin{aligned} |l = 1, m = 0\rangle &= \frac{1}{\sqrt{2}} \left(|\vec{p}_z, -\vec{p}_z\rangle + |-\vec{p}_z, +\vec{p}_z\rangle \right) \\ |l = 1, m = \pm 1\rangle &= |\pm\vec{p}_z, \pm\vec{p}_z\rangle. \end{aligned} \tag{4.7}$$

In the centre of mass frame the singlet state is forbidden, because the left and right particles transform independently, as chiral symmetry is restored.

Summarising, the $L = 0$ contributions to the partial wave expansion of the cross section would be exactly zero for massless fermions. For fermions with a small mass, the contribution is suppressed by a factor $m_f^2/M_{\rm DM}^2$ and is said to be helicity suppressed.

4.2 Inclusion of electroweak radiation

The importance of the inclusion of electroweak radiation to theoretical predictions for dark matter indirect detection experiments is a widely discussed subject in the Literature [186, 194–202, 23, 203–212]. This section is devoted to discuss the effects of including electroweak corrections when computing the Standard Model particles' energy spectra due to dark matter annihilation in the Galaxy. In the next chapter, we discuss a model-independent approximated formalism to include electroweak corrections [23]. This will be then compared against exact results, in order to assess the quality and the validity regime of the approximation.

The effects of the emission of electroweak gauge bosons are relevant when the hard scale of the process under study is much larger than the electroweak scale. For dark matter annihilation in the Galaxy, the hard scale is set by the mass of the dark matter particle as the initial state particles are non-relativistic. Electroweak corrections are therefore relevant, as we consider WIMP dark matter, namely particles with masses in the TeV-range. Indeed, the highly energetic primary annihilation products can radiate electroweak gauge bosons and this emission is logarithmically enhanced [213]. More specifically, collinear emission is enhanced by Sudakov logarithms $\ln M_{\rm DM}^2/M_{\rm EW}^2$, while soft and collinear emission is enhanced by double Sudakov logarithms $\ln^2 M_{\rm DM}^2/M_{\rm EW}^2$, where $M_{\rm EW}$ and $M_{\rm DM}$ denote the electroweak scale and the mass of the dark matter particle, respectively. On the other hand, electroweak radiation coming from the non-relativistic initial state dark matter particles is not enhanced. In many cases of interest, also the radiation from the intermediate particle is not enhanced and therefore the radiation from the Standard Model annihilation products is the dominant contribution. It is then possible to include the radiation from Standard Model particles in a model independent fashion as we will explain in Chapter 5.

As we only consider WIMP dark matter , the centre of mass energy is of $\mathcal{O}(1)$TeV. At this scale, that is roughly the same of processes that take place at the LHC, electroweak radiation can have a $\mathcal{O}(5-10\%)$ effect [23, and Refs. therein] depending on the energy and on the observable. Such corrections are a small effect compared to the large uncertainties of astrophysical origin, that affect the theoretical predictions for dark matter indirect detection. However, they are crucial in order to obtain consistent predictions. In fact, the radiated electroweak gauge boson decay and the decay products can in turn emit QED or QCD radiation, hadronise and, eventually, produce all stable Standard Model particles ($e^{\pm}$, ν, $\bar{\nu}$, p, $\bar{p}$, d), irrespective of the nature of the primary annihilation products (Fig. 4.3), that depends on the model under study. This fact is of primary importance for phenomenological studies. Indeed it allows to exploit complementary measurements of fluxes of the different Standard Model species.
In addition, the Standard Model particles produced via the decay of the electroweak gauge bosons are in general low energetic and contribute mainly to the low energy part of the spectrum of these particles. This is the region probed by experiments.

To summarise, the inclusion of electroweak radiation is crucial to obtain consistent and accurate theoretical predictions to compare against experimental data. In Chapter 7, we will give a striking example of this fact, when discussing the predictions for antiproton fluxes from dark matter annihilation in leptophilic models.

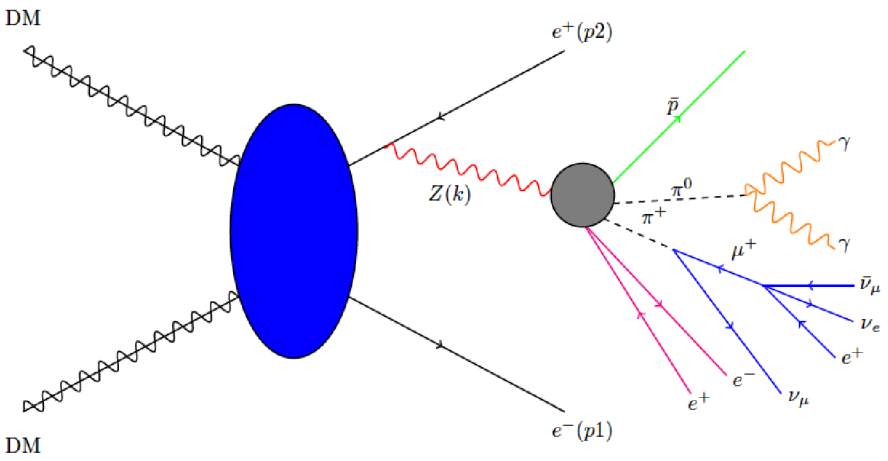

Figure 4.3: Through the emission of electroweak gauge bosons all Standard Model particles are present in the final state, irrespective of the nature of the primary annihilation products. In this example, dark matter annihilates directly only into electron and positron pairs. However, hadrons like pions or antiprotons are present in the final state as well.

4.3 Fluxes at Earth

After computing the primary flux of dark matter annihilation products[2], we take into account the decay of these primary particles, the emission of QED and QCD radiation and the hadronisation effects with `Pythia 8` [214, 215]. The fluxes obtained are the stable primary fluxes at the production point. Section 3.1 was devoted to a detailed discussion of the main effects affecting the propagation of charged cosmic rays.

For the propagation of positrons and antiprotons we use the semi-analytical formalism [107] discussed in Sec. 3.1.

For this study we consider a simple Einasto model [106, 104] to parametrise the dark matter distribution in the Galaxy:

$$\rho(r) = \rho_s \exp\left[-\frac{2}{\alpha}\left(\left(\frac{\mathrm{r}}{\mathrm{r_s}}\right)^{\alpha} - 1\right)\right], \tag{4.8}$$

where r is the distance from the Galactic Centre, $\alpha = 0.17$ according to numerical simulations, $r_s = 28.44$ kpc, $\rho_s = 0.033$ GeV/cm^3 [107], the location of the Sun is $r_\odot = 8.33$ kpc and the dark matter density at the location of the Sun is $\rho_\odot = 0.3$ GeV/cm^3.

The positron (or electron) fluxes after propagation are given by Eq. (3.13)

$$\frac{d\Phi_{e^\pm}}{dE}(\epsilon, r_\odot) = \frac{1}{4\pi}\frac{v_{e^\pm}}{b_T(\epsilon)}\frac{1}{2}\left(\frac{\rho_\odot}{M_{\mathrm{DM}}}\right)^2 \langle\sigma v_{\mathrm{cm}}\rangle \int_\epsilon^{M_{\mathrm{DM}}} d\epsilon_s \frac{dN_{e^\pm}}{dE}(\epsilon_s)\mathcal{I}\left(\lambda_D(\epsilon, \epsilon_s)\right), \tag{4.9}$$

with

$$\frac{dN_{e^\pm}}{dE} = \frac{1}{\langle\sigma v_{\mathrm{cm}}\rangle_{\mathrm{DM\ DM\to I}}} \frac{d\langle\sigma v_{\mathrm{cm}}\rangle_{\mathrm{DM\ DM\to I}} \times BR_{\mathrm{I}\to e^\pm}}{dE}, \tag{4.10}$$

[2]This is done including also the radiation of electroweak gauge bosons.

where ϵ is the energy in GeV units, $I = \{e^+e^-, e^+e^-Z\}$ and $v_{e^\pm}$ is the velocity of the electron or positron. The energy spectrum is normalised to the total annihilation cross section. The functions λ_D and $\mathcal{I}$ are defined in Eqs (3.14) and (3.15):

$$\lambda_D = \sqrt{4\mathcal{K}_0\tau_\odot(\epsilon^{\delta-1} - \epsilon_s^{\delta-1})/(1-\delta)} \tag{4.11}$$

and

$$\mathcal{I}(\lambda_D) = a_0 + a_1 \tanh\left(\frac{b_1-\ell}{c_1}\right)\left[a_2 \exp\left(-\frac{(\ell-b_2)^2}{c_2}\right) + a_3\right], \quad \ell = \log_{10}(\lambda_D/\text{kpc}). \tag{4.12}$$

We take from Ref. [107] the values of the parameters of the Green functions $\mathcal{K}_0$, δ, a_0, a_1, a_2, a_3, b_1 and b_2 for the medium propagation model and for the dark matter Einasto profile (Ein MED):

$$\begin{aligned} a_0 &= 0.507, & a_1 &= 0.345, & a_2 &= 2.095, & a_3 &= 1.469, \\ b_1 &= 0.905, & b_2 &= 0.741, & c_1 &= 0.160, & c_2 &= 0.063, \\ & & \delta &= 0.70, & \mathcal{K}_0 &= 0.0112. \end{aligned}$$

Analogously, the flux of antiprotons after propagation is given by Eq. (3.19):

$$\frac{d\Phi_{\bar{p}}}{dK}(\epsilon, r_\odot) = \frac{1}{2}\frac{v_p}{4\pi}\left(\frac{\rho_\odot}{M_{DM}}\right)^2 R(K)\langle\sigma v_{\text{cm}}\rangle\frac{dN_{\bar{p}}}{dK}, \tag{4.13}$$

where $K = E - m_p$ and m_p denote the kinetic energy and the mass of the antiproton. We recall that the function R is defined as

$$\log_{10}[R(K)/\text{Myr}] = a_0 + a_1\kappa + a_2\kappa^2 + a_3\kappa^3 + a_4\kappa^4 + a_5\kappa^5, \quad \kappa = \log_{10}(K/\,\text{GeV}) \tag{4.14}$$

The coefficients (again from Ref. [107]) read:

$$\begin{aligned} a_0 &= 1.8804, & a_1 &= 0.5813, & a_2 &= -0.2960, & a_3 &= -0.0502, \\ & & a_4 &= 0.0271, & a_5 &= -0.0027. \end{aligned}$$

The fluxes after propagation constitute the expected signal due to dark matter annihilation in the Galactic Halo that has to be combined with the expected fluxes of astrophysical origin in order to compare with experimental measurements. These issues will be the central topics of Chapters 6 and 7.

Chapter 5

Fragmentation functions approximation

In this Chapter we present a model independent formalism to describe electroweak gauge boson radiation [23, 216, 217], where generalised splitting functions for massive partons (the electroweak bosons) are introduced, analogously to the well known splitting functions in QCD [218]. We first discuss the generalised splitting functions and we then investigate the quality and the applicability of this approximated formalism. To this purpose, we consider the process DM DM $\to e^+e^-Z$ and we compute the energy spectrum of the Z boson and the fluxes of the leptons using the generalised splitting functions. These quantities will be compared to the results obtained performing the full tree-level $2 \to 3$ calculation in the simple models described in Sections 4.1.1 and 4.1.2. At this stage we just want to assess the quality of the approximation, therefore we just consider the radiation of a Z boson. For phenomenological application also the radiation of W boson must be taken into account. This will be the case when we compare our predictions to the AMS measurements in Chapter 7.

5.1 The formalism

We assume that the dark matter candidate is a heavy particle, with mass $M_{\rm DM} \gg M_{\rm EW}$, annihilating into Standard Model particles, like electron-positron pairs. This is the final state we will assume throughout the discussion, however the formalism applies to all Standard Model final states. The hard scale of the process is given by the centre of mass energy, namely $s \simeq 4M_{\rm DM}^2$, as the dark matter particles are essentially at rest. In this case the emission of electroweak gauge bosons off the highly energetic final state particles is enhanced by Sudakov logarithms, namely by factors of the form $\ln(M_{\rm DM}^2/M_{\rm EW}^2)$ for the collinear emission and of the form $\ln^2(M_{\rm DM}^2/M_{\rm EW}^2)$ for soft-collinear emission. Emission of electroweak gauge bosons off the non-relativistic initial state particles does not exhibit such an enhancement as well as the emission from the intermediate particle mediating the dark matter interactions with the Standard Model sector. These logarithmically enhanced contributions from the Standard Model final states are model independent and can be expressed in terms of generalised splitting functions. This formalism has been presented in Ref. [23]. Here, we revise its main features. In the following sections, we investigate its range of applicability.

In general, the energy spectrum of a given Standard Model final state particle $f = \{e^{\pm}, \gamma, p, \bar{p}, \nu, \bar{\nu}\}$ originating from dark matter annihilation is given by

$$\frac{dN_f}{dx} = \frac{1}{\langle \sigma v_{\rm cm} \rangle} \frac{d\langle \sigma v_{\rm cm} \rangle}{dx}\,, \tag{5.1}$$

with $x = E_f/\sqrt{s}$, E_f the energy of the final state particle f, and $\sqrt{s} = 2M_{\rm DM}/\sqrt{1 - v_{\rm cm}^2}$ the centre-of-mass energy of the non-relativistic dark matter particles. Therefore, the energy fraction x can be also written as $x \simeq E_f/M_{\rm DM}$. Throughout this work, the energy spectrum defined in Eq. (5.1) is normalised to one:

$$\int dx \frac{dN_f}{dx} = 1, \tag{5.2}$$

in contrast with other conventions in the Literature, where the energy spectrum is normalised for instance to the leading-order cross section .

We consider the process DM DM $\to e^+e^- + (Z \to f)$, as in Fig. 4.3, and we want to compute the spectrum of the Standard Model species f, $\frac{dN_f}{d\ln x}$ taking into account the emission of electroweak radiation. This can be written as [23]

$$\frac{dN_f}{d\ln x}(M_{\rm DM}, x) = \sum_J \int_x^1 dz\, D^{\rm EW}_{I\to J}(z) \frac{dN_{J\to f}}{d\ln x}\left(zM_{\rm DM}, \frac{x}{z}\right), \tag{5.3}$$

where the generalised fragmentation functions $D^{\rm EW}_{I\to J}(z)$ represent the probability that the particle I becomes a particle J with a fraction z of the momentum of the particle I via the emission of an electroweak gauge boson. At lowest order we have $D^{\rm EW}_{I\to J}(z) = \delta_{IJ}\delta(1-z)$, namely no radiation occurs. For the process we consider, the final state of the $(2 \to 2)$ annihilation process I is an electron-positron pair $I = \{e^+_L e^-_L, e^+_R e^-_R\}$ and after the radiation of the electroweak boson we have $J = \{e^+_{L,R} e^-_{L,R}, e^+_{L,R} e^-_{L,R} Z\}$. The function $\frac{dN_{J\to f}}{d\ln x}$ takes into account the further particle physics evolution of the final state $J \to f$, namely the decay of the electroweak gauge boson, the fragmentation and the hadronisation of its decay products as well as QCD and QED radiation. This can be computed using Monte Carlo events generators.

At leading order in the electroweak coupling, the fragmentation functions are given by [23, 216, 217]

$$D^{\rm EW}_{I\to J}(z) = \delta_{IJ}\delta(1-z) + \frac{\alpha_2}{2\pi}\int_{M^2_{\rm EW}}^{s} \frac{d\mu^2}{\mu^2} P^{\rm EW}_{I\to J}(z, \mu^2), \tag{5.4}$$

where μ is the virtuality of the particle I, $M_{\rm EW}$ is the mass of the emitted electroweak boson, α_2 the SU(2) coupling constant and $P^{\rm EW}_{I\to J}(z, \mu^2)$ are the unintegrated splitting functions. For the sake of simplicity, we refer to the electroweak fragmentation functions and splitting functions as to $D_{I\to J}$ and $P_{I\to J}$ and drop the superscript EW. To compute the fragmentation functions, it is necessary to compute the generalised splitting function P. The main difference of these splitting functions with respect to the QED and QCD ones is that the emitted partons are massive. Indeed, the mass of the emitted boson not only set a kinematical threshold, but also induce the presence of more factors in comparison with the standard QCD and QED case, where the emitted partons are massless. A complete discussion of this issue can be found in Ref. [23].

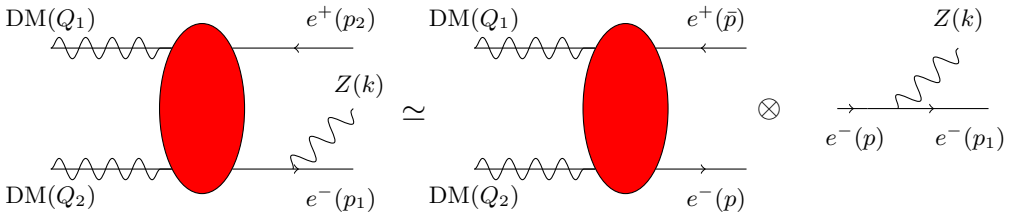

Figure 5.1: Pictorial example of the computation of a $(2 \to 3)$ cross section using the splitting functions approximation. The red ellipse represents the unknown DM-SM interaction.

5.1.1 Generalised splitting functions

We consider the general splitting of an initial particle i into two partons f_1, f_2, for which we have the following kinematically allowed energy region:

$$\frac{m_{f_1}}{E_i} < x < 1 - \frac{m_{f_2}}{E_i}, \tag{5.5}$$

where E_i is the energy of one of the initial state particles. Note that the definition of x here differs from Eq. (5.1) by a factor 2, as $\sqrt{s} = 2E_i$.

In general, in order to capture the correct behaviour for the emission of soft gauge bosons ($x \to 0, 1$), one can write the $(2 \to 3)$ amplitude using the eikonal approximation. From a practical point of view, this amounts to neglecting the soft momenta in the numerator of the amplitude.

However, in order to capture the complete structure of the splitting functions the collinear approximation is introduced. In the collinear limit, both the squared amplitude for the tree-level $(2 \to 3)$ process and the phase space factorise, as sketched in Fig. 5.1. The collinear approximation is implemented by writing the external momenta with the Sudakov parametrisation

$$p_1 = \left((1-x)E, -k_\perp, 0, (1-x)E - \frac{k_\perp^2}{2(1-x)E}\right) + \mathcal{O}(k_\perp^4) \tag{5.6a}$$

$$k = \left(xE, k_\perp, 0, xE - \frac{k_\perp^2}{2xE}\right) + \mathcal{O}(k_\perp^4) \tag{5.6b}$$

$$p_2 = \left(E, 0, 0, E + \frac{k_\perp^2}{2Ex(1-x)}\right) + \mathcal{O}(k_\perp^4) \tag{5.6c}$$

$$s = 4E^2, \tag{5.6d}$$

where $k_\perp$ is the transverse momentum, such that $k_\perp \ll E$, and the last terms in Eq. (5.6a) and Eq. (5.6b) have been chosen[1] such that $p_1^2 = 0$, $k^2 = 0$ up to terms $\mathcal{O}(k_\perp^4)$. Note that we treat the gauge bosons as massless particles, as far as the amplitude is concerned. Indeed, $M_{\text{EW}} \ll \sqrt{s}$.

On the other hand, the masses of the gauge bosons are relevant when performing the integration over the phase space. The generalised splitting functions can be non zero only in the kinematically allowed range, Eq. (5.5). However, if one integrates the factorised

[1] There are other possibilities, for instance for the event generation we used the equivalent parametrisation (5.12b) and (5.12c). More about the Sudakov parametrisation can be found in Appendix A.

squared amplitude with the phase space expressed with the Sudakov parametrisation Eq. (5.6), the splitting functions are not vanishing outside the allowed region. In order to obtain the correct kinematical behaviour, the phase space has to be written using the exact parametrisation of the momenta and the masses of the electroweak gauge bosons have to be taken into account when determining the integration boundaries. In this way, the integration over the phase space yields splitting functions, vanishing outside the allowed kinematical region. In Appendix A, the steps described above are discussed in detail.

For the case under study, the relevant splitting functions describe the splitting of a massless fermion F into a massless fermion and a massive vector boson V, and are given by [23]

$$P_{F\to F}(x) = \frac{1+x^2}{1-x} L(1-x), \tag{5.7a}$$

$$P_{F\to V}(x) = \frac{1+(1-x)^2}{x} L(x), \tag{5.7b}$$

with

$$\mathcal{L}(x) = \ln \frac{sx^2}{4M_{\mathrm{EW}}^2} + 2\ln\left(1+\sqrt{1-\frac{4M_{\mathrm{EW}}^2}{sx^2}}\right), \tag{5.8}$$

which correctly vanishes outside the kinematically allowed range $2M_{\mathrm{EW}}/\sqrt{s} \leq x \leq 1-2M_{\mathrm{EW}}/\sqrt{s}$. This more complicated universal function $\mathcal{L}(x)$ replaces the usual factors $\ln s/m^2$, when massive partons are involved.

The fragmentation functions are

$$D_{F\to F} = \frac{\alpha_2}{2\pi\cos^2\theta_w} g_f^2 P_{F\to F}, \tag{5.9a}$$

$$D_{F\to V} = \frac{\alpha_2}{2\pi\cos^2\theta_w} g_f^2 P_{F\to V}, \tag{5.9b}$$

where θ_w is the weak angle. The factor $g_f = T_3^f - \sin^2\theta_w Q_f$ accounts for the coupling of the fermions to the Z boson, where T_3^f and Q_f are the isospin and the charge of the fermion, in our case $e_L^\pm$ or $e_R^\pm$.

The $(2\to 3)$ tree-level annihilation cross section is given in this formalism by

$$\left.\frac{d\sigma_{(2\to 3)}}{dx}\right|_{\mathrm{approx}} = 2\left(\sigma_{(\mathrm{DM\,DM}\to e_L^+ e_L^-)} D_{e_L\to Z} + \sigma_{(\mathrm{DM\,DM}\to e_R^+ e_R^-)} D_{e_R\to Z}\right). \tag{5.10}$$

and the spectrum of the final state Standard Model particle f can be computed as

$$\frac{dN_f}{dx} = \frac{1}{\langle\sigma v_{\mathrm{cm}}\rangle} \frac{d\langle\sigma v_{\mathrm{cm}}\rangle_{\mathrm{DMDM}\to \mathrm{I}} \times \mathrm{BR}_{\mathrm{I}\to \mathrm{f}}}{dx}. \tag{5.11}$$

Detailed calculations of generalised splitting functions are presented in Appendix A. In the next section, we study the range of applicability of the splitting functions approach.

5.2 Comparison to full calculation

To assess the quality of the fragmentation functions approximation we consider dark matter annihilation into electron-positron pairs plus the radiation of a Z boson, and

compare the predictions for the fluxes obtained both with the full calculation and with the fragmentation functions approximation in the two concrete models we described in the previous chapter. More specifically, we compare the energy spectrum of the emitted Z boson and the positron flux before and after propagation for the two scenarios. We use `CalcHep` [191, 219] to obtain the matrix element for the exact calculation in the vector dark matter case, while we use `FeynArts` and `FeynCalc` [220, 221] for the Majorana fermion scenario. Both calculations have been checked against `MadGraph 5` [190] results.

For the event generation and integration we use a in-house Monte Carlo events generator. To implement the splitting functions approximation we use the following Sudakov parameterization of the phase space [23]:

$$Q_1^\mu + Q_2^\mu = S^\mu = (2E, 0, 0, 0)\,, \qquad E = \frac{M_{\rm DM}}{\sqrt{1 - v_{\rm cm}^2}}, \tag{5.12a}$$

$$p_1 = \left((1-x)E + \frac{k_\perp^2}{4E\,(1-x)}, -k_\perp, 0, (1-x)E - \frac{k_\perp^2}{4E\,(1-x)}, \right) \tag{5.12b}$$

$$k = \left(xE + \frac{k_\perp^2 + M_Z^2}{4Ex}, k_\perp, 0, xE - \frac{k_\perp^2 + M_Z^2}{4Ex}\right), \tag{5.12c}$$

$$p_2 = \left(E\,(1 - R(x, k_\perp))\,, 0, 0, -E\,(1 - R(x, k_\perp))\right), \tag{5.12d}$$

where p_1 is the four-momentum of the particle that radiates the Z boson, k is the four-momentum of the radiated boson and p_2 the four-momentum of the particle that does not radiate. The function R is defined as

$$R(x, k_\perp) = \frac{k_\perp^2}{4E^2 x} + \frac{k_\perp^2 + M_Z^2}{4E^2(1-x)}. \tag{5.13}$$

With this parametrisation the conservation of the four-momentum and the on-shellness condition are ensured.

5.2.1 UED model - vector dark matter

We compute the annihilation cross section for the process $B^{(1)}B^{(1)} \to e^+e^-Z$. The tree-level $(2 \to 3)$ cross section does not have any singularity, and we do not include virtual corrections in our computation, as we are interested in the shape of the energy distribution of the Z boson and of the secondary flux due to the Z boson decay. Therefore, only the real emissions of Z bosons are taken into account. The relevant diagrams are shown in Fig. 5.2. Using the splitting functions approximation amounts to neglecting the contributions of type (c), as it is assumed that diagrams (a,b) give the dominant contributions.

The first quantity we compare is the energy distribution of the radiated Z boson. Within the approximation we have

$$\left.\frac{d\sigma_{(2\to3)}}{dx}\right|_{\rm approx} = 2\left(\sigma_{(\rm DM\,DM\to e_L^+ e_L^-)} D_{e_L\to Z} + \sigma_{(\rm DM\,DM\to e_R^+ e_R^-)} D_{e_R\to Z}\right), \tag{5.14}$$

where $D_{e_L\to Z}$ and $D_{e_R\to Z}$ are given in Eq. (5.9).

In the centre of mass frame the differential cross section times velocity reads

$$\frac{v d\sigma}{dx_1 dx_2} = \frac{\overline{|\mathcal{M}|}^2}{256\pi^3}, \tag{5.15}$$

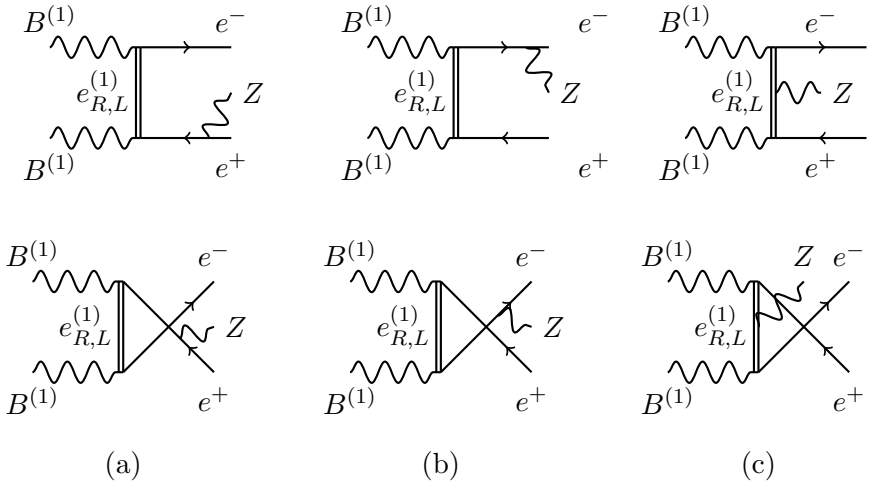

Figure 5.2: Contributions to the dark matter annihilation cross section , including the real emission of a Z boson. The emission in diagrams (a,b) are logarithmically enhanced for $M_{\rm DM} \gg M_{\rm EW}$ and are dominant with respect to the contributions in (c). The latter are not taken into account using the splitting functions approximation.

where $|\overline{\overline{\mathcal{M}}}|^2$ denotes the summed and averaged squared matrix elements, and x_1,x_2 are the fractions of the centre of mass energy carried by the final-state particles and the integration over the solid angle has already been performed. More specifically, the energies of the final state particles are parametrised as

$$k^0 = \frac{\sqrt{s}}{2}(1 - x_2), \tag{5.16a}$$

$$p_1^0 = \frac{\sqrt{s}}{2}x_1, \tag{5.16b}$$

$$p_2^0 = \frac{\sqrt{s}}{2}(1 - x_1 + x_2), \tag{5.16c}$$

where p_1, p_2 and k are the four momenta of the positron, the electron, and the Z boson, respectively. The range for the phase space integration for the variables x_1 and x_2 are

$$x_- \leq x_1 \leq x_+, \tag{5.17}$$

with

$$x_\pm = \frac{1 + x_2}{2} \pm \sqrt{\frac{(1 - x_2)^2}{4} - \frac{M_Z^2}{s}}. \tag{5.18}$$

and

$$-\frac{M_Z^2}{s} \leq x_2 \leq 1 - 2\frac{M_Z}{\sqrt{s}}. \tag{5.19}$$

In the small velocity limit and neglecting terms vanishing for $M_Z \to 0$, Eq. (5.15) reads [222]

$$\frac{d\langle\sigma v\rangle}{dx_2} = \frac{\alpha}{2304\, M_{\rm DM}^2 \pi^2} \frac{(1 - 2\sin^2\theta_w)^2}{\sin^2\theta_w \cos^2\theta_w} |g_L|^4 F(x_2), \tag{5.20}$$

where the integration over x_1 has been performed. The function F is given by [222]

$$F(x_2) = A \ln\left(\frac{\overline{x}_+}{\overline{x}_-}\right) + B + C \ln(x_2), \tag{5.21}$$

with $\overline{x}_\pm = 1 - x_2 \pm \sqrt{(1-x_2)^2 - M_Z^2/M_{\rm DM}^2}$. The coefficients A, B and C read

$$A = \frac{1+x_2^2}{1-x_2}, \tag{5.22a}$$

$$B = \frac{3(1-x_2)}{4(1+x_2)^2}\left(5 + 8x_2 + 5x_2^2\right), \tag{5.22b}$$

$$C = \frac{(1 + 4x_2 + 9x_2^2 + 4x_2^3 + x_2^4)}{(1+x_2)^3}. \tag{5.22c}$$

The Born cross section factorises and Eq. (5.20) can be recast in the form

$$\frac{d\langle\sigma v\rangle}{dx_2} = 2\langle\sigma v\rangle_{\rm Born} \frac{\alpha}{2\pi} \frac{g_f^2}{\sin^2\theta_w \cos^2\theta_w} F(x_2). \tag{5.23}$$

Comparing to Eqs. (5.7), (5.8) and (5.9), one can see that this is precisely the structure of the contributions captured by the splitting functions approximation. In fact, for vanishing Z-boson mass one obtains

$$\ln\left(\frac{\overline{x}_+}{\overline{x}_-}\right) \to \ln\left((1-x_2)^2 \frac{M_{\rm DM}^2}{M_Z^2}\right) + \ln(2), \tag{5.24}$$

to be compared to Eq. (5.7). The result of the comparison are shown in Fig. 5.3. The approximation correctly reproduce the log-enhanced parts of the amplitude and the quality of the approximation improves as the masses of the dark matter particle becomes larger, as the logarithms $\ln^2 M_{\rm DM}^2/M_{\rm EW}^2$ are more and more dominant. The splitting functions approximation reproduces accurately the energy spectrum of the radiated Z boson for $M_{\rm DM} \gtrsim 500\,\text{GeV}$. This can be seen in Tab. 5.1, where the results for the $(2 \to 3)$ cross section are compared and we find that also the cross section is accurately reproduced by the approximation (within 10%) for $M_{\rm DM} \gtrsim 500\,\text{GeV}$.

$M_{\rm DM}$ (GeV)	$\langle\sigma v\rangle_{2\to2}$ (pb)	$\langle\sigma v\rangle_{2\to3}\vert_{\rm exact}$ (pb)	$\langle\sigma v\rangle_{2\to3}\vert_{\rm approx}$ (pb)
150	2.642	4.583×10^{-3}	1.459×10^{-3}
300	0.6604	2.078×10^{-3}	1.597×10^{-3}
500	0.2378	1.202×10^{-3}	1.104×10^{-3}
1000	5.944×10^{-2}	5.362×10^{-4}	5.282×10^{-4}
3000	6.605×10^{-3}	1.221×10^{-4}	1.227×10^{-4}

Table 5.1: Thermally averaged cross section $\langle\sigma v\rangle$ for the lowest-order annihilation cross section of vector dark matter into an electron-positron pair, compared to the exact cross section including Z-boson emission, and the splitting functions approximation, for different dark matter masses. For the weak angle and the electroweak coupling we have used $\sin^2\theta_w = 0.23113$ and $\alpha = 1/127.9$, respectively.

We have also computed the coefficients A, B and C for the case where the dark matter particle and the mediator are not mass degenerate [222]. Their explicit form is given in Appendix B[2].

We compare now the fluxes of positrons and antiprotons after parton shower and before propagation through the Galaxy, as shown in Fig. 5.4 and 5.5. The results from the splitting function approximation are in good agreement with the fluxes obtained with the full calculation both for positron and antiproton fluxes, as expected given the good agreement at the Z energy spectrum level. The dip in the splitting functions prediction for the positron flux is a remnant of the kinematics of the leading order process and disappears for larger ratios $M_{\rm DM}/M_{\rm EW}$, as one can see comparing the predictions for 500 GeV and 3000 GeV.

The comparison after propagation is shown in Fig. 5.6 and 5.7[3]. For the positron fluxes we show both the positron component coming from the leading order annihilation and the contribution coming from the decay and evolution of the Z boson. The latter is significantly smaller than the prompt positron component as the cross section of the $(2 \to 3)$ process constitutes an electroweak higher-order corrections of $\mathcal{O}(\alpha \ln^2(M^2_{\rm DM}/M^2_Z))$. However, these higher-order corrections are relevant, as they are the only source of antiprotons in our simple leptophilic model.

We find that the splitting functions approximation gives reliable results for the $(2 \to 3)$ cross section , for the energy spectrum of the radiated electroweak boson and for the fluxes of stable standard model particles before and after propagation for masses $M_{\rm DM} \gtrsim 500\,\text{GeV}$ for the simple vector dark matter model under study.

5.2.2 SUSY model - Majorana dark matter

We perform now the same comparisons as in the previous section for Majorana fermion dark matter. The leading-order cross section given in Eq. (4.5) is helicity suppressed and vanishes for $m_e \to 0$. Again, we compute the $(2 \to 3)$ tree-level cross section for the process $\tilde{\chi}_0\tilde{\chi}_0 \to e^+e^-Z$. Note that the emission of electroweak gauge bosons from both the final and the intermediate state lifts the helicity suppression of the leading-order cross section [206]. However, the splitting function approximation does not describes the emission from the t- and u-channel selectron. Therefore, the approximation is not expected to work in this specific case. Comparing the s-wave contribution to the bino annihilation cross section computed in Ref. [206] against the form obtained from the splitting functions approximation, one can see explicitly that the approximation does not reproduce the dominant behaviour:

$$\frac{dN_Z}{dx} = \frac{(1-x)}{(1+(1-x)^2)^2}\left[\frac{(1-x)}{(2-x)}\ln(1-x) - \frac{1-(1-x)^2}{4\,(1-x)}\right], \tag{5.25}$$

where x is the energy fraction carried away by the radiated Z boson. According to the splitting functions approximation, the Z spectrum is given by Eq. (5.14), that in this particular case would be zero.

The comparison of the two distributions is shown in Fig. 5.8. Clearly the approximation does not capture the dominant contributions of the $(2 \to 3)$ process, that is the emission from the intermediate state. This applies to all processes with Majorana

[2]Mathieu Pellen has performed this calculation.

[3]The plots in Figs. 5.3-5.9 were made by Mathieu Pellen.

fermions in the initial states as the leading-order cross section is helicity suppressed. To further confirm that the approximation does not work because the $(2 \to 2)$ cross section is helicity suppressed, we have compared the Z energy distributions obtained giving a fictitious mass to the electrons in the final state, as shown in Fig. 5.9. With increasing masses, the suppression is reduced. However, the splitting function approximation is still not expected to correctly reproduce the distributions. In fact, the splitting functions correctly reproduce the kinematics for massless fermions in the final state, while they have now masses comparable to the Z boson mass.

5.3 Summary

The splitting functions approximation gives reliable results for the cross section , the energy distribution of the emitted Z boson and for the secondary fluxes in model where the lowest order cross section is not suppressed and for $M_{\rm DM} \gtrsim 500$ GeV. This boundary is expected to be slightly different if the mediator mass is taken different from the dark matter candidate mass. The computations using the splitting functions approximation is simpler as only the $(2 \to 2)$ cross section is needed for a specific model, while the factors taking into account the radiations of electroweak bosons are model independent.

On the other hand, the approximation does not correctly reproduce neither the shape nor the normalisation (namely the cross section) of the Z energy distribution for processes with Majorana fermions in the initial state. Therefore, also the fluxes induced by Z decay are not correctly described by the approximation.

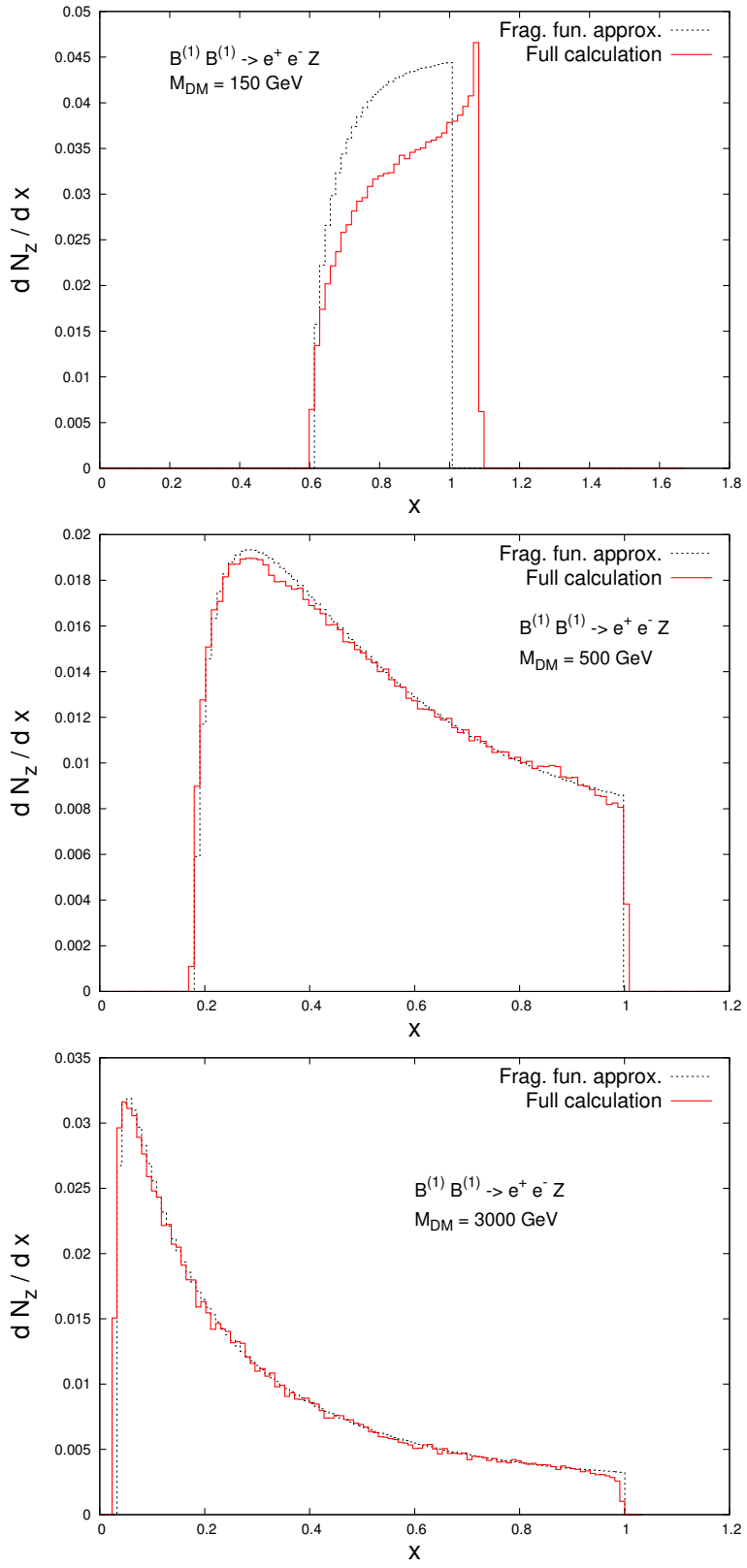

Figure 5.3: Comparison of the Z boson energy spectrum in the process $B^{(1)}B^{(1)} \to e^+e^-Z$ obtained from the exact calculation (red solid line) and from the generalised splitting functions (black dashed line), with $x = 2E_Z/\sqrt{s}$ and $M_{\rm DM} = 150, 500, 3000$ GeV.

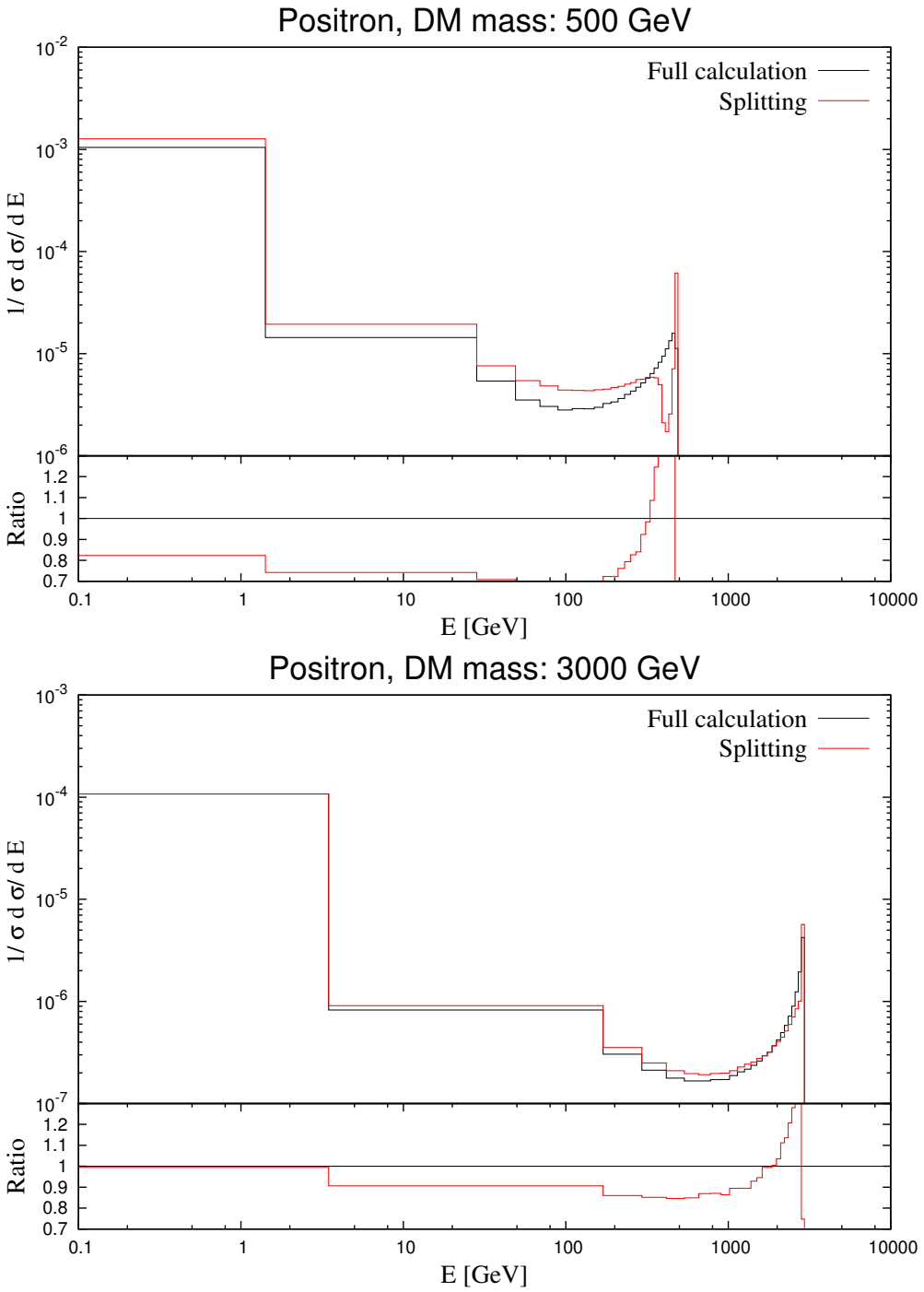

Figure 5.4: Comparison of the positron fluxes from the process $B^{(1)}\,B^{(1)} \to e^+e^-Z$ after parton shower and before propagation through the Galaxy obtained from the exact calculation (red line) and from the generalised splitting functions (black line), with $x = 2E_Z/\sqrt{s}$ and $M_{\rm DM} = 500, 3000$ GeV.

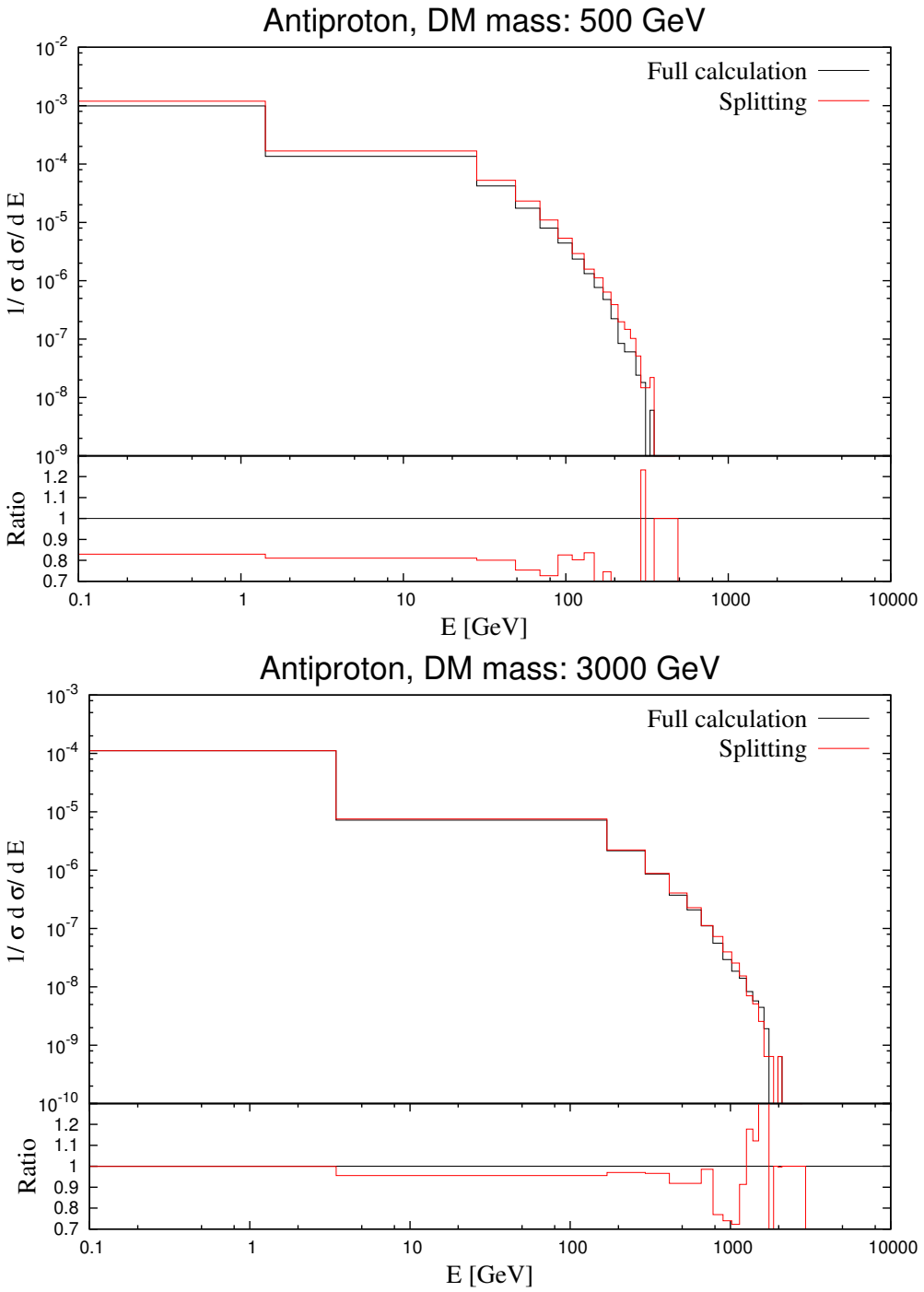

Figure 5.5: Comparison of the antiproton fluxes from the process $B^{(1)}\,B^{(1)} \to e^+e^-Z$ after parton shower and before propagation through the Galaxy obtained from the exact calculation (red line) and from the generalised splitting functions (black line), with $x = 2E_Z/\sqrt{s}$ and $M_{\rm DM} = 500, 3000$ GeV.

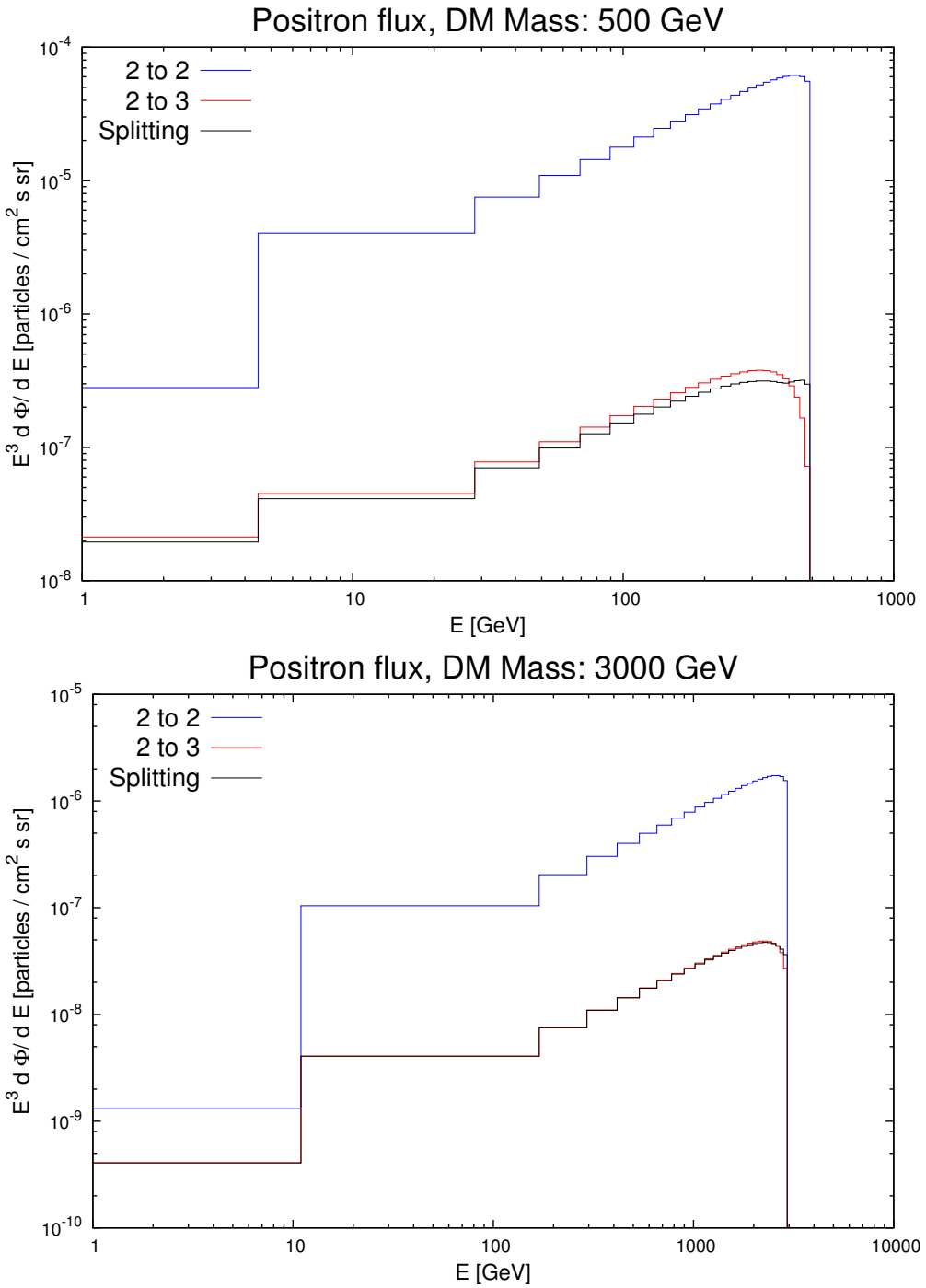

Figure 5.6: Comparison of the positron fluxes from the process $B^{(1)}\,B^{(1)} \to e^+e^-Z$ after parton shower and after propagation through the Galaxy obtained from the exact calculation (red line) and from the generalised splitting functions (black line), with $x = 2E_Z/\sqrt{s}$ and $M_{\rm DM} = 500, 3000$ GeV.

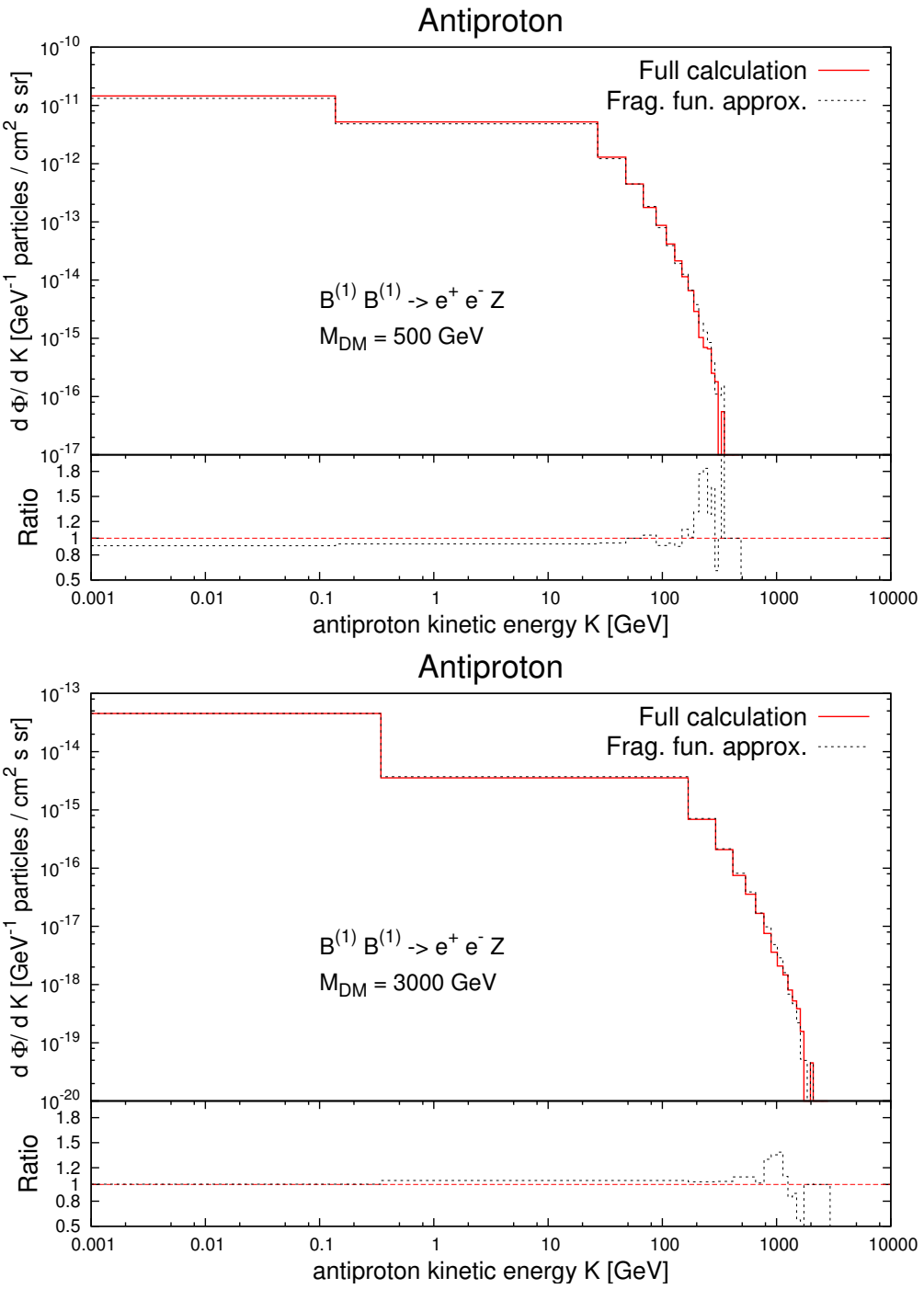

Figure 5.7: Comparison of the antiproton fluxes from the process $B^{(1)}\,B^{(1)} \to e^+e^-Z$ after parton shower and after propagation through the Galaxy obtained from the exact calculation (red line) and from the generalised splitting functions (black line), with $x = 2E_Z/\sqrt{s}$ and $M_{\rm DM} = 500, 3000$ GeV.

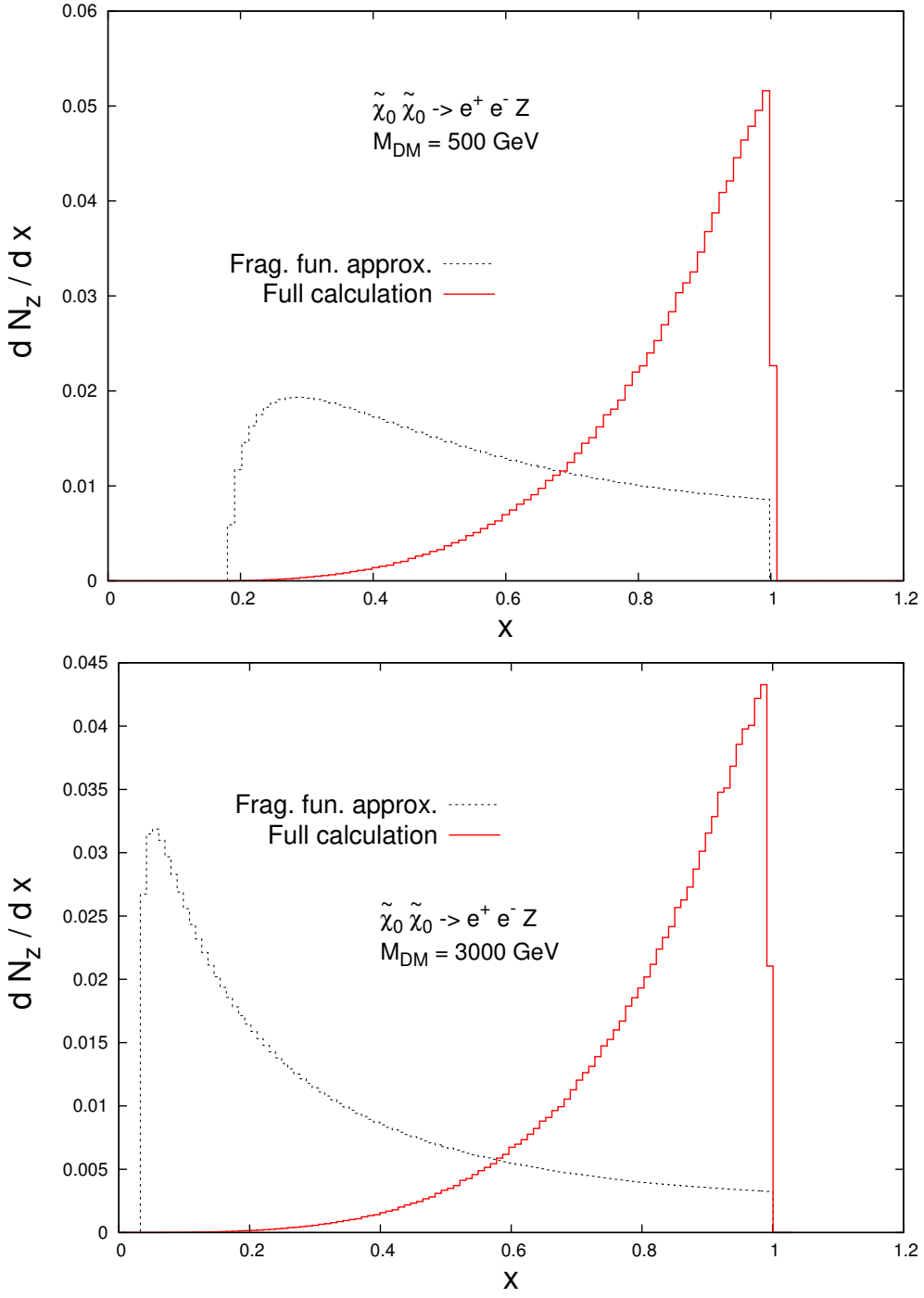

Figure 5.8: Comparison of the Z boson energy spectrum in the process $\tilde{\chi}_0\tilde{\chi}_0 \to e^+e^-Z$ obtained from the exact calculation (red solid line) and from the generalised splitting functions (black dashed line), with $x = 2E_Z/\sqrt{s}$ and $M_{\rm DM} = 500, 3000$ GeV.

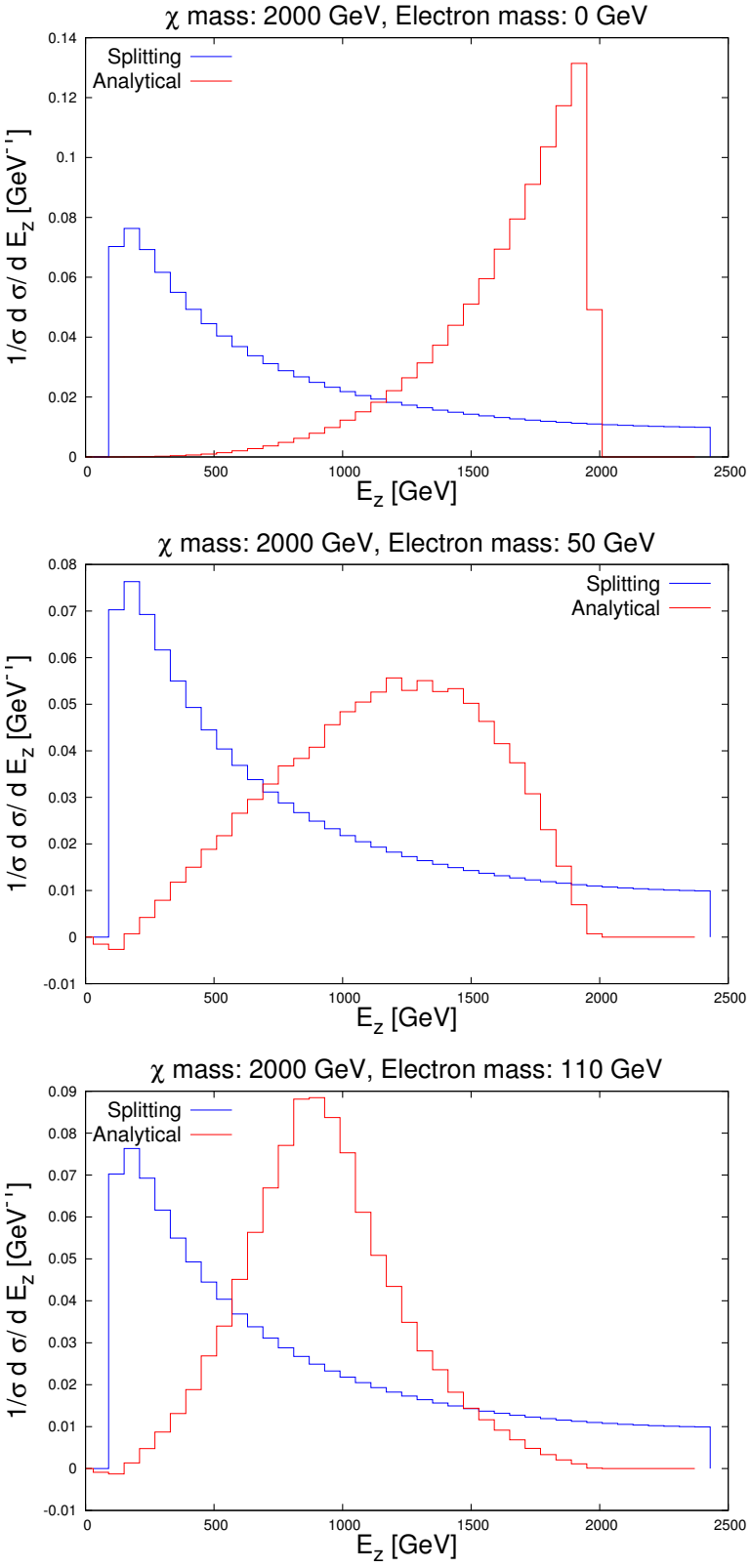

Figure 5.9: Comparison of the Z boson energy spectrum in the process $\tilde{\chi}_0\tilde{\chi}_0 \to e^+e^-Z$ obtained from the exact calculation (red solid line) and from the generalised splitting functions (black dashed line), with $x = 2E_Z/\sqrt{s}$, $M_{\rm DM} = 2000$ GeV for massive final states leptons, $m_e = 0, 50, 110$ GeV.

Part III

Dark Matter searches with AMS-02 data

Chapter 6

Modelling of the background

The AMS-02 experiment [22] measures fluxes and composition of charged cosmic rays with unprecedented precision. Recently, the most precise measurements of the positron fraction [17, 18], total electron and positron flux [223] and separate electron and positron fluxes [173] have been published. These measurements have revealed significant deviations from the expectations according to conventional cosmic rays models. The rise in the positron fraction above $E \gtrsim 10$ GeV had already been observed by previous experiments like AMS-01 [170], HEAT [224], PAMELA [171, 225] and Fermi-LAT [226] and, since then, has received a lot of interest. Analysing the separate fluxes, one finds that for $E \gtrsim 10$ GeV the flux of positrons is harder than the electrons, while it is expected to be softer, as the positrons are assumed to be only secondary particles in standard scenarios. The measurements seem to suggest the presence of a source of primary positrons.

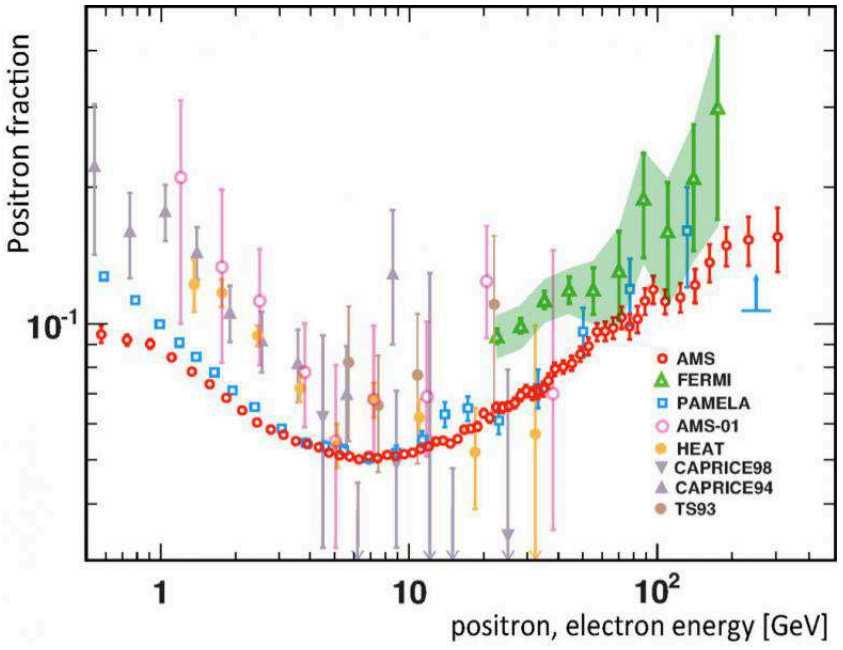

Figure 6.1: The positron fraction measured by the AMS-02 experiment, compared to previous measurements. Credit: AMS-02 collaboration, from `www.ams02.org`.

Several possible explanations have been proposed in the Literature to account for

these discrepancies. These can be sorted into three classes. First, one can assume that the excess in the positrons is of purely astrophysical origin, namely that sources like pulsars or supernovae remnants have not been correctly taken into account [227, 228]. Second, the positron excess can be explained in terms of new exotic sources, like dark matter annihilating in the Galaxy, as for instance in [229]. However, a pure dark matter explanation for the positron excess would require very large cross sections even within models where dark matter purely annihilates into electron-positron pairs and this solution requires rather contrived scenarios [227, 230–237]. The third option consists in assuming that some astrophysical source injects primary positrons (and electrons, as we assume that the sources are charge symmetric) with a smooth spectrum, namely without characteristic spectral features, while dark matter annihilation in the halo might be responsible for additional structures on top of the astrophysical background, as for instance in [238, 239]. This is the scenario we will consider throughout our discussion. Searching for these structures allows to constrain possible dark matter models proposed in the Literature. Thus, an appropriate description of the astrophysical background fluxes is of primary importance, in order to determine reliable and robust constraints on dark matter scenarios.

A first-principle modelling and understanding of the fluxes of astrophysical origin is *per se* relevant and a considerable effort is devoted to the study of this issue. However, no completely satisfactory model has been proposed yet. We do not attempt to provide a first-principle model to describe the fluxes measured by AMS-02. Under the assumption that the background fluxes are smooth, we study a phenomenological parametrisation of the the astrophysical background, whose parameters are determined by fitting the AMS-02 data for lepton fluxes.

In this Chapter, we first discuss a very simple phenomenological model presented in the Literature [17, 18] and widely used to describe the astrophysical background measured by the AMS experiment, for instance in [238]. For this reason, it is interesting to understand its limitations and the possible ways to improve it. After, we discuss an *improved phenomenological model* and the fits to the AMS-02 data, performed to determine its parameters.

This modelling of the background will be subsequently used for the determination of model independent upper limits on the dark matter annihilation cross section, as discussed in Chapter 7.

6.1 Background modelling

Our working assumption is that the positron and electron fluxes measured by the AMS collaboration are made of two contributions. The first one is the astrophysical background. It consists of primary electrons, secondary positrons and electrons, produced via interaction with the interstellar medium, and an additional term, due to possible charge symmetric sources, for instance pulsars. The second contribution is due to dark matter annihilation in the galactic halo. The fluxes of electrons and positrons can be written as

$$\Phi_{e^\pm} = \Phi_{e^\pm}^{bkg} + \Phi_{e^\pm}^{\mathrm{DM}}, \tag{6.1}$$

A simple phenomenological model is presented in [17, 18], where the fluxes are de-

scribed as

$$\begin{aligned}\Phi_{e^+}(E) &= C_{e^+}E^{-\gamma_{e^+}} + C_s E^{-\gamma_s} e^{-E/E_s},\\ \Phi_{e^-}(E) &= C_{e^-}E^{-\gamma_{e^-}} + C_s E^{-\gamma_s} e^{-E/E_s}.\end{aligned} \tag{6.2}$$

Here both the positron and the electron fluxes are described as the sum of a diffuse term, the individual power law in the first term, and a common, charge symmetric, source term, that exhibits an exponential cut off at energy E_s. The fluxes are parametrised by 7 parameters ($\{C_{e^-}, \gamma_{e^-}, C_{e^+}, \gamma_{e^+}, C_s, \gamma_s, 1/E_s\}$), however, the positron fraction measured by AMS depends only on 5 parameters:

$$R(E) = \frac{\Phi_{e^+}}{\Phi_{e^+} + \Phi_{e^-}} = \frac{C_{e^+}/C_{e^-}E^{-(\gamma_{e^+}-\gamma_{e^-})} + C_s/C_{e^-}E^{-(\gamma_s-\gamma_{e^-})}e^{-E/E_s}}{C_{e^+}/C_{e^-}E^{-(\gamma_{e^+}-\gamma_{e^-})} + 2C_s/C_{e^-}E^{-(\gamma_s-\gamma_{e^-})}e^{-E/E_s} + 1}. \tag{6.3}$$

We perform the fit of this model to the positron fraction measurement, as presented by

Parameter	best-fit value	best-fit value in [18]
C_{e^+}/C_{e^-}	0.091 ± 0.001	0.091 ± 0.001
$\gamma_{e^-} - \gamma_{e^+}$	-0.56 ± 0.02	-0.56 ± 0.03
C_s/C_{e^-}	0.0062 ± 0.0007	0.0061 ± 0.0009
$\gamma_{e^-} - \gamma_s$	0.72 ± 0.04	0.72 ± 0.04
$1/E_s$	$(1.82 \pm 0.51)\,\mathrm{TeV}^{-1}$	$(1.84 \pm 0.58)\,\mathrm{TeV}^{-1}$
$\chi^2/d.o.f.$	36.8/58	36.4/58

Table 6.1: Fit to the AMS-02 data in the range $1 - 500$ GeV*, in agreement within the uncertainties with the results in [18]. The differences between our results and the published ones may be due to rounding applied to the published data.*

the AMS collaboration in [17, 18], using the data in [18], namely up to 500 GeV. Note that solar modulation (Cfr. Eq. (3.21)) is not taken into account in this fit. The fit was performed minimising the χ^2 given in Eq. (6.4) with `Minuit` and the best-fit values for the parameters agrees within the uncertainties with the published results, as one can see in Tab. 6.1.

$$\chi^2 = \sum_i \frac{(R_i^{\mathrm{AMS}} - R_i^{\mathrm{model}})^2}{\sigma_i^2}, \tag{6.4}$$

where the index i labels the bins of the positron fraction and σ_i is obtained adding the published statistical and systematic uncertainties in quadrature. Although this model produces a good quality fit[1] to the AMS-02 positron fraction data, it fails in describing the separate fluxes or the total lepton flux [223]. In particular, it does not reproduce the low energy part of the spectrum ($E \lesssim 10$ GeV). This region is extremely relevant to our discussion. First, the fluxes originating from dark matter annihilation in the Galaxy consist mainly of low energetic particles, even if the mass of the dark matter candidate is in the TeV range. This is due to significant energy losses during propagation through the Galaxy, see Sec. 3.1. Therefore, the signal due to dark matter is concentrated in the low energy part of the spectrum. Second, the inclusion of electroweak corrections affects the low energy part of the spectra, as argued in Sec. 4.2. Hence, a reliable description of the fluxes for $E \lesssim 10$ GeV is crucial for our study.

[1] Note that the smallness of the $\chi^2/d.o.f$ suggests that correlations among the uncertainties need to be accounted for.

Improved phenomenological model

An extension of the simple model in Eq. (6.2) has been proposed [240] and provides a more accurate description of the electron and positron fluxes:

$$\begin{aligned}\Phi_{e^+} &= \frac{E^2}{\hat{E}_+^2}[C_{e^+}(\hat{E}_+/E_0)^{-\gamma_{e^+}} + C_s(\hat{E}_+/E_0)^{-\gamma_s}e^{-\hat{E}_+/E_s}],\\ \Phi_{e^-} &= \frac{E^2}{\hat{E}_-^2}[C_{e^-}(\hat{E}_-/E_0)^{-\gamma_{e^-}}F(\hat{E}_-) + C_s(\hat{E}_-/E_0)^{-\gamma_s}e^{-\hat{E}_-/E_s}],\end{aligned} \tag{6.5}$$

with

$$\hat{E}_+ = E + \Psi_+, \tag{6.6a}$$

$$\hat{E}_- = E + \Psi_-, \tag{6.6b}$$

$$F(\hat{E}_-) = \left(1 + \left(\frac{\hat{E}_-}{E_B}\right)^{\Delta\Gamma/\Lambda}\right)^{\Lambda}. \tag{6.6c}$$

The positron diffuse term is assumed to consist of secondary positrons only, therefore the sum of simple power law (the diffuse term) and a source term as in Eq. (6.5) gives an appropriate description for the total positron flux. Contrary to this, the electron diffuse term receives contributions both from primary and secondary electrons. Therefore, the electron flux is described by the sum of a smoothly broken power law, Eq. (6.6c), for the diffuse term, and of a source term. The position of the spectral break is given by E_B, the parameter Λ quantifies the smoothness of the transition and $\Delta\Gamma$ is the difference between the spectral indeces before and after the break. The energies $\hat{E}_\pm$ in Eqs. (6.6a) and (6.6b) are the energies outside the solar system for the positron and the electron, respectively. They both contain an effective charged-dependent potential, $\Psi_\pm$, that takes into account shifts of the energy scale due solar modulation effects, within the force field approximation[2]. The pivot energy E_0 is set to $E_0 = 5\,\mathrm{GeV}$ throughout this work.

6.2 Fit to electron and positron fluxes

To obtain the 12 parameters $\theta = \{\Psi_\pm, C_{e^\pm}, \gamma_{e^\pm}, C_s, \gamma_s, E_s, E_B, \Delta\gamma, \Lambda\}$, describing the improved phenomenological model, we perform a combined fit of the model to the electron and positron fluxes. We use the data in [173], that cover the energy range from 0.5 GeV up to 500 GeV and up to 700 GeV for the positrons and the electrons, respectively. The uncertainty σ is obtained for both data sets summing in quadrature the published statistical uncertainties with an uncorrelated systematic uncertainty of 0.25%. In fact, our goal is to obtain a good description of the background fluxes in terms of smooth functions and with this choice for the systematic uncertainty we obtain good quality fits to the data. We minimise the combined χ^2

$$\chi^2 = \sum_i \frac{(\Phi_{e^+,i}^{\mathrm{AMS}} - \tilde{\Phi}_{e^+,i}^{\mathrm{model}})^2}{\sigma_i^2} + \sum_j \frac{(\Phi_{e^-,j}^{\mathrm{AMS}} - \tilde{\Phi}_{e^-,j}^{\mathrm{model}})^2}{\sigma_j^2} \tag{6.7}$$

[2]Note that the potentials should in principle be time dependent. However, this effective parametrisation already gives a reliable description of the fluxes. Moreover, only time averaged data are available.

where the indeces i, j label the bins of the positron and electron fluxes, respectively and

$$\tilde{\Phi}^{\text{model}}_{e^+,i} = \frac{1}{E^{\text{max}}_i - E^{\text{min}}_i} \int_{E^{\text{min}}_i}^{E^{\text{max}}_i} \Phi^{\text{model}}_{e^+,i}(E) dE, \tag{6.8a}$$

$$\tilde{\Phi}^{\text{model}}_{e^-,j} = \frac{1}{E^{\text{max}}_j - E^{\text{min}}_j} \int_{E^{\text{min}}_j}^{E^{\text{max}}_j} \Phi^{\text{model}}_{e^-,j}(E) dE, \tag{6.8b}$$

where E^{min} and E^{max} are the boundaries of the bin. We first perform two separate fits of the positron flux and electron flux, to obtain initial values for the parameters for the combined fit. Using this set of values as starting point, we obtain the best-fit values for the parameters minimising the χ^2 in Eq. (6.7) with `Minuit`. We fit in the energy range from 3 GeV up to 500 GeV for the positron flux and 700 GeV for the electron flux. The energy bins below 3 GeV are excluded from the fit in order to avoid the region where the electron and positron fluxes are dominated by solar modulation. Moreover, in that low energy region some hints for a structure possibly due to systematic effects is observed, therefore we perform the fit only using energy bins above 3 GeV. The results of the fit are collected in Tab. 6.2 and in Fig. 6.3 and 6.2. A pictorial representation of the correlation matrix is given in Fig. 6.4, where significant correlations among some of the parameters are observed, as for instance among the parameters describing the electron flux. Moreover, we find that the parameters in Tab. 6.2 also describe the positron fraction and the total lepton flux.

Parameter	Best-fit value
Ψ_+	(0.82 ± 0.03) GV
Ψ_-	(1.45 ± 0.03) GV
C_{e^+}	(0.18 ± 0.01) GeV^{-1}m^{-2}s^{-1}sr^{-1}
γ_{e^+}	-3.59 ± 0.03
C_{e^-}	(2.26 ± 0.04) GeV^{-1}m^{-2}s^{-1}sr^{-1}
γ_{e^-}	-3.278 ± 0.007
C_s	(0.019 ± 0.003) GeV^{-1}m^{-2}s^{-1}sr^{-1}
γ_s	-2.36 ± 0.05
$1/E_B$	(0.034 ± 0.002) GeV^{-1}
$\Delta\Gamma$	-0.64 ± 0.03
Λ	0.31 ± 0.03
$1/E_s$	(0.0016 ± 0.0005) GeV^{-1}
$\chi^2/d.o.f$	136/113

Table 6.2: Best-fit values for the parameters describing the improved phenomenological model, obtained fitting the model to the AMS-02 data in the range $3 - 500$ GeV *for the positron flux and* $3 - 700$ GeV *for the electron flux.*

6.3 Overall energy uncertainty

We also study the impact of the overall uncertainty on the energy scale of the detector. According to Ref. [173], the uncertainty is 5% at 0.5 GeV, 2% between 10 GeV and 290 GeV and 4% at 700 GeV, as in Fig. 6.5.

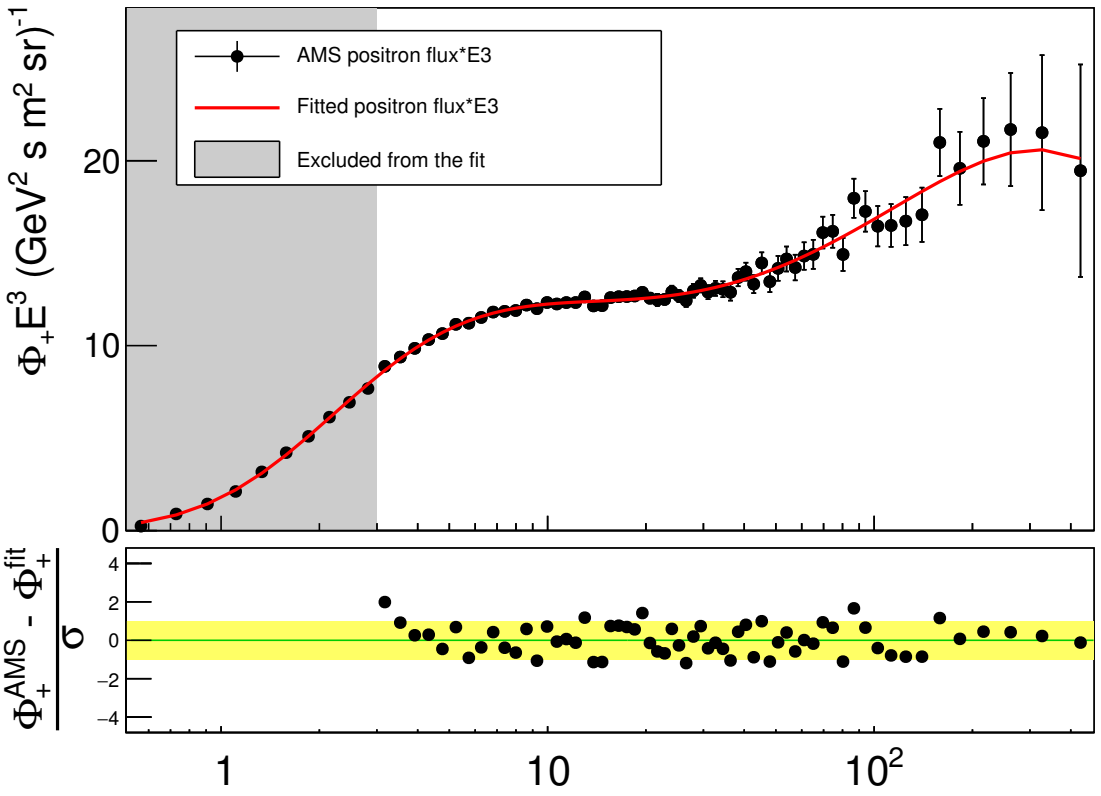

Figure 6.2: Panel above: best-fit curve for the positron flux, obtained setting the parameters of the model in Eq. (6.5) *to the values in Tab. 6.2. The errors bars represent the errors used for the fit, namely statistical error plus 0.25% systematic error, not the published total uncertainty. The grey shaded region represents the region with* $E < 3$ GeV*, that is excluded from the fit. Panel below: difference of the measured positron flux and the fit curve relative to the error. The yellow band represents the* $1\,\sigma$ *region.*

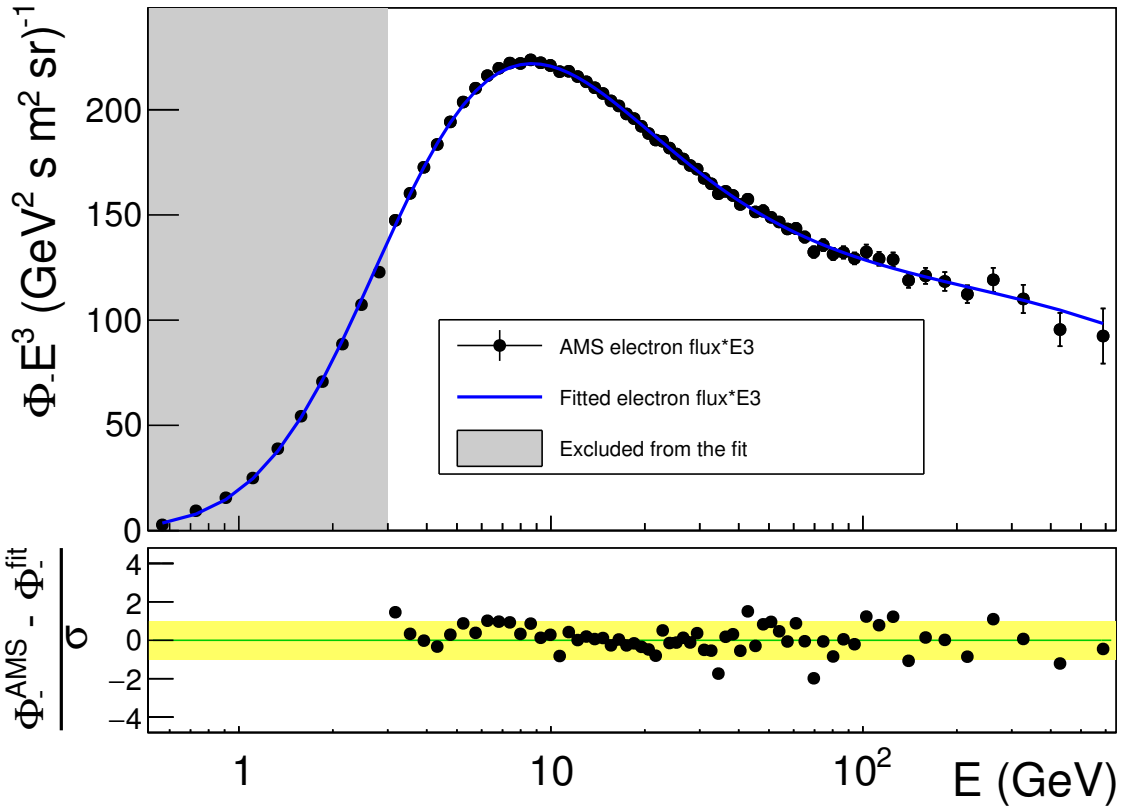

Figure 6.3: Panel above: best-fit curve for the electron flux, obtained setting the parameters of the model in Eq. (6.5) to the values in Tab. 6.2. As for the positron flux, the error bars represent the reduced error used for the fit. The grey shaded region represents the region with $E < 3$ GeV, that is excluded from the fit. Panel below: difference of the measured electron flux and the fit curve relative to the error. The yellow band represents the $1\,\sigma$ region.

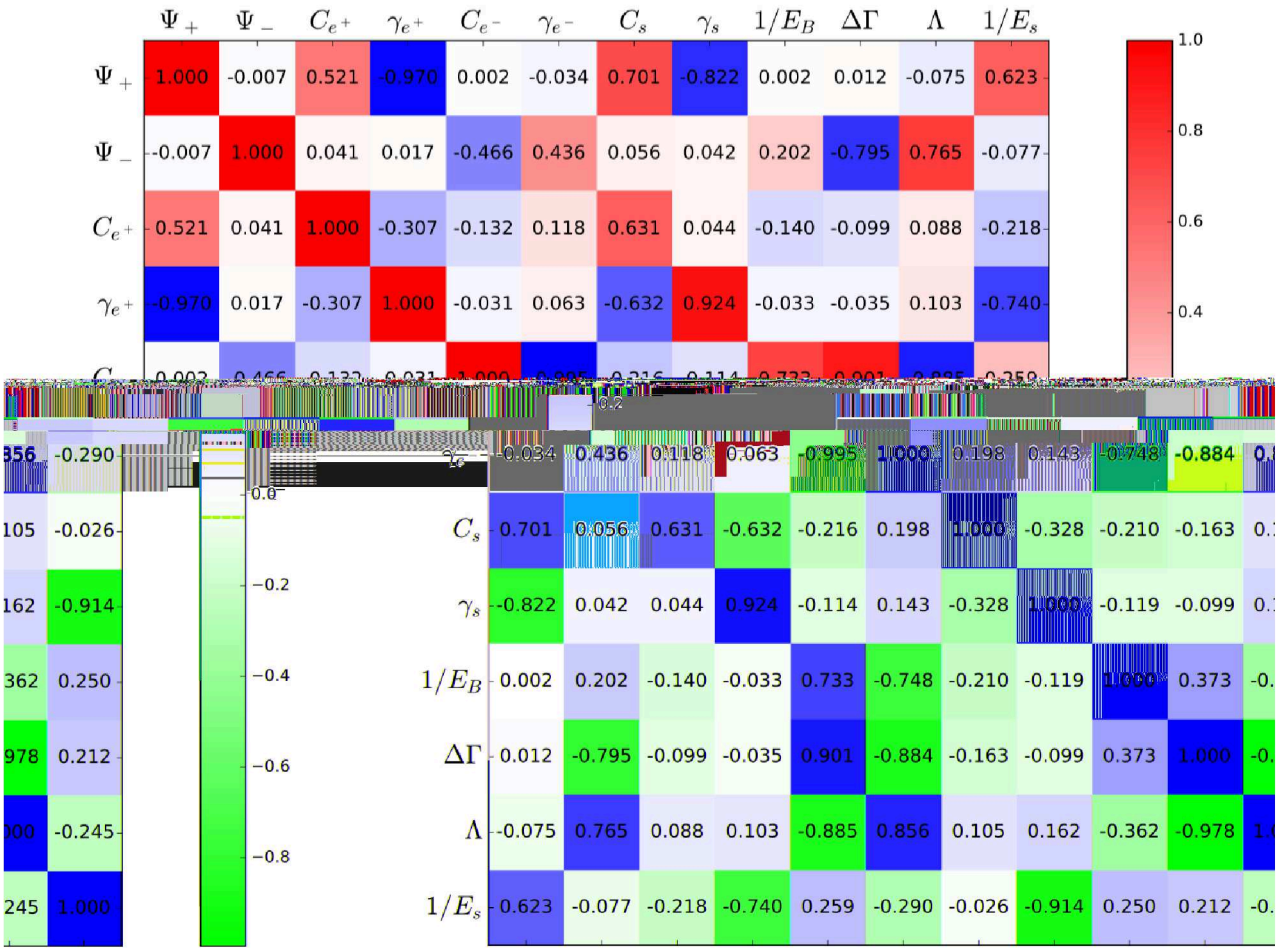

Figure 6.4: Pictorial representation of the correlation matrix from the fit to the electron and positron fluxes. Significant correlations among some of the parameters are observed. Red: positive correlation coefficients. Blue: negative correlation coefficients.

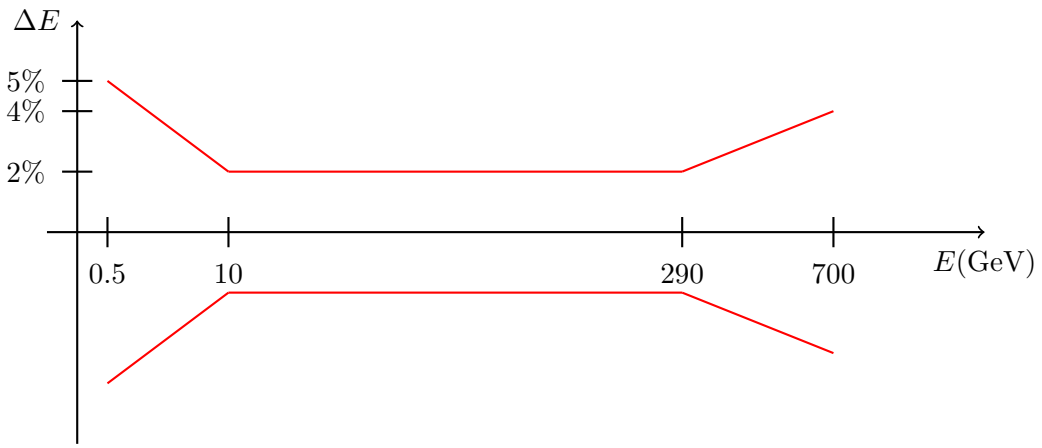

Figure 6.5: Overall uncertainty on the energy scale of the AMS detector. The red line shows the quoted error.

To quantify the effects of this uncertainty on the fit result, we extract for each bin a value for the uncertainty that lies within the envelope given by the uncertainties in [173] (red solid line in Fig. 6.5) and perform the fit. This has an impact on the integration in Eqs. (6.8) as the energy bin boundaries $E_j^{\rm min}$ and $E_j^{\rm max}$ have to be corrected accordingly. For this study, we repeat this procedure 1000 times with a Montecarlo program and for each set of uncertainties we perform the fit. For each parameter we take the median value.

Performing a fit using the quoted uncertainties, we find that the best-fit values for the parameters deviate[3] from those in Tab 6.2 of about 5% for the parameters $C_s, \Lambda, 1/E_s$, while for the other parameters the deviation is in the range $[0.1\% - 2\%]$. Comparing the best-fit values of Tab 6.2 with the median best-fit values obtained considering 1000 values for θ we find significantly smaller deviations. For example, for $1/E_s$ the relative deviation decreases to 0.3%. The largest deviation is 1% for the Λ and the $\Delta\Gamma$ parameters. For all other parameters the effect is below 0.3%.

For the calculation of the upper limits on the dark matter annihilation cross section, we do not take into account these uncertainties on the description of the background, as they are smaller then the uncertainties on the dark matter distribution in the Galaxy and on the modelling of the propagation of CR.

6.4 Fit to positron fraction and total lepton flux

We now perform a combined fit to the positron fraction and total lepton flux data. However, we cannot take into account effects due to the correlation between the two data sets using the published data. Therefore, this has to be considered as a consistency check for the fit using electron and positron fluxes, that are two uncorrelated data sets.

The fits is consistent with the fit to electron and positron fluxes. The results are collected in Appendix C.

[3]By deviation we denote the difference between the best-fit values from Tab 6.2 and the best-fit values obtained including the overall uncertainty on the energy scale, relative to the values in Tab 6.2.

Chapter 7

Constraining the DM annihilation cross section

In this Chapter we compute upper limits on the dark matter annihilation cross section for a generic class of models, where dark matter annihilates at leading order only into electron-positron pairs, namely the so-called leptophilic models. These models were first introduced to explain within the dark matter scenario the presence of an excess in the positron fraction and the absence of such a significant excess in hadronic channels, like the antiprotons. It is interesting to notice that according to the new preliminary antiproton ratio measurements presented by the AMS collaboration [175], an additional exotic contribution to the antiproton fluxes is not excluded. However, it is yet too early to make robust statements. Leptophilic models are also interesting, as the inclusion of electroweak radiation is particularly relevant. In fact, one would naively expect that no antiprotons (or hadrons in general) are produced via the annihilation of leptophilic dark matter in the halo, as only leptons are produced. However, as argued in Sec. 4.2, highly energetic final state leptons can radiate EW gauge bosons, that further decay and evolve, and fluxes of all SM stable particles are produced, including antiprotons. In leptophilic models, EW radiation is the only source of antiprotons.

Furthermore, within these models one has the highest sensitivity when comparing against AMS-02 measured lepton fluxes. Therefore, we consider this class of models and place constraints on the $(2 \to 2)$ annihilation cross section. These first limits do not depend on the specific leptophilic model under study.

After this, we study the effects of including electroweak radiation when obtaining the predictions for the fluxes originating from dark matter annihilation. For dark matter candidates with masses $M_{\rm DM} \gtrsim 500$ GeV it would be possible to use the fragmentation function approximation, to include the electroweak radiation and obtain conclusions independent from the specific model under study. However, we want to exploit all the information contained in the energy range probed by AMS. Therefore, we consider dark matter candidates with masses in the range $M_{\rm DM} \in (4, 500)$ GeV. In this range the fragmentation function approximation cannot be used, because the approximation gives reliable results for $M_{\rm DM} \gtrsim 500$ GeV, as shown in Chap. 5. Hence, we use the simple UED model presented in Sec. 4.1.1 to investigate the impact of including electroweak corrections. Therefore, the upper limits obtained including EW emission are strictly speaking model dependent, in contrast to the first limits we computed. In Sec. 7.3 we show that EW gauge boson emission not only provides an additional contri-

bution to the electron and positron fluxes, but also induces a flux of antiprotons, that would have been completely neglected otherwise. While the impact on the upper limits of including EW emission turns out to be very modest, the induced antiproton fluxes are sizeable for large masses. These additional predictions can be compared to PAMELA and preliminary AMS-02 data. The complementarity among different measurements can possibly allow for further constraining this class of models.

7.1 Limits setting

We place 95% CL upper limits on the normalisation of a signal originating from dark matter annihilating in the Galaxy. These limits can be easily translated into upper limits on the cross section for the process DM DM $\to e^- e^+$. We use the separate measurements of electron and positron fluxes, as in Sec. 6.2, as these constitute uncorrelated data sets. To compute the upper limits on the normalisation, we consider the following profile likelihood ratio:

$$q_N = \begin{cases} -2 \ln \lambda(N) & N \geq 0 \\ 0 & N < 0, \end{cases} \tag{7.1}$$

with

$$\lambda(N) = \frac{\mathcal{L}(N, \theta)}{\mathcal{L}(0, \theta)} \tag{7.2}$$

where $\mathcal{L}(0, \theta)$ is the maximum likelihood for the fit for $N = 0$, namely in the null-hypothesis, while $\mathcal{L}(N, \theta)$ is the maximum likelihood for the fit where positrons and electron fluxes due to dark matter annihilation with normalisation N are added to the background fluxes described by Eqs. 6.5.
The nuisance parameters $(\{\Psi_\pm, C_{e^\pm}, \gamma_{e^\pm}, C_s, \gamma_s, E_s, E_B, \Delta\gamma, \Lambda\})$ describe the background fluxes and are left free to vary. In other words, to compute the upper limit value of the normalisation $N_{\rm UL}$, we fit the electron and positron fluxes with both dark matter and background contributions to the AMS data with different values of N and determine N such that the p-value is 5%:

$$p_N = \int_{q_{N_{UL}}}^{\infty} f(q_N|N) dq_N = 0.05, \tag{7.3}$$

where f is the probability distribution function. We actually implement the equivalent requirement

$$\chi^2_{\rm min}(N) - \chi^2_{\rm min}(N = 0) = 2.61, \tag{7.4}$$

using Wilks' theorem [241]. This is justified as the statistics is large enough.

Figure 7.1 shows an example of signal-plus-background flux compared to the AMS-02 data, both for positrons and electrons. The background flux of electrons is significantly larger than the flux of positrons, that is in turn significantly more sensitive to the presence of an additional contribution.

The signal is obtained propagating the primary flux due to the annihilation process DM DM $\to e^- e^+$. Note that in this case dark matter annihilation is a charge-symmetric source, as the same amount of electrons and positrons is produced and the primary signal both for positrons and electrons is simply a Dirac delta at $E = M_{\rm DM}$. Due to energy

losses during propagation, the secondary signal is smeared out and at considerably lower energies (see blue line in Figs. 7.2 and 7.3). Moreover, we take into account the effects of solar modulation, correcting the signal as follows:

$$\Phi_{e^\pm}^{\rm SolMod}(E) = \left(\frac{E}{E+\Psi_\pm}\right)^2 \Phi(E+\Psi_\pm). \tag{7.5}$$

As one can see from Figs. 7.2 and 7.3, because of solar modulation a significant portion of low energy particles is deflected away and the signal at Earth is consequently reduced. The shape of the signal is determined by these sequence of steps, while the normalisation is arbitrary, and this is the quantity we place limits on. For this study, we consider the NFW dark matter halo model [105, 104]

$$\rho(r) = \rho_s \frac{r}{r_s}\left(1+\frac{r}{r_s}\right)^2 \tag{7.6}$$

and the MED propagation scenario (see Ref. [107]).

7.2 Results for the upper limits on the $2 \to 2$ annihilation cross section and discussion

We first perform a significance scan. We do not observe significant deviations from the expected background, described by Eqs. (6.5). Therefore we compute constrains on the dark matter annihilation cross section into electrons and positrons. From the procedure described in Sec. 7.1, the upper limit value for the normalisation of the electron and positron signals, N_{UL} is obtained. This can be converted into an upper limit on the leading order annihilation cross section $\langle\sigma v\rangle_{UL}$, multiplying N_{UL} times the cross section $\langle\sigma v\rangle_{2\to2}$ according to which the events have been generated. To do this, two procedures are completely equivalent. First, one can generate the events for all masses according to the same fictitious cross section (say $\sigma v = 1$ pb, where by v we as usual mean v/c, namely a dimensionless quantity) and compute the upper limits on the normalisation using the fluxes obtained this way. Second, one can generate the events according the cross section given in Eq. (4.2), that depends on the mass of the dark matter candidate, and compute the upper limits on the normalisation. The upper limits on the normalisation of the signal will clearly differ in the two cases, but the product

$$\langle\sigma v\rangle_{UL} = N_{UL} \times \langle\sigma v\rangle_{2\to2} \tag{7.7}$$

is the same in both cases[1].

Points in the parameter space where the maximum value of the annihilation cross section is below the thermal cross section $\langle\sigma v\rangle_{\rm thermal} = 3\cdot10^{-26}{\rm cm}^3/{\rm s}$ are not allowed. In fact, the relic abundance corresponding to these scenarios would be higher than the measured one as the annihilation of dark matter would have been less efficient and the overabundance of dark matter would overclose the Universe. On the other hand, the scenarios corresponding to a maximum annihilation cross section larger than $\langle\sigma v\rangle_{\rm thermal}$

[1]The $\langle\sigma v\rangle_{UL}$ obtained this way is in pb. To convert it into the units ${\rm cm}^3/{\rm s}$, one has to multiply it time the factor $F = F_{\rm pb\to cm^2}\times c \simeq 3\cdot10^{-26}{\rm cm}^3/{\rm s\,pb}$.

are still viable. These are scenarios where leptophilic WIMPs constitute only a given fraction of the total dark matter in the Universe.

The results for the observed upper limits are shown in Fig. 7.4, where the shaded band represents the total uncertainty due to propagation parameters, different dark matter halo models and different values of the local dark matter density. More specifically, for each propagation scenario and halo model we have used a different Green function (cfr. Secs 2.3 and 3.1), according to the parametrisation in Ref. [107]. The uncertainties due to the propagation model are estimated by choosing a specific dark matter halo model (NFW, in our case) and varying the parameters describing the propagation models (MIN, MED, MAX) in the range considered in Ref. [107]. For the uncertainties due to the choice of the dark matter halo model, we choose a specific propagation scenario (MED, in our case) and vary the parameters describing the dark matter distribution, again according to Ref. [107]. For the local density, we have considered the range $\rho_\odot = 0.25 - 0.7\,\mathrm{GeV/cm^3}$, as in Ref. [107]. The most relevant uncertainty comes from the value of the local density. To take different values into account it is sufficient to simply rescale the fluxes and therefore the results for the upper limits (Cfr. Eq. (3.13)). In Appendix D we separately show the impact of the different sources of uncertainties.
From this study, we can exclude all purely leptophilic WIMP dark matter scenarios with masses $M \lesssim 100$ GeV. This result is consistent with the expected limits, obtained dicing 1000 pseudo-experiments for each dark matter mass hypothesis probed. For each bin we consider a gaussian centred at the prediction for that bin according to the background functions. We take as width the reduced error (statistic uncertainty quoted in the paper, plus 0.25% of the systematic uncertainty). The correlations among bins is not taken into account. In Fig. 7.5 shows the comparison of the observed upper limits to the expected limits (green dashed line) and to the projected limits (red dashed line), namely the limits one would obtained assuming that AMS-02 takes data for 10 years, namely, roughly 4 times longer than the data-set we considered. Therefore the statistical uncertainties reduce of about a factor 2. The systematic uncertainties would in principle also change, both because some part of the instrument deteriorate with time but also because some of the systematic uncertainties are estimated using data-driven methods and the estimate would become better with higher statistics. However, we do not account for these effects and our projected limits should be regarded as an estimate. Fig. 7.6 shows again the expected limits and the projected limits, respectively, with the corresponding 1σ and 2σ bands. One can see that the observed limits essentially completely lie within the 1σ band. Our observed bounds are consistent with previous studies [238, 239]. However, for our analysis we have used the most recent data available for the electron and positron fluxes and an improved description of the background, that is reliable also at low energies.
As for the fits, we repeat our procedure using the total lepton flux and positron fraction to have a consistency check of our results. We obtain consistent limits using these data sets. However, an accurate study is not possible, as already discussed for the fits.

7.3 Inclusion of EW radiation: predictions for antiproton fluxes

In the previous Section we have computed 95% CL upper limits on the dark matter annihilation cross section for a generic model where dark matter annihilates at leading order only into positrons and electrons. We now study the impact of the inclusion of electroweak corrections on these results. Using the fragmentation functions approximation one could include the electroweak corrections in a model independent way. However, the approximation is known to be reliable for $M_{\rm DM} \gtrsim 500$ GeV, while we are interested also in smaller dark matter masses. Therefore, we use again the simple UED model introduced in Sec. 4.1.1. Concerning the upper limits from positron and electron fluxes, the inclusion of electroweak corrections introduces an additional yield of electrons and positrons, due to the decay of the electroweak gauge bosons or of evolution of other decay products. In this case, we consider the contribution due to the emission both of Z and W bosons, shown in Fig. 7.7.

Electroweak corrections have a negligible impact on the upper limits from positron and electron fluxes even for very large dark matter masses. In fact, most of the particles coming from the emission of EW bosons are at very low energies. As one can see from Fig. 7.8, most of the effect due to EW radiation is concentrated in the energy region that we exclude from the fit. This explains why the impact on the upper limits is mostly below 1% even though the additional yield of electrons and positrons is of order 10%. However, electroweak corrections are crucial in order to obtain consistent predictions from dark matter models, to compare with experimental results. As already discussed, through the emission of electroweak gauge bosons all stable Standard Model particles will be present in the final state, independently of the nature of the primary annihilation products and a correlation among the fluxes of different species is introduced. Therefore antiprotons and other hadrons will be produced through dark matter annihilation even when considering leptophilic models.

Assuming to be on the edge of discovering dark matter, namely that the dark matter $(2 \to 2)$ annihilation cross section is close to its the upper limits value, we obtain predictions for the antiproton flux we expect from dark matter annihilation. Example of these fluxes are shown in Fig. F.1.

These predictions can then be compared with the antiproton flux measurements by the PAMELA collaboration [242]. To have a more complete understanding of the potential information contained in the antiproton measurements, we consider also the preliminary AMS-02 antiproton-to-proton ratio presented in [175] and compare our signal-plus-background expectations to the antiproton-to-proton data measured by PAMELA [242] and AMS-02. At this stage, we take as estimate of the antiproton background flux the "fiducial" antiproton-to-proton astrophysical ratio presented in [243]. Indeed, our first goal is to understand whether it is possible to obtain further constrains by consistently including the antiproton flux due to dark matter annihilation in the Galaxy.

7.4 Results for the antiproton predictions and discussion

In Figs. 7.10 and 7.11 we show the predictions for antiproton fluxes for some representative masses, obtained adding to the expected background an additional component due to dark matter annihilation in the Galaxy, normalised to the upper limit value of the

annihilation cross section [2]. Correctly taking into account the emission of electroweak gauge boson we obtain predictions for the antiproton flux even within a leptophilic model. Even though the electroweak corrections do not play a relevant role when computing upper limits on the $2 \to 2$ annihilation cross section they are of crucial importance and the contribution to the antiproton flux we obtain is sizeable, especially for very large masses.

Our results in Fig. 7.11 seem to suggest that leptophilic scenarios with very large masses could be excluded by future antiproton flux measurements. This shows once again the importance of correctly including the radiation of electroweak gauge bosons to exploit all the information contained in the available measurements.

However, one has to carefully examine the relevant sources of uncertainty, in order to make robust statements. Relevant to us are the uncertainties due to different propagation scenarios (MIN, MED, MAX, as in Ref. [107]), as shown in Fig. 7.12.

Another relevant uncertainty source is the poor knowledge of the antiproton production cross section [3] outside the range where measurements are available, as remarked in Refs. [244, 245] and Refs. therein. Outside this range (kinetic energy $K \in [20, 300]$ GeV), the value of the antiproton production cross section is extrapolated according to phenomenological models. These models all reproduce the measured values satisfactorily but strongly disagree for $K \lesssim 20$ GeV and $K \gtrsim 300$ GeV. For low energies, the dominant uncertainties are of astrophysical nature (solar modulation effects, choice of propagation model, etc.), while for high energies the uncertainties on the cross section are the dominant ones[4]. Here the uncertainty is of the order of 50%, as argued for instance in Ref. [244] and we give a rough estimate of the effect of this uncertainty in Fig. 7.13, where we show the expected antiproton flux assuming that the cross section is a factor 2 smaller and larger, respectively. Note that this gives an estimate of the uncertainties at high energies ($K \gtrsim 300$ GeV), while the uncertainty we show is overestimated in the energy region $K \in [20, 300]$ GeV, where measurements are available.

Including electroweak corrections opens the possibility of exploiting different complementary measurements of cosmic rays fluxes, such as antiprotons, but also neutrinos and photons[5] to place robust and consistent constraints on dark matter models. However, a significant reduction of the uncertainties due to cosmic rays propagation models and to the antiproton cross section knowledge is necessary in order to draw solid conclusions.

7.5 Summary

In Chapter 6 we have studied a phenomenological parametrisation of the astrophysical electron and positron fluxes. We have determined the parameters fitting the model to the AMS separate measurements of the electron and positron fluxes. This phenomenological model provides a reliable description of the measurements. Under the assumption that astrophysical fluxes are smooth and that dark matter annihilation in the Galaxy contributes with structures on top of the smooth background, we have computed upper limits on the annihilation cross section of leptophilic dark matter into electron-positron

[2] Even though the difference is negligible, we use the values obtained including EW radiation.

[3] We will always refer to the inclusive antiproton cross section in proton-proton collisions as so far no data is available on proton-helium or helium-helium collision. This last process are also of astrophysical interest.

[4] For a more complete and very clear discussion see Ref. [244]

[5] In this thesis, we do not study neutrinos or gamma-rays fluxes.

pairs and exclude these models for masses below 100 GeV, as discussed in Chapter 7. These limits can be also applied to models where dark matter *also* annihilates into electron-positron pairs, by rescaling them according to the branching ratio into electron-positron pairs. Moreover, we have studied the effects of the inclusion of EW radiation, as discussed in Chapter 4. The impact on the upper limits on the annihilation cross section is essentially of no consequence. However, the emission of EW radiation induces a flux of antiprotons even in leptophilic models, that would be otherwise completely neglected. These fluxes can be sizeable for high dark matter masses and comparing to the measured antiproton flux or antiproton-to-proton ratio can allow for obtaining further constrain this class of models. Nevertheless, to be able to make robust statements using the antiproton measurements, a better modelling of the propagation in the Galaxy and better measurements of the inclusive antiproton production cross section are necessary.

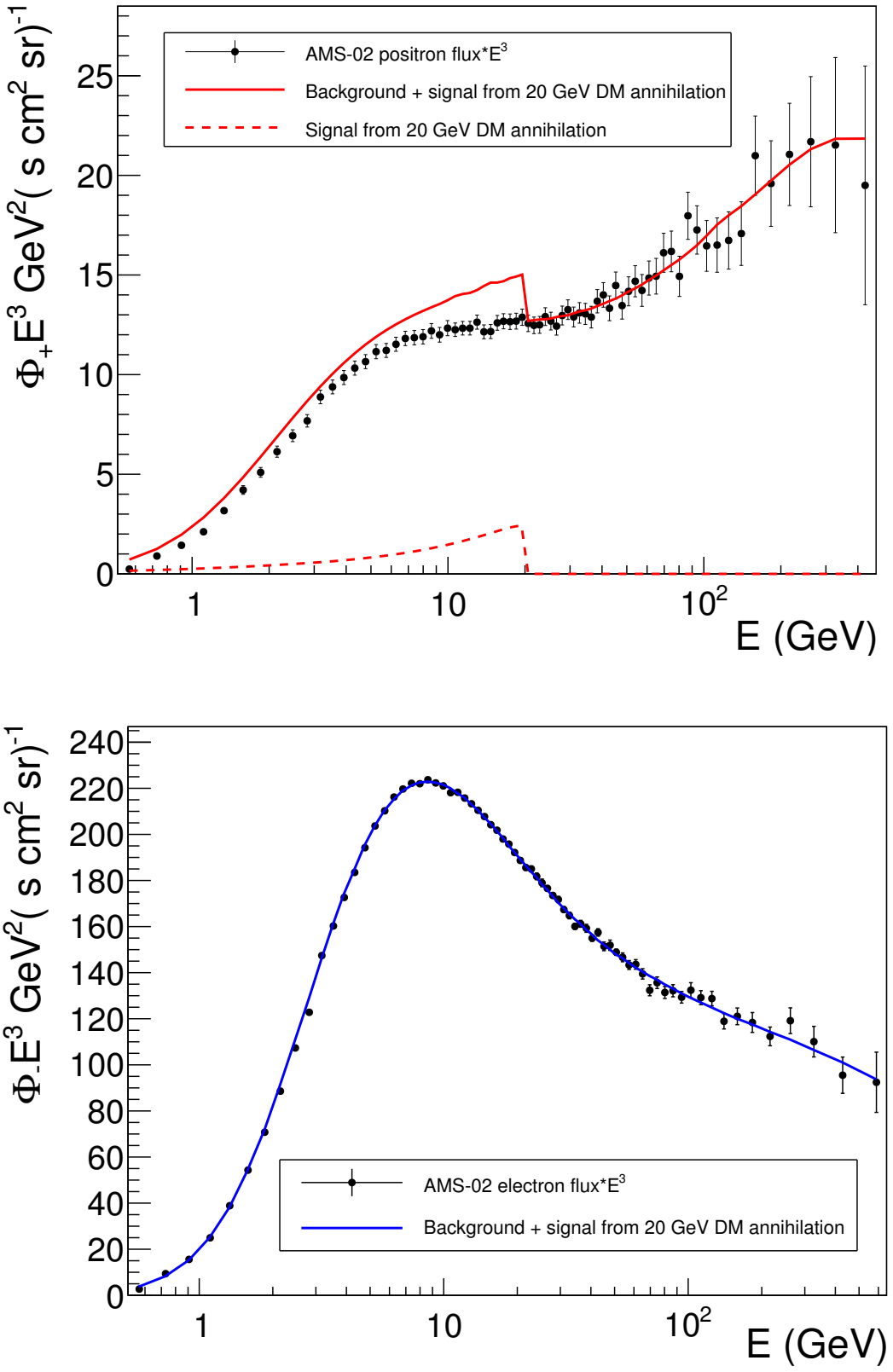

Figure 7.1: Signal plus background curve for a $M_{\mathrm{DM}} = 20$ GeV leptophilic dark matter candidate and $N \simeq 0.002$ for the positron flux (top) and the electron flux (bottom). The normalisation of the signal is the quantity we constrain by comparing against the AMS-02 measurements for the fluxes.

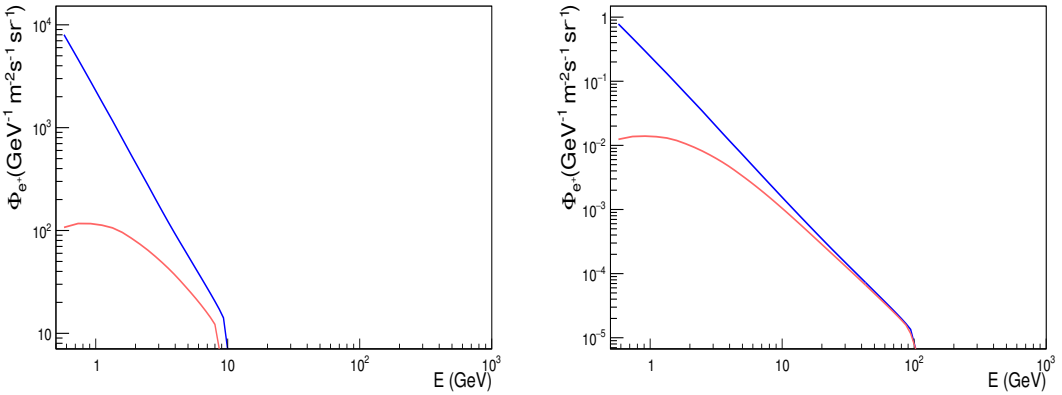

Figure 7.2: Effects of solar modulation on the positron flux due to 10 GeV (left) and 100 GeV (right) dark matter annihilation. Blue line: flux after propagation through the Galaxy and before solar modulation. Red line: flux after propagation through the Galaxy and solar modulation. The solar modulation effective potential is set to $\Psi_+ = 1\,\mathrm{GV}$. *Note that the break at the end of the spectrum is an artifact of the binning used.*

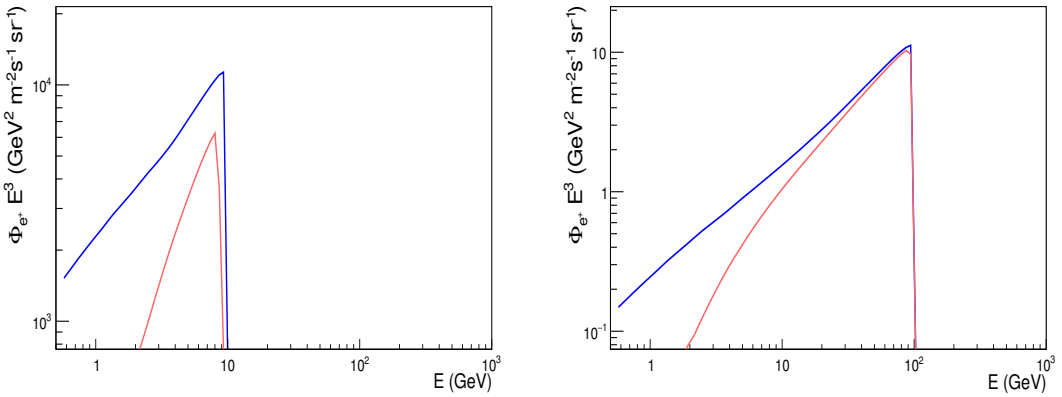

Figure 7.3: Effects of solar modulation on the positron flux times E^3 *due to 10 GeV (left) and 100 GeV (right) dark matter annihilation. Blue line: flux times* E^3 *after propagation through the Galaxy and before solar modulation. Red line: flux times* E^3 *after propagation through the Galaxy and solar modulation. The solar modulation effective potential is set to* $\Psi_+ = 1\,\mathrm{GV}$.

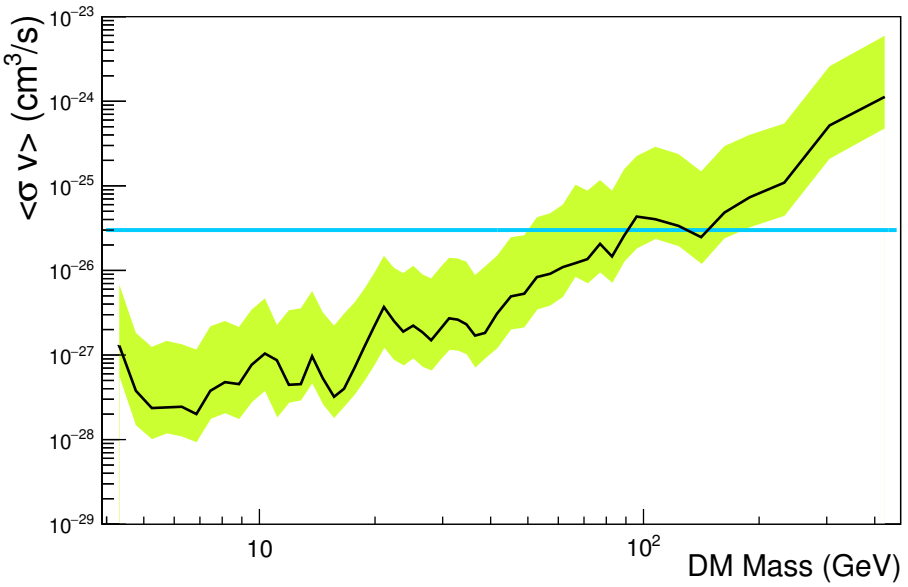

Figure 7.4: Black solid line: 95% CL upper limits on the $(2 \to 2)$ dark matter annihilation cross section . Shaded area: total uncertainty due to different propagation parameters and dark matter distribution models. Blue line: thermal relic cross section corresponding to the right relic abundance. Models where the cross section is smaller than this value are excluded, as dark matter would overclose the Universe.

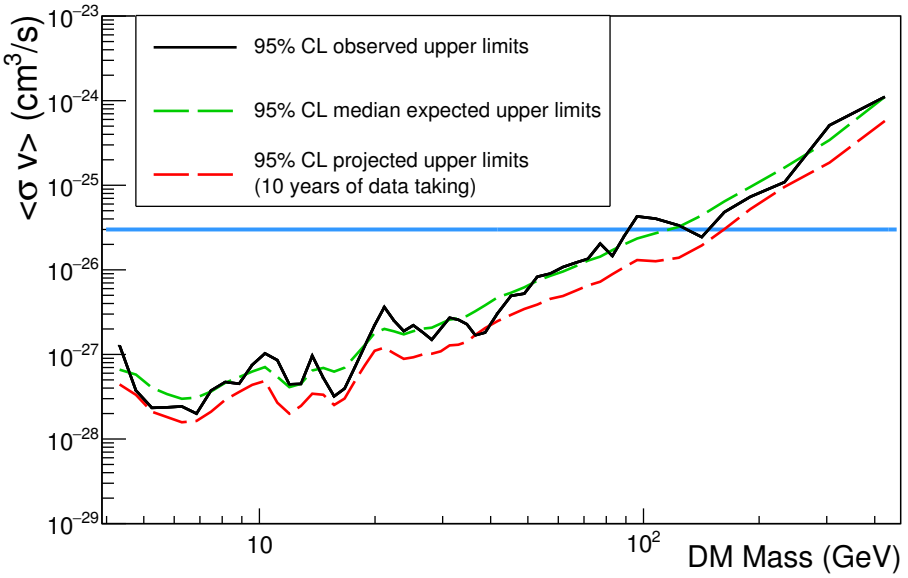

Figure 7.5: Black solid line: 95% CL observed upper limits on the $(2 \to 2)$ dark matter annihilation cross section as in Fig. 7.4. Green dashed line: median expected limits, obtained from 1000 pseudo-experiments. Red dashed line: projected limits for 10 years of data taking, obtained from pseudo-experiments. Blue line: thermal relic cross section corresponding to the right relic abundance as in Fig. 7.4.

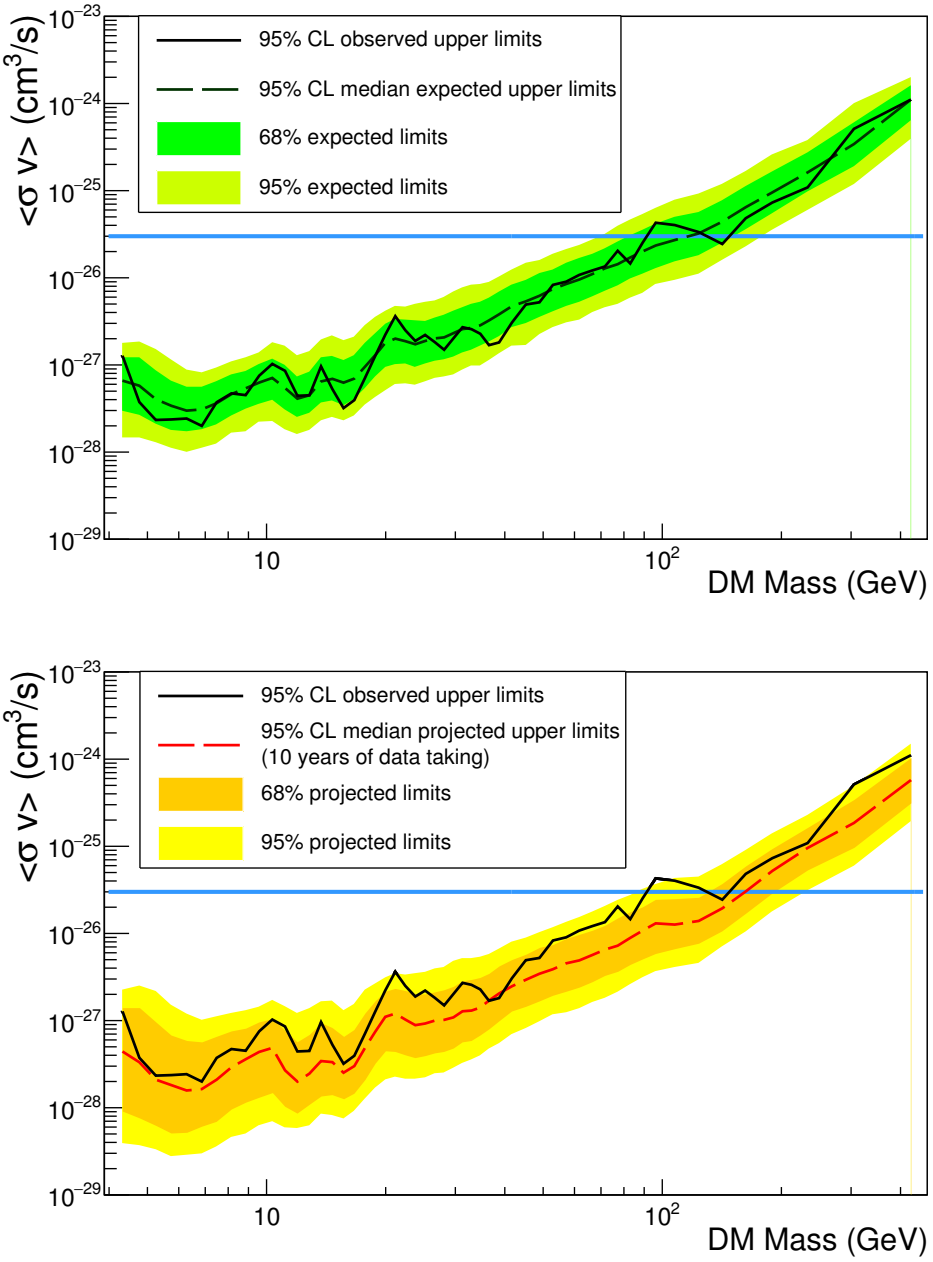

Figure 7.6: Top: comparison of the computed limits to the expected limits. The shaded regions represent the 1σ and the 2σ bands. Bottom: comparison of the observed limits to the projected limits. The shaded regions represent the 1σ and the 2σ bands, as in the figure above. Blue line: thermal relic cross section corresponding to the right relic abundance as in Fig. 7.4

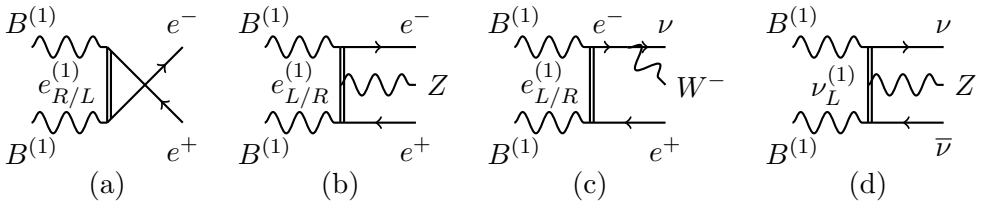

Figure 7.7: (a): leading order contributions to Kaluza-Klein dark matter annihilation into an electron-positron pair. (b,c): contributions including the radiation of an EW gauge boson. (d): this diagram does not contribute at tree-level to the electron/positron fluxes. It is present because of gauge invariance.

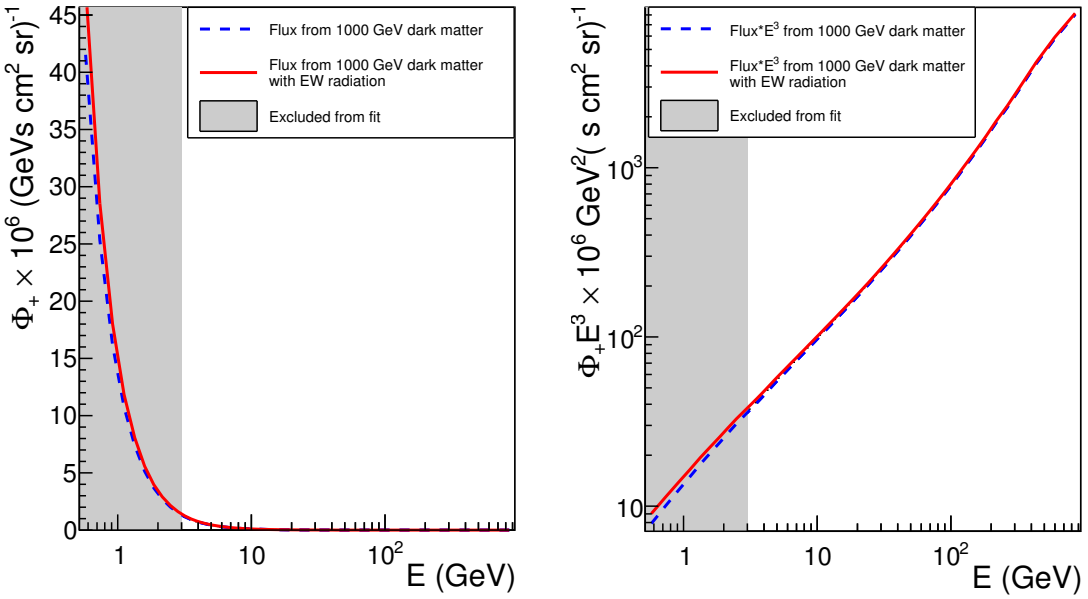

Figure 7.8: The effect of including EW radiation on the fluxes is shown for the positron flux. The left panel shows the positron flux due to $M_{\rm DM} = 1000$ GeV dark matter, while the right panel shows the flux time E^3. In both figures, we show the flux without the inclusion of EW radiation (blue shaded line) and with the EW radiation (red solid line).

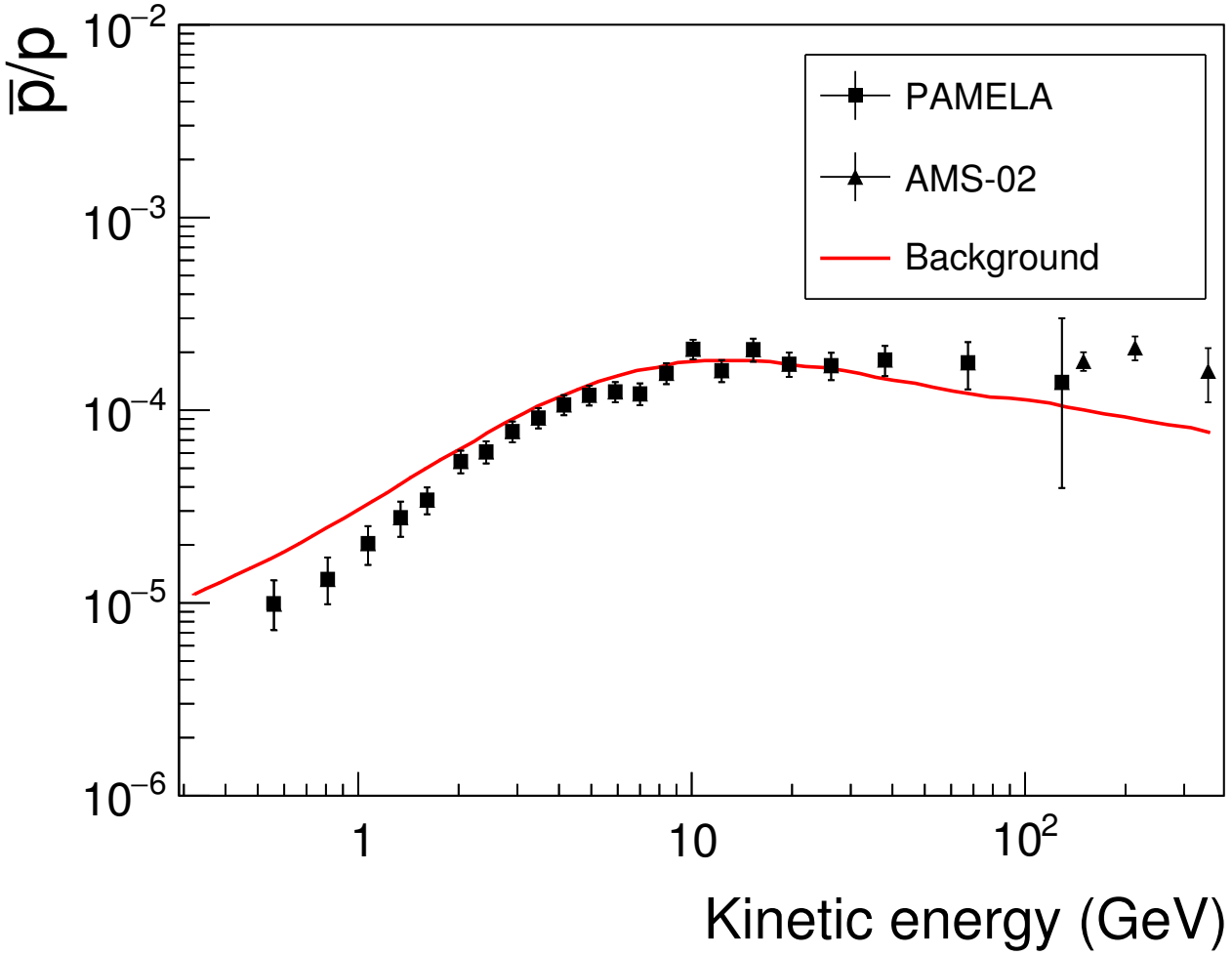

Figure 7.9: Antiproton-to-proton ratio from Ref. [243] compared to the available measurements. The AMS-02 data points are preliminary results presented in [175]. The model does not accurately reproduced the low energy PAMELA data points. However, this region is at this stage not the most relevant, since we expect that a possible dark matter induced signal would contribute in the high energy region. For an accurate study of the antiproton-to-proton flux a better description of the background is required. We postpone this to future work, when the official antiproton-to-proton measurement by AMS will be public.

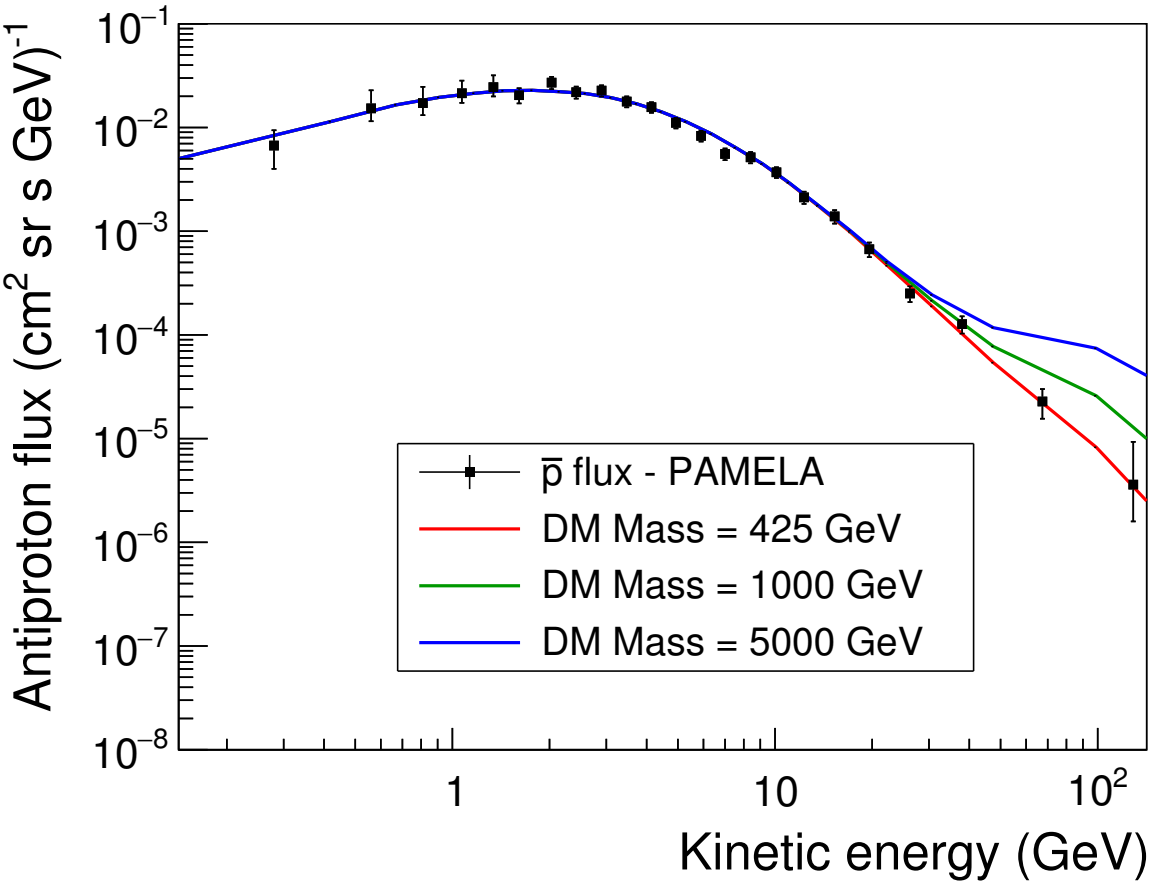

Figure 7.10: Comparison of the predictions for $M_{\mathrm{DM}} = 425, 1000, 5000$ GeV for the antiproton flux to the expected background and to the PAMELA measurement. The predictions for the antiproton flux are obtained summing them contribution due to dark matter annihilation to the expected background.

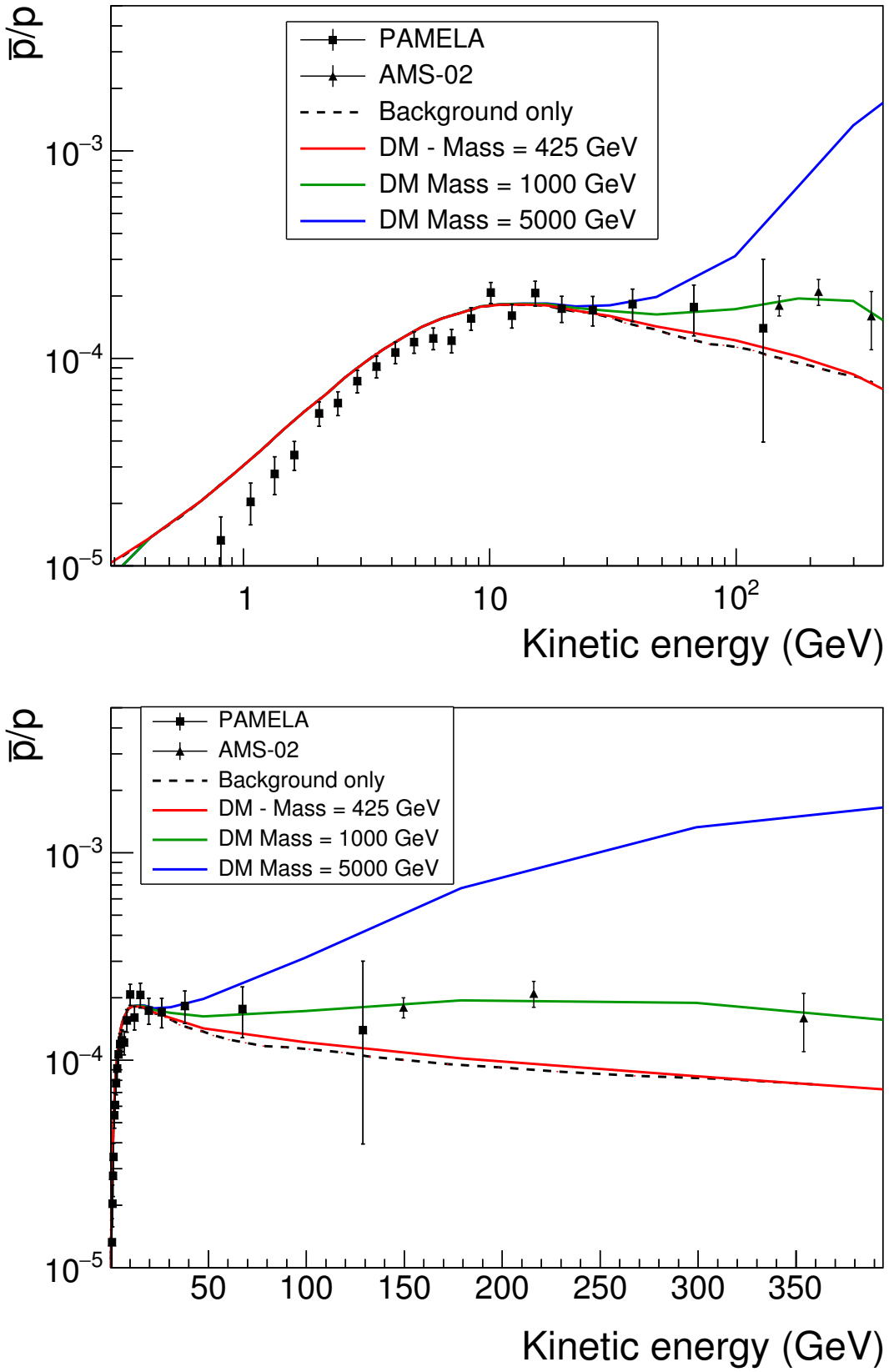

Figure 7.11: Comparison of the predictions for $M_{\rm DM} = 425, 1000, 5000$ GeV for the antiproton-to-proton ratio. We include also the plot with linear scale on the energy axis, to show more clearly the behaviour for high energy.

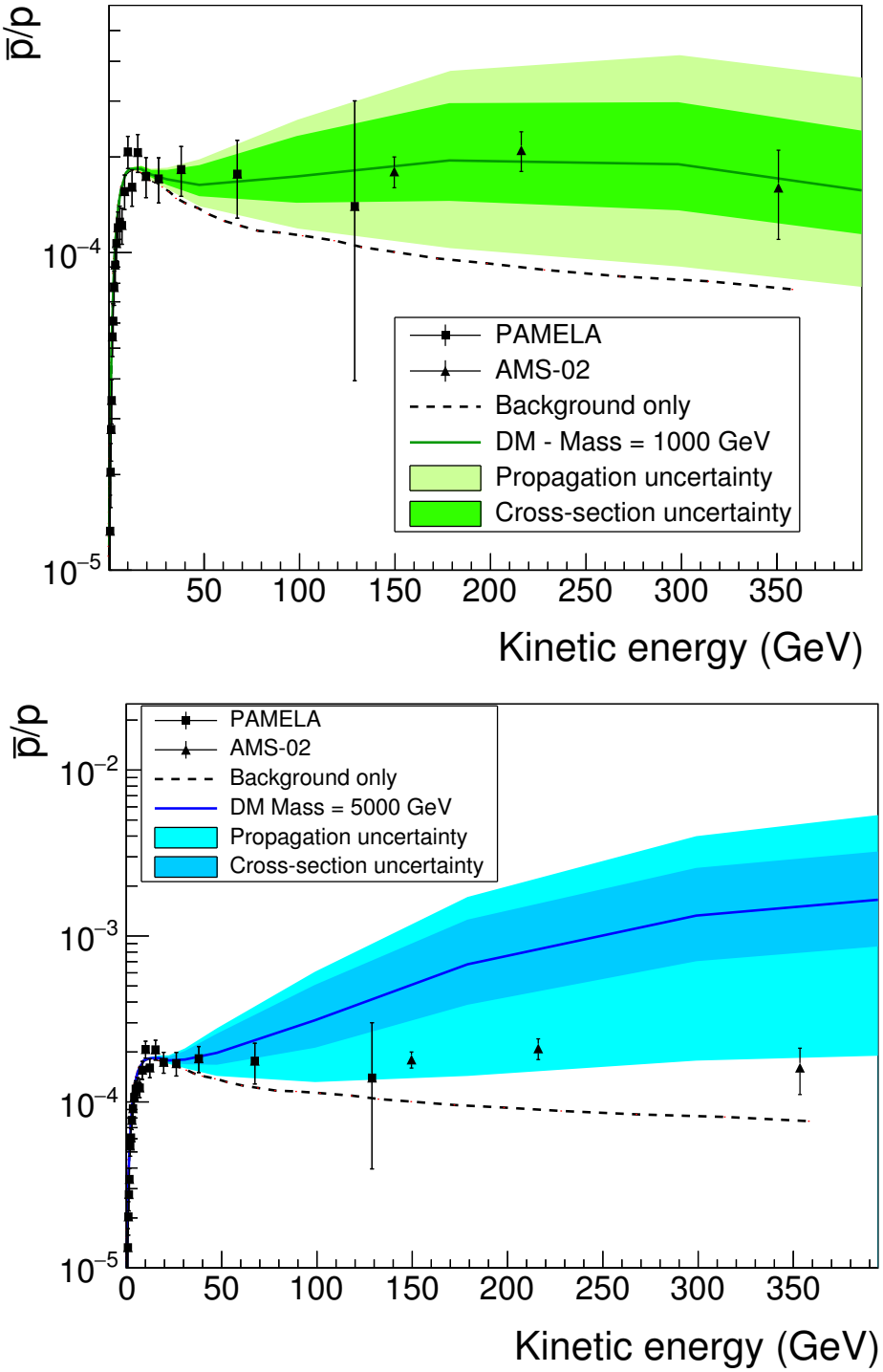

Figure 7.12: Total antiproton-to-proton ratio (signal due to dark matter annihilation in the Galaxy, as in Fig. F.1 plus expected astrophysical component) for two representative masses, $M_{\rm DM} = 1000, 5000$ GeV. The astrophysical component is inferred from the prediction for the antiproton to proton ratio in Ref. [243]. These fluxes are obtained considering a Einasto dark matter profile and the impact of the choice of the propagation parameters is shown (MIN, MED, MAX). Note that the background predictions are affected by the same uncertainties, even though we do not explicitly plot them. The two uncertainty band on the total flux are the separate contributions. The total uncertainty obtained combining the two sources of uncertainties is not displayed.

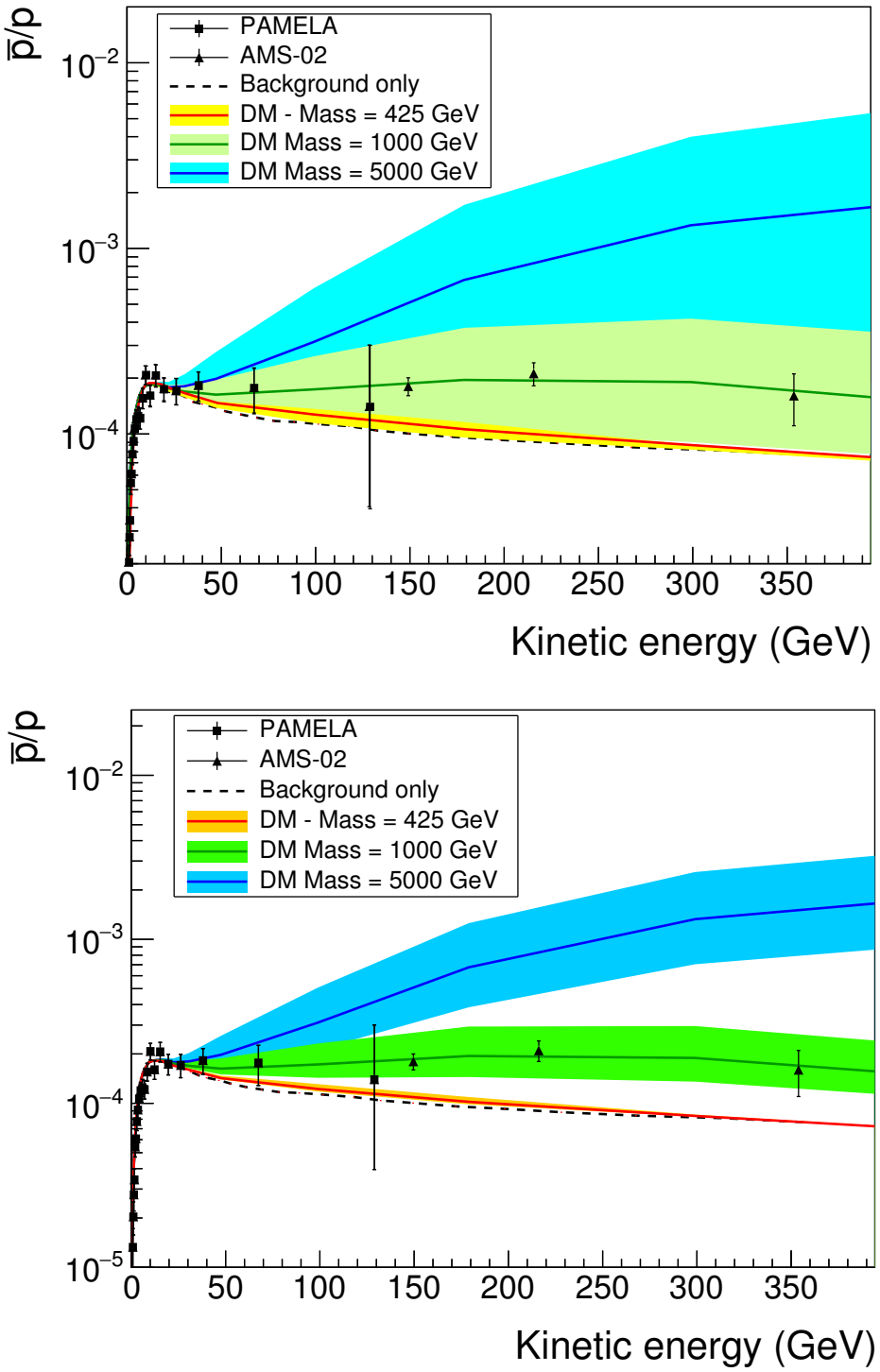

Figure 7.13: Total antiproton-to-proton ratio (signal due to dark matter annihilation in the Galaxy, as in Fig. F.1 plus expected astrophysical component) for three representative masses, $M_{\mathrm{DM}} = 425, 1000, 5000$ GeV. The impact of the choice of propagation scenarios (top) and of the uncertainties on the antiproton production cross section (bottom) is shown.

Part IV

Dark Matter searches at the LHC

Chapter 8

Leptophilic dark matter at the LHC

In this Chapter we present a preliminary study of leptophilic dark matter models at the LHC. In fact, it is interesting to investigate whether it is possible to distinguish leptophilic dark matter from dark matter with more general couplings to the SM, by looking for particular features or signatures. For such a study, the dark matter hadronic production cross section plus and additional photon or jet has to be computed. Our preliminary study consists in the calculation of the dark matter production cross section within a very simple model, where dark matter couples only to right handed electrons[1] , *i.e.* $SU(2)_L$ singlets, namely we consider the process $p\ p \to \chi\ \chi$. The computation of the process $p\ p \to \chi\ \chi + \gamma/j$ is left to future work. The aim of this calculation is to estimate the cross section for the loop-induced process, to understand whether a phenomenological study of leptophilic dark matter at the LHC is feasible. To estimate the expected number of events we consider the nominal integrated luminosity expected for the Run II of the LHC.

We first introduce the model we have used for this calculation and discuss the relevant contributions. We then perform the calculation of the loop-induced partonic cross section and we conclude presenting a preliminary calculation of the hadronic cross section.

8.1 The model

We consider a minimal model, that consists in adding to the SM a Dirac fermion χ, the dark matter candidate, and a charged scalar ρ, mediating the interactions between SM particles and the dark matter. In particular, the dark matter particle is coupled only to right handed charged leptons, via a Yukawa interaction. The Lagrangian for this simple model reads:

$$\mathcal{L} = \mathcal{L}_{\rm SM} + i\bar{\chi}\gamma^\mu D_\mu \chi + (D_\mu \rho)^\dagger (D^\mu \rho) + Y \bar{l_R} \rho \chi_L - m_\chi \bar{\chi}\chi_L - m_\rho^2 \rho^\dagger \rho + h.c. \qquad (8.1)$$

At the LHC, the production process of dark matter particles is loop-initiated and the lowest order diagrams for the process are shown in Fig. 8.1. For the sake of simplicity we assume that the scalar mediator couples only to first generation charged leptons, namely

[1] The discussion can be generalised to the case where dark matter couples also to left handed electrons. In this case, also a coupling to neutrinos is generated.

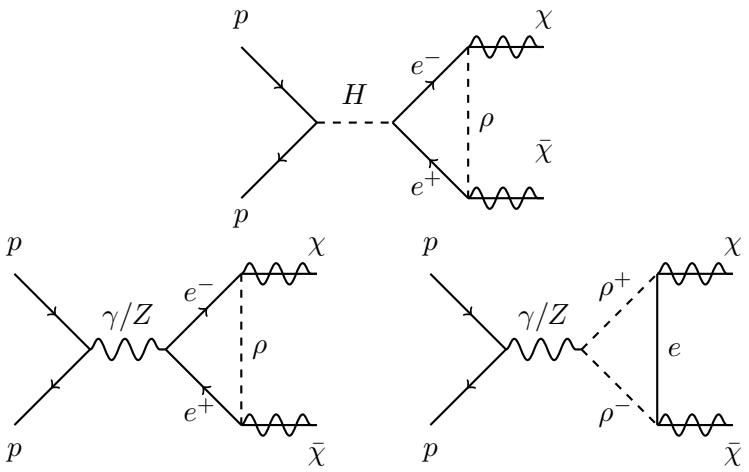

Figure 8.1: Lowest order contributions to leptophilic dark matter production at the LHC. In our calculation, the diagram with Higgs boson exchange will not be taken into account, as we neglect the electron's mass.

to right handed electrons. In the following, we consider only the Drell-Yan-like diagrams with the exchange of a photon or a Z boson, while the diagram with Higgs exchange does not contribute, as we neglect the electron's mass.

8.2 Computation of the partonic cross section

In this section, we compute the cross section for the process $q\,\bar{q} \to \chi\,\chi$ to study whether it is possible to have a detectable signal at the LHC.

The model in Eq. (8.1) has been implemented using `FeynRules 2.3` [246]. We compute analytically the one-loop amplitudes for the relevant diagrams and we obtain expressions in terms of Passarino-Veltman functions [247]. Several checks are performed in order to validate our calculation. We first compute the lowest order matrix elements squared for scalar production and scalar decay, as shown in Fig. 8.2 and compare our results against `MadGraph5_aMC@NLO` [189, 248]. We obtain perfect agreement and we proceed to the computation of the loop-induced process. We first compute the matrix elements for the diagrams in Fig. 8.3 and explicitly check that the sum of the diagrams with photon exchange and Z exchange are respectively finite. This is done analytically and checked using `FeynCalc` [249, 250]. We check our results for the total matrix elements against a computation performed with `FeynArts 3.8` and `FormCalc 8.4` [220, 251]. The computation of the matrix elements squared is also performed with `FormCalc`, while the numerical evaluation of the Passarino-Veltman functions is done with `LoopTools 2.13` [252, 253].
In the following we explicitly compute the amplitudes for dark matter production via u quark annihilation.

8.2.1 The amplitudes

The relevant diagrams for dark matter productions are shown in Fig. 8.3. Note that the total amplitude for the process is finite, as we are considering a leading-order process.

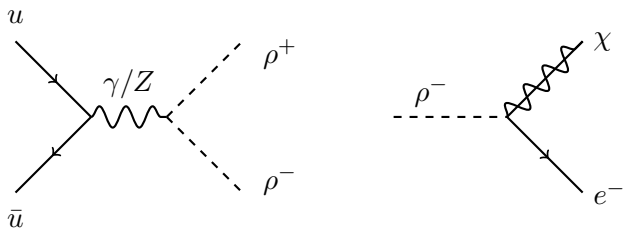

Figure 8.2: Relevant diagrams for scalar production and scalar decay used for preliminary tests of our calculation.

The two diagrams with photon exchange (1,2) form a gauge invariant subset of diagrams and the sum of the two loop amplitudes is finite. The same holds for the two diagrams due to Z boson exchange (3,4). The amplitude corresponding to the first diagram is

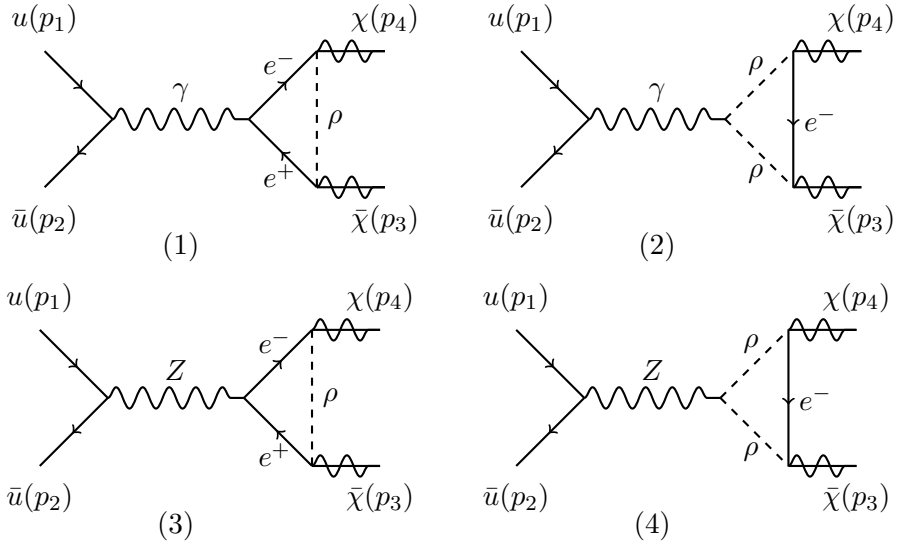

Figure 8.3: Relevant diagrams for dark matter production from u quark annihilation with the exchange of a photon and of a Z boson.

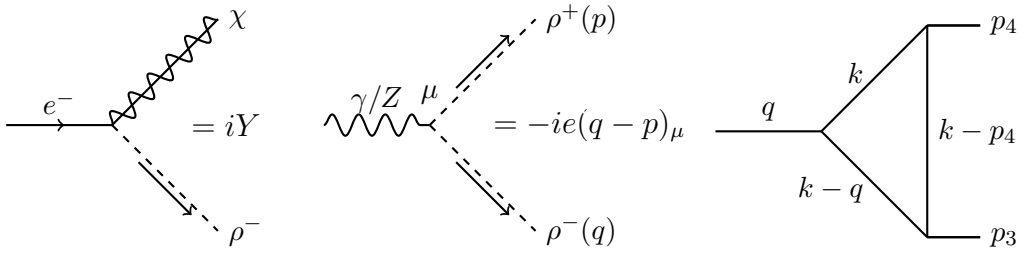

Figure 8.4: Relevant vertices and definition of the momenta used for the calculation of $\mathcal{M}_1$, $\mathcal{M}_2$, $\mathcal{M}_3$ and $\mathcal{M}_4$.

given in dimensional regularisation by

$$
\begin{aligned}
-i\mathcal{M}_1 = \frac{2}{3}e^2Y^2\bar{u}(p_4,\sigma_4)\left(\int\frac{d^dk}{(2\pi)^d}\frac{\not{k}+m_e}{k^2-m_e^2}\gamma^\nu\frac{\not{k}-\not{q}+m_e}{(k-q)^2-m_e^2}\frac{1}{(k-p_4)^2-m_\rho^2}\right)\times \\
v(p_3,\sigma_3)\frac{-ig_{\mu\nu}}{q^2}\bar{v}(p_2,\sigma_2)\gamma^\mu u(p_1,\sigma_1) = \\
= \frac{2}{3}e^2Y^2\bar{u}(p_4,\sigma_4)\left(\int\frac{d^dk}{(2\pi)^d}\mathcal{I}_1(k,q,p_4,m_e,m_\rho)\right)v(p_3,\sigma_3)\frac{-ig_{\mu\nu}}{q^2}\bar{v}(p_2,\sigma_2)\gamma^\mu u(p_1,\sigma_1).
\end{aligned}
\tag{8.2}
$$

The amplitude corresponding to the second diagram is given by

$$
\begin{aligned}
-i\mathcal{M}_2 = \frac{2}{3}e^2Y^2\bar{u}(p_4,\sigma_4)\left(\int\frac{d^dk}{(2\pi)^d}\frac{\not{k}-\not{p}_4+m_e}{(k-p_4)^2-m_e^2}\frac{(2k-q)^\nu}{(k^2-m_\rho^2)((k-q)^2-m_\rho^2)}\right)\times \\
v(p_3,\sigma_3)\frac{-ig_{\mu\nu}}{q^2}\bar{v}(p_2,\sigma_2)\gamma^\mu u(p_1,\sigma_1) = \\
= \frac{2}{3}e^2Y^2\bar{u}(p_4,\sigma_4)\left(\int\frac{d^dk}{(2\pi)^d}\mathcal{I}_2(k,q,p_4,m_e,m_\rho)\right)v(p_3,\sigma_3)\frac{-ig_{\mu\nu}}{q^2}\bar{v}(p_2,\sigma_2)\gamma^\mu u(p_1,\sigma_1).
\end{aligned}
\tag{8.3}
$$

Similarly, the amplitudes with Z exchange are given by[2]

$$
\begin{aligned}
-i\mathcal{M}_3 = \frac{2}{3}e^2Y^2\bar{u}(p_4,\sigma_4)\left(\int\frac{d^dk}{(2\pi)^d}\frac{\not{k}+m_e}{k^2-m_e^2}\gamma^\nu\frac{\not{k}-\not{q}+m_e}{(k-q)^2-m_e^2}\frac{1}{(k-p_4)^2-m_\rho^2}\right)\times \\
v(p_3,\sigma_3)\frac{-i(g_{\mu\nu}-q_\mu q_\nu/M_Z^2))}{q^2-M_Z^2}\bar{v}(p_2,\sigma_2)\gamma^\mu u(p_1,\sigma_1) = \\
= \frac{2}{3}e^2Y^2\bar{u}(p_4,\sigma_4)\left(\int\frac{d^dk}{(2\pi)^d}\mathcal{I}_1(k,q,p_4,m_e,m_\rho)\right)\times \\
v(p_3,\sigma_3)\frac{-i(g_{\mu\nu}-q_\mu q_\nu/M_Z^2))}{q^2-M_Z^2}\bar{v}(p_2,\sigma_2)\gamma^\mu u(p_1,\sigma_1).
\end{aligned}
\tag{8.4}
$$

$$
\begin{aligned}
-i\mathcal{M}_4 = \frac{2}{3}e^2Y^2\bar{u}(p_4,\sigma_4)\left(\int\frac{d^dk}{(2\pi)^d}\frac{\not{k}-\not{p}_4+m_e}{(k-p_4)^2-m_e^2}\frac{(2k-q)^\nu}{(k^2-m_\rho^2)((k-q)^2-m_\rho^2)}\right)\times \\
v(p_3,\sigma_3)\frac{-i(g_{\mu\nu}-q_\mu q_\nu/M_Z^2))}{q^2-M_Z^2}\bar{v}(p_2,\sigma_2)\gamma^\mu u(p_1,\sigma_1) = \\
= \frac{2}{3}e^2Y^2\bar{u}(p_4,\sigma_4)\left(\int\frac{d^dk}{(2\pi)^d}\mathcal{I}_2(k,q,p_4,m_e,m_\rho)\right)\times \\
v(p_3,\sigma_3)\frac{-i(g_{\mu\nu}-q_\mu q_\nu/M_Z^2)}{q^2-M_Z^2}\bar{v}(p_2,\sigma_2)\gamma^\mu u(p_1,\sigma_1).
\end{aligned}
\tag{8.5}
$$

[2]Note that the Z boson propagator is written in unitary gauge. With this gauge choice only physical degrees of freedom are relevant. For the photon diagrams we have used the Feynman gauge to write the amplitudes. We made this choice in order to have the simplest expressions for the two pairs of amplitudes we separately consider. However, for the full calculation performed with `FormCalc` where all four diagrams are taken into account the Feynman gauge has been used.

8.2.2 The loop integrals

We explicitly decompose the loop integrals $\mathcal{I}_1$ and $\mathcal{I}_2$ to show that the sum of the loop amplitudes is finite. The loop integral $\mathcal{I}_1$ can be conveniently rewritten as

$$\begin{aligned}\int \frac{d^dk}{(2\pi)^d}\mathcal{I}_1 = \int \frac{d^dk}{(2\pi)^d}\Bigg[&\frac{2\gamma_\rho k^\nu k^\rho}{k^2(k-q)^2[(k-p_4)^2-m_\rho^2]} - \frac{k^\rho(2q^\nu - q^\sigma\gamma_\rho\gamma_\sigma\gamma^\nu)}{k^2(k-q)^2[(k-p_4)^2-m_\rho^2]} \\ &- \frac{\gamma_\nu}{(k-q)^2[(k-p_4)^2-m_\rho^2]}\Bigg] = 2C^{\nu\rho}\gamma_\rho - C^\rho(2q^\nu - q^\sigma\gamma_\rho\gamma_\sigma\gamma^\nu) - B^0\gamma_\nu,\end{aligned} \tag{8.6}$$

with

$$\begin{aligned}C^{\nu\rho} &= C^{\nu\rho}(-p_4,-q,0,m_\rho,0);\\ C^\rho &= C^\rho(-p_4,-q,0,m_\rho,0);\\ B^0 &= B^0(q-p_4,0,m_\rho).\end{aligned} \tag{8.7}$$

The functions B and C are the two-point and three-point Passarino-Veltman functions, respectively and are defined in Appendix G. From dimensional analysis, from the definition of the Passarino-Veltman functions it is clear that the functions B^0 and $C^{\nu\rho}$ are divergent, while the function C^ρ are finite.

The second loop integral con be analogously decomposed:

$$\begin{aligned}\int \frac{d^dk}{(2\pi)^d}\mathcal{I}_2 = \int \frac{d^dk}{(2\pi)^d}\Bigg[&\frac{2\gamma_\rho k^\nu k^\rho}{(k^2-m^2\rho)[(k-q)^2-m_\rho^2][(k-p_4)^2-m_e^2]} \\ &- \frac{k^\nu(-2\not{p}_4) + k^\rho(-q^\nu\gamma_\rho)}{(k^2-m^2\rho)[(k-q)^2-m_\rho^2][(k-p_4)^2-m_e^2]} \\ &- \frac{q^\nu\not{p}_4}{(k^2-m^2\rho)[(k-q)^2-m_\rho^2][(k-p_4)^2-m_e^2]}\Bigg] \\ &= 2C^{\nu\rho}\gamma_\rho - 2\not{p}_4 C^\nu - q^\nu\gamma_\rho C^\rho - q^\nu\not{p}_4 C^0.\end{aligned} \tag{8.8}$$

The divergent part of the amplitudes $\mathcal{M}_1+\mathcal{M}_2$ and $\mathcal{M}_3+\mathcal{M}_4$ is the same and reads

$$\int \frac{d^dk}{(2\pi)^d}\mathcal{I}_1 + \int \frac{d^dk}{(2\pi)^d}\mathcal{I}_2\Bigg|_{div} = 4\gamma_\rho C^{\nu\rho}(-p_4,-q,0,m_\rho,0) - \gamma^\nu B^0(q-p_4,0,m_\rho). \tag{8.9}$$

The function $C^{\rho\nu}$ can be further decomposed into scalar integrals B^0 and C^0, where only B^0 is divergent. The divergent part of the two-point scalar function is universal. Performing the decomposition with `FeynCalc`, one can check explicitly that the divergent parts cancel. Hence the amplitudes $\mathcal{M}_1+\mathcal{M}_2$ and $\mathcal{M}_3+\mathcal{M}_4$ are separately finite, as expected.

8.2.3 The cross section

The partonic cross section for the process $u\,\bar{u}\to\chi\,\chi$ is given by

$$\hat{\sigma}_{u\bar{u}}(\sqrt{\hat{s}}) = \frac{|\overline{\overline{\mathcal{M}}}_{\rm tot}|^2}{\mathcal{F}}d\Phi_2, \tag{8.10}$$

where $\sqrt{\hat{s}}$ is the partonic centre of mass energy, $|\overline{\overline{\mathcal{M}}_{\rm tot}}|^2$ is the total matrix element squared ($-i\mathcal{M}_{\rm tot} = \sum_i -i\mathcal{M}_i$), averaged and summed over colour and helicity. We neglect the u-quark and electron masses in the calculation. For massless initial state particles, the flux factor $\mathcal{F}$ is simply given by

$$\mathcal{F} = 2\hat{s}, \tag{8.11}$$

while the 2-body phase space for massive final state particles after integration over the azimuthal angle is given by

$$d\Phi_2 = \frac{\lambda^{1/2}(\hat{s}, M_{\rm DM}^2, M_{\rm DM}^2)}{16\pi\hat{s}} d\cos\theta, \tag{8.12}$$

with

$$\lambda(x, y, z) = x^2 + y^2 + z^2 - 2xy - 2xz - 2zy, \tag{8.13}$$

that reduces to

$$d\Phi_2 = \sqrt{1 - \frac{4M_{\rm DM}^2}{\hat{s}}} \frac{d\cos\theta}{16\pi\hat{s}}. \tag{8.14}$$

The squared matrix elements are written in terms of the Mandelstam variables in the partonic centre of mass. Their structure in terms of the variable $\hat{s}, \hat{t}, \hat{u}$ is simple but the expressions are rather lengthy, therefore we do not write them explicitly here, but we give the results for the partonic cross section for some benchmark points. In the centre of mass frame we have

$$\begin{aligned} \hat{t} &= -\frac{\hat{s}}{2}(1 + \cos\theta), \\ \hat{u} &= -\frac{\hat{s}}{2}(1 - \cos\theta). \end{aligned} \tag{8.15}$$

The integration over $\cos\theta \in (-1, 1)$ is performed with `FormCalc`.
The setting for the relevant parameters are:

$$\begin{aligned} m_e = 0\,\text{GeV}, \quad & \mathrm{m_u} = 0\,\text{GeV} \\ M_Z = 91.188\,\text{GeV} \quad & \cos\theta_{\rm w} = 0.8819, \\ M_{\rm DM} = 100\,\text{GeV}, \quad & \mathrm{m}_\rho = 300\,\text{GeV}, \\ \alpha = (1/127.9), \quad & Y = 1. \end{aligned} \tag{8.16}$$

The results for the partonic cross section are shown in Tab. 8.1, while Figs. 8.5 and 8.6 show its dependence on the partonic centre of mass energy for a fixed choice of the mass and its dependence on the dark matter mass for a fixed choice of $\hat{s}$. The cross section for the process $d\ \bar{d} \to \chi\ \chi$ is obtained by simply replacing the charge $Q_u = \frac{2}{3}e$ with $Q_d = -\frac{1}{3}e$ in the amplitudes.

8.3 Computation of the hadronic cross section

For the computation of the hadronic cross section, $p\ p \to \chi\ \chi$, we have performed the convolution of the partonic cross section with the probability density functions (pdfs from now on). We have considered only the contributions due to up and down quarks,

$\hat{s}$ (GeV)	$\hat{\sigma}_{u\bar{u}}(\hat{s})$ (pb)
500	2.24×10^{-5}
1000	7.85×10^{-6}
2000	1.37×10^{-6}
5000	1.81×10^{-7}
14000	2.20×10^{-8}

Table 8.1: Cross section for the process $u\ \bar{u} \to \chi\ \chi$ for $M_{\rm DM} = 100\,\text{GeV}$, $m_\rho = 300\,\text{GeV}$ and $Y = 1$ as a function of the centre of mass energy.

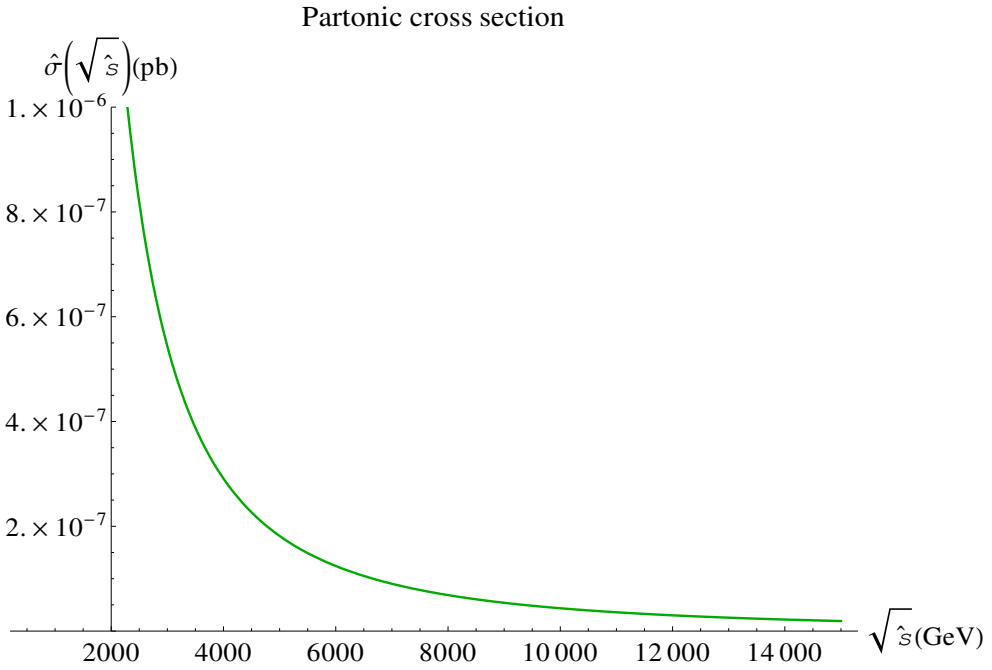

Figure 8.5: Cross section for the process $u\ \bar{u} \to \chi\ \chi$ for $M_{\rm DM} = 100\,\text{GeV}$, $m_\rho = 300\,\text{GeV}$ and $Y = 1$ as a function of the centre of mass energy.

as these are the most relevant contributions. For this, we have used the `NNPDF3.0` [254] leading order pdf set `NNPDF30_lo_as_0118_nf_6`. The hadronic cross section is given by

$$\sigma_{pp\to\chi\chi}(s) = \sum_q \hat{\sigma}_{q\bar{q}}(\hat{s}) \int_0^1 \int_0^1 dx_1 dx_2 \left(f_q^p(x_1) f_{\bar{q}}^p(x_2) + f_{\bar{q}}^p(x_1) f_q^p(x_2)\right) \delta(\hat{s} - x_1 x_2 s), \tag{8.17}$$

where $f_q^p(x)$ represents the probability to find a quark q in a proton, with fraction x of the momentum of the proton. In our calculation $q = \{u, d\}$. The convolution of the partonic cross section with the pdfs can be conveniently rewritten in terms of the parton luminosity defined as

$$\frac{dL_{q\bar{q}}}{d\tau} = \int_\tau^1 \frac{dx}{x} \left(f_q^p(x) f_{\bar{q}}^p(\tau/x) + f_{\bar{q}}^p(x) f_q^p(\tau/x)\right), \quad \text{with} \quad \tau = \frac{\hat{s}}{s}. \tag{8.18}$$

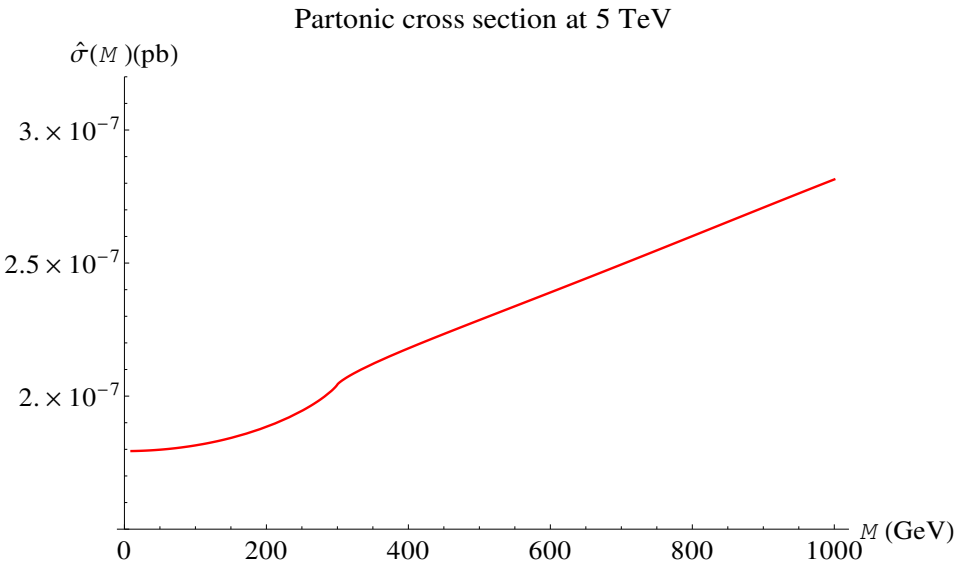

Figure 8.6: Cross section for the process $u\,\bar{u} \to \chi\,\chi$ for $\sqrt{\hat{s}} = 5\,\text{TeV}$, $m_\rho = 300\,\text{GeV}$ and $Y = 1$ as a function of the mass of the dark matter particle. The kink is at 300 GeV, namely the mass of the mediatior.

The hadronic cross section can then be recast in the form

$$\sigma(s) = \sum_q \int_{\tau_0}^1 \frac{d\tau}{\tau} \hat{\sigma}_{q\bar{q}}(\tau s) \int_\tau^1 \frac{dx}{x} \tau \left(f_q^p(x) f_{\bar{q}}^p(\tau/x) + f_{\bar{q}}^p(x) f_q^p(\tau/x) \right), \tag{8.19}$$

where $\tau_0 = 4M_{\text{DM}}^2/s$ represents the minimal energy required for the process to take place. The factorisation scale is set to $\mu = M_Z$ for the pdfs. For $\sqrt{s} = 14\,\text{TeV}$ we obtain

$$\sigma_{pp\to\chi\chi}(14\,\text{TeV}) \simeq 1.4 \cdot 10^{-4}\,\text{pb}. \tag{8.20}$$

For a complete phenomenological study, the cross section for the dark matter production

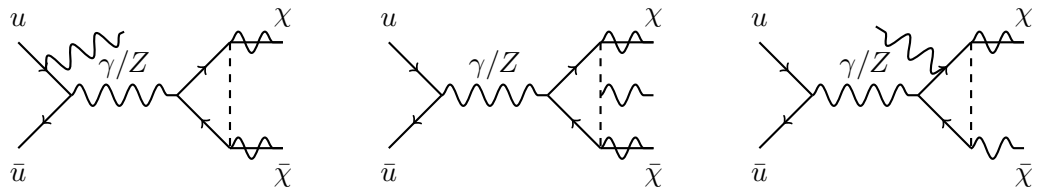

Figure 8.7: Contributions to the cross section for the process $p\,p \to \chi\,\chi + \gamma$. The same contributions would arise from the diagrams with two scalars and a lepton in the loop.

with an additional photon or jet is needed. To have an estimate of the expected number of events, we assume to consider a monophoton analysis, as in Fig. 8.7. An additional suppression factor of order $\mathcal{O}(10^{-2})$ has to be included, to take into account the radiation of the photon. The nominal integrated luminosity expected at the Run II of the LHC is $\mathcal{L} = 300\,\text{fb}^{-1}$. The number of events is given by

$$N_{\text{expected}} = \mathcal{L} \times \sigma_{pp\to\chi\chi+\gamma} \sim 300 \cdot 10^3\,\text{pb}^{-1} \times 1.4 \cdot 10^{-6}\,\text{pb} \sim 0.4. \tag{8.21}$$

Assuming the luminosity expected for the high luminosity run (HL-LHC), $\mathcal{L}^{\mathrm{HL}} = 3000\,\mathrm{fb}^{-1}$, the expected number of events is about 4. Since monophoton searches are affected by large backgrounds, the search for leptophilic dark matter at the LHC seems to be very challenging. However, the complete computation of the $p\ p \to \chi\ \chi + \gamma$ cross section is necessary, in order to draw robust conclusions. This calculation as well as further validation of the hadronic cross section calculation are left to future work.

Chapter 9

Conclusions

In this thesis, two different but yet related issues have been addressed. In Chapters 4 and 5 we have discussed the importance of EW emission for predictions for dark matter-induced cosmic ray fluxes. This problem has been extensively discussed in the Literature. Indeed, the radiation of EW gauge bosons plays a crucial rôle in obtaining consistent predictions for a given dark matter model and may allow to obtain more stringent constraints. This is the connection with the second issue we have investigated, namely the possibility of constraining a specific class of dark matter models using experimental data. In Chapter 6 and 7, we have derived new constraints on generic leptophilic models using the most recent electron and positron flux measurements [173]. We have also shown how the inclusion of EW corrections opens the possibility of exploiting the antiproton measurements to deduce further limits. In Chapter 8 we have computed the DM production cross section at the LHC as a preliminary study of DM leptophilic models at the LHC.

More specifically, regarding theoretically predictions for dark matter indirect detection, we have first reviewed the motivations for the inclusion of EW radiation to the computation. We have then studied the approximate formalism proposed in Ref. [202] to account for the radiation of EW gauge bosons in a model-independent manner, where generalised splitting functions for the emission of massive partons are introduced. We have reproduced the calculation of the splitting functions, as shown in detail in Appendix A. We have then investigate the range of applicability and the limitations of this approximation. We have considered two specific models with leptophilic dark matter and obtained the exact $(2 \to 3)$ tree-level dark matter annihilation cross section for the process $\mathrm{DM}\,\mathrm{DM} \to e^+e^-Z$, for the energy spectrum of the Z boson, and for the electron/positron fluxes expected at Earth. We have compared these results to the corresponding quantities obtained using the generalised splitting functions. We find excellent agreement between the approximate and the exact quantities for models with vector dark matter and masses above 500 GeV. For $M = 500\,\mathrm{GeV}$ the difference between the exact and the approximate cross section is below 10%. On the contrary, we have found that the approximation does not reproduce the dominant contributions due to EW gauge bosons emission if the leading-order cross section is suppressed, as in the case of Majorana fermion dark matter , where the $(2 \to 2)$ cross section is helicity-suppressed and hence exactly zero for massless leptons. In summary, the approximation gives reliable results, that are obtained with simpler calculation than the exact $(2 \to 3)$ computations for models with $M_{\mathrm{DM}} \gtrsim 5M_{\mathrm{EW}}$ that do not feature a suppressed leading order cross section. This is the first result of this thesis.

In the second part of the thesis, we have placed limits on the parameter space of leptophilic models, using the most recent AMS-02 measurements. For this, two ingredients are necessary. First, an appropriate description of the expected background fluxes is required. We have used the model proposed in [240], based on the assumption that fluxes of astrophysical origin are smooth and consist of a diffuse contribution and a source term. In this model, the diffuse term is different for electrons and positrons. In fact, astrophysical electrons are both primary and secondary, while for positrons only a secondary contribution is expected. The source term is charge symmetric and features an exponential cut-off. This phenomenological model is described by 12 parameters and we have determined their values by fitting the model to the AMS electron and positron fluxes. We have found that the phenomenological model accurately reproduces the separate electron and positron fluxes, as well as the total lepton flux and the positron fraction measured by AMS. This model constitutes an improvement with respect to previous models [17], that could very accurately reproduce the positron fraction, but failed to reproduce the lepton fluxes, especially at low energy. As we argued in Sec. 4.2, the low energy tail of the energy spectrum is particularly relevant to constrain leptophilic models. Indeed, after propagation most of the dark matter-induced signal is concentrated at low energies. Moreover, this is the part of the spectrum most affected by the inclusion of EW radiation. Obtaining a reliable phenomenological description of the background flux constitute the second result of this work. The second ingredient is a prediction for the CR fluxes due to dark matter annihilation in the Galaxy. Assuming that a dark matter contribution to the CR fluxes would add structures on top of the smooth astrophysical background, we compute new upper limits on the normalisation of the dark matter induced signal. This assumption is crucial for our analysis. With this strategy, our results for the upper limits do not depend on a first-principle understanding of the phenomena producing the background fluxes. The limits we obtain can be interpreted as limits on the annihilation cross section. We find that all purely leptophilic scenarios with $M_{\rm DM} \lesssim 100\,\text{GeV}$ are excluded at 95 % CL for the NFW MED scenario. In fact, for these points of the parameter space, dark matter is overproduced, in disagreement with the measured abundance. However, this result depend on the choice of a specific dark matter halo model and on the parametrisation of the propagation of charged particles in the Galaxy. We have studied the impact of these uncertainties and find that the boundary $M_{\rm DM} \lesssim 100\,\text{GeV}$ can change of about a factor 2, when considering different dark matter local density. More precisely, considering the dark matter local density in the range $\rho_\odot \in [0.2 - 0.8]\,\text{GeV/m}^3$, the lowest allowed value for the mass of the dark matter particles lies approximately in the range $M_{\rm DM} \in [50 - 200]\,\text{GeV}$. This constitutes the most relevant source of uncertainty on the exclusion limits. Our results apply to all models where dark matter annihilates at tree-level only into electron-positrons pairs, and can be reinterpreted in terms of models where dark matter annihilates also in other final states, as long as the branching ratio into electron-positron pairs is known. Our results are consistent with previous studies in the Literature [238, 239]. However, they constitute an improvement with respect to previous work, as they are based on a reliable description of the background fluxes and on the most recent measurements for electron and positron fluxes.

We have also obtained the expected signal including EW corrections. In this way, we not only obtain an additional contributions to the electron and positron fluxes, but also an antiproton flux that would have been completely neglected without taking into account

EW gauge boson emissions. For this, we need to choose a specific model, because we are interested in a mass range for the dark matter candidates beyond the range of validity of the model-independent splitting function approximation. We have considered the vector dark matter model presented in Sec. 4.1.1 and the results we obtain do not apply any longer to leptophilic models in general. We find that the additional yield of electrons and positrons due to the EW gauge bosons emission has a very limited impact on the upper limits on the annihilation cross section. However, the induced flux of antiprotons is sizeable for high masses, if we assume that the dark matter annihilation cross section is close to its 95 % CL upper limit value, determined from the electron and positron fluxes. Comparing to the measurements performed by PAMELA and the preliminary results by AMS, we found that additional constraints could be obtained studying this contribution at high energy. However, the AMS measurements are required for this study as they will extend to higher energy than the measurements performed by PAMELA, that are the only published data for the antiproton flux and antiproton-to-proton ratio. Moreover, we argue that in order to draw robust conclusions, a better understanding of the propagation of charged CR and a more precise modelling of the dark matter distribution in the Galaxy are necessary. This would reduce the large uncertainties on the upper limits on the annihilation cross section. Furthermore, the inclusive antiproton production cross section is affected by large uncertainties and constitutes another relevant source of uncertainty for the predictions.

Finally, we have investigated the possibility of studying leptophilic dark matter at the LHC. For this study, we consider a minimal leptophilic model, with Dirac dark matter and an additional charged scalar mediator. In this case, the dark matter production is loop-induced and therefore in general further suppressed with respect to models where dark matter is produced at tree-level. We compute the cross section for the annihilation process $p\,p \to \text{DM DM}$. We discuss in detail the calculation of the partonic cross section $u\,\bar{u} \to \text{DM DM}$ performed using the Passarino-Veltman decomposition. We give an estimate of the expected number of dark matter signal events for the expected integrated luminosity $\mathcal{L} = 300\,\text{fb}^{-1}$. The computation of the $p\,p \to \text{DM DM} + \gamma/\text{j}$ cross sections that are relevant for a full phenomenological study are left to future work.

Outlook

In our analysis, we exclude leptophilic models, where the mass of the dark matter candidates is below about 100 GeV. This lower bound on the allowed mass depends on the parameters describing the dark matter distribution in the halo and on the modelling of the propagation of charged particles in the Galaxy. This result is subject to large uncertainties, as already discussed. A better modelling of the dark matter distribution in our Galaxy and, in particular, a better determination of the local dark matter density would significantly reduce these uncertainties. To this end, both accurate measurements of the rotation curve of our Galaxy and a better modelling of the dark matter distribution in the Galaxy are necessary. In fact, on one hand, more precise measurements of the rotation curve of the Milky Way would allow for a more accurate determination of the galactic potential. These studies are very challenging, as we are located inside the Galaxy. On the other hand, a large effort is ongoing in order to correctly include the effects of baryons in the N-body simulations used to determine the shape of the dark matter profile. Improvements in both these directions are crucial to obtain more precise estimates of the local halo density.

The uncertainties due to the modelling of CR propagation in the Galaxy are significantly smaller than those coming from the local dark matter density. A deeper understanding of CR propagation in the Galaxy would not drastically reduce the uncertainty on the exclusion bound, but it would allow for a more precise description of the CR fluxes of astrophysical origin, namely of the background. The expected AMS-02 measurements for heavier nuclei and for the B/C ratio will allow for a better determination of the parameters that enter the modelling of the propagation of CR.
Further constraints might be obtained from future antiproton measurements and might open the possibility of deducing an upper bound for the allowed dark matter mass. The prediction for the antiproton background flux are also subject to large uncertainties. A better understanding of CR propagation is again crucial. In addition to this, new measurements of the inclusive antiproton production cross section in the energy range relevant for astrophysical studies are necessary. In fact, the available phenomenological parametrisations of the cross section strongly disagree outside the range where measurements are available ($K \in [20, 300]$ GeV).

EW gauge boson emission is particularly relevant for leptophilic models, as it is the only source of hadrons, photons and neutrinos. The inclusion of EW might play a relevant rôle also in models where dark matter has more generic couplings to the SM. More specifically, it would offer the possibility to fully exploit the complementarity among different measurements, by consistently combining constraints obtained from charged CR, neutrinos and photon flux measurements.

The search for leptophilic dark matter at colliders might be very challenging because the production cross section is small and because monojet and monophoton searches are affected by very large backgrounds. However, to draw robust conclusions the computation of the cross section with an additional jet or photon is necessary, in order to perform a full phenomenological study.

Part V

Appendix

Appendix A

Computation of generalised splitting functions

In this appendix, we reproduce in detail some of the calculation of the generalise splitting functions for real emission of electroweak gauge bosons, introduce in Table 1 of Ref. [23]. We do not consider virtual corrections and therefore we do not compute the corresponding splitting functions, that can be found in Ref. [23]. In fact, the $(2 \to 3)$ tree-level cross section is finite in the processes under study and we are mainly interested in correctly reproducing the shape of the energy distribution of the emitted boson. The inclusion of virtual corrections would affect the overall normalisation.

Note that it is crucial to correctly include the masses of the emitted gauge bosons, in order to have the correct phase space integration boundaries to compute the integrated splitting functions. Indeed the simple Sudakov logarithm is replaced by a more complicated universal function $\mathcal{L}$, that vanishes below the kinematical threshold set by the electroweak gauge boson mass:

$$\mathcal{L}(x) = \ln \frac{sx^2}{4M_Z^2} + 2 \ln \left(1 + \sqrt{1 - \frac{4M_Z^2}{sx^2}} \right). \tag{A.1}$$

A.1 More on the Sudakov parametrisation

The Sudakov parametrisation for the external momenta is a key ingredient in the calculation of the splitting functions, as it allows to highlight the behaviour in the soft and collinear regime.
Let k be the soft momentum. Choosing the vectors $P = (E, 0, 0, E)$ and $\bar{P} = (E, 0, 0, -E)$ as a basis, we can parametrise the soft momentum as

$$k^\mu = xP^\mu + \bar{x}\bar{P}^\mu - k_\perp^\mu = ((x + \bar{x})E, -k_\perp, 0, (x - \bar{x})E), \tag{A.2}$$

where the vector $k_\perp$ is in general $k_\perp = (0, k_\perp \cos\varphi, k_\perp \sin\varphi, 0)$, see Fig. A.1. We can set $\varphi = 0$ without loss of generality. For the moment we assume that the radiated particle is massless. This is a good approximation when computing the dominant behaviour of the matrix elements, since $\sqrt{s} \gg M_{\mathrm{EW}}$. Clearly logarithmic singularities appear both when the soft gauge boson is emitted along p_1 and along p_2 and this corresponds to $x \gg \bar{x}$ and $x \ll \bar{x}$, respectively. The form of the logarithmic term one obtains is the same in

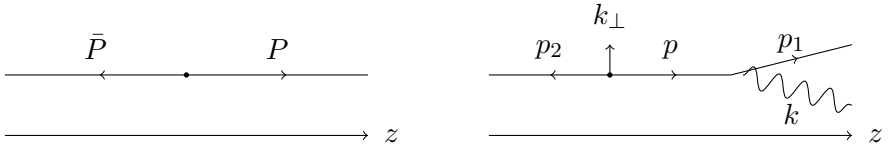

Figure A.1: The figure on the left shows the basis vectors P and $\bar{P}$. The figure on the right shows the parametrisation of the momenta we use in the calculations of the splitting functions.

the two kinematical regimes.

In the explicit calculation of the splitting functions we consider k collinear to p_1. In this case, we can parametrise the final state momenta as

$$k = \left((1-x)E, -k_\perp, 0, \sqrt{(1-x)^2E^2 - k_\perp^2}\right) \tag{A.3a}$$

$$p_1 = \left(xE, k_\perp, 0, \sqrt{x^2E^2 - k_\perp^2}\right) \tag{A.3b}$$

$$p_2 = \bar{P} = (E, 0, 0, -E). \tag{A.3c}$$

Taylor expanding in $k_\perp$ we obtain

$$k = \left((1-x)E, -k_\perp, 0, (1-x)E - \frac{k_\perp^2}{2(1-x)E}\right) + \mathcal{O}(k_\perp^4), \tag{A.4a}$$

$$p_1 = \left(xE, +k_\perp, 0, xE - \frac{k_\perp^2}{2xE}\right) + \mathcal{O}(k_\perp^4), < \tag{A.4b}$$

such that

$$p_1^2 = 0, \;\; p_2^2 = 0, \;\; k^2 = 0 \tag{A.5}$$

as all masses are much smaller than the centre-of-mass energy, and

$$p = (p_1 + k) = (E, 0, 0, E - \frac{k_\perp^2}{2x(1-x)E}) \;\Rightarrow p^2 = \frac{k_\perp^2}{x(1-x)}. \tag{A.6}$$

We now turn to the phase space factor. In the collinear approximation the 3-body phase space factorises into the 2-body phase space and a term accounting for the emission. The 2- and 3-body phase space factors are in general

$$d\phi_2 = (2\pi)^4\delta(Q_1 + Q_2 - p_1 - p_2)\frac{d^3p_1}{(2\pi)^3 2p_1^0}\frac{d^3p_2}{(2\pi)^3 2p_2^0}, \tag{A.7a}$$

$$d\phi_3 = (2\pi)^4\delta(Q_1 + Q_2 - p_1 - p_2 - k)\frac{d^3p_1}{(2\pi)^3 2p_1^0}\frac{d^3p_2}{(2\pi)^3 2p_2^0}\frac{d^3k}{(2\pi)^3 2k^0}, \tag{A.7b}$$

where Q_1 and Q_2 are the momenta of the initial state particles. From (A.6) we can write $p_1^0 = xp^0$ and the 3-body phase space becomes

$$\begin{aligned} d\phi_3 &\simeq (2\pi)^4\delta(Q_1 + Q_2 - p - p_2)\frac{d^3p}{(2\pi)^3 2xp^0}\frac{d^3p_2}{(2\pi)^3 2p_2^0}\frac{d^3k}{(2\pi)^3 2k^0} \\ &= \frac{d\phi_2}{x}\frac{d^3k}{(2\pi)^3 2k^0}. \end{aligned} \tag{A.8}$$

Moreover, we have written the vector k as $k = k(x, k_\perp, \varphi)$. The determinant of the Jacobian matrix of this transformation is
$detJ = -Ek_\perp - \frac{k_\perp^3}{2E(1-x)^2} = -Ek_\perp + \mathcal{O}(k_\perp^3)$. We can therefore write

$$\frac{d^3k}{(2\pi)^3 2k^0} = \frac{k_\perp dk_\perp dx d\varphi}{(2\pi)^3 2(1-x)} = \frac{\pi dk_\perp^2 dx}{(2\pi)^3 2(1-x)}, \tag{A.9}$$

where for the last equality is obtained performing the integration over the angle φ. The 3-body phase space factor becomes

$$d\phi_3 \simeq \frac{d\phi_2}{x} \frac{\pi dk_\perp^2 dx}{(2\pi)^3 2(1-x)}. \tag{A.10}$$

If we instead use the parametrisation in (A.3), namely without expanding in $k_\perp$,with analogous steps we obtain

$$d\phi_3 \simeq \frac{d\phi_2}{x} \frac{\pi E dk_\perp^2 dx}{(2\pi)^3 2\sqrt{(1-x)^2 E^2 k_\perp^2}}. \tag{A.11}$$

The last expression for the phase space is the one needed to compute the generalised splitting functions. We show at the end of the next paragraph that using (A.10) for the phase space integration yields to generalised splitting functions that do not have the right kinematical behaviour. On the contrary, using Eq. (A.11) they correctly vanish outside the allowed region $2M_{\rm EW}/\sqrt{s} < x < 1 - 2M_{\rm EW}/\sqrt{s}$.

A.2 Explicit calculations

$P_{F\to F}$

The computation is performed in the *axial gauge* (physical gauge).
The tree-level squared amplitude for the process is given in Fig. A.2. The final state

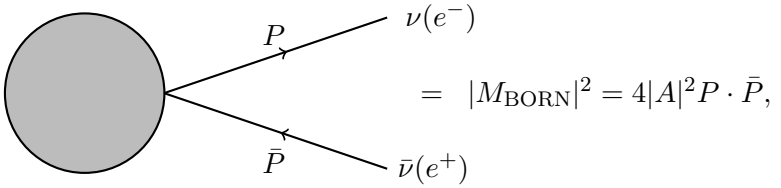

Figure A.2: Relevant diagram for the computation of the Born cross section for $P_{F\to F}$.

momenta P and $\bar{P}$ in the centre of mass are defined as

$$P = (E, 0, 0, E) \tag{A.12}$$
$$\bar{P} = (E, 0, 0, -E) \tag{A.13}$$

and A takes into account the remaining part of the process.

We now consider the amplitude for the emission of a Z-boson as in Fig. A.3. In the collinear approximation the squared amplitude for this process factorises into the tree-level contribution $|M_{\rm BORN}|^2$ and a piece that accounts for the emission.

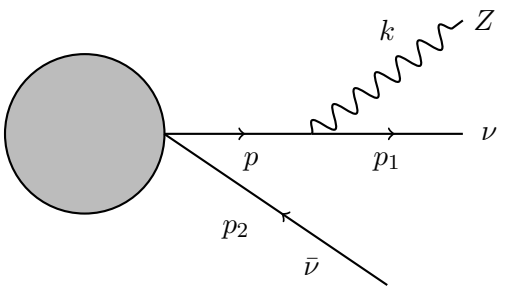

Figure A.3: Relevant diagram for the computation of the splitting function for a massless fermion into a massless fermion and a massive boson, $P_{F\to F}$.

$$M = A\bar{u}(p_1)\frac{g}{2c_W}\gamma_\mu\frac{\not{p}_1+\not{k}}{2p_1\cdot k}v(p_2)\epsilon^{*\mu}(k) \tag{A.14}$$

$$M^\dagger = A^\dagger\bar{v}(p_2)\frac{g}{2c_W}\frac{\not{p}_1+\not{k}}{2p_1\cdot k}\gamma_\nu u(p_1)\epsilon^{\nu}(k) \tag{A.15}$$

hence

$$\begin{aligned}|M|^2 &= \frac{g^2}{4c_W^2}\frac{|A|^2}{(2p_1\cdot k)^2}Tr[\bar{u}\gamma_\mu(\not{p}_1+\not{k})v(p_2)\bar{v}(p_2)(\not{p}_1+\not{k})\gamma_\nu u(p_1)]\epsilon^{*\mu}(k)\epsilon^{\nu}(k)\\ &= \frac{g^2}{4c_W^2}\frac{|A|^2}{(2p_1\cdot k)^2}Tr[\not{p}_1\gamma_\mu(\not{p}_1+\not{k})\not{p}_2(\not{p}_1+\not{k})\gamma_\nu u(p_1)]\cdot\left(-g^{\mu\nu}+\frac{k^\mu p_2^\nu+k^\nu p_2^\mu}{k\cdot p_2}\right)\\ &= |A|^2\frac{g^2}{4c_W^2}\frac{x(1-x)}{k_\perp^2}\frac{16}{2p_1\cdot k}[(p_1\cdot k)(p_2\cdot k)+2(p_1\cdot p_2)(p_1\cdot k)+2\frac{(p_1\cdot p_2)^2(p_1\cdot k)}{p_2\cdot k}]\end{aligned} \tag{A.16}$$

In the collinear approximation we have $\bar{P}\simeq p_2$, $xP\simeq p_1$ and $(1-x)P\simeq k$, where we neglect terms $\mathcal{O}(k_\perp^2)$ as they would result into terms $\mathcal{O}(k_\perp^4)$, while we want to retain terms in the amplitude squared up to $\mathcal{O}(k_\perp^2)$.
The squared amplitudes becomes

$$\begin{aligned}|M|^2 &= \frac{2|A|^2g^2}{c_W^2}\frac{x(1-x)}{k_\perp^2}\frac{(1+x)(1-x)+2x^2}{1-x}P\cdot\bar{P} = \frac{2|A|^2g^2}{c_W^2}\frac{x(1+x^2)}{k_\perp^2}P\cdot\bar{P}\\ &= |M_{\rm BORN}|^2\frac{g^2}{2c_W^2}\frac{x(1+x^2)}{k_\perp^2}\end{aligned} \tag{A.17}$$

The cross section for the tree-level process is

$$d\sigma_{\rm BORN} = \frac{|M_{\rm BORN}|^2}{\mathcal{F}}d\phi_2, \tag{A.18}$$

where $\mathcal{F}$ is the flux factor:

$$\mathcal{F} = 4\sqrt{(Q_1\cdot Q_2)^2-M_{\rm DM}^4}. \tag{A.19}$$

For the process in Fig. A.3 the cross section is given by

$$d\sigma = \frac{|M|^2}{\mathcal{F}}d\phi_3. \tag{A.20}$$

Writing the phase space as Eq. (A.10) we obtain

$$\begin{aligned} d\sigma &= \frac{|M_{\mathrm{BORN}}|^2}{\mathcal{F}} \frac{g^2}{2c_W^2} \frac{x(1+x^2)}{k_\perp^2} \frac{d\phi_2}{x} \frac{\pi}{2(2\pi)^2(1-x)} dk_\perp^2 dx \\ &= d\sigma_{\mathrm{BORN}} \frac{g^2}{2c_W^2} \frac{\pi}{2(2\pi)^3} \frac{1+x^2}{1-x} \frac{dk_\perp^2}{k_\perp^2} dx \end{aligned} \tag{A.21}$$

after integrating in $d\phi_2$.

$$\begin{aligned} d\sigma &= \int_0^1 \int_{dk^2_{\perp\min}}^{dk^2_{\perp\max}} d\sigma_{\mathrm{BORN}} \frac{g^2}{4\pi} \frac{1}{(2\pi)c_W^2} \frac{1+x^2}{1-x} \frac{dk_\perp^2}{k_\perp^2} dx \\ &= \int_0^1 d\sigma_{\mathrm{BORN}} \frac{\alpha}{2\pi} \frac{1}{c_W^2} P_{F\to F}(x) dx \end{aligned} \tag{A.22}$$

with

$$P_{F\to F}(x) = \int_{k^2_{\perp\min}}^{k^2_{\perp\max}} \frac{1+x^2}{1-x} \frac{dk_\perp^2}{k_\perp^2}. \tag{A.23}$$

For the integration boundaries we have $k^2_{\perp\min} = M_Z^2$ and $k^2_{\perp\max} = (1-x)^2 s/4$. Performing the integration in $k_\perp^2$ we obtain (in this case $M_{\mathrm{EW}} = M_Z$)

$$P_{F\to F}(x) = \int_{M_Z^2}^{(1-x)^2 s/4} \frac{1+x^2}{1-x} \frac{dk_\perp^2}{k_\perp^2} = \frac{1+x^2}{1-x} \ln \frac{(1-x)^2 s}{4M_Z^2}. \tag{A.24}$$

It is clear from the form of the splitting function that it does not vanish for $x < 2M_{\mathrm{EW}}/\sqrt{s}$ and $x > 1 - 2M_{\mathrm{EW}}/\sqrt{s}$. On the other hand, using the form in Eq. (A.11) we obtain

$$\begin{aligned} P_{F\to F}(x) &= \int_{k^2_{\perp\min}}^{k^2_{\perp\max}} \frac{(1+x^2)E}{\sqrt{(1-x)^2E^2 - k_\perp^2}} \frac{dk_\perp^2}{k_\perp^2} \\ &= \frac{1+x^2}{1-x} \left(\ln \frac{s(1-x)^2}{4M_Z^2} + 2 \ln \left(1 + \sqrt{1 - \frac{4M_Z^2}{s(1-x)^2}} \right) \right) \\ &= \frac{1+x^2}{1-x} L(1-x), \end{aligned} \tag{A.25}$$

that has the correct kinematical behaviour.

$P_{F\to V}$

This splitting function is related to the previous one by the substitution $x \to (1-x)$. Therefore the momenta are in the collinear approximation $\bar{P} \sim p_2$, $(1-x)P \sim p_1$ and $xP \sim k$, and the splitting function is given by

$$P_{F\to V} = \frac{1+(1-x)^2}{x} \mathcal{L}(x). \tag{A.26}$$

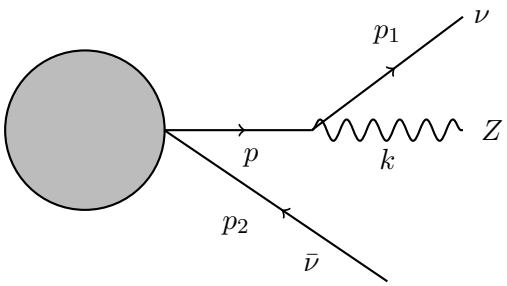

Figure A.4: Relevant diagram for the computation of the splitting function for a massless fermion into a massless fermion and a massive boson, $P_{F\to V}$.

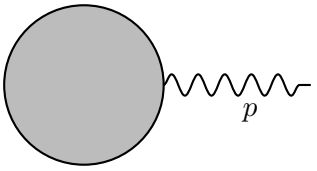

$$= \quad M_{\mathrm{BORN}} = A_\mu(p)\epsilon^*_\lambda(p)$$

Figure A.5: Relevant diagram for the computation of the Born cross section for $P_{V\to F}$.

$P_{V\to F}$

The Born amplitude is given in this case in Fig. A.5. The squared amplitude, after summing over the polarisations of the photon, is given by

$$\begin{aligned}\sum_\lambda |M_{\mathrm{BORN}}|^2 = \sum_\lambda A_\mu(p)A^\dagger_\nu(\bar{p})\epsilon^*_\lambda(p)\epsilon_\lambda(\bar{p}) = A_\mu(p)A^\dagger_\nu(\bar{p})\left(-g_{\mu\nu}+\frac{p^\mu\bar{p}^\nu+p^\nu\bar{p}^\mu}{p\cdot\bar{p}}\right) = \\ = -A_\mu A^{\dagger\mu},\end{aligned} \tag{A.27}$$

where the second term in brackets does not contribute because of Ward identities

$$p_\mu A^\mu(p) = 0. \tag{A.28}$$

The amplitude for the diagram in Fig. A.6 is given by

$$M = G\bar{u}(k,\sigma)\gamma_\mu v(p_1,\sigma_1)\frac{-g_{\mu\nu}+\frac{p^\mu\bar{p}^\nu+p^\nu\bar{p}^\mu}{p\cdot\bar{p}}}{p^2+i\epsilon}A_\nu(p), \tag{A.29}$$

where we generically call G the vector boson-fermion-antifermion coupling and, again, the second term in the numerator of the propagator vanishes thanks to the Ward identities (A.28). Using the Sudakov parametrisation in Eqs. (A.3) the amplitude squared reads

$$\begin{aligned}|M|^2 &= G^2\frac{x^2(1-x)^2}{k_\perp^4}Tr[\not{k}\gamma_\mu\not{p}_1\gamma_\rho]A^\mu A^{\dagger\rho} \\ &= G^2\frac{x^2(1-x)^2}{k_\perp^4}4(k_\mu p_{1\rho}+k_\rho p_{1\mu}-g_{\mu\rho}k\cdot p_1)A^\mu A^{\dagger\rho},\end{aligned} \tag{A.30}$$

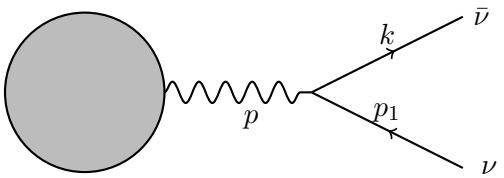

Figure A.6: Relevant diagram for the computation of the splitting function for a massive vector boson splitting into a massless fermion-antifermion pair, $P_{V\to F}$

.

where

$$k_\mu p_{1\rho} = x(1-x)p_\mu p_\nu + xk_{\perp\mu}p_\rho - (1-x)k_{\perp\rho}p_\mu - k_{\perp\mu}k_{\perp\nu} = -k_{\perp\mu}k_{\perp\nu}, \tag{A.31}$$

as the contribution due to the first three terms will vanish because of the Ward identities. The same holds for $k_\rho p_{1\mu}$. Eq. (A.30) becomes

$$\begin{aligned}
|M|^2 &= 4G^2\frac{x^2(1-x)^2}{k_\perp^4}(-2k_{\perp\mu}k_{\perp\nu} - g_{\mu\rho}k\cdot p_1)A^\mu A^{\dagger\rho} = \\
&= 2G^2\frac{x(1-x)}{k_\perp^2}(-4x(1-x)\frac{k_{\perp\mu}k_{\perp\nu}}{k_\perp^2} - g_{\mu\rho})A^\mu A^{\dagger\rho} = \\
&= 2G^2\frac{x(1-x)}{k_\perp^2}(2x(1-x)-1)A^\mu A^{\dagger\rho} = \\
&= 2G^2\frac{x(1-x)}{k_\perp^2}(1-2x+2x^2)|M_{\text{BORN}}|^2
\end{aligned} \tag{A.32}$$

where we have averaged over all possible directions of $k_\perp$:

$$\frac{1}{V}\int d\Omega^{2-2\epsilon}\frac{k_{\perp\mu}k_{\perp\nu}}{k_\perp^2} = \frac{1}{2(1-\epsilon)}(-g^{\mu\rho} - \frac{p^\mu p_2^\rho + p^\rho p_2^\nu}{p\cdot p_2}), \quad \text{with} \quad \epsilon\to 0, \tag{A.33}$$

and used again the Ward identities.

Factorising the Born cross section in the $(2\to 3)$ cross section expression we identify the splitting function term. Writing the phase space as in Eq. (A.11) and performing the integration in $k_\perp^2$ we obtain

$$P_{V\to F} = [(1-x)^2 + x^2]\ln\frac{s}{M_Z^2}. \tag{A.34}$$

$P_{S\to S}$

The Born amplitude is shown in Fig. A.7. In this case the Born squared amplitude is simply $|M_{\text{BORN}}|^2 = |A|^2$. Including the radiation of a Z boson (Fig. A.8), the amplitude reads

$$M = G\frac{(p+p_1)_\mu \epsilon^{*\mu}(k)}{p^2}A(p), \tag{A.35}$$

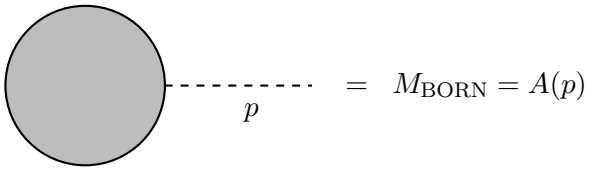

Figure A.7: Relevant diagram for the computation of the Born cross section for $P_{S\to V}$.

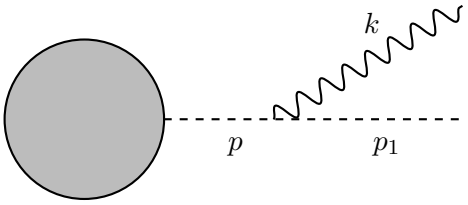

Figure A.8: Relevant diagram for the computation of the splitting function for a scalar into a vector boson and a scalar, $P_{S\to V}$

.

where G is the generic vertex factor for the scalar-scalar-vector vertex. Summing over the polarisation of the emitted boson, the amplitude squared is given by

$$\begin{aligned}\sum_{\lambda}|M|^2 &= G^2|A|^2\frac{(p+p_1)_\mu(p+p_1)_\nu}{p^4}\left(-g^{\mu\nu}+\frac{k^\mu p_2^\nu + k^\nu p_2^\mu}{k\cdot p_2}\right) = \frac{2G^2|A|^2}{2p_1\cdot k}\frac{2p\cdot p_1}{k\cdot p_2}\\ &\simeq 2G^2|A|^2\frac{x(1-x)}{k_\perp^2}\frac{2xP\cdot\bar{P}}{(1-x)P\cdot\bar{P}} = 4G^2|A|^2\frac{x^2}{k_\perp^2},\end{aligned} \tag{A.36}$$

where the collinear approximation has been introduced between the first and the second line. As in the previous cases, the cross section for the tree-level $(2\to 3)$ process factorises in the form

$$d\sigma = \frac{|M_{\mathrm{BORN}}|^2}{4\sqrt{(Q_1\cdot Q_2)^2 - M_{\mathrm{DM}}^4}}\frac{d\phi_2}{x}4G^2|A|^2\frac{x^2}{k_\perp^2}. \tag{A.37}$$

After integration using Eq. (A.11) to express the phase space factor for the emisson of the soft particle, the splitting function reads

$$P_{S\to S} = \frac{2x}{1-x}L(1-x), \tag{A.38}$$

with L defined in Eq. (A.1).

$P_{V\to S}$

The leading order amplitude is given again by Fig. A.5. The amplitude for the process in Fig. A.9 reads

$$|M|^2 = G(k-p_1)_\mu\frac{-g^{\mu\nu}}{p^2}A_\nu(p) \tag{A.39}$$

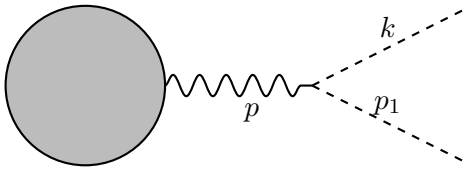

Figure A.9: Relevant diagram for the computation of the splitting function for a vector boson splitting into two scalars, $P_{V\to S}$

.

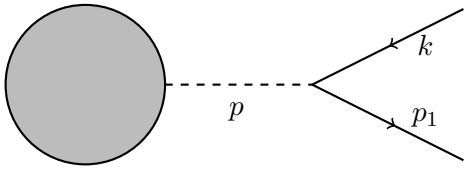

Figure A.10: Relevant diagram for the computation of the splitting function for a scalar splitting into a fermion-antifermion pair, $P_{S\to F}$

.

up to terms in the propagator that will not contribute because of the Ward identities. The squared amplitude is given by

$$|M^2| = G^2 \frac{(k-p_1)_\mu (k-p_1)_\nu}{p^4} A^\mu(p) A^{\dagger\nu}(p). \tag{A.40}$$

Using the Sudakov parametrisation, $(k-p_1)^\mu = (1-2x)p^\mu + 2k_\perp^\mu$. Only the second term will give non vanishing contributions to the amplitude, while the first term gives vanishing contributions because of Ward identities (A.28). The amplitude squared in the collinear approximation becomes

$$\begin{aligned} |M|^2 &= 4G^2 \frac{k_{\perp\mu} k_{\perp\nu}}{p^4} A^\mu(p) A^{\dagger\nu}(p) = 2G^2 \frac{x^2(1-x)^2}{k_\perp^2} (-g^{\mu\nu}) A^\mu(p) A^{\dagger\nu}(p) \\ &= 2G^2 \frac{x^2(1-x)^2}{k_\perp^2} |M_{\text{BORN}}|^2. \end{aligned} \tag{A.41}$$

Proceeding as in the previous calculations we obtain

$$P_{V\to S} = x(1-x) \ln \frac{s}{M_{\text{EW}}^2}. \tag{A.42}$$

$P_{S\to F}$

We consider now the splitting of a massive scalar into two massless fermions. The Born amplitude is given again by Fig. A.8. The amplitude for the splitting is depicted in Fig. A.10. The amplitude is given by

$$M = \bar{u}(p_1) v(k) \frac{M_{\text{BORN}}}{p^2} \tag{A.43}$$

and the squared amplitude reads

$$|M|^2 = \frac{|M_{\text{BORN}}|^2}{p^4} 4 p_1 \cdot k = \frac{2|M_{\text{BORN}}|^2 x(1-x)}{k_\perp^2}. \tag{A.44}$$

The cross section is

$$d\sigma = \frac{|M_{\text{BORN}}|^2}{8\pi^2} d\phi_2 \frac{dk_\perp^2}{k_\perp^2} dx = \frac{d\sigma_{\text{BORN}}}{8\pi^2} \frac{dk_\perp^2}{k_\perp^2} dx. \tag{A.45}$$

In this case, the dependence on x is trivial and the splitting function is $P_{S\to F} = \ln s/m^2$.

$P_{V\to V}$

As last example, we consider the splitting of a massive vector boson into two massive vector bosons as for instance in Fig. A.11. The Born amplitude squared is given again by $|M_{\text{BORN}}|^2 = -A_\mu A^{\dagger\mu}$. The amplitude for the process in Fig. A.11 reads

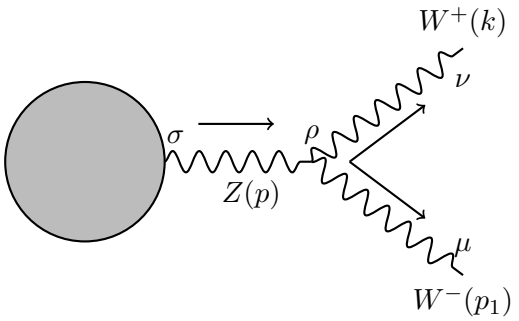

Figure A.11: Relevant diagram for the computation of the splitting function accounting for the splitting of a massive gauge boson into two massive gauge bosons. The arrows represent the direction of the momenta.

$$\begin{aligned} M &= g\cos\theta_w \left[g_{\mu\nu}(p_1-k)_\rho - g_{\nu\rho}(p_1+p)_\mu + g_{\mu\rho}(p+k)_\nu\right] \frac{(-g^{\rho\sigma})}{p^2} \\ &\quad \times A_\sigma(p)\epsilon^{*\mu}(k)\epsilon^{*\nu}(p_1) \\ &= -\frac{g\cos\theta_w}{2p_1\cdot k}\left[g_{\mu\nu}(p_1-k)_\rho - g_{\nu\rho}(2p_1+k)_\mu + g_{\mu\rho}(p_1+2k)_\nu\right] \\ &\quad \times A^\rho(p)\epsilon^{*\mu}(k)\epsilon^{*\nu}(p_1) \end{aligned} \tag{A.46}$$

where θ_w is the Weinberg angle. The complex conjugate of the amplitude is

$$\begin{aligned} M^\dagger &= -\frac{g\cos\theta_w}{2p_1\cdot k}\left[g_{\alpha\beta}(p_1-k)_\delta - g_{\beta\delta}(2p_1+k)_\alpha + g_{\alpha\delta}(p_1+2k)_\beta\right] \\ &\quad \times A^{\dagger\delta}(p)\epsilon^\alpha(k)\epsilon^\beta(p_1) \end{aligned} \tag{A.47}$$

Summing over the polarisations of the final state gauge bosons, the squared amplitudes is

$$\begin{aligned} |M|^2 &= \frac{g^2\cos^2\theta_w}{(2p_1\cdot k)^2} A^\rho(p)A^{\dagger\delta}(p)\left[g_{\mu\nu}(p_1-k)_\rho - g_{\nu\rho}(2p_1+k)_\mu + g_{\mu\rho}(p_1+2k)_\nu\right] \\ &\quad \times \left[g_{\alpha\beta}(p_1-k)_\delta - g_{\beta\delta}(2p_1+k)_\alpha + g_{\alpha\delta}(p_1+2k)_\beta\right] \\ &\quad \times \left(-g^{\mu\alpha} + \frac{k^\mu p_2^\alpha + k^\alpha p_2^\mu}{k\cdot p_2}\right) \times \left(-g^{\nu\beta} + \frac{p_1^\nu p_2^\beta + p_1^\beta p_2^\nu}{p_1\cdot p_2}\right) \end{aligned} \tag{A.48}$$

$$
\begin{aligned}
&= \frac{g^2\cos^2\theta_w}{(2p_1\cdot k)^2}A^\rho A^{\dagger\delta}\Big[-2p_1^\rho p_1^\delta - 6p_1^\rho k^\delta - 6p_1^\delta k^\rho - 2k^\delta k^\rho \\
&+ 2(p_1^\rho k^\delta + p_1^\delta k^\rho)\left(\frac{k\cdot p_2}{p_1\cdot p_2}+\frac{p_1\cdot p_2}{k\cdot p_2}\right) + 4p_1^\rho p_1^\delta\left(\frac{k\cdot p_2}{p_1\cdot p_2}\right) + 4k^\rho k^\delta\left(\frac{p_1\cdot p_2}{k\cdot p_2}\right) \\
&2p_1\cdot k\left(\frac{p_1^\rho p_2^\delta + p_1^\delta p_2^\rho + 3k^\rho p_2^\delta + 3k^\delta p_2^\rho}{p_1\cdot p_2} + \frac{k^\rho p_2^\delta + k^\delta p_2^\rho + 3p_1^\rho p_2^\delta + 3p_1^\delta p_2^\rho}{k\cdot p_2}\right) \\
&- \frac{8(p_1\cdot k)^2 p_2^\rho p_2^\delta}{p_1\cdot p_2 k\cdot p_2} - 8g^{\delta\rho}p_1\cdot k\left(\frac{k\cdot p_2}{p_1\cdot p_2}+\frac{p_1\cdot p_2}{k\cdot p_2}\right)\Big].
\end{aligned}
$$

Given that $p_1^\rho = xp^\rho - k_\perp^\rho$ and $p_1^\rho = (1-x)p^\rho + k_\perp^\rho$, up to terms that would vanish because of the Ward identities Eq. (A.28) we have

$$
\begin{aligned}
p_1^\rho p_1^\delta &= k_\perp^\rho k_\perp^\delta \qquad k^\rho k^\delta = k_\perp^\rho k_\perp^\delta && \text{(A.49a)}\\
p_1^\rho k^\delta &= k_\perp^\rho k_\perp^\delta \qquad k^\rho p_1^\delta = k_\perp^\rho k_\perp^\delta && \text{(A.49b)}\\
p_1^\rho p_2^\delta &= -k_\perp^\rho \bar{P}^\delta \quad k^\rho p_2^\delta = k_\perp^\delta \bar{P}^\rho. && \text{(A.49c)}
\end{aligned}
$$

Moreover, $\frac{k\cdot p_2}{p_1\cdot p_2} = \frac{1-x}{x}$, $2p_1\cdot k = \frac{x(1-x)}{k_\perp^2}$. The amplitude squared becomes

$$
\begin{aligned}
|M|^2 &= g^2\cos^2\theta_w A^\rho(p)A^{\dagger\delta}(p)\frac{x^2(1-x)^2}{k_\perp^4} \\
&\times\left[8k_\perp^\rho k_\perp^\delta + \frac{4k_\perp^2}{x(1-x)}\Big(\frac{k_\perp^\rho\bar{P}^\delta + k_\perp^\delta\bar{P}^\rho}{xP\cdot\bar{P}} - \frac{k_\perp^\rho\bar{P}^\delta + k_\perp^\delta\bar{P}^\rho}{(1-x)P\cdot\bar{P}}\Big)\right. \\
&\left.- \frac{8k_\perp^4}{x^2(1-x)^2}\frac{\bar{P}^\rho\bar{P}^\delta}{x(1-x)(P\cdot\bar{P})^2} - g^{\rho\delta}\frac{4k_\perp^2}{x(1-x)}\Big(\frac{x}{1-x}+\frac{1-x}{x}\Big)\right].
\end{aligned}
\tag{A.50}
$$

The leading contribution to obtain the splitting function is given by the terms $\propto 1/k_\perp^2$, hence we retain only the first and the last terms in the expression above:

$$
\begin{aligned}
|M|^2 &= 4g^2\cos^2\theta_w A^\rho(p)A^{\dagger\delta}(p)\frac{x(1-x)}{k_\perp^2} \\
&\times\left[-g^{\rho\delta}\Big(\frac{x}{1-x}+\frac{1-x}{x}\Big)2x(1-x)\frac{k_\perp^\rho k_\perp^\delta}{k_\perp^2}\right] \\
&= 4g^2\cos^2\theta_w(-A^\rho A^{\dagger\rho})\frac{x(1-x)}{k_\perp^2}\left[\frac{x}{1-x}+\frac{1-x}{x}+x(1-x)\right]
\end{aligned}
\tag{A.51}
$$

after averaging over the possible directions of $k_\perp$ as in Eq. (A.33). The splitting function reads

$$
P_{V\to V} = 2\left[\frac{x}{1-x}L(1-x) + \frac{1-x}{x}L(x) + x(1-x)\ln\frac{M_{\rm EW}^2}{s}\right]. \tag{A.52}
$$

A complete list of the generalised splitting functions both for real and virtual emission can be found in Table 1 of Ref. [23].

Appendix B

Coefficients A, B and C for generic mediator mass

The coefficients A, B and C defined in Eq. (5.21) are listed here for the case where the mediator and the dark matter particle not mass degenerate. They are given by[1]

$$
\begin{aligned}
A &= \frac{4}{(1+w^2)^2}\frac{-1+4x_2-3x_2^2+2x_2^3+w^2\left(1-2x_2+3x_2^2\right)}{(1-x_2)(-1+w^2+2x_2)},\\
B &= \frac{(1+w^2)}{2(1+w^2)^2}\frac{1}{(w^2+x_2)^2}\frac{(x_2-1)}{w^4-1+2x_2(1+w^2)}\\
&\Big(-3+w^{10}+w^8\left(-3+x_2\right),-14x_2-28x_2^2-20x_2^3+w^6\left(6-23x_2+6x_2^2-2x_2^3\right)\\
&-w^4\left(2-7x_2+44x_2^2+2x_2^3\right)-w^2\left(-1+31x_2+30x_2^2+36x_2^3\right)\Big)\\
C &= \frac{1}{(w^2+x_2)^3}\frac{1}{(1+w^2)^2}\frac{1}{(-1+w^2+2x_2)}\\
&\Big(3-w^{14}-3w^{12}(-1+x_2)+8x_2-10x_2^2-20x_2^3-16x_2^4+32x_2^5-\\
&w^{10}\left(-9-31x_2-6x_2^2+2x_2^3\right)-w^2\left(1-7x_2+14x_2^2+110x_2^3-148x_2^4\right)-\\
&w^4\left(11-21x_2+176x_2^2-308x_2^2-4x_2^4\right)-w^6\left(-9+102x_2-232x_2^2-96x_2^3+4x_2^4\right)\\
&-w^8\left(11-70x_2-90x_2^2-16x_2^3+4x_2^4\right)\Big),
\end{aligned}
$$

with $w = m_i/M_{\mathrm{DM}}$. To obtain the full expression of the cross section in this case, the factor $\ln(x_2)$ in Eq. (5.21) has to be replaced by the generalised factor $\ln\left(\frac{w^2-1+2x_2}{w^2+1}\right)$.

[1] This computation has been performed by Mathieu Pellen.

Appendix C

Fit to positron fraction and total lepton flux: results.

In this appendix we collect the results of the fit of the improved phenomenological model to the positron fraction data [18] and total lepton flux [223]. As one can see comparing Tabs 6.2 and C.1, the two fits are strictly speaking not consistent within the uncertainties. The fit to the positron fraction and total lepton flux has to be regarded as a consistency check for the fit to the separate electron and positron fluxes. In fact, it is not possible to correctly take into account the correlations between the two data sets using the published data. This explains the smallness of the $\chi^2/d.o.f.$ corresponding to the fit. The best-fit values for the parameters are collected in Tab. C.1 and the resulting fit functions are shown in Fig. C.1 and C.2. To obtain a stable fit, we fixed the cut off energy of the source term to the value obtained fitting the positron and electron fluxes (see Tab 6.2).

Parameter	Best-fit value
Ψ_+	(0.86 ± 0.11) GV
Ψ_-	(1.36 ± 0.03) GV
C_{e^+}	(0.18 ± 0.02) GeV^{-1}m^{-2}s^{-1}sr^{-1}
γ_{e^+}	-3.67 ± 0.14
C_{e^-}	(2.88 ± 0.15) GeV^{-1}m^{-2}s^{-1}sr^{-1}
γ_{e^-}	-3.35 ± 0.17
C_s	(0.025 ± 0.007) GeV^{-1}m^{-2}s^{-1}sr^{-1}
γ_s	-2.43 ± 0.07
$1/E_B$	(0.034 ± 0.001) GeV^{-1}
$\Delta\Gamma$	-0.44 ± 0.04
Λ	0.13 ± 0.03
$1/E_s$	0.0016 GeV^{-1} fixed
$\chi^2/d.o.f$	81/126

Table C.1: Best-fit values for the parameters describing the improved phenomenological model, obtained fitting the model to the AMS-02 data in the range $3 - 500$ GeV *for the positron fraction and* $3 - 1000$ GeV *for the total lepton flux.*

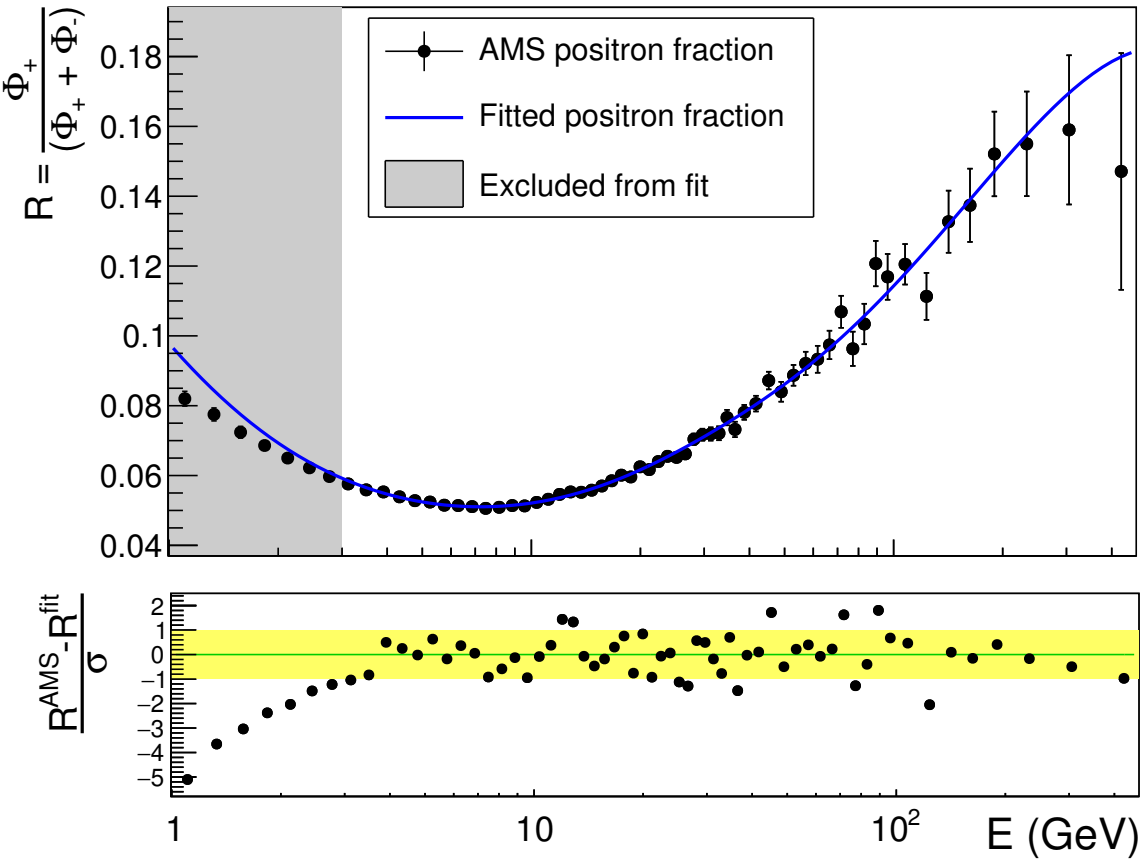

Figure C.1: Panel above: best-fit curve for the positron fraction, obtained expressing the positron fraction from the model in Eq. (6.5) *and setting the parameters to the values in Tab. C.1. The grey shaded region represents the region with* $E < 3$ GeV*, that is excluded from the fit. Panel below: difference of the measured positron fraction and the fit curve relative to the error. The yellow band represents the* $1\,\sigma$ *region.*

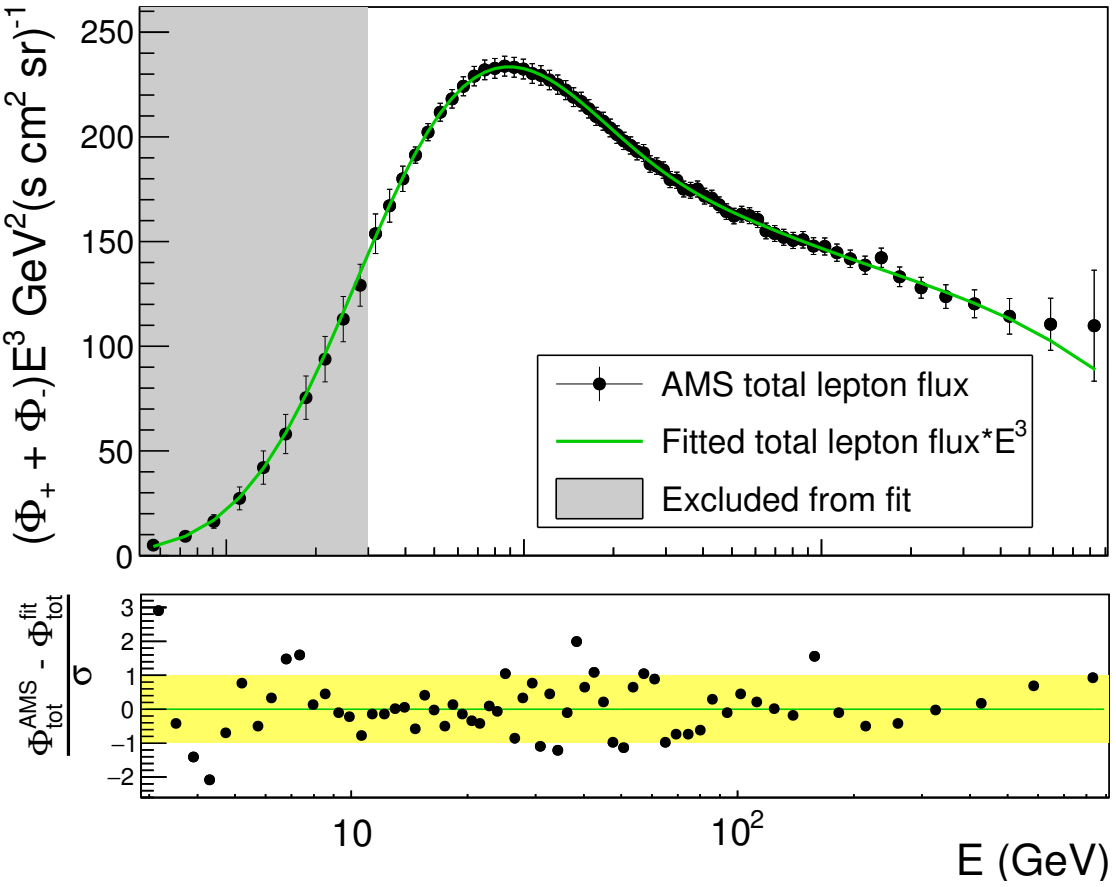

Figure C.2: Panel above: best-fit curve for the total lepton flux, obtained setting the parameters of the model in Eq. (6.5) *to the values in Tab. C.1. The error bars represent the reduced error used for the fit. The grey shaded region represents the region with* $E < 3$ GeV*, that is excluded from the fit. Panel below: difference of the measured electron flux and the fit curve relative to the error. The yellow band represents the* $1\,\sigma$ *region.*

Appendix D

Upper limits - uncertainties

The uncertainties affecting the upper limits on the dark matter annihilation cross section are due to the fact that the distribution of the dark matter in the Galaxy is not precisely known, as well as the local value of the dark matter density, and that the parameters describing the propagation of charged particles in the Galaxy are affected by large uncertainties. From a practical point of view, for each scenario and each propagation model we use a different set of parameters to evaluate the Green functions for the propagation, according to the parameterisation in [107]. More specifically, to estimate the uncertainty due to the choice of the propagation scenario, we choose a dark matter profile model (NFW in our case) and we repeat the upper limits for the three propagation scenarios MIN ($\delta = 0.55$, $K_0 = 0.00595\,\mathrm{kpc}^2/\mathrm{Myr}$), MED ($\delta = 0.70$, $K_0 = 0.0112\,\mathrm{kpc}^2/\mathrm{Myr}$) and MAX ($\delta = 0.46$, $K_0 = 0.00765\,\mathrm{kpc}^2/\mathrm{Myr}$), as in [255, 256, 107]. Analogously, to estimate the impact of the choice of the dark matter profile, we choose the "MED" propagation model and produce the signals expected at Earth considering the NFW, Einasto, Einasto B, Moore, Isothermal and Burkert dark matter profile. For each of these choices, the parameters can be found in Figure 7 of Ref. [107]. Finally, a change in the local dark matter density implies a rescaling of the fluxes, since the local dark matter density appears (squared) as a prefactor in the expression for the fluxes at Earth. For this study, we choose the NFW profile, the "MED" propagation scenario and $\rho_\odot \in (0.25, 0.7)\,\mathrm{GeV/m}^3$, as in [107].
In Fig. D.1 we show the impact of these effects. The most relevant uncertainty comes from the normalisation of the dark matter profile at the Solar System location (bottom figure). The uncertainties due to propagation scenarios and halo models have an impact at most of order $5 - 10\%$ on the upper limit values of the cross section.

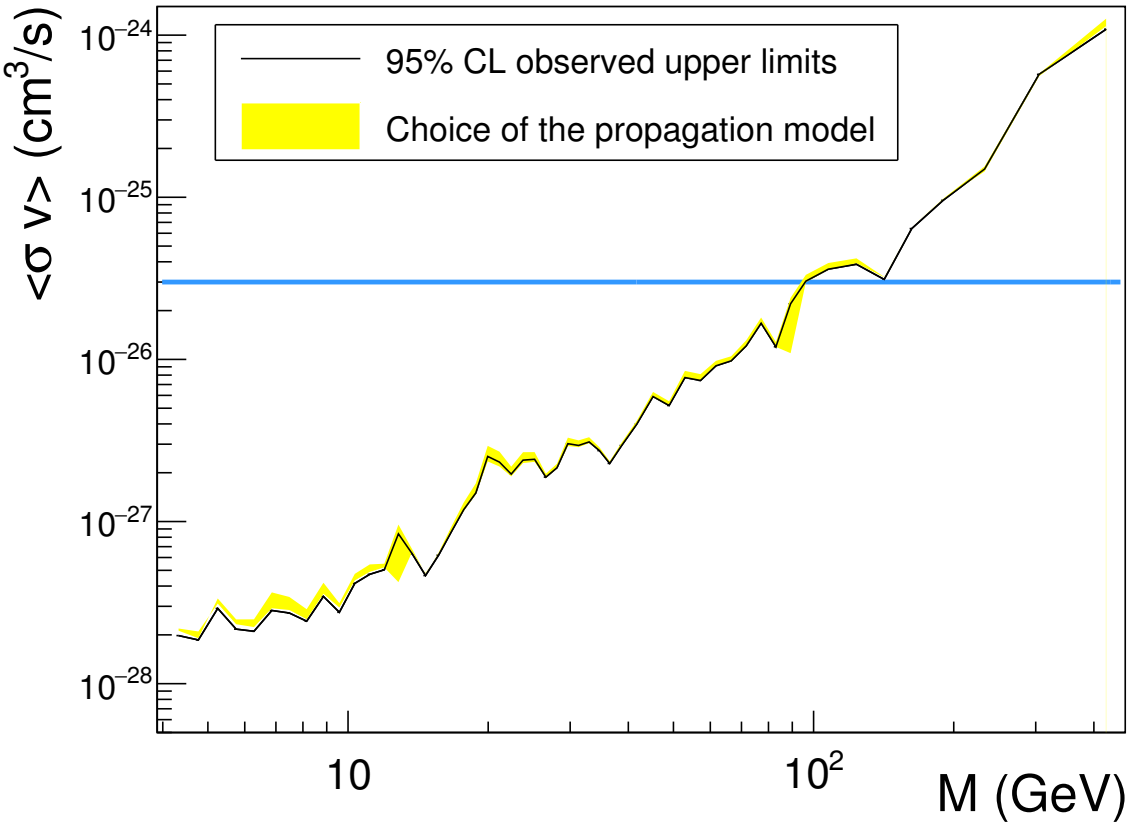
95% CL observed upper limits
Choice of the propagation model
<σ v> (cm³/s)
10⁻²⁴
10⁻²⁵
10⁻²⁶
10⁻²⁷
10⁻²⁸
10
10²
M (GeV)

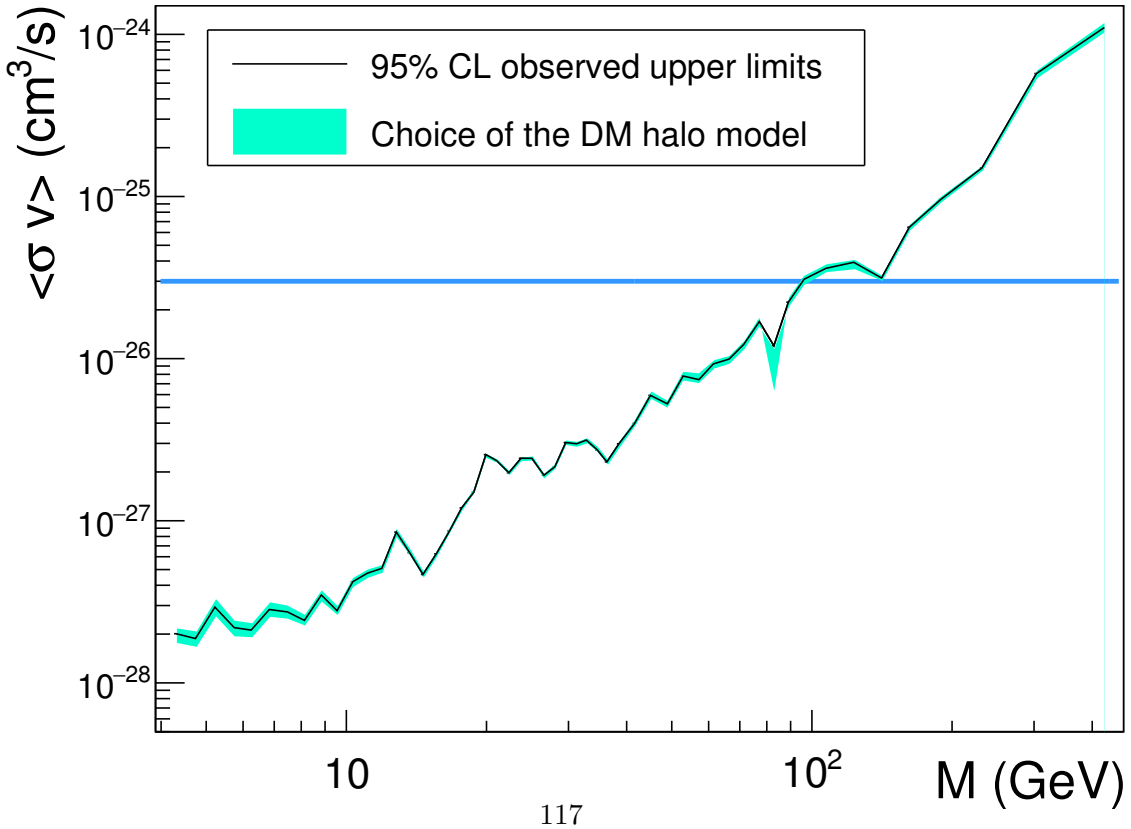
95% CL observed upper limits
Choice of the DM halo model
<σ v> (cm³/s)
10⁻²⁴
10⁻²⁵
10⁻²⁶
10⁻²⁷
10⁻²⁸
10
10²
M (GeV)

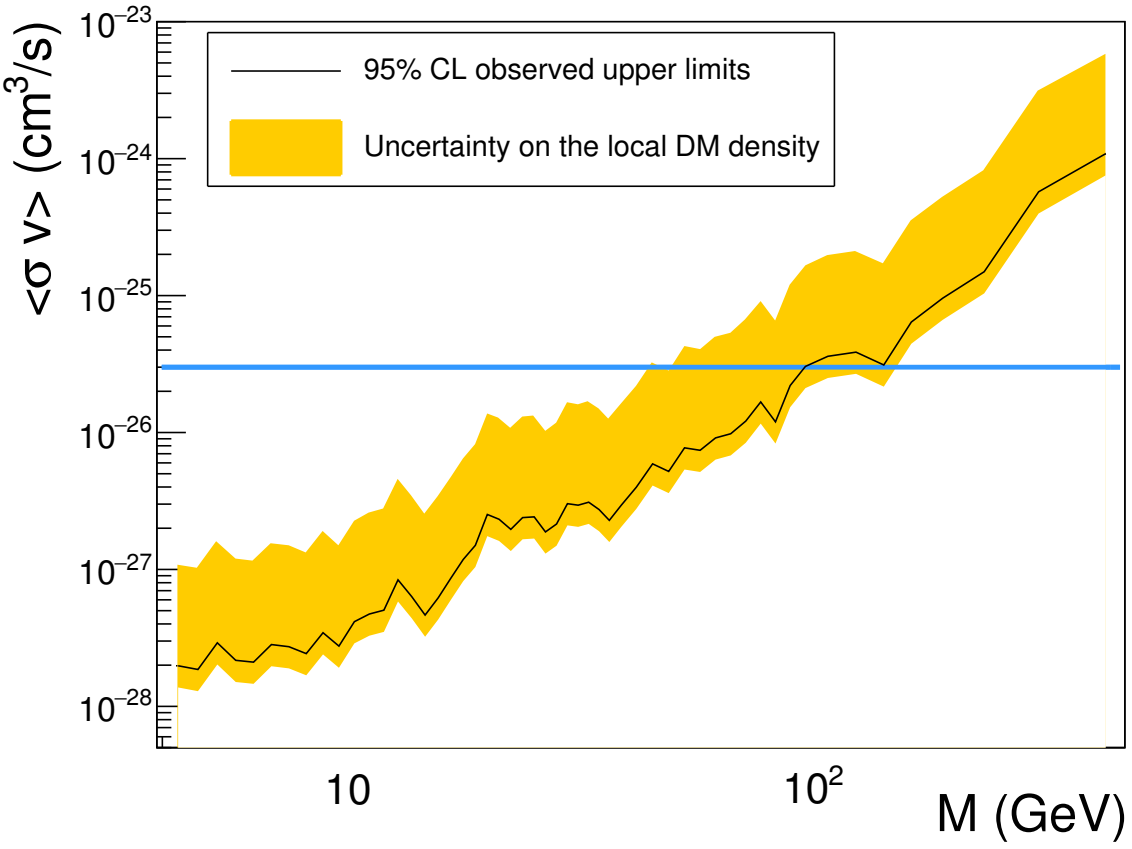

Figure D.1: Top: uncertainties due to the choice of the propagation scenario for electrons and positrons. Centre: uncertainties due to the choice of the dark matter distribution in the Galaxy. Bottom: impact of the uncertainty on the local dark matter density.

Appendix E

Upper limits from other channels

In this appendix we consider the scenarios where dark matter annihilates into other channels, namely $\{\mu^+\mu^-, \tau^+\tau^-, b\bar{b}, ZZ, W^+W^-\}$. For each of these final states we assume that dark matter exclusively annihilates into the given final state. From the particle physics evolution of the final states, electrons and positrons are always produced. For instance, from the evolution of $b\bar{b}$ final state, charged pions are produced, that decay into muons, that in turn produce electrons and positrons. The fluxes of electrons and positrons can be used to place limits on the primary annihilation cross-section, as we do for leptophilic models. For leptophilic models, the electron and positron fluxes due to dark matter annihilation are made of two contributions: The primary electron and positron flux and those produced by the further evolution of the final state (radiation of EW gauge boson, emission of QED radiation, etc.) For the other final states we consider, the electron and positron fluxes are constituted only by particles produced by the evolution of the primary annihilation products. Therefore the signal is completely concentrated at low energies and correctly taking into account effects like solar modulation is crucial. The results for the upper limits are shown in Fig. E.1. As expected, one has the highest sensitivity for leptophilic models. For all final states, we have assumed the NFW halo model and the MED propagation scenario.

Assuming that dark matter primarily annihilates into $\tau^-\,\tau^+$ or $b\,\bar{b}$, good fits of the galactic center excess in gamma rays can be obtained, with thermal cross sections [20, 21]. For instance, assuming that dark matter annihilates only into $b\,\bar{b}$, the best fit values for the dark matter mass and annihilation cross section are $M_{\rm DM} \simeq 49\,{\rm GeV}$ and $\langle\sigma v\rangle \simeq 2 \cdot 10^{-26}{\rm cm}^3/{\rm s}$. We find that this scenario is consistent with the AMS-02 electron and positron flux measurements.

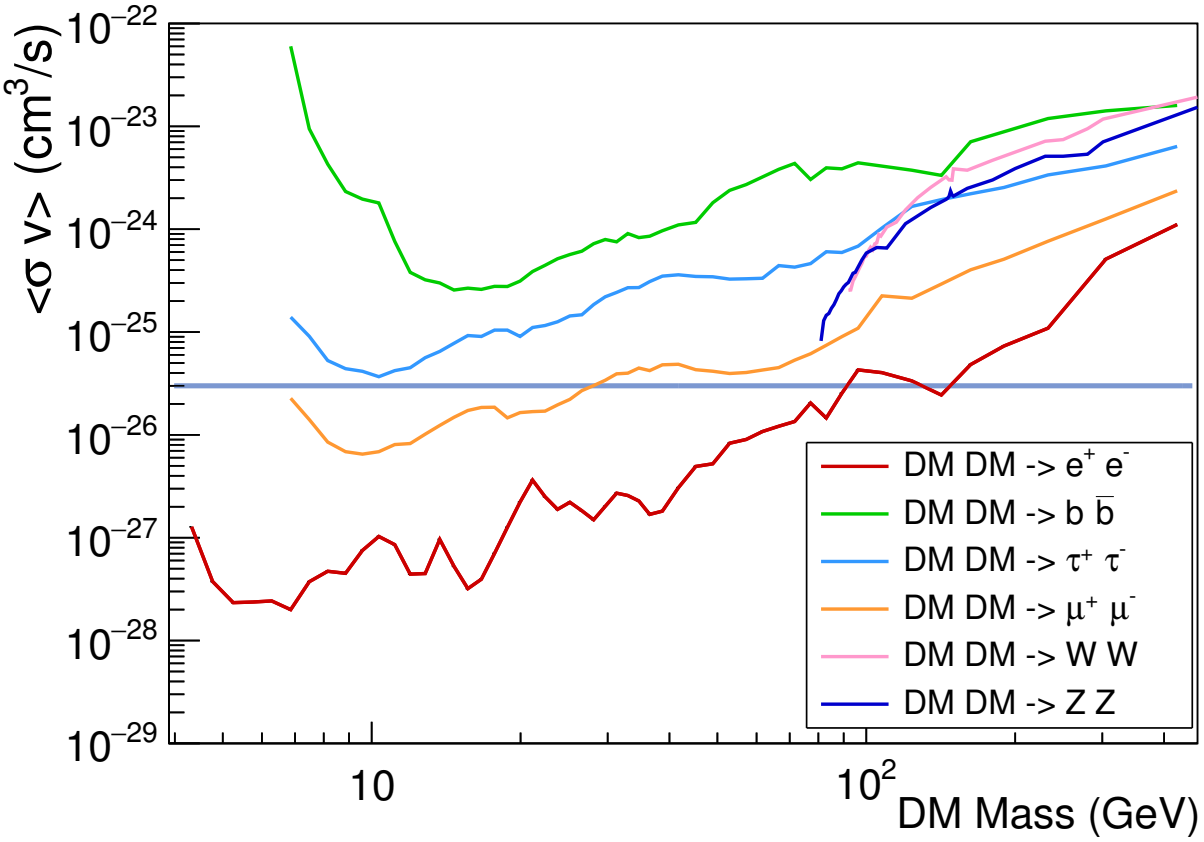

Figure E.1: Upper limits on the dark matter annihilation cross section for the process $\mathrm{DM}, \mathrm{DM} \to f\bar{f}$*, with* $f = \{\mu^-, \tau^-, b, Z, W^-\}$*, compared to the upper limits on the annihilation cross section into electron-positron pairs (red solid line). The horizontal blue line represents the thermal annihilation cross section* $\langle \sigma v \rangle = 3 \cdot 10^{-26} \mathrm{cm}^3/\mathrm{s}$.

Appendix F

Antiproton signals from DM annihilation

In this appendix we show three examples of antiproton signals due to leptophilic dark matter annihilation in the Galaxy. We choose three very large values for the dark matter mass, as for lower masses the contribution to the antiproton flux is negligible. The flux of antiprotons is induced by the emission and decay of EW gauge bosons and further evolution of the decay products.

The shaded bands represents the uncertainties due to propagation modelling and due to the knowledge of the inclusive antiproton production cross section, respectively. The total uncertainty on the fluxes can be obtained combining these two contributions.

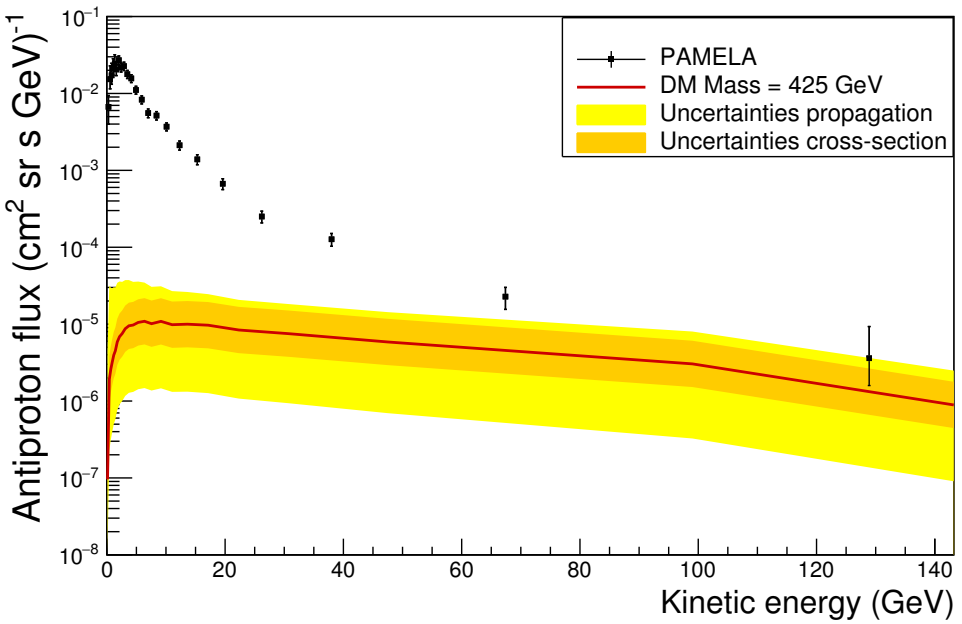

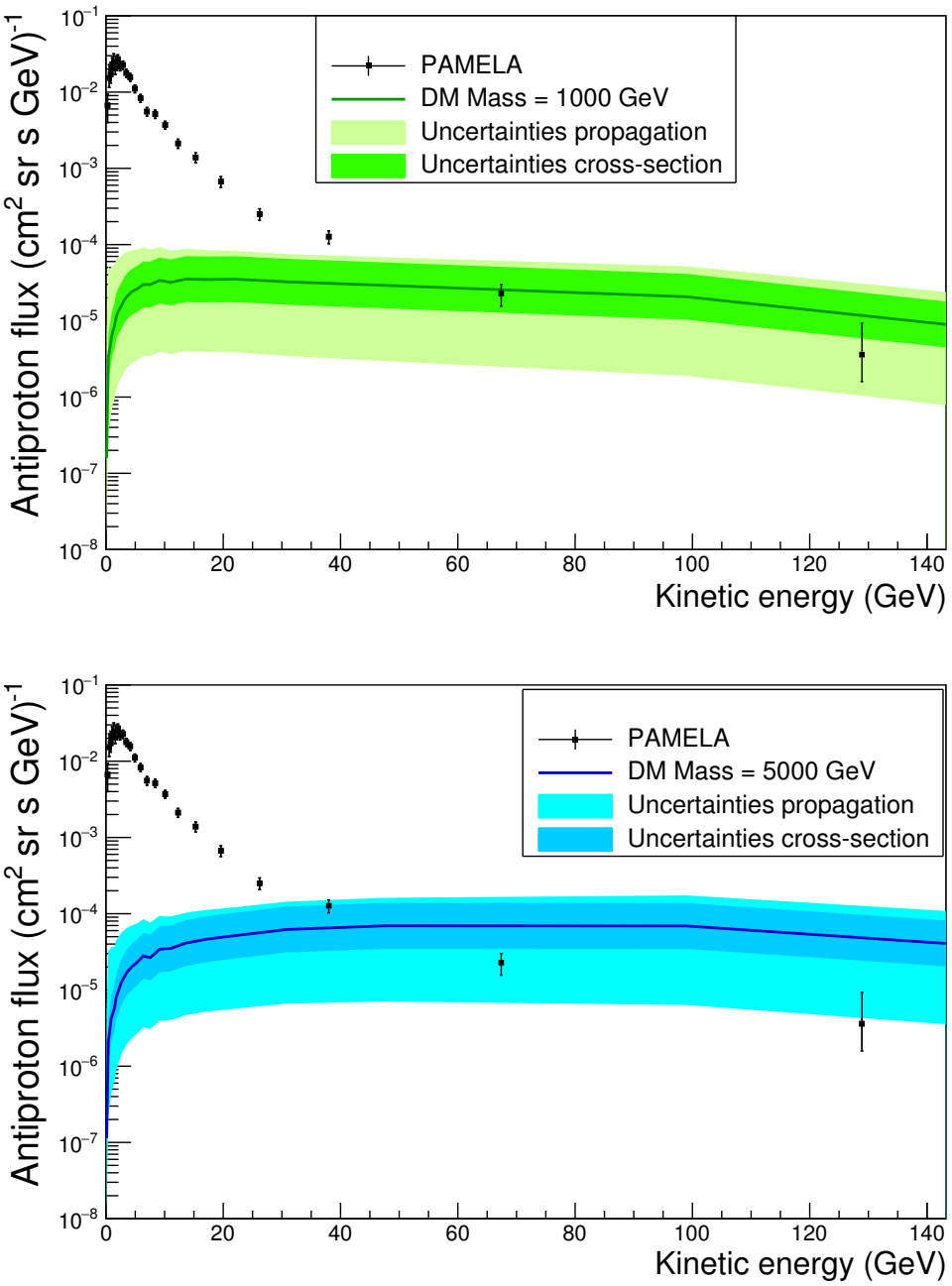

Figure F.1: Antiproton fluxes induced by dark matter annihilation in the Galaxy, normalized to the upper limit value of the $2 \to 2$ annihilation cross section for three representative masses, $M_{\rm DM} = 425, 1000, 5000$ GeV. These fluxes are obtained considering a Einasto dark matter profile and the impact of the choice of the propagation parameters (MIN, MED, MAX) and of the uncertainties on the antiproton production cross section is shown.

Appendix G

Passarino Veltman reduction

Tadpole function or one-point function A_0

$$A_0(m^2) = \frac{\mu^\epsilon}{i\pi^2}\int d^dk \frac{1}{k^2-m^2} = m^2\left(\frac{2}{\epsilon} - \ln\pi - \gamma_E + 1 + \ln\frac{\mu^2}{m^2}\right) + \mathcal{O}(\epsilon), \tag{G.1}$$

with $d = 4-\epsilon$ in dimensional regularisation.

The two-point functions B

$$B_0(p^2, m_1^2, m_2^2) = \frac{\mu^\epsilon}{i\pi^2}\int d^dk \frac{1}{(k^2-m_1^2)[(k+p)^2-m_2^2]}, \tag{G.2a}$$

$$B_\mu(p^2, m_1^2, m_2^2) = \frac{\mu^\epsilon}{i\pi^2}\int d^dk \frac{k_\mu}{(k^2-m_1^2)[(k+p)^2-m_2^2]}, \tag{G.2b}$$

$$B_{\mu\nu}(p^2, m_1^2, m_2^2) = \frac{\mu^\epsilon}{i\pi^2}\int d^dk \frac{k_\mu k_\nu}{(k^2-m_1^2)[(k+p)^2-m_2^2]}, \tag{G.2c}$$

From dimensional analysis we see that the only divergent two-point function is B_0. In particular, we have

$$B_0(p^2, m_1^2, m_2^2) = \frac{2}{\epsilon} - \ln\pi - \gamma_E + \ln\frac{\mu^2}{-p^2} - \int_0^1 dx \ln\left(x(1-x) - (1-x)\frac{m_1^2}{p^2} - x\frac{m_2^2}{p^2}\right) + \mathcal{O}(\epsilon). \tag{G.3}$$

Note that in general it is not possible to solve the integral over x analytically.

Moreover,

$$B_\mu(p^2, m_1^2, m_2^2) = p_\mu B_1; \tag{G.4a}$$

$$B_{\mu\nu}(p^2, m_1^2, m_2^2) = g_{\mu\nu}B_{00} + p_\mu p_\nu B_{11}, \tag{G.4b}$$

and the explicit forms of the scalar functions B_1, B_{00} and B_{11} can be found in the Literature, for instance in [257].

The two-point functions C

$$C_0(p^2,(p-q)^2,q^2,m_1^2,m_2^2,m_3^2) = \\ = \frac{\mu^\epsilon}{i\pi^2}\int d^dk \frac{1}{(k^2-m_1^2)[(k+p)^2-m_2^2][(k+q)^2-m_3^2]}, \tag{G.5a}$$

$$C_\mu(p^2,(p-q)^2,q^2,m_1^2,m_2^2,m_3^2) = \\ = \frac{\mu^\epsilon}{i\pi^2}\int d^dk \frac{k_\mu}{(k^2-m_1^2)[(k+p)^2-m_2^2][(k+q)^2-m_3^2]}, \tag{G.5b}$$

$$C_{\mu\nu}(p^2,(p-q)^2,q^2,m_1^2,m_2^2,m_3^2) = \\ = \frac{\mu^\epsilon}{i\pi^2}\int d^dk \frac{k_\mu k_\nu}{(k^2-m_1^2)[(k+p)^2-m_2^2][(k+q)^2-m_3^2]}, \tag{G.5c}$$

$$C_{\mu\nu\rho}(p^2,(p-q)^2,q^2,m_1^2,m_2^2,m_3^2) = \\ = \frac{\mu^\epsilon}{i\pi^2}\int d^dk \frac{k_\mu k_\nu k_\rho}{(k^2-m_1^2)[(k+p)^2-m_2^2][(k+q)^2-m_3^2]}, \tag{G.5d}$$

with

$$C_\mu = p_\mu C_1 + q_\mu C_2; \tag{G.6a}$$

$$C_{\mu\nu} = g_{\mu\nu}C_{00} + p_\mu p_\nu C_{11} + (p_\mu q_\nu + p_\nu q_\mu)C_{12} + q_\mu q_\nu C_{22}. \tag{G.6b}$$

The expression for $C_{\mu\nu\rho}$ as well as the explicit expressions of the scalar integrals appearing above can again be found in [257]. We do not provide the expressions for the four-points functions D as they are not relevant to our calculation. These can also be found in [257].

Divergent parts of the Passarino-Veltman functions

From dimensional analysis, one can see that the functions A_0, B_0, B_1, B_{00}, B_{11}, C_{00}, C_{001} and C_{002} are divergent. In particular, the divergent part of these functions is universal, namely it does not depend on the arguments of the Passarino-Veltman functions. The functions B_0 and C_{00} are relevant for the calculation in Chapter 8 and their divergent parts are

$$B_0|_{div} = \frac{2}{\epsilon} \qquad\qquad C_{00}|_{div} = \frac{1}{2\epsilon}, \tag{G.7}$$

with $\epsilon \to 0$.

Acknowledgements

First of all, I would like to thank my first supervisor, Prof. Michael Krämer, for countless discussions about my research projects, support and motivation, during the past three and a half years. The guidance and the enthusiasm for physics of my second supervisor, Prof. Stefan Schael, were crucial during the second part of my PhD.

I received priceless help from all persons who read parts of the draft and helped me improving it: Henning Gast, Andreas Güth, Michael Korsmeier, Alexander Mück, Mathieu Pellen and Claudia Pistone.
Special thanks to Mathieu, because working with him is great. We discussed all possible physics issue that came to our mind, factors 55 and many other things...drinking a good cup of water!
Lennart Oymanns provided (very patient) technical help and explanations every time I needed them.
I am very grateful to Henning Gast, who always found time to discuss with me whenever I had doubts. I am happy to continue working with him.
Alex is at all times ready to help, discuss and smile. Talking with him has always been a great opportunity to learn new things, have new ideas and motivation for my work.
I had very useful discussions with many other people, in particular with Joachim Kopp, Jan Heisig and Vedran Brdar regarding leptophilic dark matter at the LHC, and with Fabrizio Parodi at the very beginning of this work about ROOT and statistics.
Giovanni Ridolfi and Alessandro Petrolini at the University of Genova were not directly involved in this work, but never stopped motivating me. I am very greatful to both of them.
I thank Andreas, Simon, Klaas at Insitute IIIA for useful discussions about statistics, ROOT and all desparate questions about colliders that came to my mind.
Mrs. Anke Bachtenkirch and Dr. Georg Schwering are always ready to help and give explanations about bureaucracy and other organisational issues.

Ladies first: I had very good time outside the office with Jory, Claudia, Sarah, Debbie, Federica and Janine. Also Mathieu, Lennart, Manfred, Sebastian, Fredo, Alex, Dennis, Matthias, Simon, Klaas and Michael B. made coffee breaks and lunches at the Physikzentrum particularly amusing and relaxing.

I cannot thank Andreas enough, for everything.

When I was at the end of high-school my grandfather asked me why I had decided to study medicine (as he did), instead of doing “something fun and fascinating, like physics”. I thank him for asking that question.

List of Figures

2.1 Multipole expansion of the temperature power spectrum measured by Planck. . . . 10
2.2 Evolution of the dark matter number density with time. . . . 15
2.3 Examples of diagrams for monophoton and monojet processes. . . . 21
2.4 Status of DM direct detection. . . . 24

3.1 Cosmic rays components and spectrum 29
3.2 Effects of solar modulation on the carbon flux 34

4.1 Leading order contributions to the KK photon annihilation into electron/positron pairs, $B^{(1)}B^{(1)} \to e^+e^-$. . . . 38
4.2 Leading order contributions to the bino neutralino annihilation into electron-positron pairs, $\tilde{\chi}_0\tilde{\chi}_0 \to e^+e^-$. . . . 38
4.3 Generic process with EW gauge boson radiation 41

5.1 Pictorial example of the computation of a $(2 \to 3)$ cross section using the splitting functions approximation. The red ellipse represents the unknown DM-SM interaction. . . . 45
5.2 Contributions to the dark matter annihilation cross section , including the real emission of a Z boson. . . . 48
5.3 Comparison of the Z boson energy spectrum in the process $B^{(1)}B^{(1)} \to e^+e^-Z$ obtained from the exact calculation and from the generalised splitting functions. . . . 52
5.4 Comparison of the positron fluxes from the process $B^{(1)}\,B^{(1)} \to e^+e^-Z$ before propagation through the Galaxy obtained with the full calculation and with the generalised splitting functions. . . . 53
5.5 Comparison of the antiproton fluxes from the process $B^{(1)}\,B^{(1)} \to e^+e^-Z$ before propagation through the Galaxy obtained with the full calculation and with the generalised splitting functions. . . . 54
5.6 Comparison of the positron fluxes from the process $B^{(1)}\,B^{(1)} \to e^+e^-Z$ after propagation through the Galaxy obtained with the full calculation and with the generalised splitting functions. . . . 55
5.7 Comparison of the antiproton fluxes from the process $B^{(1)}\,B^{(1)} \to e^+e^-Z$ after propagation through the Galaxy obtained with the full calculation and with the generalised splitting functions. . . . 56

5.8 Comparison of the Z boson energy spectrum in the process $\tilde{\chi}_0\tilde{\chi}_0 \to e^+e^-Z$ obtained from the exact calculation and from the generalised splitting functions. 57
5.9 Comparison of the Z boson energy spectrum in the process $\tilde{\chi}_0\tilde{\chi}_0 \to e^+e^-Z$ obtained from the exact calculation and from the generalised splitting functions for massive final state leptons. 58

6.1 The positron fraction measured by AMS-02. 60
6.2 Results of the fit: the positron flux. 65
6.3 Results of the fit: the electron flux. 66
6.4 Pictorial representation of the correlation matrix 67
6.5 Overall uncertainty on the energy scale of the detector. 68

7.1 Signal plus background curve for a $M_{\rm DM} = 20$ GeV leptophilic dark matter candidate and $N \simeq 0.002$ for the positron and the electron flux. 76
7.2 Effects of solar modulation on the positron flux. 77
7.3 Effects of solar modulation on the positron flux times E^3. 77
7.4 95% CL upper limits on the $(2 \to 2)$ dark matter annihilation cross section . 78
7.5 95% CL upper limits on the $(2 \to 2)$ dark matter annihilation cross section and projected limits 78
7.6 95% CL upper limits on the $(2 \to 2)$ dark matter annihilation cross section , expected and projected limits. 79
7.7 Relevant contributions to the DM annihilation cross section, including EW radiation. 80
7.8 Signal for $M_{\rm DM} = 1000$ GeV, without and with the inclusion of EW radiation. 80
7.9 Antiproton-to-proton ratio from Ref. [243] compared to the available measurements. 81
7.10 Comparison of the predictions for $M_{\rm DM} = 425, 1000, 5000$ GeV for the antiproton flux. 82
7.11 Comparison of the predictions for $M_{\rm DM} = 425, 1000, 5000$ GeV for the antiproton flux. 83
7.12 Impact of the choice of the propagation scenario on the total antiproton-to-proton ratio for three representative masses, $M_{\rm DM} = 1000, 5000$ GeV. . 84
7.13 Impact of the uncertainties on the antiproton production cross section on the total antiproton-to-proton ratio for three representative masses, $M_{\rm DM} = 1000, 5000$ GeV. 85

8.1 Lowest order contributions to leptophilic dark matter production at the LHC. 88
8.2 Relevant diagrams for scalar production and scalar decay used for preliminary tests of our calculation. 89
8.3 Relevant diagrams for dark matter production from u quark annihilation with the exchange of a photon and of a Z boson. 89
8.4 Relevant vertices and definition of the momenta used for the calculation of $\mathcal{M}_1$, $\mathcal{M}_2$, $\mathcal{M}_3$ and $\mathcal{M}_4$. 89
8.5 Cross section for the process $u\ \bar{u} \to \chi\ \chi$ for $M_{\rm DM} = 100\,\text{GeV}$, $m_\rho = 300\,\text{GeV}$ and $Y = 1$ as a function of the centre of mass energy. 93

8.6 Cross section for the process $u\ \bar{u} \to \chi\ \chi$ for $\sqrt{\hat{s}} = 5\,\text{TeV}$, $m_\rho = 300\,\text{GeV}$ and $Y = 1$ as a function of the mass of the dark matter particle. The kink is at 300 GeV, namely the mass of the mediatior. 94
8.7 Contributions to the cross section for the process $p\ p \to \chi\ \chi + \gamma$. The same contributions would arise from the diagrams with two scalars and a lepton in the loop. 94

A.1 The Sudakov parametrisation. 102
A.2 Relevant diagram for the computation of the Born cross section for $P_{F\to F}$. 103
A.3 Relevant diagram for the computation of the splitting function for a massless fermion into a massless fermion and a massive boson, $P_{F\to F}$. 104
A.4 Relevant diagram for the computation of the splitting function for a massless fermion into a massless fermion and a massive boson, $P_{F\to V}$. 106
A.5 Relevant diagram for the computation of the Born cross section for $P_{V\to F}$. 106
A.6 Relevant diagram for the computation of the splitting function for a massive vector boson splitting into a massless fermion-antifermion pair, $P_{V\to F}$ 107
A.7 Relevant diagram for the computation of the Born cross section for $P_{S\to V}$. 108
A.8 Relevant diagram for the computation of the splitting function for a scalar into a vector boson and a scalar, $P_{S\to V}$ 108
A.9 Relevant diagram for the computation of the splitting function for a vector boson splitting into two scalars, $P_{V\to S}$ 109
A.10 Relevant diagram for the computation of the splitting function for a scalar splitting into a fermion-antifermion pair, $P_{S\to F}$ 109
A.11 Relevant diagram for the computation of the splitting function accounting for the splitting of a massive gauge boson into two massive gauge bosons. The arrows represent the direction of the momenta. 110

C.1 Results of the fit: the positron fraction. 114
C.2 Results of the fit: the total lepton flux. 115

D.1 Uncertainties on the upper limits on the DM annihilation cross section. . 118

E.1 Upper limits on the dark matter annihilation cross section for the process $\text{DM}, \text{DM} \to f\bar{f}$, with $f = \{\mu^-, \tau^-, b, Z, W^-\}$. 120

F.1 Antiproton fluxes induced by dark matter annihilation in the Galaxy, normalized to the upper limit value of the $2 \to 2$ annihilation cross section for three representative masses, $M_{\text{DM}} = 425, 1000, 5000$ GeV. 122

List of Tables

2.1 Supersymmetric particles and their quantum numbers in the MSSM. . . . 16

5.1 Thermally averaged cross section $\langle \sigma v \rangle$ for the lowest-order annihilation cross section of vector dark matter into an electron-positron pair, compared to the exact cross section including Z-boson emission, and the splitting functions approximation, for different dark matter masses. For the weak angle and the electroweak coupling we have used $\sin^2 \theta_w = 0.23113$ and $\alpha = 1/127.9$, respectively. 49

6.1 Fit to the AMS-02 data in the range $1 - 500$ GeV, in agreement within the uncertainties with the results in [18]. The differences between our results and the published ones may be due to rounding applied to the published data. 62

6.2 Best-fit values for the parameters describing the improved phenomenological model, obtained fitting the model to the AMS-02 data in the range $3 - 500$ GeV for the positron flux and $3 - 700$ GeV for the electron flux. . 64

8.1 Cross section for the process $u\ \bar{u} \to \chi\ \chi$ for $M_{\rm DM} = 100\,{\rm GeV}$, $m_\rho = 300\,{\rm GeV}$ and $Y = 1$ as a function of the centre of mass energy. 93

C.1 Best-fit values for the parameters describing the improved phenomenological model, obtained fitting the model to the AMS-02 data in the range $3 - 500$ GeV for the positron fraction and $3 - 1000$ GeV for the total lepton flux. 113

Bibliography

[1] J. Goldstone, A. Salam, and S. Weinberg, *Broken Symmetries*. Phys. Rev. **127** (1962) 965–970.

[2] S. Weinberg, *A Model of Leptons*. Phys. Rev. Lett. **19** (1967) 1264–1266.

[3] S. L. Glashow, *Partial Symmetries of Weak Interactions*. Nucl. Phys. **22** (1961) 579–588.

[4] S. L. Glashow, J. Iliopoulos, and L. Maiani, *Weak Interactions with Lepton-Hadron Symmetry*. Phys. Rev. **D2** (1970) 1285–1292.

[5] P. W. Higgs, *Broken symmetries, massless particles and gauge fields*. Phys. Lett. **12** (1964) 132–133.

[6] P. W. Higgs, *Broken Symmetries and the Masses of Gauge Bosons*. Phys. Rev. Lett. **13** (1964) 508–509.

[7] F. Englert and R. Brout, *Broken Symmetry and the Mass of Gauge Vector Mesons*. Phys. Rev. Lett. **13** (1964) 321–323.

[8] G. S. Guralnik, C. R. Hagen, and T. W. B. Kibble, *Global Conservation Laws and Massless Particles*. Phys. Rev. Lett. **13** (1964) 585–587.

[9] **ATLAS** Collaboration, G. Aad *et al.*, *Observation of a new particle in the search for the Standard Model Higgs boson with the ATLAS detector at the LHC*. Phys. Lett. **B716** (2012) 1–29, `arXiv:1207.7214 [hep-ex]`.

[10] **CMS** Collaboration, S. Chatrchyan *et al.*, *Observation of a new boson at a mass of 125 GeV with the CMS experiment at the LHC*. Phys. Lett. **B716** (2012) 30–61, `arXiv:1207.7235 [hep-ex]`.

[11] R. M. Wald, *General Relativity*. 1984.

[12] R. Bernabei *et al.*, *New Results from DAMA/LIBRA: Final Model-Independent Results of Dama/Libra-Phase1 and Perspectives of Phase2*. Frascati Phys. Ser. **58** (2014) 41.

[13] **DAMA** Collaboration, R. Bernabei *et al.*, *First results from DAMA/LIBRA and the combined results with DAMA/NaI*. Eur. Phys. J. **C56** (2008) 333–355, `arXiv:0804.2741 [astro-ph]`.

[14] E. Bulbul, M. Markevitch, A. Foster, R. K. Smith, M. Loewenstein, and S. W. Randall, *Detection of An Unidentified Emission Line in the Stacked X-ray spectrum of Galaxy Clusters*. Astrophys. J. **789** (2014) 13, `arXiv:1402.2301 [astro-ph.CO]`.

[15] A. Boyarsky, O. Ruchayskiy, D. Iakubovskyi, and J. Franse, *Unidentified Line in X-Ray Spectra of the Andromeda Galaxy and Perseus Galaxy Cluster*. Phys. Rev. Lett. **113** (2014) 251301, `arXiv:1402.4119 [astro-ph.CO]`.

[16] **PAMELA Collaboration** Collaboration, O. Adriani *et al.*, *An anomalous positron abundance in cosmic rays with energies 1.5-100 GeV*. Nature **458** (2009)

607–609, arXiv:0810.4995 [astro-ph].

[17] **AMS Collaboration** Collaboration, M. Aguilar *et al.*, *First Result from the Alpha Magnetic Spectrometer on the International Space Station: Precision Measurement of the Positron Fraction in Primary Cosmic Rays of 0.5 – 350 GeV*. Phys.Rev.Lett. **110** (2013) 141102.

[18] **AMS Collaboration** Collaboration, L. Accardo *et al.*, *High Statistics Measurement of the Positron Fraction in Primary Cosmic Rays of 0.5 – 500 GeV with the Alpha Magnetic Spectrometer on the International Space Station*. Phys.Rev.Lett. **113** (2014) 121101.

[19] D. Hooper and L. Goodenough, *Dark Matter Annihilation in The Galactic Center As Seen by the Fermi Gamma Ray Space Telescope*. Phys. Lett. **B697** (2011) 412–428, arXiv:1010.2752 [hep-ph].

[20] F. Calore, I. Cholis, and C. Weniger, *Background model systematics for the Fermi GeV excess*. JCAP **1503** (2015) 038, arXiv:1409.0042 [astro-ph.CO].

[21] F. Calore, I. Cholis, C. McCabe, and C. Weniger, *A Tale of Tails: Dark Matter Interpretations of the Fermi GeV Excess in Light of Background Model Systematics*. Phys. Rev. **D91** (2015) no. 6, 063003, arXiv:1411.4647 [hep-ph].

[22] **AMS 02** Collaboration, R. Battiston, *The antimatter spectrometer (AMS-02): A particle physics detector in space*. Nucl. Instrum. Meth. **A588** (2008) 227–234.

[23] P. Ciafaloni, D. Comelli, A. Riotto, F. Sala, A. Strumia, *et al.*, *Weak Corrections are Relevant for Dark Matter Indirect Detection*. JCAP **1103** (2011) 019, arXiv:1009.0224 [hep-ph].

[24] F. Zwicky, *Die Rotverschiebung von extragalaktischen Nebeln*. Helv.Phys.Acta **6** (1933) 110–127.

[25] G. Jungman, M. Kamionkowski, and K. Griest, *Supersymmetric dark matter*. Phys.Rept. **267** (1996) 195–373, arXiv:hep-ph/9506380 [hep-ph].

[26] G. Bertone, D. Hooper, and J. Silk, *Particle dark matter: Evidence, candidates and constraints*. Phys.Rept. **405** (2005) 279–390, arXiv:hep-ph/0404175 [hep-ph].

[27] J. L. Feng, *Dark Matter Candidates from Particle Physics and Methods of Detection*. Ann. Rev. Astron. Astrophys. **48** (2010) 495–545, arXiv:1003.0904 [astro-ph.CO].

[28] V. Rubin, N. Thonnard, and J. Ford, W.K., *Rotational properties of 21 SC galaxies with a large range of luminosities and radii, from NGC 4605 /R = 4kpc/ to UGC 2885 /R = 122 kpc/*. Astrophys.J. **238** (1980) 471.

[29] M. Bartelmann and P. Schneider, *Weak gravitational lensing*. Phys. Rept. **340** (2001) 291–472, arXiv:astro-ph/9912508 [astro-ph].

[30] A. Einstein, *Lens-Like Action of a Star by the Deviation of Light in the Gravitational Field*. Science **84** (1936) 506–507.

[31] D. Clowe, A. Gonzalez, and M. Markevitch, *Weak lensing mass reconstruction of the interacting cluster 1E0657-558: Direct evidence for the existence of dark matter*. Astrophys. J. **604** (2004) 596–603, arXiv:astro-ph/0312273 [astro-ph].

[32] M. Markevitch, A. H. Gonzalez, D. Clowe, A. Vikhlinin, L. David, W. Forman, C. Jones, S. Murray, and W. Tucker, *Direct constraints on the dark matter self-interaction cross-section from the merging galaxy cluster 1E0657-56*. Astrophys. J. **606** (2004) 819–824, arXiv:astro-ph/0309303 [astro-ph].

[33] **WMAP** Collaboration, G. Hinshaw *et al.*, *Nine-Year Wilkinson Microwave Anisotropy Probe (WMAP) Observations: Cosmological Parameter Results*. Astrophys. J. Suppl. **208** (2013) 19, arXiv:1212.5226 [astro-ph.CO].

[34] **Planck** Collaboration, P. A. R. Ade *et al.*, *Planck 2013 results. I. Overview of products and scientific results*. Astron. Astrophys. **571** (2014) A1, arXiv:1303.5062 [astro-ph.CO].

[35] **Planck Collaboration** Collaboration, P. Ade *et al.*, *Planck 2013 results. XVI. Cosmological parameters*. Astron.Astrophys. (2014) , arXiv:1303.5076 [astro-ph.CO].

[36] **Planck** Collaboration, P. A. R. Ade *et al.*, *Planck 2015 results. XIII. Cosmological parameters*. arXiv:1502.01589 [astro-ph.CO].

[37] M. Milgrom, *A Modification of the Newtonian dynamics as a possible alternative to the hidden mass hypothesis*. Astrophys. J. **270** (1983) 365–370.

[38] M. D. Seifert, *Stability of spherically symmetric solutions in modified theories of gravity*. Phys. Rev. **D76** (2007) 064002, arXiv:gr-qc/0703060 [gr-qc].

[39] N. E. Mavromatos, M. Sakellariadou, and M. F. Yusaf, *Can the relativistic field theory version of modified Newtonian dynamics avoid dark matter on galactic scales?* Phys. Rev. **D79** (2009) 081301, arXiv:0901.3932 [astro-ph.GA].

[40] P. Ivanov, P. Naselsky, and I. Novikov, *Inflation and primordial black holes as dark matter*. Phys. Rev. **D50** (1994) 7173–7178.

[41] B. J. Carr and J. Primack, *Searching for MACHOs*. Nature **345** (1990) 478–479.

[42] K. Griest, *Galactic Microlensing as a Method of Detecting Massive Compact Halo Objects*. Astrophys. J. **366** (1991) 412–421.

[43] **MACHO** Collaboration, C. Alcock *et al.*, *The MACHO project: Microlensing results from 5.7 years of LMC observations*. Astrophys. J. **542** (2000) 281–307, arXiv:astro-ph/0001272 [astro-ph].

[44] F. Iocco, G. Mangano, G. Miele, O. Pisanti, and P. D. Serpico, *Primordial Nucleosynthesis: from precision cosmology to fundamental physics*. Phys. Rept. **472** (2009) 1–76, arXiv:0809.0631 [astro-ph].

[45] S. D. M. White, C. S. Frenk, and M. Davis, *Clustering in a Neutrino Dominated Universe*. Astrophys. J. **274** (1983) L1–L5.

[46] V. Avila-Reese, P. Colin, O. Valenzuela, E. D'Onghia, and C. Firmani, *Formation and structure of halos in a warm dark matter cosmology*. Astrophys. J. **559** (2001) 516–530, arXiv:astro-ph/0010525 [astro-ph].

[47] T. Asaka, M. Shaposhnikov, and A. Kusenko, *Opening a new window for warm dark matter*. Phys. Lett. **B638** (2006) 401–406, arXiv:hep-ph/0602150 [hep-ph].

[48] A. Boyarsky, J. Lesgourgues, O. Ruchayskiy, and M. Viel, *Lyman-alpha constraints on warm and on warm-plus-cold dark matter models*. JCAP **0905** (2009) 012, arXiv:0812.0010 [astro-ph].

[49] M. Davis, G. Efstathiou, C. S. Frenk, and S. D. M. White, *The Evolution of Large Scale Structure in a Universe Dominated by Cold Dark Matter*. Astrophys. J. **292** (1985) 371–394.

[50] L. Visinelli and P. Gondolo, *Dark Matter Axions Revisited*. Phys. Rev. **D80** (2009) 035024, arXiv:0903.4377 [astro-ph.CO].

[51] L. D. Duffy and K. van Bibber, *Axions as Dark Matter Particles*. New J. Phys. **11** (2009) 105008, arXiv:0904.3346 [hep-ph].

[52] R. D. Peccei and H. R. Quinn, *CP Conservation in the Presence of Instantons*. Phys. Rev. Lett. **38** (1977) 1440–1443.

[53] R. D. Peccei and H. R. Quinn, *Constraints Imposed by CP Conservation in the Presence of Instantons*. Phys. Rev. **D16** (1977) 1791–1797.

[54] S. Weinberg, *A New Light Boson?* Phys. Rev. Lett. **40** (1978) 223–226.

[55] M. Dine, W. Fischler, and M. Srednicki, *A Simple Solution to the Strong CP Problem with a Harmless Axion*. Phys. Lett. **B104** (1981) 199.

[56] M. Dine and W. Fischler, *The Not So Harmless Axion*. Phys. Lett. **B120** (1983) 137–141.

[57] P. Sikivie, *Of Axions, Domain Walls and the Early Universe*. Phys. Rev. Lett. **48** (1982) 1156–1159.

[58] P. Sikivie, *Experimental Tests of the Invisible Axion*. Phys. Rev. Lett. **51** (1983) 1415–1417. [Erratum: Phys. Rev. Lett.52,695(1984)].

[59] L. F. Abbott and P. Sikivie, *A Cosmological Bound on the Invisible Axion*. Phys. Lett. **B120** (1983) 133–136.

[60] G. G. Raffelt, *Astrophysical methods to constrain axions and other novel particle phenomena*. Phys. Rept. **198** (1990) 1–113.

[61] G. G. Raffelt, *Astrophysical axion bounds*. Lect. Notes Phys. **741** (2008) 51–71, arXiv:hep-ph/0611350 [hep-ph]. [,51(2006)].

[62] **CAST** Collaboration, J. I. Collar *et al.*, "CAST: A Search for solar axions at CERN," in *Conference on Astronomical Telescopes and Instrumenation Waikoloa, Hawaii, August 22-28, 2002*. 2003. arXiv:hep-ex/0304024 [hep-ex]. http://alice.cern.ch/format/showfull?sysnb=2372465.

[63] **ADMX** Collaboration, S. J. Asztalos *et al.*, *A SQUID-based microwave cavity search for dark-matter axions*. Phys. Rev. Lett. **104** (2010) 041301, arXiv:0910.5914 [astro-ph.CO].

[64] S. Dodelson and L. M. Widrow, *Sterile-neutrinos as dark matter*. Phys. Rev. Lett. **72** (1994) 17–20, arXiv:hep-ph/9303287 [hep-ph].

[65] A. Boyarsky, A. Neronov, O. Ruchayskiy, M. Shaposhnikov, and I. Tkachev, *Where to find a dark matter sterile neutrino?* Phys. Rev. Lett. **97** (2006) 261302, arXiv:astro-ph/0603660 [astro-ph].

[66] A. Boyarsky, A. Neronov, O. Ruchayskiy, and M. Shaposhnikov, *Restrictions on parameters of sterile neutrino dark matter from observations of galaxy clusters*. Phys. Rev. **D74** (2006) 103506, arXiv:astro-ph/0603368 [astro-ph].

[67] V. Kuzmin and I. Tkachev, *Ultrahigh-energy cosmic rays, superheavy long living particles, and matter creation after inflation*. JETP Lett. **68** (1998) 271–275, arXiv:hep-ph/9802304 [hep-ph]. [Pisma Zh. Eksp. Teor. Fiz.68,255(1998)].

[68] V. Kuzmin and I. Tkachev, *Matter creation via vacuum fluctuations in the early universe and observed ultrahigh-energy cosmic ray events*. Phys. Rev. **D59** (1999) 123006, arXiv:hep-ph/9809547 [hep-ph].

[69] D. J. H. Chung, E. W. Kolb, and A. Riotto, *Superheavy dark matter*. Phys. Rev. **D59** (1999) 023501, arXiv:hep-ph/9802238 [hep-ph].

[70] E. W. Kolb, D. J. H. Chung, and A. Riotto, "WIMPzillas!," in *Trends in theoretical physics II. Proceedings, 2nd La Plata Meeting, Buenos Aires, Argentina, November 29-December 4, 1998*, pp. 91–105. 1998. arXiv:hep-ph/9810361 [hep-ph]. http://lss.fnal.gov/cgi-bin/find_paper.pl?conf-98-325. [,91(1998)].

[71] A. Kusenko and M. E. Shaposhnikov, *Supersymmetric Q balls as dark matter*. Phys. Lett. **B418** (1998) 46–54, arXiv:hep-ph/9709492 [hep-ph].

[72] A. Kusenko, L. Loveridge, and M. Shaposhnikov, *Supersymmetric dark matter Q-balls and their interactions in matter*. Phys. Rev. **D72** (2005) 025015, arXiv:hep-ph/0405044 [hep-ph].

[73] M. Yu. Khlopov and C. Kouvaris, *Strong Interactive Massive Particles from a Strong Coupled Theory*. Phys. Rev. **D77** (2008) 065002, arXiv:0710.2189 [astro-ph].

[74] L. J. Hall, K. Jedamzik, J. March-Russell, and S. M. West, *Freeze-In Production of FIMP Dark Matter*. JHEP **03** (2010) 080, arXiv:0911.1120 [hep-ph].

[75] Y. B. Zel'dovich, L. B. Okun, and S. B. Pikelner, *something*. Usp. Fiz. Nauk. **84** (1965) 113.

[76] H.-Y. Chiu, *Symmetry between particle and anti-particle populations in the universe*. Phys. Rev. Lett. **17** (1966) 712.

[77] E. Kolb and M. Turner, *The Early Universe*. Westview Press, 1994.

[78] M. Srednicki, R. Watkins, and K. A. Olive, *Calculations of Relic Densities in the Early Universe*. Nucl.Phys. **B310** (1988) 693.

[79] S. R. Coleman and J. Mandula, *All Possible Symmetries of the S Matrix*. Phys. Rev. **159** (1967) 1251–1256.

[80] R. Haag, J. T. Lopuszanski, and M. Sohnius, *All Possible Generators of Supersymmetries of the s Matrix*. Nucl. Phys. **B88** (1975) 257.

[81] G. 't Hooft and M. J. G. Veltman, *One loop divergencies in the theory of gravitation*. Annales Poincare Phys. Theor. **A20** (1974) 69–94.

[82] P. van Nieuwenhuizen and J. A. M. Vermaseren, *One Loop Divergences in the Quantum Theory of Supergravity*. Phys. Lett. **B65** (1976) 263.

[83] S. P. Martin, *A Supersymmetry primer*. arXiv:hep-ph/9709356 [hep-ph]. [Adv. Ser. Direct. High Energy Phys.18,1(1998)].

[84] M. Drees, R. Godbole, and P. Roy, *Theory and phenomenology of sparticles: An account of four-dimensional N=1 supersymmetry in high energy physics*. 2004.

[85] S. Weinberg, *The quantum theory of fields. Vol. 3: Supersymmetry*. Cambridge University Press, 2013.

[86] L. Girardello and M. T. Grisaru, *Soft Breaking of Supersymmetry*. Nucl. Phys. **B194** (1982) 65.

[87] L. J. Hall and M. Suzuki, *Explicit R-Parity Breaking in Supersymmetric Models*. Nucl. Phys. **B231** (1984) 419.

[88] J. R. Ellis, G. Gelmini, C. Jarlskog, G. G. Ross, and J. W. F. Valle, *Phenomenology of Supersymmetry with Broken R-Parity*. Phys. Lett. **B150** (1985) 142.

[89] I. J. R. Aitchison, *Supersymmetry and the MSSM: An Elementary introduction*. arXiv:hep-ph/0505105 [hep-ph].

[90] N. Arkani-Hamed, S. Dimopoulos, and G. R. Dvali, *The Hierarchy problem and new dimensions at a millimeter*. Phys. Lett. **B429** (1998) 263–272, arXiv:hep-ph/9803315 [hep-ph].

[91] N. Arkani-Hamed, S. Dimopoulos, and G. R. Dvali, *Phenomenology, astrophysics and cosmology of theories with submillimeter dimensions and TeV scale quantum gravity*. Phys. Rev. **D59** (1999) 086004, arXiv:hep-ph/9807344 [hep-ph].

[92] H. Davoudiasl, R. Kitano, G. D. Kribs, and H. Murayama, *Models of neutrino*

mass with a low cutoff scale. Phys. Rev. **D71** (2005) 113004, arXiv:hep-ph/0502176 [hep-ph].

[93] L. Randall and R. Sundrum, *A Large mass hierarchy from a small extra dimension*. Phys. Rev. Lett. **83** (1999) 3370–3373, arXiv:hep-ph/9905221 [hep-ph].

[94] L. Randall and R. Sundrum, *An Alternative to compactification*. Phys. Rev. Lett. **83** (1999) 4690–4693, arXiv:hep-th/9906064 [hep-th].

[95] T. Kaluza, *On the Problem of Unity in Physics*. Sitzungsber.Preuss.Akad.Wiss.Berlin (Math.Phys.) **1921** (1921) 966–972.

[96] O. Klein, *Quantum Theory and Five-Dimensional Theory of Relativity. (In German and English)*. Z.Phys. **37** (1926) 895–906.

[97] G. Servant and T. M. Tait, *Is the lightest Kaluza-Klein particle a viable dark matter candidate?* Nucl.Phys. **B650** (2003) 391–419, arXiv:hep-ph/0206071 [hep-ph].

[98] D. Hooper and S. Profumo, *Dark matter and collider phenomenology of universal extra dimensions*. Phys.Rept. **453** (2007) 29–115, arXiv:hep-ph/0701197 [hep-ph].

[99] I. Antoniadis, C. Munoz, and M. Quiros, *Dynamical supersymmetry breaking with a large internal dimension*. Nucl. Phys. **B397** (1993) 515–538, arXiv:hep-ph/9211309 [hep-ph].

[100] I. Antoniadis, S. Dimopoulos, A. Pomarol, and M. Quiros, *Soft masses in theories with supersymmetry breaking by TeV compactification*. Nucl. Phys. **B544** (1999) 503–519, arXiv:hep-ph/9810410 [hep-ph].

[101] T. Appelquist, B. A. Dobrescu, E. Ponton, and H.-U. Yee, *Proton stability in six-dimensions*. Phys. Rev. Lett. **87** (2001) 181802, arXiv:hep-ph/0107056 [hep-ph].

[102] B. A. Dobrescu and E. Poppitz, *Number of fermion generations derived from anomaly cancellation*. Phys. Rev. Lett. **87** (2001) 031801, arXiv:hep-ph/0102010 [hep-ph].

[103] H.-C. Cheng, K. T. Matchev, and M. Schmaltz, *Radiative corrections to Kaluza-Klein masses*. Phys. Rev. **D66** (2002) 036005, arXiv:hep-ph/0204342 [hep-ph].

[104] J. F. Navarro, A. Ludlow, V. Springel, J. Wang, M. Vogelsberger, *et al.*, *The Diversity and Similarity of Cold Dark Matter Halos*. arXiv:0810.1522 [astro-ph].

[105] J. F. Navarro, C. S. Frenk, and S. D. White, *The Structure of cold dark matter halos*. Astrophys.J. **462** (1996) 563–575, arXiv:astro-ph/9508025 [astro-ph].

[106] A. W. Graham, D. Merritt, B. Moore, J. Diemand, and B. Terzic, *Empirical models for Dark Matter Halos. I. Nonparametric Construction of Density Profiles and Comparison with Parametric Models*. Astron.J. **132** (2006) 2685–2700, arXiv:astro-ph/0509417 [astro-ph].

[107] M. Cirelli, G. Corcella, A. Hektor, G. Hutsi, M. Kadastik, *et al.*, *PPPC 4 DM ID: A Poor Particle Physicist Cookbook for Dark Matter Indirect Detection*. JCAP **1103** (2011) 051, arXiv:1012.4515 [hep-ph].

[108] V. R. Eke, J. F. Navarro, and M. Steinmetz, *The Power spectrum dependence of dark matter halo concentrations*. Astrophys. J. **554** (2001) 114–125, arXiv:astro-ph/0012337 [astro-ph].

[109] N. Fornengo, L. Pieri, and S. Scopel, *Neutralino annihilation into gamma-rays in the Milky Way and in external galaxies*. Phys. Rev. **D70** (2004) 103529, arXiv:hep-ph/0407342 [hep-ph].

[110] D. Abercrombie *et al.*, *Dark Matter Benchmark Models for Early LHC Run-2 Searches: Report of the ATLAS/CMS Dark Matter Forum*. arXiv:1507.00966 [hep-ex].

[111] T. M. Undagoitia and L. Rauch, *Dark matter direct-detection experiments*. J. Phys. **G43** (2016) no. 1, 013001, arXiv:1509.08767 [physics.ins-det].

[112] **CMS** Collaboration, S. Chatrchyan *et al.*, *The CMS experiment at the CERN LHC*. JINST **3** (2008) S08004.

[113] **ATLAS** Collaboration, G. Aad *et al.*, *The ATLAS Experiment at the CERN Large Hadron Collider*. JINST **3** (2008) S08003.

[114] **ATLAS** Collaboration, G. Aad *et al.*, *Search for new phenomena in events with a photon and missing transverse momentum in pp collisions at $\sqrt{s} = 8$ TeV with the ATLAS detector*. Phys. Rev. **D91** (2015) no. 1, 012008, arXiv:1411.1559 [hep-ex]. [Erratum: Phys. Rev.D92,no.5,059903(2015)].

[115] **ATLAS** Collaboration, G. Aad *et al.*, *Search for new phenomena in final states with an energetic jet and large missing transverse momentum in pp collisions at $\sqrt{s}$ =8 TeV with the ATLAS detector*. Eur. Phys. J. **C75** (2015) no. 7, 299, arXiv:1502.01518 [hep-ex]. [Erratum: Eur. Phys. J.C75,no.9,408(2015)].

[116] **CMS** Collaboration, V. Khachatryan *et al.*, *Search for physics beyond the standard model in final states with a lepton and missing transverse energy in proton-proton collisions at sqrt(s) = 8 TeV*. Phys. Rev. **D91** (2015) no. 9, 092005, arXiv:1408.2745 [hep-ex].

[117] **CMS** Collaboration, V. Khachatryan *et al.*, *Search for dark matter and unparticles produced in association with a Z boson in proton-proton collisions at sqrt(s) = 8 TeV*. arXiv:1511.09375 [hep-ex].

[118] J. D. Lewin and P. F. Smith, *Review of mathematics, numerical factors, and corrections for dark matter experiments based on elastic nuclear recoil*. Astropart. Phys. **6** (1996) 87–112.

[119] **DAMA** Collaboration, R. Bernabei *et al.*, *The DAMA/LIBRA apparatus*. Nucl. Instrum. Meth. **A592** (2008) 297–315, arXiv:0804.2738 [astro-ph].

[120] R. Bernabei *et al.*, *DAMA/LIBRA-phase1 results and perspectives of the phase2*. EPJ Web Conf. **95** (2015) 03001.

[121] K. Abe *et al.*, *XMASS detector*. Nucl. Instrum. Meth. **A716** (2013) 78–85, arXiv:1301.2815 [physics.ins-det].

[122] **XMASS** Collaboration, J. Liu, *The XMASS experiment*. AIP Conf. Proc. **1604** (2014) 397–401.

[123] **CoGeNT** Collaboration, C. E. Aalseth *et al.*, *Results from a Search for Light-Mass Dark Matter with a P-type Point Contact Germanium Detector*. Phys. Rev. Lett. **106** (2011) 131301, arXiv:1002.4703 [astro-ph.CO].

[124] M. Buehler *et al.*, *Status and low background considerations for the CRESST dark matter search*. Nucl. Instrum. Meth. **A370** (1996) 237–240.

[125] **CRESST** Collaboration, M. Bravin *et al.*, *The CRESST dark matter search*. Astropart. Phys. **12** (1999) 107–114, arXiv:hep-ex/9904005 [hep-ex].

[126] **XENON** Collaboration, J. Angle *et al.*, *First Results from the XENON10 Dark Matter Experiment at the Gran Sasso National Laboratory*. Phys. Rev. Lett. **100**

(2008) 021303, arXiv:0706.0039 [astro-ph].

[127] **XENON** Collaboration, E. Aprile *et al.*, *Design and Performance of the XENON10 Dark Matter Experiment*. Astropart. Phys. **34** (2011) 679–698, arXiv:1001.2834 [astro-ph.IM].

[128] **XENON100** Collaboration, E. Aprile *et al.*, *First Dark Matter Results from the XENON100 Experiment*. Phys. Rev. Lett. **105** (2010) 131302, arXiv:1005.0380 [astro-ph.CO].

[129] **XENON100** Collaboration, E. Aprile *et al.*, *The XENON100 Dark Matter Experiment*. Astropart. Phys. **35** (2012) 573–590, arXiv:1107.2155 [astro-ph.IM].

[130] **XENON** Collaboration, E. Aprile *et al.*, *Physics reach of the XENON1T dark matter experiment*. Submitted to: JCAP (2015) , arXiv:1512.07501 [physics.ins-det].

[131] **LUX** Collaboration, D. S. Akerib *et al.*, *The Large Underground Xenon (LUX) Experiment*. Nucl. Instrum. Meth. **A704** (2013) 111–126, arXiv:1211.3788 [physics.ins-det].

[132] **LUX** Collaboration, D. S. Akerib *et al.*, *First results from the LUX dark matter experiment at the Sanford Underground Research Facility*. Phys. Rev. Lett. **112** (2014) 091303, arXiv:1310.8214 [astro-ph.CO].

[133] **LUX** Collaboration, D. S. Akerib *et al.*, *Improved WIMP scattering limits from the LUX experiment*. arXiv:1512.03506 [astro-ph.CO].

[134] **DarkSide** Collaboration, P. Agnes *et al.*, *First Results from the DarkSide-50 Dark Matter Experiment at Laboratori Nazionali del Gran Sasso*. Phys. Lett. **B743** (2015) 456–466, arXiv:1410.0653 [astro-ph.CO].

[135] C. E. Aalseth *et al.*, *The DarkSide Multiton Detector for the Direct Dark Matter Search*. Adv. High Energy Phys. **2015** (2015) 541362.

[136] S. Cebrian *et al.*, *First results of the ROSEBUD dark matter experiment*. Astropart. Phys. **15** (2001) 79–85, arXiv:astro-ph/0004292 [astro-ph].

[137] S. Cebrian *et al.*, *The ROSEBUD experiment at Canfranc: 2001 report*. Nucl. Phys. Proc. Suppl. **110** (2002) 97–99, arXiv:astro-ph/0112272 [astro-ph]. [,97(2001)].

[138] G. Angloher *et al.*, *Results from 730 kg days of the CRESST-II Dark Matter Search*. Eur. Phys. J. **C72** (2012) 1971, arXiv:1109.0702 [astro-ph.CO].

[139] **CRESST-II** Collaboration, G. Angloher *et al.*, *Results on low mass WIMPs using an upgraded CRESST-II detector*. Eur. Phys. J. **C74** (2014) no. 12, 3184, arXiv:1407.3146 [astro-ph.CO].

[140] **SuperCDMS** Collaboration, R. Agnese *et al.*, *Search for Low-Mass Weakly Interacting Massive Particles Using Voltage-Assisted Calorimetric Ionization Detection in the SuperCDMS Experiment*. Phys. Rev. Lett. **112** (2014) no. 4, 041302, arXiv:1309.3259 [physics.ins-det].

[141] **SuperCDMS** Collaboration, R. Agnese *et al.*, *Search for Low-Mass Weakly Interacting Massive Particles with SuperCDMS*. Phys. Rev. Lett. **112** (2014) no. 24, 241302, arXiv:1402.7137 [hep-ex].

[142] **EDELWEISS** Collaboration, A. Benoit *et al.*, *First results of the EDELWEISS WIMP search using a 320-g heat-and-ionization Ge detector*. Phys. Lett. **B513** (2001) 15–22, arXiv:astro-ph/0106094 [astro-ph].

[143] **EDELWEISS** Collaboration, E. Armengaud *et al.*, *A search for low-mass*

WIMPs with EDELWEISS-II heat-and-ionization detectors. Phys. Rev. **D86** (2012) 051701, arXiv:1207.1815 [astro-ph.CO].

[144] D. Feldman, Z. Liu, and P. Nath, *The Stueckelberg Z-prime Extension with Kinetic Mixing and Milli-Charged Dark Matter From the Hidden Sector*. Phys. Rev. **D75** (2007) 115001, arXiv:hep-ph/0702123 [HEP-PH].

[145] E. Bulbul, M. Markevitch, A. R. Foster, R. K. Smith, M. Loewenstein, and S. W. Randall, *Comment on "Dark matter searches going bananas: the contribution of Potassium (and Chlorine) to the 3.5 keV line"*. arXiv:1409.4143 [astro-ph.HE].

[146] **IceCube** Collaboration, J. Ahrens *et al.*, *Icecube - the next generation neutrino telescope at the south pole*. Nucl. Phys. Proc. Suppl. **118** (2003) 388–395, arXiv:astro-ph/0209556 [astro-ph]. [,388(2002)].

[147] **IceCube** Collaboration, M. G. Aartsen *et al.*, *Improved limits on dark matter annihilation in the Sun with the 79-string IceCube detector and implications for supersymmetry*. arXiv:1601.00653 [hep-ph].

[148] **Super-Kamiokande** Collaboration, T. Tanaka *et al.*, *An Indirect Search for WIMPs in the Sun using 3109.6 days of upward-going muons in Super-Kamiokande*. Astrophys. J. **742** (2011) 78, arXiv:1108.3384 [astro-ph.HE].

[149] **Super-Kamiokande** Collaboration, K. Choi *et al.*, *Search for neutrinos from annihilation of captured low-mass dark matter particles in the Sun by Super-Kamiokande*. Phys. Rev. Lett. **114** (2015) no. 14, 141301, arXiv:1503.04858 [hep-ex].

[150] L. E. Strigari, *Galactic Searches for Dark Matter*. Phys. Rept. **531** (2013) 1–88, arXiv:1211.7090 [astro-ph.CO].

[151] **HESS** Collaboration, J. A. Hinton, *The Status of the H.E.S.S. project*. New Astron. Rev. **48** (2004) 331–337, arXiv:astro-ph/0403052 [astro-ph].

[152] **HESS** Collaboration, F. Aharonian *et al.*, *H.E.S.S. observations of the Galactic Center region and their possible dark matter interpretation*. Phys. Rev. Lett. **97** (2006) 221102, arXiv:astro-ph/0610509 [astro-ph]. [Erratum: Phys. Rev. Lett.97,249901(2006)].

[153] **HESS** Collaboration, A. Abramowski *et al.*, *Search for Photon-Linelike Signatures from Dark Matter Annihilations with H.E.S.S.* Phys. Rev. Lett. **110** (2013) 041301, arXiv:1301.1173 [astro-ph.HE].

[154] **VERITAS** Collaboration, R. W. Lessard, *VERITAS: the Very Energetic Radiation Imaging Telescope Array System*. Astropart. Phys. **11** (1999) 243–246.

[155] **VERITAS** Collaboration, R. G. Wagner, *Indirect Dark Matter Searches with VERITAS*. arXiv:0910.4563 [astro-ph.HE].

[156] **VERITAS** Collaboration, T. Arlen *et al.*, *Constraints on Cosmic Rays, Magnetic Fields, and Dark Matter from Gamma-Ray Observations of the Coma Cluster of Galaxies with VERITAS and Fermi*. Astrophys. J. **757** (2012) 123, arXiv:1208.0676 [astro-ph.HE].

[157] **MAGIC** Collaboration, J. Aleksic *et al.*, *Searches for Dark Matter annihilation signatures in the Segue 1 satellite galaxy with the MAGIC-I telescope*. JCAP **1106** (2011) 035, arXiv:1103.0477 [astro-ph.HE].

[158] **MAGIC** Collaboration, C. Baixeras, *The MAGIC telescope*. Nucl. Phys. Proc. Suppl. **114** (2003) 247–252. [,247(2003)].

[159] **Fermi-LAT** Collaboration, W. B. Atwood *et al.*, *The Large Area Telescope on the Fermi Gamma-ray Space Telescope Mission*. Astrophys. J. **697** (2009) 1071–1102, arXiv:0902.1089 [astro-ph.IM].

[160] **Fermi-LAT** Collaboration, M. Ackermann *et al.*, *Search for gamma-ray spectral lines with the Fermi large area telescope and dark matter implications*. Phys. Rev. **D88** (2013) 082002, arXiv:1305.5597 [astro-ph.HE].

[161] **Fermi-LAT** Collaboration, M. Ackermann *et al.*, *Dark matter constraints from observations of 25 Milky Way satellite galaxies with the Fermi Large Area Telescope*. Phys. Rev. **D89** (2014) 042001, arXiv:1310.0828 [astro-ph.HE].

[162] **Fermi-LAT** Collaboration, M. Ackermann *et al.*, *Limits on Dark Matter Annihilation Signals from the Fermi LAT 4-year Measurement of the Isotropic Gamma-Ray Background*. JCAP **1509** (2015) no. 09, 008, arXiv:1501.05464 [astro-ph.CO].

[163] **Fermi-LAT** Collaboration, M. Ackermann *et al.*, *Searching for Dark Matter Annihilation from Milky Way Dwarf Spheroidal Galaxies with Six Years of Fermi Large Area Telescope Data*. Phys. Rev. Lett. **115** (2015) no. 23, 231301, arXiv:1503.02641 [astro-ph.HE].

[164] **Fermi-LAT** Collaboration, M. Ackermann *et al.*, *Updated search for spectral lines from Galactic dark matter interactions with pass 8 data from the Fermi Large Area Telescope*. Phys. Rev. **D91** (2015) no. 12, 122002, arXiv:1506.00013 [astro-ph.HE].

[165] **CTA Consortium** Collaboration, M. Actis *et al.*, *Design concepts for the Cherenkov Telescope Array CTA: An advanced facility for ground-based high-energy gamma-ray astronomy*. Exper. Astron. **32** (2011) 193–316, arXiv:1008.3703 [astro-ph.IM].

[166] **CTA Consortium** Collaboration, M. Doro *et al.*, *Dark Matter and Fundamental Physics with the Cherenkov Telescope Array*. Astropart. Phys. **43** (2013) 189–214, arXiv:1208.5356 [astro-ph.IM].

[167] P. Salati, *Indirect and direct dark matter detection*. PoS **CARGESE2007** (2007) 009.

[168] M. Boezio *et al.*, *The Cosmic-Ray Electron and Positron Spectra Measured at 1 AU during Solar Minimum Activity*. Astrophys. J. **532** (2000) 653–669.

[169] **HEAT** Collaboration, S. W. Barwick *et al.*, *Measurements of the cosmic ray positron fraction from 1-GeV to 50-GeV*. Astrophys. J. **482** (1997) L191–L194, arXiv:astro-ph/9703192 [astro-ph].

[170] **AMS** Collaboration, J. Alcaraz *et al.*, *Leptons in near earth orbit*. Phys. Lett. **B484** (2000) 10–22. [Erratum: Phys. Lett.B495,440(2000)].

[171] **PAMELA Collaboration** Collaboration, O. Adriani *et al.*, *An anomalous positron abundance in cosmic rays with energies 1.5-100GeV*Nature **458** (Apr., 2009) 607–609, arXiv:0810.4995.

[172] **Fermi-LAT** Collaboration, M. Ackermann *et al.*, *Measurement of separate cosmic-ray electron and positron spectra with the Fermi Large Area Telescope*. Phys. Rev. Lett. **108** (2012) 011103, arXiv:1109.0521 [astro-ph.HE].

[173] **AMS Collaboration** Collaboration, M. Aguilar *et al.*, *Electron and Positron Fluxes in Primary Cosmic Rays Measured with the Alpha Magnetic Spectrometer on the International Space Station*. Phys.Rev.Lett. **113** (2014) 121102.

[174] **PAMELA Collaboration** Collaboration, O. Adriani *et al.*, *PAMELA Results*

*on the Cosmic-Ray Antiproton Flux from 60 MeV to 180 GeV in Kinetic Energy*Physical Review Letters **105** (Sept., 2010) 121101, arXiv:1007.0821 [astro-ph.HE].

[175] **AMS** Collaboration, A. collaboration, *Talk at the AMS Days at CERN, April 15-17, 2015*. AMS Days at CERN, April 15-17, 2015 .

[176] V. Hess, *ber Beobachtungen der durchdringenden Strahlung bei sieben Freiballonfahrten*. Physikalische Zeitschrift **13** (1912) 1084–1091.

[177] V. Ginzburg and S. Syrovatskii, *The origin of Cosmic Rays*. Pergamon Press, 1964.

[178] T. Gaisser, *Cosmic Rays and Particle Physics*. Cambridge University Press, 1990.

[179] **Particle Data Group** Collaboration, K. A. Olive *et al.*, *Review of Particle Physics*. Chin. Phys. **C38** (2014) 090001.

[180] M. Kachelriess, *Lecture notes on high energy cosmic rays*. arXiv:0801.4376 [astro-ph].

[181] **AMS** Collaboration, M. Aguilar *et al.*, *Precision Measurement of the Proton Flux in Primary Cosmic Rays from Rigidity 1 GV to 1.8 TV with the Alpha Magnetic Spectrometer on the International Space Station*. Phys.Rev.Lett. **114** (2015) no. 17, 171103.

[182] A. E. Vladimirov, S. W. Digel, G. Johannesson, P. F. Michelson, I. V. Moskalenko, P. L. Nolan, E. Orlando, T. A. Porter, and A. W. Strong, *GALPROP WebRun: an internet-based service for calculating galactic cosmic ray propagation and associated photon emissions*. Comput. Phys. Commun. **182** (2011) 1156–1161, arXiv:1008.3642 [astro-ph.HE].

[183] L. Gleeson and W. Axford, *Solar Modulation of Galactic Cosmic Rays*. Astrophys.J. **154** (1968) 1011.

[184] H.-C. Cheng, J. L. Feng, and K. T. Matchev, *Kaluza-Klein dark matter*. Phys.Rev.Lett. **89** (2002) 211301, arXiv:hep-ph/0207125 [hep-ph].

[185] J. R. Ellis, J. Hagelin, D. V. Nanopoulos, K. A. Olive, and M. Srednicki, *Supersymmetric Relics from the Big Bang*. Nucl.Phys. **B238** (1984) 453–476.

[186] N. F. Bell, J. B. Dent, T. D. Jacques, and T. J. Weiler, *Electroweak Bremsstrahlung in Dark Matter Annihilation*. Phys.Rev. **D78** (2008) 083540, arXiv:0805.3423 [hep-ph].

[187] K. Kong and K. T. Matchev, *Precise calculation of the relic density of Kaluza-Klein dark matter in universal extra dimensions*. JHEP **0601** (2006) 038, arXiv:hep-ph/0509119 [hep-ph].

[188] K. Griest, *Cross-Sections, Relic Abundance and Detection Rates for Neutralino Dark Matter*. Phys. Rev. **D38** (1988) 2357. [Erratum: Phys. Rev.D39,3802(1989)].

[189] J. Alwall, R. Frederix, S. Frixione, V. Hirschi, F. Maltoni, O. Mattelaer, H. S. Shao, T. Stelzer, and M. Zaro, *The automated computation of tree-level and next-to-leading order differential cross sections, a and their matching to parton shower simulations.* JHEP **07** (2014) 079, arXiv:1405.0301 [hep-ph].

[190] J. Alwall, M. Herquet, F. Maltoni, O. Mattelaer, and T. Stelzer, *MadGraph 5 : Going Beyond*. JHEP **1106** (2011) 128, arXiv:1106.0522 [hep-ph].

[191] A. Belyaev, N. D. Christensen, and A. Pukhov, *CalcHEP 3.4 for collider physics within and beyond the Standard Model*. Comput.Phys.Commun. **184** (2013) 1729–1769, arXiv:1207.6082 [hep-ph].

[192] H. Goldberg, *Constraint on the Photino Mass from Cosmology*. Phys.Rev.Lett. **50** (1983) 1419.

[193] H. Goldberg, *Erratum: Constraint on the Photino Mass from Cosmology*. Phys. Rev. Lett. **103** (2009) 099905.

[194] C. Barbot and M. Drees, *Production of ultraenergetic cosmic rays through the decay of superheavy X particles*. Phys.Lett. **B533** (2002) 107–115, arXiv:hep-ph/0202072 [hep-ph].

[195] V. Berezinsky, M. Kachelriess, and S. Ostapchenko, *Electroweak jet cascading in the decay of superheavy particles*. Phys.Rev.Lett. **89** (2002) 171802, arXiv:hep-ph/0205218 [hep-ph].

[196] C. Barbot and M. Drees, *Detailed analysis of the decay spectrum of a super heavy X particle*. Astropart.Phys. **20** (2003) 5–44, arXiv:hep-ph/0211406 [hep-ph].

[197] M. Kachelriess and P. Serpico, *Model-independent dark matter annihilation bound from the diffuse γ ray flux*. Phys.Rev. **D76** (2007) 063516, arXiv:0707.0209 [hep-ph].

[198] J. B. Dent, R. J. Scherrer, and T. J. Weiler, *Toward a Minimum Branching Fraction for Dark Matter Annihilation into Electromagnetic Final States*. Phys.Rev. **D78** (2008) 063509, arXiv:0806.0370 [astro-ph].

[199] V. Barger, Y. Gao, W. Y. Keung, and D. Marfatia, *Generic dark matter signature for gamma-ray telescopes*. Phys.Rev. **D80** (2009) 063537, arXiv:0906.3009 [hep-ph].

[200] J.-F. Fortin, J. Shelton, S. Thomas, and Y. Zhao, *Gamma Ray Spectra from Dark Matter Annihilation and Decay*. arXiv:0908.2258 [hep-ph].

[201] M. Kachelriess, P. Serpico, and M. A. Solberg, *On the role of electroweak bremsstrahlung for indirect dark matter signatures*. Phys.Rev. **D80** (2009) 123533, arXiv:0911.0001 [hep-ph].

[202] P. Ciafaloni and A. Urbano, *TeV scale Dark Matter and electroweak radiative corrections*. Phys.Rev. **D82** (2010) 043512, arXiv:1001.3950 [hep-ph].

[203] N. F. Bell, J. B. Dent, T. D. Jacques, and T. J. Weiler, *W/Z Bremsstrahlung as the Dominant Annihilation Channel for Dark Matter*. Phys.Rev. **D83** (2011) 013001, arXiv:1009.2584 [hep-ph].

[204] N. F. Bell, J. B. Dent, T. D. Jacques, and T. J. Weiler, *Dark Matter Annihilation Signatures from Electroweak Bremsstrahlung*. Phys.Rev. **D84** (2011) 103517, arXiv:1101.3357 [hep-ph].

[205] N. F. Bell, J. B. Dent, A. J. Galea, T. D. Jacques, L. M. Krauss, *et al.*, *W/Z Bremsstrahlung as the Dominant Annihilation Channel for Dark Matter, Revisited*. Phys.Lett. **B706** (2011) 6–12, arXiv:1104.3823 [hep-ph].

[206] P. Ciafaloni, M. Cirelli, D. Comelli, A. De Simone, A. Riotto, *et al.*, *On the Importance of Electroweak Corrections for Majorana Dark Matter Indirect Detection*. JCAP **1106** (2011) 018, arXiv:1104.2996 [hep-ph].

[207] M. Garny, A. Ibarra, and S. Vogl, *Antiproton constraints on dark matter annihilations from internal electroweak bremsstrahlung*. JCAP **1107** (2011) 028, arXiv:1105.5367 [hep-ph].

[208] M. Garny, A. Ibarra, and S. Vogl, *Dark matter annihilations into two light fermions and one gauge boson: General analysis and antiproton constraints*. JCAP **1204** (2012) 033, arXiv:1112.5155 [hep-ph].

[209] P. Ciafaloni, D. Comelli, A. De Simone, A. Riotto, and A. Urbano, *Electroweak*

Bremsstrahlung for Wino-Like Dark Matter Annihilations. JCAP **1206** (2012) 016, arXiv:1202.0692 [hep-ph].

[210] N. F. Bell, A. J. Brennan, and T. D. Jacques, *Neutrino signals from electroweak bremsstrahlung in solar WIMP annihilation*. JCAP **1210** (2012) 045, arXiv:1206.2977 [hep-ph].

[211] P. Ciafaloni, D. Comelli, A. De Simone, E. Morgante, A. Riotto, *et al.*, *The Role of Electroweak Corrections for the Dark Matter Relic Abundance*. JCAP **1310** (2013) 031, arXiv:1305.6391 [hep-ph].

[212] T. Bringmann and F. Calore, *Significant Enhancement of Neutralino Dark Matter Annihilation from Electroweak Bremsstrahlung*. Phys.Rev.Lett. **112** (2014) 071301, arXiv:1308.1089 [hep-ph].

[213] P. Ciafaloni and D. Comelli, *Sudakov enhancement of electroweak corrections*. Phys.Lett. **B446** (1999) 278–284, arXiv:hep-ph/9809321 [hep-ph].

[214] T. Sjostrand, S. Mrenna, and P. Z. Skands, *PYTHIA 6.4 Physics and Manual*. JHEP **0605** (2006) 026, arXiv:hep-ph/0603175 [hep-ph].

[215] T. Sjostrand, S. Mrenna, and P. Z. Skands, *A Brief Introduction to PYTHIA 8.1*. Comput.Phys.Commun. **178** (2008) 852–867, arXiv:0710.3820 [hep-ph].

[216] M. Ciafaloni, P. Ciafaloni, and D. Comelli, *Towards collinear evolution equations in electroweak theory*. Phys.Rev.Lett. **88** (2002) 102001, arXiv:hep-ph/0111109 [hep-ph].

[217] P. Ciafaloni and D. Comelli, *Electroweak evolution equations*. JHEP **0511** (2005) 022, arXiv:hep-ph/0505047 [hep-ph].

[218] G. Altarelli and G. Parisi, *Asymptotic Freedom in Parton Language*. Nucl. Phys. **B126** (1977) 298.

[219] A. Datta, K. Kong, and K. T. Matchev, *Minimal Universal Extra Dimensions in CalcHEP/CompHEP*. New J.Phys. **12** (2010) 075017, arXiv:1002.4624 [hep-ph].

[220] T. Hahn, *Generating Feynman diagrams and amplitudes with FeynArts 3*. Comput.Phys.Commun. **140** (2001) 418–431, arXiv:hep-ph/0012260 [hep-ph].

[221] T. Hahn and C. Schappacher, *The Implementation of the minimal supersymmetric standard model in FeynArts and FormCalc*. Comput.Phys.Commun. **143** (2002) 54–68, arXiv:hep-ph/0105349 [hep-ph].

[222] L. Ali Cavasonza, M. Kraemer, and M. Pellen, *Electroweak fragmentation functions for dark matter annihilation*. JCAP **1502** (2015) no. 02, 021, arXiv:1409.8226 [hep-ph].

[223] **AMS** Collaboration, M. Aguilar *et al.*, *Precision Measurement of the $(e^+ + e)$ Flux in Primary Cosmic Rays from 0.5 GeV to 1 TeV with the Alpha Magnetic Spectrometer on the International Space Station*. Phys.Rev.Lett. **113** (2014) 221102.

[224] J. J. Beatty, A. Bhattacharyya, C. Bower, S. Coutu, M. A. Duvernois, S. McKee, S. A. Minnick, D. Müller, J. Musser, S. Nutter, A. W. Labrador, M. Schubnell, S. Swordy, G. Tarlé, and A. Tomasch, *New Measurement of the Cosmic-Ray Positron Fraction from 5 to 15GeV*Physical Review Letters **93** (Dec., 2004) 241102, arXiv:astro-ph/0412230.

[225] **PAMELA Collaboration** Collaboration, O. Adriani *et al.*, *Cosmic-Ray Positron Energy Spectrum Measured by PAMELA*Physical Review Letters **111** (Aug., 2013) 081102, arXiv:1308.0133 [astro-ph.HE].

[226] M. t. **FERMI LAT** collaboration, Ackermann, *Measurement of Separate Cosmic-Ray Electron and Positron Spectra with the Fermi Large Area Telescope*Physical Review Letters **108** (Jan., 2012) 011103, arXiv:1109.0521 [astro-ph.HE].

[227] I. Cholis and D. Hooper, *Dark Matter and Pulsar Origins of the Rising Cosmic Ray Positron Fraction in Light of New Data From AMS*. Phys. Rev. **D88** (2013) 023013, arXiv:1304.1840 [astro-ph.HE].

[228] T. Linden and S. Profumo, *Probing the Pulsar Origin of the Anomalous Positron Fraction with AMS-02 and Atmospheric Cherenkov Telescopes*. Astrophys. J. **772** (2013) 18, arXiv:1304.1791 [astro-ph.HE].

[229] L. Feng, R.-Z. Yang, H.-N. He, T.-K. Dong, Y.-Z. Fan, and J. Chang, *AMS-02 positron excess: new bounds on dark matter models and hint for primary electron spectrum hardening*. Phys. Lett. **B728** (2014) 250–255, arXiv:1303.0530 [astro-ph.HE].

[230] M. Boudaud, S. Aupetit, S. Caroff, A. Putze, G. Belanger, *et al.*, *A new look at the cosmic ray positron fraction*. arXiv:1410.3799 [astro-ph.HE].

[231] M. Cirelli, M. Kadastik, M. Raidal, and A. Strumia, *Model-independent implications of the e+-, anti-proton cosmic ray spectra on properties of Dark Matter*. Nucl.Phys. **B813** (2009) 1–21, arXiv:0809.2409 [hep-ph].

[232] F. Donato, D. Maurin, P. Brun, T. Delahaye, and P. Salati, *Constraints on WIMP Dark Matter from the High Energy PAMELA $\bar{p}/p$ data*. Phys.Rev.Lett. **102** (2009) 071301, arXiv:0810.5292 [astro-ph].

[233] L. Bergstrom, J. Edsjo, and G. Zaharijas, *Dark matter interpretation of recent electron and positron data*. Phys.Rev.Lett. **103** (2009) 031103, arXiv:0905.0333 [astro-ph.HE].

[234] D. P. Finkbeiner, L. Goodenough, T. R. Slatyer, M. Vogels er, and N. Weiner, *Consistent Scenarios for Cosmic-Ray Excesses from Sommerfeld-Enhanced Dark Matter Annihilation*. JCAP **1105** (2011) 002, arXiv:1011.3082 [hep-ph].

[235] Q. Yuan, X.-J. Bi, G.-M. Chen, Y.-Q. Guo, S.-J. Lin, *et al.*, *Implications of the AMS-02 positron fraction in cosmic rays*. Astropart.Phys. **60** (2015) 1–12, arXiv:1304.1482 [astro-ph.HE].

[236] H.-B. Jin, Y.-L. Wu, and Y.-F. Zhou, *Implications of the first AMS-02 measurement for dark matter annihilation and decay*. JCAP **1311** (2013) 026, arXiv:1304.1997 [hep-ph].

[237] G. Bertone, M. Cirelli, A. Strumia, and M. Taoso, *Gamma-ray and radio tests of the e+e- excess from DM annihilations*. JCAP **0903** (2009) 009, arXiv:0811.3744 [astro-ph].

[238] L. Bergstrom, T. Bringmann, I. Cholis, D. Hooper, and C. Weniger, *New limits on dark matter annihilation from AMS cosmic ray positron data*. Phys.Rev.Lett. **111** (2013) 171101, arXiv:1306.3983 [astro-ph.HE].

[239] A. Ibarra, A. S. Lamperstorfer, and J. Silk, *Dark matter annihilations and decays after the AMS-02 positron measurements*. Phys. Rev. **D89** (2014) no. 6, 063539, arXiv:1309.2570 [hep-ph].

[240] **AMS** Collaboration, S. Schael, *The Electron Spectrum and Positron Spectrum from AMS*. AMS Days at CERN, April 15-17, 2015 .

[241] S. S. Wilks, *The Large-Sample Distribution of the Likelihood Ratio for Testing Composite Hypotheses*. Annals Math. Statist. **9** (1938) no. 1, 60–62.

[242] **PAMELA** Collaboration, O. Adriani *et al.*, *PAMELA results on the cosmic-ray antiproton flux from 60 MeV to 180 GeV in kinetic energy*. Phys.Rev.Lett. **105** (2010) 121101, arXiv:1007.0821 [astro-ph.HE].

[243] G. Giesen, M. Boudaud, Y. Genolini, V. Poulin, M. Cirelli, *et al.*, *AMS-02 antiprotons, at last! Secondary astrophysical component and immediate implications for Dark Matter*. arXiv:1504.04276 [astro-ph.HE].

[244] M. di Mauro, F. Donato, A. Goudelis, and P. D. Serpico, *New evaluation of the antiproton production cross section for cosmic ray studies*. Phys. Rev. **D90** (2014) no. 8, 085017, arXiv:1408.0288 [hep-ph].

[245] R. Kappl and M. W. Winkler, *The Cosmic Ray Antiproton Background for AMS-02*. JCAP **1409** (2014) 051, arXiv:1408.0299 [hep-ph].

[246] N. D. Christensen and C. Duhr, *FeynRules - Feynman rules made easy*. Comput. Phys. Commun. **180** (2009) 1614–1641, arXiv:0806.4194 [hep-ph].

[247] G. Passarino and M. J. G. Veltman, *One Loop Corrections for e+ e- Annihilation Into mu+ mu- in the Weinberg Model*. Nucl. Phys. **B160** (1979) 151.

[248] V. Hirschi and O. Mattelaer, *Automated event generation for loop-induced processes*. JHEP **10** (2015) 146, arXiv:1507.00020 [hep-ph].

[249] R. Mertig, M. Bohm, and A. Denner, *FEYN CALC: Computer algebraic calculation of Feynman amplitudes*. Comput. Phys. Commun. **64** (1991) 345–359.

[250] V. Shtabovenko, R. Mertig, and F. Orellana, *New Developments in FeynCalc 9.0*. arXiv:1601.01167 [hep-ph].

[251] T. Hahn and M. Perez-Victoria, *Automatized one loop calculations in four-dimensions and D-dimensions*. Comput.Phys.Commun. **118** (1999) 153–165, arXiv:hep-ph/9807565 [hep-ph].

[252] T. Hahn, *Loop calculations with FeynArts, FormCalc, and LoopTools*. Acta Phys. Polon. **B30** (1999) 3469–3475, arXiv:hep-ph/9910227 [hep-ph].

[253] T. Hahn, *Automatic loop calculations with FeynArts, FormCalc, and LoopTools*. Nucl. Phys. Proc. Suppl. **89** (2000) 231–236, arXiv:hep-ph/0005029 [hep-ph].

[254] **NNPDF** Collaboration, R. D. Ball *et al.*, *Parton distributions for the LHC Run II*. JHEP **04** (2015) 040, arXiv:1410.8849 [hep-ph].

[255] F. Donato, N. Fornengo, D. Maurin, and P. Salati, *Antiprotons in cosmic rays from neutralino annihilation*. Phys. Rev. **D69** (2004) 063501, arXiv:astro-ph/0306207 [astro-ph].

[256] T. Delahaye, R. Lineros, F. Donato, N. Fornengo, and P. Salati, *Positrons from dark matter annihilation in the galactic halo: Theoretical uncertainties*. Phys. Rev. **D77** (2008) 063527, arXiv:0712.2312 [astro-ph].

[257] M. Bohm, A. Denner, and H. Joos, *Gauge theories of the strong and electroweak interaction*. 2001.